



University
of Glasgow

Bregenzer, Josef Johann (2010) *Integrated polarisation rotators*. PhD thesis.

<http://theses.gla.ac.uk/1573/>

Copyright and moral rights for this thesis are retained by the author

A copy can be downloaded for personal non-commercial research or study, without prior permission or charge

This thesis cannot be reproduced or quoted extensively from without first obtaining permission in writing from the Author

The content must not be changed in any way or sold commercially in any format or medium without the formal permission of the Author

When referring to this work, full bibliographic details including the author, title, awarding institution and date of the thesis must be given.

INTEGRATED POLARISATION ROTATORS

Josef Johann Bregenzer

A thesis
submitted to the Department of Electronics & Electrical Engineering,
Faculty of Engineering, of the University of Glasgow
in partial fulfilment of the requirements for the degree of
Doctor of Philosophy

*Es ist nicht genug zu wissen, man muss auch anwenden;
es ist nicht genug zu wollen, man muss auch tun.*

JOHANN WOLFGANG VON GOETHE, MAXIMEN UND REFLEXIONEN

Abstract

The ability to control and manipulate the state of polarisation of optical signals is becoming an increasingly desirable feature in numerous photonic applications including integrated optical circuits, semiconductor optical amplifiers (SOAs) and optical communication systems.

This thesis introduces the design, optimisation, fabrication and operation of two novel integrated reciprocal single-section passive polarisation converter devices based upon mode-beating. The converter designs consist of asymmetric profiled waveguides, which were realised in a single reactive ion dry-etch process step. An in-situ custom built sample holder was utilised to place the samples at a predetermined angle to the incoming ions, which resulted in waveguide profiles with sloped sidewalls. This fabrication technique also allowed the incorporation of adiabatic taper sections within the device design.

The converter section waveguide profile of the first design consists of two sloped sidewalls. Devices realised on a GaAs/AlGaAs material structure achieved a converted transverse magnetic (TM) polarisation purity of 81.4% at a device length of $30\text{ }\mu\text{m}$ for a transverse electric (TE) polarised input signal at an operating wavelength of $\lambda = 1064\text{ nm}$. The convention used is that TE refers to light polarised in the plane of the wafer and TM refers to light polarised perpendicular to the plane of the wafer. The total optical loss imposed by this device was evaluated to be 1.72 dB. This design was also used for the monolithic integration of a passive polarisation converter incorporated within a Fabry-Perot semiconductor laser diode on an unstrained GaAs/AlGaAs double quantum well heterostructure material system. A predominantly TM polarised optical output from the converter facet of greater than 80% is demonstrated for a converter length of $20\text{ }\mu\text{m}$ at an emitting wavelength of 867.1 nm. The about 1.4 mm long fabricated device has a current threshold level of 100 mA and a side mode suppression ratio (SMSR) of 25 dB.

The second converter design is based on the modification of an already existing stripe waveguide structure. The converter section is defined by applying the above mentioned angled dry-etch process on a certain length of the stripe waveguide. The fabricated asymmetric waveguide core profile consists of a sloped undercut. A TM polarisation purity of 90% at a device length of $55\text{ }\mu\text{m}$ for a TE polarised input signal at an operating wavelength of $\lambda = 1064\text{ nm}$ was achieved at the output. The total optical loss imposed by this device was evaluated to be 0.47 dB.

Publications

Peer-reviewed journal

Bregenzer J. J., McMaster S., Sorel M., Holmes B. M., and Hutchings D. C., "Compact Polarization Mode Converter Monolithically Integrated within a Semiconductor Laser", *IEEE Journal of Lightwave Technology*, vol. **27**, no. 14, pp. 2732 - 2736, (2009).

Conference papers

McMaster S., **Bregenzer J. J.**, Sorel M., Holmes B. M., and Hutchings D. C., "Monolithic Integration of a Compact Passive Polarisation Converter within a Laser Diode", *Proceedings of the 14th. European Conference on Integrated Optics 2008 (ECIO'08)*, Eindhoven, The Netherlands, 11 - 13 June 2008, paper WeC5.

Bregenzer J. J., McMaster S., Sorel M., Holmes B. M., and Hutchings D. C., "Polarisation Mode Converter Monolithically Integrated within a Semiconductor Laser", *Proceedings of the Conference on Lasers & Electro-Optics 2008 (CLEO'08)*, San Jose, California, USA, 4 - 9 May 2008, paper CThM2.

Holmes B. M., **Bregenzer J. J.**, and Hutchings D. C., "Enabling Technologies for the Monolithic Integration of Semiconductor Lasers and Waveguide Optical Isolators", *Proceedings of the Conference on Lasers & Electro-Optics 2007 (CLEO'07)*, Baltimore, Maryland, USA, 8 - 10 May 2007, paper CTuH3.

Holmes B. M., **Bregenzer J. J.**, and Hutchings D. C., "Novel Fabrication Techniques for the Realisation of Passive Waveguide Polarisation Converters", *Proceedings of the Conference on Lasers & Electro-Optics 2005 (CLEO'05)*, Baltimore, Maryland, USA, 22 - 27 May 2005, paper CWD4.

Holmes B. M., Hutchings D. C., and **Bregenzer J. J.**, "Experiments Towards the Realisation of a Monolithically-Integrated Optical Isolator Incorporating Quasi-Phase Matched Magneto-Optical Effects", *Proceedings of the Material Research Society (MRS) Fall Meeting 2004*, Boston, MA, USA, 29 November - 3 December 2004, paper J4.4.

Bregenzer J. J., Holmes B. M., Sorel M., and Hutchings D. C., "Realization of a Single-section Passive Polarization Converter using a Single-step Etch Process", *Proceedings of the 17th Annual Meeting of the IEEE Lasers & Electro-Optics Society 2004 (LEOS'04)*, Rio Grande, Puerto Rico, 7 - 11 November 2004, paper TuA1.

Boardman A. D., Xie M., Egan P., Velasco L., Holmes B., **Bregenzer J.**, and Hutchings D., (invited), "Magneto-optic Devices, Materials and Technologies", *Proceedings of the NATO Advanced Research Workshop on Frontiers in Planar Lightwave Circuit Technology: Design, Simulation and Fabrication*, Ottawa, Canada, 21 - 25 September 2004.

Hutchings D. C., Holmes B. M., and **Bregenzer J. J.**, "Single Etch Step Fabrication of Passive Waveguide Mode Converters", *Proceedings of the 16th Conference on Quantum Electronics and Photonics 2004 (QEP-16)*, Glasgow Caledonian University, Glasgow, United Kingdom, 6 - 9 September 2004, paper QEP.P1.35.

Acknowledgements

I am deeply indebted to my academic supervisor Professor David C. Hutchings for accepting me as his PhD student and giving me the opportunity to work on this interesting and challenging project. His guidance, support and technical advices have been invaluable throughout the course of this project. He was always there when help, not only in academic matters, was needed. Thank you, Dave.

I also express my gratitude to my second academic supervisor Dr. Marc Sorel for his suggestions, critical comments and technical advice.

I would also like to thank the Engineering and Physical Sciences Research Council (EPSRC) and the Faculty of Engineering at the University of Glasgow for the financial support.

I also thank for the fruitful collaboration with the project partners at the University of Salford - led by Professor Allan D. Boardman and his co-workers Ming Xie and Larry Velasco - and at the University of Cambridge - led by the late Professor Tony Bland, who sadly already passed away too early in his life, and his co-workers Jean-Baptiste Laloe and Marina Tselepi.

Many thanks are due to the technical staff of the James Watt Nanofabrication Centre (JWNC), especially the dry-etch team Colin Roberts, Ronnie Roger and Mark Dragsnes and the electron-beam writer operators Dave Gourlay, Susan Ferguson, Mary Robertson, Helen McLelland, Davie McCloy, Linda Pollock, Robert Harkins, Eve Aitkenhead, Sara McFarlane and Fiona McEwan. Also, special thanks go to Bill Ward for his help and support regarding the laser lab facilities and Thomas Reilly for his help regarding thin-film evaporation.

Great thanks for the very good company and atmosphere in the office go to my colleagues Pierre Pottier, Lianping Hou, Thomas Slight, Corrie Farmer and Barry Holmes.

Thanks to my fellow students in the department Steven McMaster, John Harris, Iain Eddie, Masoud Murad, Sonia Holik, Ali Khokhar, Jennifer MacRitchie, Stanislav Markov, Urban Kovac, Marco Gnan, Francesca Pozzi, Basudev Lahiri, Grant Erwin, Daniel Balasz, Cheng Xing, Harold Chong, Iraklis Ntaklis, Edilson Camargo and Aju Jugessur for their good company and the many good laughs.

Contents

List of abbreviations	xi
List of mathematical symbols	xiii
List of Tables	xv
List of Figures	xvi

Chapter 1 Introduction	1
1.1 Background	1
1.1.1 Polarisation division multiplexing	2
1.1.2 Polarisation mode dispersion	3
1.1.3 Photonic integrated circuits	4
1.2 Potential applications of integrated passive polarisation rotators	5
1.2.1 Semiconductor heterostructure laser emitting transverse magnetic polarised signal	5
1.2.2 Integrated polarisation-independent amplification of optical signals	6
1.2.3 Integrated polarisation diversity scheme	7
1.2.4 Polarisation independent PHASAR-demultiplexer	8
1.2.5 Integrated optical isolator	9
1.3 Objectives and organisation of the thesis	10
1.4 References	11

Chapter 2 Theoretical background	18
2.1 Governing equations	18
2.2 Birefringence	20
2.2.1 Uniaxial crystal	22
2.3 Wave equation	23
2.4 Plane waves	24
2.5 Polarisation	25
2.6 Boundary conditions	26
2.7 Modal analysis of optical waveguides	27
2.7.1 One dimensional confinement: slab waveguide	28
2.7.2 Two dimensional confined waveguides	36
2.7.2.1 Semi-vectorial approximation	37
2.7.2.2 Scalar approximation	43
2.7.3 Beam propagation method	43
2.7.4 Mode solver	45
2.7.5 Optimisation of a passive optical stripe waveguide	46
2.8 Waveplates	48
2.9 References	53
	vii

Chapter 3 Integrated passive polarisation rotators:	
State of the art	56
3.1 Mode beating based device designs	57
3.1.1 Multiple section beating	57
3.1.2 Single section beating	61
3.2 Mode evolution based device designs	65
3.3 Concluding remarks	66
3.4 References	66
 Chapter 4 Fabrication method and measurement setups	 71
4.1 Dry-etch fabrication process utilising an in-situ sloped sample holder	71
4.1.1 Background	71
4.1.2 Principle	72
4.1.3 Realisation	74
4.2 Measurement setup	76
4.2.1 Evolution of waveguide losses	77
4.3 References	78
 Chapter 5 Passive polarisation converter comprising an asymmetric waveguide structure	 80
5.1 Introduction	80
5.2 Device optimisation	82
5.2.1 Optimisation of the waveguide width w	82
5.2.2 Optimisation of the waveguide top width w_T	83
5.2.3 Optimisation of the front slope angle ξ and undercut slope angle α	86
5.2.4 Optimisation of the taper section length L_{Taper}	88
5.2.5 Optimisation of the transversal offset τ	89
5.3 Analysis of the optimised converter section	91
5.4 Device fabrication	98
5.4.1 Fabrication process steps	98
5.4.2 Fabrication hurdle: mask misalignment	103
5.4.3 Solution to mask misalignment	105
5.4.4 Realised device	107
5.5 Device characterisation	107
5.5.1 Converted TM polarisation purity	107
5.5.2 Losses	109
5.5.3 Wavelength dependence	109
5.6 Summary	110
5.7 References	111

Chapter 6 Passive polarisation converter on a double quantum well structure

113

6.1 Introduction	113
6.2 Double quantum well material structure	114
6.3 Double quantum well material evaluation	115
6.4 Polarisation converter device design	119
6.5 Device optimisation	120
6.6 Analysis of the optimised device	122
6.7 Device fabrication	129
6.7.1 Fabrication steps	129
6.7.2 Realised device	131
6.8 Device characterisation	132
6.8.1 Converted TM polarisation purity	132
6.8.2 Losses	134
6.8.3 Wavelength stability	135
6.9 Summary	136
6.10 References	137

Chapter 7 Passive polarisation converter monolithically integrated within a semiconductor laser diode

138

7.1 Introduction	138
7.2 Device configuration	139
7.3 Device optimisation	140
7.3.1 Optimisation of the transversal offset τ	140
7.4 Device fabrication	142
7.4.1 Fabrication process steps	142
7.4.2 Realised device	149
7.5 Device characterisation	150
7.5.1 Emitting wavelength	150
7.5.2 Converted TM polarisation purity	151
7.5.3 Optical power emission versus injected current	153
7.5.4 Mode structure	155
7.6 Summary	157
7.7 References	157

Chapter 8 Passive polarisation converter comprising an undercut stripe waveguide

159

8.1 Introduction	159
8.2 Device configuration	160

8.3 Device optimisation	161
8.3.1 Optimisation of the waveguide top width w_T	161
8.3.2 Optimisation of the undercut angle α	163
8.3.3 Converter section fabrication tolerances	165
8.3.4 Optimisation of the taper section length L_{Taper}	165
8.3.5 Optimisation of the transversal offset τ	166
8.4 Analysis of the optimised device structure	167
8.5 Device fabrication	174
8.5.1 Fabrication process steps	174
8.5.2 Realised device	177
8.6 Device characterisation	178
8.6.1 Converted TM polarisation purity	178
8.6.2 Losses	179
8.6.3 Wavelength dependence	180
8.7 Summary	181
 Chapter 9 Conclusions and future perspectives	 182
9.1 References	184

List of abbreviations

Alphabetically listed are the major abbreviations that appear in this thesis. The *italic figure in brackets* indicates the page on which an abbreviation makes its first appearance or has its main definition.

ARDE	aspect-ratio dependent etching	[64]
BPM	beam propagation method	[43]
DGD ₁	differential group delay	[3]
DPSS	diode pumped solid state	[31]
DQW	double quantum well	[114]
DWDM	dense wavelength division multiplex	[1]
EDFA	erbium doped fibre amplifier	[1]
EME	eigenmode expansion	[45]
f	fast	[48]
FD	finite difference	[45]
FEM	finite element method	[33]
FFT	fast fourier transform	[45]
FPR	free propagation range	[8]
hh	heavy-hole	[5]
HSQ	hydrogen silsequioxane	[183]
IPA	isopropyl alcohol	[98]
ITU	International Telecommunication Union	[1]
lh	light-hole	[5]
MIBK	methyl isobutyl ketone	[98]
MMI	multimode interference	[4]
MO	magneto-optic	[9]
MOCVD	metal-organic chemical-vapour deposition	[47]
MZI	Mach-Zehnder interferometer	[4]
NGN	next generation network services	[1]
OEIC	optoelectronic integrated circuit	[1]
OSL	oxide stripe laser	[115]
PDM	polarisation division multiplex	[2]
PECVD	plasma enhanced chemical vapour deposition	[74]
PHASAR	phased-arrays	[8]
PIC	photonic integrated circuit	[1]
PMD	polarisation mode dispersion	[3]
PMF	polarisation maintaining fibre	[4]
PMMA	polymethyl methacrylate	[98]
PSP	principal state of polarisation	[3]
QW	quantum well	[5]

QWI	quantum well intermixing	[183]
RF	radio frequency	[72]
RIE	reactive ion etch	[64]
RO	reverse osmosis	[74]
RTA	rapid thermal annealer	[148]
s	slow	[48]
SCH	separate confinement heterostructure	[114]
SMSR	side mode suppression ratio	[150]
SOA	semiconductor optical amplifier	[6]
SOI	silicon on insulator	[56]
SOP	state of polarisation	[3]
SSMF	standard single mode fibre	[4]
SVEA	slowly varying envelope approximation	[43]
TE	transverse electric	[29]
TEM	transverse electromagnetic	[25]
TM	transverse magnetic	[33]
VLSI	very large scale integrated	[1]

List of mathematical symbols

Alphabetically listed are the major mathematical symbols that appear in this thesis. The *italic figure in brackets* indicates the page on which a symbol makes its first appearance or has its main definition.

$\mathfrak{B}(\mathbf{r}, t)$	magnetic flux density vector	[18]
c_0	velocity of light in vacuum	[18]
d	waveguide layer thickness	[28]
D_{PMD}	PMD parameter	[4]
D_x, D_y, D_z	components of \mathbf{D} in Cartesian coordinate system	[20]
\mathbf{D}	time-invariant electric displacement vector	[20]
$\mathcal{D}(\mathbf{r}, t)$	electric displacement vector	[18]
e	charge of an electron	[116]
E_x, E_y, E_z	components of \mathbf{E} in Cartesian coordinate system	[20]
\mathbf{E}	time-invariant electric field vector	[19]
$\mathcal{E}(\mathbf{r}, t)$	electric field vector	[18]
f	laser frequency	[116]
h	Planck's constant	[116]
h_{stripe}	stripe waveguide height	[46]
H_x, H_y, H_z	components of \mathbf{H} in Cartesian coordinate system	[28]
\mathbf{H}	time-invariant magnetic field vector	[19]
$\mathcal{H}(\mathbf{r}, t)$	magnetic field vector	[18]
I_{th}	laser threshold current	[116]
J_{INF}	threshold current density for infinite length	[118]
J_{th}	threshold current density	[118]
$\mathcal{J}(\mathbf{r}, t)$	current density	[18]
k	wave number	[24]
k_0	wave number in vacuum	[24]
L	converter section length	[81]
L_{Beat}	beat length	[49]
$L_{\text{Beat}/2}$	half beat length	[49]
$L_{\text{Beat}/4}$	quarter beat length	[50]
L_{CAVITY}	laser cavity length	[115]
L_{Taper}	length of linear taper	[88]
n	refractive index of the material	[24]
\mathbf{n}	unit normal vector	[22]
N	number of half-wave plates	[51]
n_{eff}	effective refractive index	[27]
$n_{\text{eff}, \text{group}}$	effective group index	[156]
n_{REF}	reference index	[44]

P_C	TM polarisation purity	[51]
P_{INPUT}	input power	[90]
P_{OUTPUT}	transmitted power	[90]
\mathbf{r}	position vector	[18]
R_1, R_2	power reflectivity of laser facet	[117]
t	time	[3]
v_p	phase velocity	[24]
w	symmetric stripe waveguide width	[80]
$w_{realign}$	transversal mask realignment stripe width	[105]
w_s	injection window stripe width	[115]
w_{stripe}	stripe waveguide width	[46]
w_T	waveguide top width	[81]
x	Cartesian coordinate system axis	[18]
y	Cartesian coordinate system axis	[18]
z	Cartesian coordinate system axis	[18]
α	undercut slope angle	[74]
α_{ABS}	absorption coefficient	[117]
β	propagation constant	[27]
δ	rotation of optical axis with respect to vertical y -axis	[52]
$\Delta\lambda$	fringe period	[156]
$\Delta\tau_1$	differential group delay	[3]
Δn	refractive index contrast	[28]
$\Delta v_{p,eff}$	differential phase velocity	[3]
ε_0	dielectric permittivity of vacuum	[18]
ε_r	relative dielectric permittivity of the material	[18]
η_{INT}	internal stimulated quantum efficiency	[116]
η_{EXT}	differential external quantum efficiency	[116]
κ	power overlap	[52]
λ	spatial wavelength	[24]
λ_0	wavelength in vacuum	[24]
Λ	insertion loss coefficient	[77]
μ_0	magnetic permeability of vacuum	[18]
μ_r	relative magnetic permeability of the material	[18]
ν	mode label	[27]
ξ	front slope angle	[74]
ρ	volume density of free electric charges	[18]
τ	transversal offset	[89]
φ	rotation of optical axis with respect to horizontal x -axis	[48]
ϕ_x, ϕ_y	phase factor	[25]
Ψ	phase difference	[48]
Ψ_{REL}	relative phase difference	[48]
ω	angular frequency	[19]
Ω	propagation loss coefficient	[77]
Ω_W	computational window	[31]

List of Tables

Chapter 3

Table 3-1:	Overview of proposed and realised passive polarisation rotators based on asymmetric periodically loaded rib waveguides (λ ...operating wavelength, P_C ...Polarisation conversion).	58
Table 3-2:	Device parameter overview of a realised passive polarisation rotator based on laterally tilted rib waveguides grown on a stepped substrate structure.	59
Table 3-3:	Device parameter overview of a realised passive polarisation rotator based on asymmetric periodically loaded angled-facet rib waveguides.	60
Table 3-4:	Overview of proposed and realised longitudinally-invariant passive polarisation converter using a slanted angle rib waveguide. (The converter length denoted in the table equals the half beat length of the converter section.)	62
Table 3-5:	Overview of proposed and realised passive polarisation rotators based on deep angled-etched sub-wavelength air trenches.	63
Table 3-6:	Overview of realised passive polarisation rotators based on vertical etched sub-wavelength air trenches utilising the RIE lag phenomenon. The converter length denotes the half beat length of the converter section. (P_C ...polarisation conversion)	64
Table 3-7:	Device parameter of a theoretically proposed passive polarisation converter based on the principle of mode evolution.	65

Chapter 4

Table 4-1:	Standard RIE process recipe for GaAs material at room temperature.	74
------------	--	----

Chapter 6

Table 6-1:	Wafer material composition of the double quantum well laser structure.	114
------------	--	-----

List of Figures

Chapter 1

Figure 1-1:	Schematic of the <i>dense wavelength division multiplex</i> (DWDM) principle (unidirectional).	2
Figure 1-2:	Schematic of the principle of the <i>polarisation division multiplexing</i> (PDM) technique in optical data transmission systems (only one wavelength channel in unidirectional transmission illustrated).	2
Figure 1-3:	Conceptual illustration of the effect of <i>polarisation mode dispersion</i> (PMD) in a short, linear birefringent fibre element in the time domain. . .	3
Figure 1-4:	Schematic of an integrated monolithical combination of a semiconductor heterostructure laser and a passive polarisation rotator in order to establish a TM polarised output signal.	6
Figure 1-5:	Two possible configurations for an integrated polarisation-independent amplifier circuit: (a) parallel circuit structure and (b) series circuit structure.	6
Figure 1-6:	Integrated polarisation diversity scheme.	7
Figure 1-7:	Schematic of a polarisation-independent PHASAR demultiplexer with inserted integrated polarisation converters in the centre.	8
Figure 1-8:	Schematic of the functionality of a monolithically integrated optical isolator.	9

Chapter 2

Figure 2-1:	(a) Indicatrix for a positive uniaxial crystal ($n_x = n_y = n_o < n_z = n_e$). The inner ellipse (shaded) is the intersection of the indicatrix with the plane perpendicular to \mathbf{n} . (b) Graphical evaluation of the two allowed directions of polarisation and corresponding refractive indices ($n^{(1)}, n^{(2)}$) for a given direction \mathbf{n} from the formed ellipse.	22
Figure 2-2:	Description of polarisation as the trace of the electric field in the plane (x, y) perpendicular to the direction of propagation z . A right-hand elliptic polarised field is illustrated as an example according to the convention that a field is called right handed polarised when the field is looked at as it propagates towards the observer and performs a clockwise rotation. . .	25
Figure 2-3:	Boundary scenario between two media with different material constants. The unit normal vector \mathbf{n} is perpendicular to the surface at the transition point.	26
Figure 2-4:	Schematic of a longitudinal invariant optical waveguide and the choice of the orientation of the Cartesian coordinate system. The waveguide is described by the refractive index profile $n(x, y)$	27
Figure 2-5:	Schematic of an asymmetric slab waveguide and the chosen orientation of the Cartesian coordinate system.	28

Figure 2-6:	(Top) Illustration of the distribution of the different regimes of the propagation constant β - and therefore the types of modes - of the dielectric slab waveguide. (Bottom) Illustration of the $E_x(y)$ field distributions to the corresponding regime of β	30
Figure 2-7:	(a)-(d) Illustration of the electric vector field with corresponding profile plots of the fundamental TE mode (TE_0) components in a dielectric slab waveguide. The principal electric field component of the TE_0 mode is E_x	31
Figure 2-8:	(a)-(d) Illustration of the magnetic vector field with corresponding profile plots of the fundamental TE mode (TE_0) components in a dielectric slab waveguide. The principal magnetic field component of the TE_0 mode is H_y	32
Figure 2-9:	(a)-(d) Illustration of the electric vector field with corresponding profile plots of the fundamental TM mode (TM_0) components in a dielectric slab waveguide. The principal electric field component of the TM_0 mode is E_y	34
Figure 2-10:	(a)-(d) Illustration of the magnetic vector field with corresponding profile plots of the fundamental TM mode (TM_0) components in a dielectric slab waveguide. The principal magnetic field component of the TM_0 mode is H_x	35
Figure 2-11:	(a)-(g) Illustration of the electric vector field with corresponding profile plots of the fundamental TE mode (TE_0) components in a dielectric stripe waveguide. The predominant electric field component of the TE_0 mode is given by the E_x component.	39
Figure 2-12:	(a)-(g) Illustration of the magnetic vector field with corresponding profile plots of the fundamental TE mode (TE_0) components in a dielectric stripe waveguide. The predominant magnetic field component of the TE_0 mode is given by the H_y component.	40
Figure 2-13:	(a)-(g) Illustration of the electric vector field with corresponding profile plots of the fundamental TM mode (TM_0) components in a dielectric stripe waveguide. The predominant electric field component of the TM_0 mode is given by the E_y component.	41
Figure 2-14:	(a)-(g) Illustration of the magnetic vector field with corresponding profile plots of the fundamental TM mode (TM_0) components in a dielectric stripe waveguide. The predominant magnetic field component of the TM_0 mode is given by the H_x component.	42
Figure 2-15:	Wavelength dependence of the refractive index of GaAs and different AlGaAs compositions.	46
Figure 2-16:	Single mode regime for different stripe waveguide geometries.	47
Figure 2-17:	Decomposition of the incident \mathbf{E} field vector.	48
Figure 2-18:	Illustration of the functionality of a waveplate consisting of a uniaxial crystal. (a) Independent propagation of fast and slow ray within the waveplate. (b) Evolution of the SOP of a linearly polarised input beam through various elliptical SOP over one beat length L_{Beat} . (c) Comparison between input- and output SOP of a half-wave plate.	49

- Figure 2-19: Illustration of equivalent optical axes orientation in both (a) general bulk half-wave plate and (b) integrated TE \rightarrow TM polarisation converter. The SOP of the electric fields corresponds to linearly polarised input signals. 50
- Figure 2-20: Principle of cascading half-wave plates of alternating equal tilts of the optical axis in order to achieve an accumulated relative phase difference Ψ_{REL} of π between the two propagating rays. (a) $N = 1$ ($\varphi = 45^\circ$), (b) $N = 2$ ($\varphi = 22.5^\circ$), (c) $N = 3$, ($\varphi = 15^\circ$) and (d) $N = 4$ ($\varphi = 11.25^\circ$) 51

Chapter 3

- Figure 3-1: Overview of realised integrated passive polarisation converter technologies. 56
- Figure 3-2: Schematic of the device configuration of an asymmetrically-loaded rib waveguide polarisation converter. 57
- Figure 3-3: (a) Schematic cross section of the feeding waveguide (A-A') and the converter section (B-B'). (b) Top view of the passive 45° polarisation rotator based on periodically tilted rib waveguides. 58
- Figure 3-4: Schematic illustration of a passive polarisation converter design incorporating asymmetric periodically loaded angled-facet rib waveguides. 59
- Figure 3-5: (a) Schematic of a deeply etched bended ridge waveguide structure. (b) Top view of the schematic layout of the polarisation converter device (the segment angle is depicted as ϑ). 60
- Figure 3-6: 3D schematic of a longitudinally-invariant passive polarisation converter comprising a slanted angle rib waveguide (including input and output rib waveguides). (Insert) Waveguide profile of the converter section. 61
- Figure 3-7: 3D schematic of a passive polarisation converter based on deep angled-etched air trenches. (Insert) Waveguide profile of the converter section. . 63
- Figure 3-8: 3D schematic of a passive polarisation converter based on vertical etched sub-wavelength air trenches utilising the RIE lag phenomenon. (Insert) Waveguide profile of the cross section (here: three vertical etched air trenches). 64
- Figure 3-9: Passive polarisation converter based on mode-evolution consisting of (a) tapered upper and lower core layers and (b) tapered and separated upper and lower core layers. 65

Chapter 4

- Figure 4-1: Photograph of the *Oxford Instruments System 100TM* (S100) RIE machine in the James Watt Nanofabrication Centre (JWNC) at the University of Glasgow, which was used in order to fabricate the asymmetric waveguide profile structures (in conjunction with the specially designed sampleholder). 72
- Figure 4-2: Schematic diagram of a conventional parallel plate type RIE machine. . . 77
- Figure 4-3: Customised sample holder incorporating a recessed slanted groove. 73
- Figure 4-4: Sample holder placed on a 4" Si carrier wafer in the manually loaded load lock of the *Oxford Instruments System 100TM* RIE machine. 73

Figure 4-5:	Dependence of the etched front slope angle ζ and undercut slope angle α on the tilt of the slope of the sample holder with respect to the horizontal axis. The used GaAs RIE process parameters were: process gas: SiCl_4 , forward RF power = 100 W, process pressure = 9 mTorr, corrected gas flow = 9 sccm, BIAS = -345 V, table temperature = 35 °C.	75
Figure 4-6:	Schematic of the device measurement setup comprising a Nd:YAG laser and utilising the end-fire coupling technique.	76
 Chapter 5		
Figure 5-1:	Schematic of the design and functionality of the integrated polarisation converter (a) Evolution of the polarisation state of a TE polarised input signal in the device. (b) Device configuration (not to scale). (Insert) Waveguide profile of the converter section defined by the front slope angle ζ , undercut slope angle α and waveguide top width w_T . The orientations of the optical axes, which determine the orientation of the excited lowest order modes (mode 1 and mode 2), are indicated by the chain dotted line (mode 1) and dashed line (mode 2).	81
Figure 5-2:	Effective refractive index of the excited guided modes in a symmetric stripe waveguide versus the waveguide width w for an operating wavelength $\lambda = 1064$ nm.	83
Figure 5-3:	(a) Effective refractive index of the excited guided modes in an asymmetric ($\zeta = \alpha = 60^\circ$ and $\zeta = \alpha = 45^\circ$) stripe waveguide versus the waveguide top width w_T . (b) Power overlap κ and half beat length $L_{\text{Beat}/2}$ of an asymmetric ($\zeta = \alpha = 60^\circ$ and $\zeta = \alpha = 45^\circ$) stripe waveguide versus the waveguide top width w_T . (c) Rotation of optical axis δ with respect to the vertical axis and TM polarisation purity P_C of an asymmetric ($\zeta = \alpha = 60^\circ$ and $\zeta = \alpha = 45^\circ$) stripe waveguide versus w_T . ($\lambda = 1064$ nm).	84
Figure 5-4:	Simulated dependence of the optimised waveguide top width w_T on both the front slope angle ζ and undercut slope angle α for an operating wavelength $\lambda = 1064$ nm.	85
Figure 5-5:	Simulated corresponding half beat length $L_{\text{Beat}/2}$ for the optimised waveguide top width w_T dependent on both the front slope angle ζ and undercut slope angle α for an operating wavelength of $\lambda = 1064$ nm. . . .	86
Figure 5-6:	Simulated dependence of the power overlap at optimised w_T on both the front slope angle ζ and undercut slope angle α for an operating wavelength $\lambda = 1064$ nm.	87
Figure 5-7:	Simulated rotation of the optical axis δ with respect to the vertical axis at optimised waveguide top width w_T dependent on both the front slope angle ζ and undercut slope angle α for an operating wavelength of $\lambda = 1064$ nm.	87
Figure 5-8:	Dependence of the simulated TM polarisation purity for a TE polarised input signal at optimised w_T and device length of corresponding $L_{\text{Beat}/2}$ on	

	both the front slope angle ζ and undercut slope angle α for an operating wavelength of $\lambda = 1064$ nm.	88
Figure 5-9:	Optical power loss of the fundamental TE mode (TE_0) versus the taper length L_{Taper} ($\lambda = 1064$ nm).	89
Figure 5-10:	Illustration of the overlap of the mode profile contour plots (here: magnitude of the E_x component for the case of a TE polarised input signal) directly before ($L = 0^-$ (grey line)) and directly after ($L = 0^+$ (dashed line)) the intersection between converter- and intermediate- (or output-) waveguide section.	90
Figure 5-11:	Dependence of the intersection loss on the symmetric stripe waveguide width w and the transversal converter section offset τ at the intersection between intermediate- (or output-) waveguide section and converter waveguide section at an operating wavelength of $\lambda = 1064$ nm.	91
Figure 5-12:	(a)-(e) Electric vector field plot and corresponding mode profile and contour plot of the transverse (x, y) components of fundamental mode 1 in the optimised asymmetric waveguide. The structure comprises a front slope angle ζ and an undercut slope angle α of both 62° with respect to the horizontal axis and a waveguide top width w_T of 710 nm in the core profile for an operating wavelength $\lambda = 1064$ nm.	92
Figure 5-13:	(a)-(e) Electric vector field plot and corresponding mode profile and contour plot of the transverse (x, y) components of fundamental mode 2 in the optimised asymmetric waveguide. The structure comprises a front slope angle ζ and an undercut slope angle α of both 62° with respect to the horizontal axis and a waveguide top width w_T of 710 nm in the core profile for an operating wavelength $\lambda = 1064$ nm.	93
Figure 5-14:	(a)-(e) Magnetic vector field plot and corresponding mode profile and contour plot of the transverse (x, y) components of fundamental mode 1 in the optimised asymmetric waveguide. The structure comprises a front slope angle ζ and an undercut slope angle α of both 62° with respect to the horizontal axis and a waveguide top width w_T of 710 nm in the core profile for an operating wavelength $\lambda = 1064$ nm.	94
Figure 5-15:	(a)-(e) Magnetic vector field plot and corresponding mode profile and contour plot of the transverse (x, y) components of fundamental mode 2 in the optimised asymmetric waveguide. The structure comprises a front slope angle ζ and an undercut slope angle α of both 62° with respect to the horizontal axis and a waveguide top width w_T of 710 nm in the core profile for an operating wavelength $\lambda = 1064$ nm.	95
Figure 5-16:	Top view of the simulated contour plot of both the E_x (TE) and E_y (TM) component of a TE_0 mode launched from the intermediate waveguide section into the optimised converter section. Inserts: Magnitude of both E_x and E_y components at $L = 0 \mu\text{m}$, $L = L_{Beat/4} = 17.5 \mu\text{m}$ and $L = L_{Beat/2} = 35 \mu\text{m}$	97
Figure 5-17:	(a)-(i) Schematic process flow diagram of the realised polarisation converter device (part 1).	100

Figure 5-18: (j)-(r) Schematic process flow diagram of the realised polarisation converter device (part 2).	101
Figure 5-19: Remasking misalignment at the converter section periphery. (a) Optical micrograph of the top view of the device after definition of the waveguide outlines before conducting an etch-step in the fabrication process. (b) SEM micrograph of the top view of the misaligned intersection between the intermediate waveguide section and the converter section of the fabricated device.	104
Figure 5-20: Introduction of transversal rib waveguide mask realignment stripes at the converter section periphery in the device design.	105
Figure 5-21: Calculated dependence of the occurring insertion loss on the width $w_{realign}$ of the introduced transversal mask realignment stripes.	106
Figure 5-22: Impact of the introduced transversal stripes at the converter section periphery on the mask realignment. (a) Optical micrograph of the top view of the device after definition of the waveguide outlines and before a conducted etch-step in the fabrication process. (b) SEM micrograph of the top view of the intersection between the intermediate waveguide section and converter section of the fabricated device. The introduced transversal mask realignment stripe width $w_{realign}$ is 500 nm.	106
Figure 5-23: SEM micrograph of the fabricated polarisation converter cross section consisting of two slanted sidewalls. The realised front slope angle ξ and undercut slope angle α are about 32° and 52° , respectively, with respect to the horizontal plane. The defined waveguide top width w_T is about 570 nm.	107
Figure 5-24: TM polarisation purity versus converter section length of the fabricated device (simulated and measured) and the theoretical optimised device for an operational wavelength of $\lambda = 1064$ nm.	108
Figure 5-25: Measured normalised total output power versus different converter section lengths of the device for an operating wavelength of $\lambda = 1064$ nm. The extrapolation of the measured data is indicated by the chain-dotted line governed by the equation $y = -0.0055x + 0.58$	109
Figure 5-26: Simulated wavelength dependence of the TM polarisation purity P_C for the theoretically optimised device and the fabricated device.	110

Chapter 6

Figure 6-1: Schematic illustration of an oxide stripe injection laser with SiO_2 insulation (not to scale).	115
Figure 6-2: Measured dependence of the optical power emission on the injected current of $75 \mu\text{m}$ wide oxide stripe lasers with different laser cavity lengths L_{CAVITY} at a temperature of 25°C	116
Figure 6-3: Relationship between the inverse of the external quantum efficiency η_{EXT} and the cavity length L_{CAVITY} . The linear solid trendline is governed by the equation $y = 0.0068x + 4.1$	117

- Figure 6-4: Relationship between the natural logarithm of the threshold current density J_{th} and the inverse of the cavity length L_{CAVITY} . The linear solid trendline is governed by the equation $y = 0.024x + 6.59$ 118
- Figure 6-5: Schematic of the design and functionality of the passive linear taper and polarisation converter structure on double quantum well material. (a) Evolution of the polarisation state of a TE polarised signal launched into the device. (b) Device configuration (not to scale). (Insert) Definition of waveguide profile parameters (front slope angle ξ , undercut slope angle α and waveguide top width w) and illustration of the orientation of the optical axes which determine the orientation of the excited lowest order modes (mode 1 (chain dotted line) and mode 2 (dashed line)) in the waveguide. 119
- Figure 6-6: Calculated optimum double quantum well converter waveguide cross section profile for equal front slope angle ξ and undercut slope angle α at two different wavelengths ($\lambda = 867$ nm and $\lambda = 1064$ nm). (a) Optimised waveguide width w versus equal angles of the sidewall slopes. (b) Half beat length $L_{Beat/2}$ versus equal angles of the sidewall slopes. (c) Resulting rotation of optical axis δ of the waveguide (with respect to the vertical axis) and power overlap κ versus equal angles of the sidewall slopes. (d) Resulting TM polarisation purity P_C versus equal angles of the sidewall slopes. 121
- Figure 6-7: (a)-(e) Electric vector field plot and corresponding mode profile and contour plot of the transverse (x, y) components for one (mode 1) of two fundamental modes in the optimised asymmetric waveguide. The structure comprises a front slope angle ξ and an undercut slope angle α of both 52° with respect to the horizontal axis and a waveguide top width w of 960 nm for an operating wavelength of $\lambda = 1064$ nm. 123
- Figure 6-8: (a)-(e) Electric vector field plot and corresponding mode profile and contour plot of the transverse (x, y) components for one (mode 2) of two fundamental modes in the optimised asymmetric waveguide. The structure comprises a front slope angle ξ , and an undercut slope angle α of both 52° with respect to the horizontal axis and a waveguide top width w of 960 nm for an operating wavelength of $\lambda = 1064$ nm. 124
- Figure 6-9: (a)-(e) Magnetic vector field plot and corresponding mode profile and contour plot of the transverse (x, y) components for one (mode 1) of two fundamental modes in the optimised asymmetric waveguide. The structure comprises a front slope angle ξ , and an undercut slope angle α of both 52° with respect to the horizontal axis and a waveguide top width w of 960 nm for an operating wavelength of $\lambda = 1064$ nm. 125
- Figure 6-10: (a)-(e) Magnetic vector field plot and corresponding mode profile and contour plot of the transverse (x, y) components for one (mode 2) of two fundamental modes in the optimised asymmetric waveguide. The structure comprises a front slope angle ξ and an undercut slope angle α of

	both 52° with respect to the horizontal axis and a waveguide top width w of 960 nm for an operating wavelength of $\lambda = 1064$ nm.	126
Figure 6-11:	Top view of the simulated contour plots of the magnitude of the E_x (TE) and E_y (TM) component of a TE polarised signal launched into the theoretically optimised device ($\xi = \alpha = 52^\circ$, $w = 960$ nm) at an operating wavelength of $\lambda = 1064$ nm.	128
Figure 6-12:	(a)-(f) Schematic process flow diagram of the realised polarisation converter device on a double quantum well material structure.	130
Figure 6-13:	(a) Optical micrograph of the fabricated device showing the input waveguide, the linear adiabatic taper and the converter section waveguide. (b) SEM micrograph of the fabricated device showing the linear adiabatic taper and the beginning of the converter section. (c) Magnified SEM view of the deeply etched converter section waveguide cross section profile of the fabricated device.	131
Figure 6-14:	Top view of the simulated contour plots of the magnitude of the E_x (TE) and E_y (TM) component of a TE polarised signal launched into the fabricated device ($\xi = 50^\circ$, $\alpha = 55^\circ$, $w = 980$ nm) at an operating wavelength of $\lambda = 1064$ nm.	133
Figure 6-15:	TM polarisation purity P_C versus converter section length L of the measured fabricated device and the theoretically optimised device at an operating wavelength of $\lambda = 1064$ nm. (Insert) Magnified P_C versus L dependence at the beginning of the converter section.	134
Figure 6-16:	Measured normalised total output power versus different converter section lengths of the device for an operating wavelength of $\lambda = 1064$ nm. The extrapolation of the measured data is indicated by the chain-dotted line governed by the equation $y = -0.0009x + 0.58$	135
Figure 6-17:	Simulated wavelength dependence of the TM polarisation purity P_C for the fabricated device.	136

Chapter 7

Figure 7-1:	Schematic of the design and functionality of the monolithically integrated passive polarisation converter in a Fabry-Perot laser cavity. (a) Evolution of the electric field in the device. (b) Device configuration (not to scale). (Insert) Definition of waveguide profile parameters (front slope angle ξ , undercut slope angle α and waveguide top width w) and illustration of the orientation of the optical axes, which determine the orientation of the excited lowest order modes (mode 1 (chain dotted line) and mode 2 (dashed line)) in the waveguide.	139
Figure 7-2:	Illustration of the overlap of the mode profile contour plots (here: magnitude of the E_x component of a generated TE polarised signal in the pumped laser section) directly before ($L = 0^-$ (grey line)) and directly after ($L = 0^+$ (dashed line)) the intersection between passive converter- and pumped laser section.	141

Figure 7-3:	Dependence of the intersection loss on the converter section taper width w and the transversal converter section offset τ at the intersection between the pumped laser- and passive converter waveguide section at an operating wavelength of $\lambda = 867$ nm.	142
Figure 7-4:	(a)-(i) Schematic process flow diagram of the realised monolithically integrated passive polarisation converter within a semiconductor laser diode.(part 1)	144
Figure 7-5:	(j)-(p) Schematic process flow diagram of the realised monolithically integrated passive polarisation converter within a semiconductor laser diode.(part 2)	145
Figure 7-6:	(a) SEM micrograph top view of the fabricated device consisting of the pumped laser section (indicated by the gold pad used for p-contact) and the passive polarisation converter section. (b) Magnified SEM micrograph top view of the passive polarisation converter section. (c) Magnified SEM micrograph top view of the intersection between the pumped laser section and the passive polarisation converter section.	149
Figure 7-7:	(a) SEM micrograph of the deeply etched passive section showing the transition between the linear adiabatic taper and the converter section. (b) SEM micrograph of the waveguide cross section profile of the polarisation converter section.	149
Figure 7-8:	Measured optical spectrum at the output facet of the fabricated device, which consists of a converter section length of $20 \mu\text{m}$, at an injected current (continuous wave) of 150 mA (threshold current level = 100 mA). Measurement conducted by S. McMaster.	150
Figure 7-9:	Evaluated TM polarisation purity P_C at the converter section facet versus the length of the converter section of the fabricated devices.	151
Figure 7-10:	Top view of the simulated contour plot of the magnitude of the E_y (TM) component and calculated TM polarisation purity P_C versus the passive section length for a TE_0 polarised signal launched from the gain section into the passive section of the fabricated device ($\xi = 45^\circ$, $\alpha = 40^\circ$, $w = 650$ nm) (a, b) without output taper and -waveguide and (c, d) with a converter section length of $20 \mu\text{m}$, $50 \mu\text{m}$ long linear output taper and $20 \mu\text{m}$ long output waveguide at an operational wavelength of $\lambda = 867.1$ nm.	152
Figure 7-11:	Measured total power emission dependence on the injected current of the device without the passive section. Measurement conducted by S. McMaster.	153
Figure 7-12:	Measured power emission dependence on the injected current of the device including the passive section. The total output power and the separated TE and TM output powers at both (a) the pumped laser section facet and (b) the polarisation converter section facet is shown. (c) Resulting TM polarisation purity at both the pumped laser section facet and the polarisation converter section facet above the threshold level. Measurement conducted by S. McMaster.	154

Figure 7-13: Measured TM- and TE polarised components of the output power at the polarisation converter facet for an injection current (continuous wave) of 150 mA (threshold current level = 100 mA). Measurement conducted by S. McMaster.	155
Figure 7-14: Geometry and notation used in the description of the compound cavity configuration of the device.	155
Figure 7-15: Measured spontaneous emission spectrum at sub-threshold level (injected current = 90 mA (continuous wave), threshold current level = 100 mA). Measurement conducted by S. McMaster.	156

Chapter 8

Figure 8-1: Illustration of the simplified converter section mask alignment.	159
Figure 8-2: Schematic of the design and functionality of the integrated polarisation converter. (a) Evolution of the polarisation state of a TE polarised input signal in the device. (b) Device configuration (not to scale). (Insert) Waveguide profile of converter section and illustration of optical axes orientations, which determine the orientation of the excited lowest order modes (mode 1 (chain dotted line) and mode 2 (dashed line)).	160
Figure 8-3: (a) Effective refractive index of the excited modes in a symmetric ($\alpha = 90^\circ$) and asymmetric ($\alpha = 60^\circ$ and $\alpha = 45^\circ$) stripe waveguide versus the waveguide top width w_T . (b) power overlap κ and half beat length $L_{Beat/2}$ of an asymmetric ($\alpha = 60^\circ$ and $\alpha = 45^\circ$) stripe waveguide versus the waveguide top width w_T . (c) Rotation of optical axis δ with respect to the vertical axis and TM polarisation purity P_C of an asymmetric ($\alpha = 60^\circ$ and $\alpha = 45^\circ$) stripe waveguide versus the waveguide top width w_T . ($\lambda = 1064$ nm).	162
Figure 8-4: (a) Evaluated optimum w_T - dimension closely above single mode cut-off and corresponding $L_{Beat/2}$ versus undercut angle α . (b) Rotation of optical axis δ and power overlap κ versus undercut angle α at optimised w_T . (c) TM polarisation purity P_C versus undercut angle α at optimised w_T . ($\lambda = 1064$ nm).	164
Figure 8-5: Normalised transmitted power of the fundamental TE mode (TE_0) versus the taper length L_{taper} . ($\lambda = 1064$ nm).	165
Figure 8-6: Illustration of the overlap of the mode profile contour plots (here: magnitude of the E_x component for the case of a TE polarised input signal) directly before ($L = 0^-$ (grey line)) and directly after ($L = 0^+$ (dashed line)) the intersection between converter- and intermediate- (or output-) waveguide section.	166
Figure 8-7: Dependence of the intersection loss on the transverse converter section offset τ at the intersection between intermediate waveguide section and converter waveguide section. (Insert) Definition of the transversal converter section offset τ	167
Figure 8-8: (a)-(e) Electric vector field plot and corresponding mode profile and contour plot of the transverse (x, y) components of fundamental mode 1	

	in a stripe waveguide comprising an undercut of an angle of $\alpha = 58^\circ$ with respect to the horizontal axis and a waveguide top width w_T of 860 nm in the core profile for an operating wavelength $\lambda = 1064$ nm.	168
Figure 8-9:	(a)-(e) Electric vector field plot and corresponding mode profile and contour plot of the transverse (x, y) components of fundamental mode 2 in a stripe waveguide comprising an undercut of an angle of $\alpha = 58^\circ$ with respect to the horizontal axis and a waveguide top width w_T of 860 nm in the core profile for an operating wavelength $\lambda = 1064$ nm.	169
Figure 8-10:	(a)-(e) Magnetic vector field plot and corresponding mode profile and contour plot of the transverse (x, y) components of fundamental mode 1 in a stripe waveguide comprising an undercut of an angle of $\alpha = 58^\circ$ with respect to the horizontal axis and a waveguide top width w_T of 860 nm in the core profile for an operating wavelength $\lambda = 1064$ nm.	170
Figure 8-11:	(a)-(e) Magnetic vector field plot and corresponding mode profile and contour plot of the transverse (x, y) components of fundamental mode 2 in a stripe waveguide comprising an undercut of an angle of $\alpha = 58^\circ$ with respect to the horizontal axis and a waveguide top width w_T of 860 nm in the core profile for an operating wavelength $\lambda = 1064$ nm.	171
Figure 8-12:	Top view of the simulated contour plot of both the E_x (TE) and E_y (TM) component of a TE_0 mode launched from the intermediate waveguide section into the optimised converter section. (Inserts) Magnitude of both E_x and E_y components at $L = 0 \mu\text{m}$, $L = L_{Beat}/4 = 31 \mu\text{m}$ and $L = L_{Beat}/2 = 62 \mu\text{m}$	173
Figure 8-13:	(a)-(j) Schematic process flow diagram of the realised polarisation converter device.	176
Figure 8-14:	(a) SEM overview of the fabricated device. (b) SEM of the intersection between the converter section and the input/output waveguide section.	177
Figure 8-15:	(a) SEM top view of the intersection between the converter section and the input/output waveguide section. (b) SEM of the waveguide cross section profile of the fabricated converter section waveguide.	177
Figure 8-16:	Measured and calculated TM polarisation purity at the output of the device versus the converter section length for a TE polarised input signal at $\lambda = 1064$ nm.	178
Figure 8-17:	Normalised measured total power at the output of the device versus the converter section length. The linear extrapolation of the measured data is indicated by the chain dotted line and expressed by the mathematical formula $y = -0.0017x + 0.72$	179
Figure 8-18:	Simulated wavelength dependence of the TM polarisation purity P_C for the theoretically optimised device and the fabricated device.	180

This page intentionally left blank.

Chapter 1

Introduction

1.1 Background

The global increasing need for higher transmission- and processing capacities of telecommunication systems makes high demands on the performance, reliability, range of functions and cost efficiency of their components [1]. This refers to components in both the electronic- and optic domain in order to provide the infrastructure for enhanced *next generation network* (NGN) services [2-4].

Meeting these requirements, a successive migration of discrete active and passive components to an integrated level is desirable. In the electronic domain, various functionalities, previously provided by discrete components, have already been realised in low-cost *very large scale integrated* (VLSI) circuits [5]. This trend overlaps to their optoelectronic counterparts such as large-scale *optoelectronic integrated circuits* (OEICs) [6, 7] and *photonic integrated circuits* (PICs) [8, 9]. Integration not only reduces the number of packaging stages but also eliminates costly and time consuming assembly and manual alignment as well as losses associated with coupling to optical fibres. The compactness and stable alignment decreases the impact of mechanical vibration or temperature change on the device performance [10].

Hardware developments on the network system level, such as the introduction of optical amplifiers (*erbium doped fibre amplifiers* (EDFAs)) [11] together with the *dense wavelength division multiplexing* (DWDM) technology [12] contribute to an enhanced performance and cost efficiency of fibre optic telecommunication networks. DWDM simultaneously transmits multiple signal channels - each at different modulation format and data rate - at separate, closed spaced wavelengths over a single optical fibre (Figure 1-1). The channel spacing of the current DWDM transmission standard is specified by the *International Telecommunication Union* (ITU) G694.1 document [13], which defines an anchor frequency at 193.1 THz (corresponding to a wavelength of 1552.52 nm). The individual channel centres are defined for 12.5 GHz, 25 GHz, 50 GHz and 100 GHz separations above and below the anchor frequency.

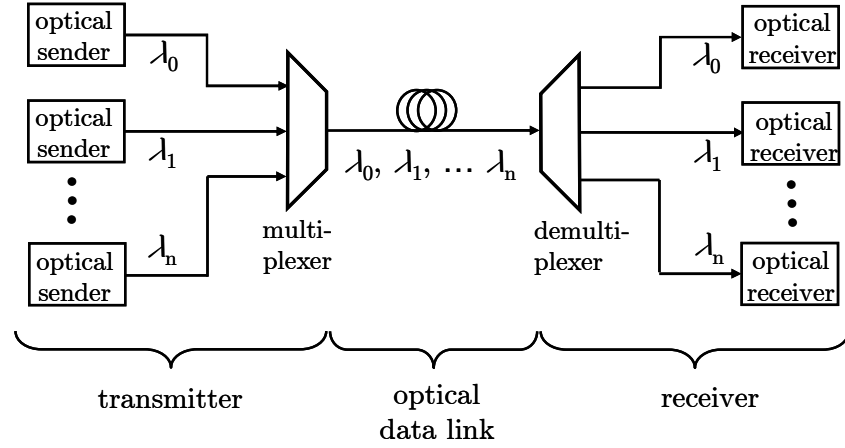


Figure 1-1: Schematic of the *dense wavelength division multiplex* (DWDM) principle (unidirectional).

1.1.1 Polarisation division multiplexing

An additional doubling of the data transmission efficiency can be achieved by coupling the DWDM technique with the *polarisation division multiplex* (PDM) technique [14]. In a PDM system, two orthogonally polarised optical signals of the *same* wavelength - but not necessarily with the same modulation format and data rate - are combined to a single optical signal and transmitted over an optical fibre to a receiver. At the receiver end, the transmitted signal is split. The split signal components are applied to each other orthogonally polarised filters in order to recover the two original, to each other orthogonally polarised signals (Figure 1-2).

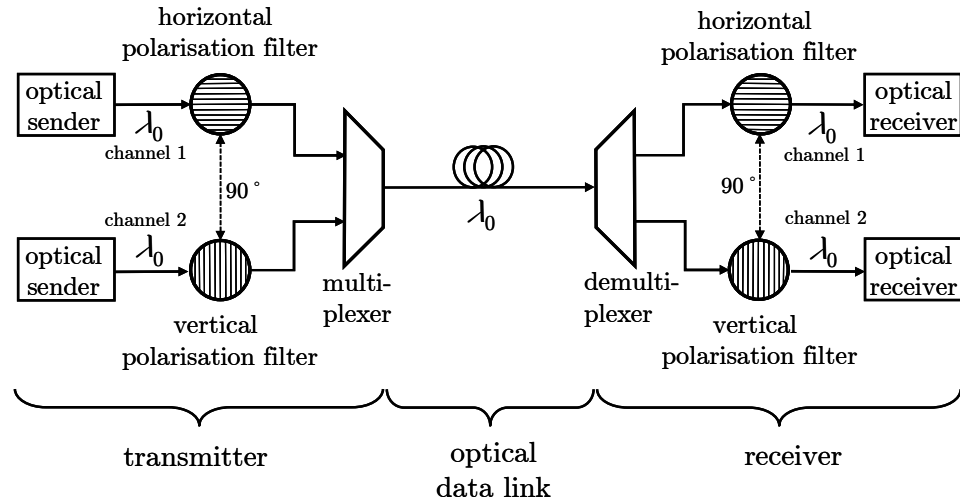


Figure 1-2: Schematic of the principle of the *polarisation division multiplexing* (PDM) technique in optical data transmission systems (only one wavelength channel in unidirectional transmission illustrated) (after [14]).

1.1.2 Polarisation mode dispersion

The *state of polarisation* (SOP) of the signals at the sender output and receiver input usually don't correspond to each other. This is due to the transmission characteristics of the optical data link caused by *polarisation mode dispersion* (PMD) [15-17]. The acronym PMD denotes both the physical phenomenon and the parameter that quantifies its magnitude [18]:

Modern spooled or field-installed optical fibres that represent the optical data link are called *single-mode* fibres, although they actually support two modes, which are orthogonally polarised to each other according to the orientation of the optical axes - also referred to as *principal states of polarisation* (PSPs) [19]. In an ideal fibre (in terms of radial refractive index symmetry over the fibre length), the two orthogonally polarised modes are degenerated. In a real fibre, however, small geometrical imperfections - which result in a non-symmetrical refractive index distribution - together with internal stress on the fibre core as well as nondeterministic external factors such as temperature, vibration, bending or twisting of the fibre, electric or magnetic fields, lead to *random* birefringence along the fibre span. A single mode fibre span can be modelled as a concatenation of short fibre sections [20]. These sections are assumed to be short enough that any perturbation acting on them is constant over their entire individual lengths. Considering such a short section within a long fibre span (Figure 1-3) and assuming that an input signal excites

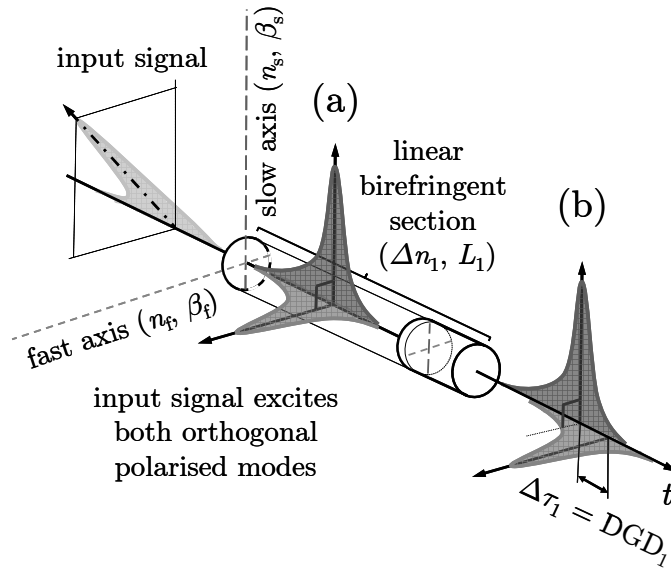


Figure 1-3: Conceptual illustration of the effect of *polarisation mode dispersion* (PMD) in a short, linear birefringent fibre element in the time domain.

both of the two orthogonally polarised modes (Figure 1-3(a)), each mode encounters a different refractive index by the fibre (n_s , n_f), resulting in different propagation constants (β_s , β_f) and therefore a *differential phase velocity* $\Delta v_{p,eff}$. $\Delta v_{p,eff}$ is usually accompanied by a difference in the local group velocities of the two excited orthogonally polarised modes, which is also referred to as *differential group delay* $\Delta\tau_1$ or DGD_1 (in ps) (Figure 1-3(b))

[21]. The quantity $\Delta\tau_1/L_1$ is referred to as the *intrinsic* PMD (in ps/km) of the fibre element. $\Delta\tau_1$ is the time-domain manifestation of PMD, which can impose system performance impairments due to pulse broadening when its value approaches a significant fraction of the bit period of the transmitted signal [22]. In the frequency-domain, PMD manifests itself as the frequency (wavelength) dependent variation of the SOP at the fibre section output for a fixed input polarisation [23].

As a fibre span is concatenated of a series of birefringent sections of random length and random orientation of the optical axes, PMD is a nondeterministic phenomenon. This results in a random SOP at the output of the fibre span. DGD accumulates in a random walk-like process in a square root dependence on the fibre span length L (in km). The *time-averaged DGD* $\langle\Delta\tau\rangle$ at the output of the fibre span is defined as $\langle\Delta\tau\rangle = D_{\text{PMD}}L^{1/2}$ (in ps), where D_{PMD} is the *PMD parameter* (in ps/km^{1/2}) [24]. D_{PMD} has a typical value of 0.15 ps/km^{1/2} for a *standard single mode fibre* (SSMF) (specified by the ITU G.652 document [25]), which is mainly deployed in optical networks [26].

1.1.3 Photonic integrated circuits

The two PSPs in PICs that consist of one-dimensional slab waveguide structures are commonly referred to as *transverse electric* (TE) and *transverse magnetic* (TM) polarisations. As shall be shown in chapter 2, TE refers to light polarised in the plane of the wafer, and TM to light polarised perpendicular to the wafer plane. In PICs consisting of two-dimensional dielectric waveguide structures, the two PSPs are not pure TE or TM. Strictly speaking, they should be referred to as quasi-TE and quasi-TM polarisations. However, it is common practice to refer to them also as TE or TM polarisations, since the magnitude of one of the two transverse field components is typically much larger than the other [27].

In general, most of the PIC structures are polarisation sensitive. Their performance strongly depends on the SOP of the input signal. The problem of a random SOP of the received signal at the output of a fibre span needs to be overcome in both the optical fibre and at the fibre-OEIC/PIC interface. While a costly installation of *polarisation maintaining fibres* (PMF) [28] can be introduced in order to minimise this unavoidable, random effect in the long-haul transmission, receivers in PICs have to be designed to operate independent of the incoming SOP. Therefore, polarisation manipulation and -control represents a desirable functionality in PICs.

Integrated optical polarisation-manipulating devices can be categorised in *polarisation splitters* and *polarisation rotators* (also called *polarisation converters* or *polarisation transformers*).

Polarisation splitters are used to split arbitrary polarised signals into two independent orthogonally polarised signals. This functionality is used for applications where specific SOPs of optical signals are needed (e.g. signal processing [29], sensors [30], etc.). Polarisation splitters have already been implemented by using structures such as

multimode interference (MMI) couplers [31, 32], *Mach-Zehnder interferometer* (MZI) coupler [33], Y-junction [34] and directional couplers [35-37].

Polarisation rotators are used to convert the SOP of a signal into another state. Polarisation rotators have been realised as both active and passive devices. Active polarisation converters have been realised by applying magnetooptic- [38], electrooptic- [39, 40] and photoelastic effects [41, 42]. However, the implementation of these active devices requires an external power supply and a control unit. Moreover, in most applications only a fixed and not a variable degree of polarisation rotation is required. Therefore, integrated passive polarisation converter devices are preferred. The following section gives an overview of potential applications of integrated passive polarisation converters.

1.2 Potential applications of integrated passive polarisation rotators

1.2.1 Semiconductor heterostructure laser emitting transverse magnetic polarised signal

Conventional lattice-matched III-V semiconductor *quantum well* (QW) and bulk heterostructure lasers based on interband transitions predominantly emit TE polarised light [43, 44]. In QW lasers, this characteristic mainly originates from the energy level difference between the *heavy-hole* (hh) and *light-hole* (lh) states in the valence band of the QW [45]. In both structures, the bigger TE mode overlap with the optical gain distribution in the waveguide core due to the cross sectional geometry [43] and the higher TE mode reflectivity of the cleaved facets [46] yields an overall lower threshold current for TE polarised modes rather than for TM polarised modes.

In order to obtain TM polarised laser output signals, several attempts to manipulate the SOP on either the integrated or discrete level have been made. On the integrated level, tensile strain in the quantum well structure due to lattice-mismatched core layers has been introduced in order to invert the hh and lh energy states in the valence band resulting in an emission of either predominantly TM or a mixture of TE and TM polarised modes [47-49]. In order to manipulate the oscillation properties of semiconductor lasers on the discrete level, structures based on injected light from external pump sources [50, 51] and external optical feedback by means of compound-cavity configurations [52-55] have been reported.

In applications such as PDM it is desired to be able to produce a TM polarised laser output signal. This functionality could be realised with an integrated monolithical combination of a semiconductor heterostructure laser and a passive polarisation rotator on an active waveguide material structure (Figure 1-4).

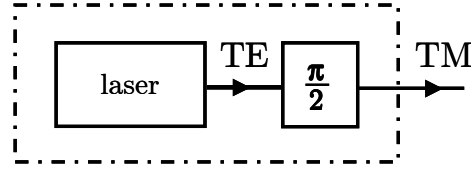


Figure 1-4: Schematic of an integrated monolithical combination of a semiconductor heterostructure laser and a passive polarisation rotator in order to establish a TM polarised output signal.

1.2.2 Integrated polarisation-independent amplification of optical signals

The polarisation dependent signal gain in *semiconductor optical amplifiers* (SOAs) represents a performance limitation in optical communication systems [56]. In order to overcome the gain differences between TE and TM polarised modes, SOAs with modified structure cross-section designs [57, 58] or strained-layer wafer materials [59-62] have been proposed and realised. Alternative approaches to overcome the gain differences are optical circuit configurations consisting for example of either two SOAs in series or in parallel, combined with other discrete devices [63, 64].

Two possible realisations of the above mentioned optical circuit configurations in integrated form can schematically be depicted in Figure 1-5. The functionality of these configurations is based on the amplification of TE polarised signals in SOAs composed of unstrained wafer structure materials.

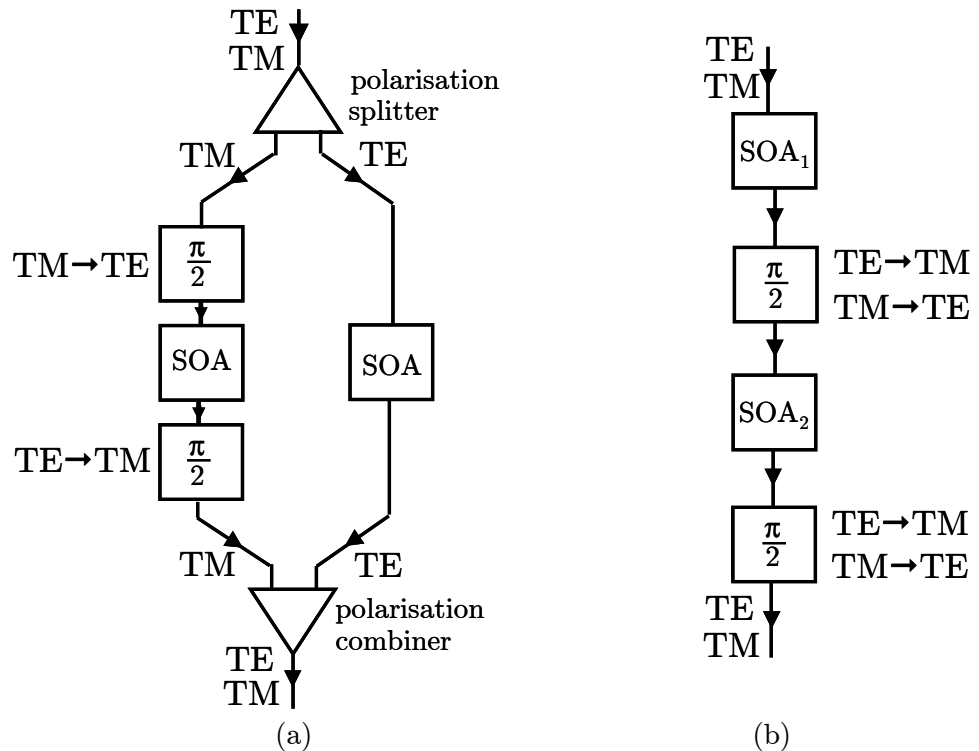


Figure 1-5: Two possible configurations for an integrated polarisation-independent amplifier circuit: (a) parallel circuit structure and (b) series circuit structure.

In the parallel circuit configuration (Figure 1-5(a)) the incident signal is split into both TE and TM polarised components via a polarisation splitter. While the TE polarised signal is directly applied to the SOA, the TM polarised signal in the other branch is converted to a TE polarised signal via a 90° polarisation rotator before it is amplified by the SOA. After its amplification, the signal imparts again a 90° polarisation rotation back to its initial TM polarisation. Both amplified signals are then recombined in order to represent an amplified signal with the same SOP as the input signal. The drawbacks of this configuration are the unequal path lengths of both branches which could cause a performance degradation due to PMD after recombination of the amplified signals at the output.

In the series circuit configuration (Figure 1-5(b)), both incident polarisation components are applied to an SOA (SOA_1), where only the TE polarised component imparts an amplification. In order to apply an equal gain to both components, each signal is converted into the opposite polarisation in a following 90° polarisation rotator. After amplification of the TE polarised component in SOA_2 , both signals are converted back to their initial SOP in a second 90° polarisation rotator before they emerge at the output of the device.

1.2.3 Integrated polarisation diversity scheme

As already mentioned above, polarisation sensitivity of integrated optical components is a major problem. A polarisation independent circuit can be realised using an integrated polarisation diversity scheme, which is illustrated in Figure 1-6.

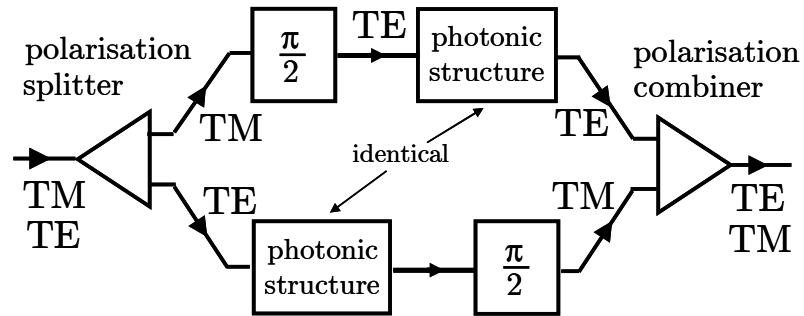


Figure 1-6: Integrated polarisation diversity scheme (after [29]).

An arbitrary input SOP is decomposed and spatially separated into two distinct and orthogonally polarised components in the polarisation splitter at the input. One of these components (here: TM component) is converted into its opposite SOP by a 90° polarisation rotator. Each of the two now TE polarised signals passes through identical photonic structures, which are arbitrary polarisation sensitive. In order to avoid an interference of the two signals at the recombination of the two signal paths, a polarisation rotation in the opposite arm is performed. This establishes an overall design symmetry in order to bypass fabrication imperfections.

1.2.4 Polarisation independent PHASAR-demultiplexer

Integrated optical demultiplexer devices based on *phased-arrays* (PHASAR) (also called *arrayed-waveguide gratings*) are key components in DWDM systems. In order to overcome the polarisation dependence of a PHASAR demultiplexer caused by waveguide birefringence, polarisation converters are inserted in the centre of the phase array. This establishes light propagation through the two halves of the device in each other orthogonally polarised SOP, regardless of the impact of the birefringence of the waveguides in both halves. Such a device has already been proposed and realised by inserting a polarisation converter based on SiO_2 in between a PHASAR based on a LiNbO_3 substrate [65, 66]. Due to radiation losses at the transitions between the two different substrates it is desired to realise this kind of polarisation-independent multiplexer on a single substrate. Figure 1-7 illustrates the schematic of a monolithically integrated solution that has been proposed and realised [67, 68] utilising an integrated passive polarisation rotator based on bends [69].

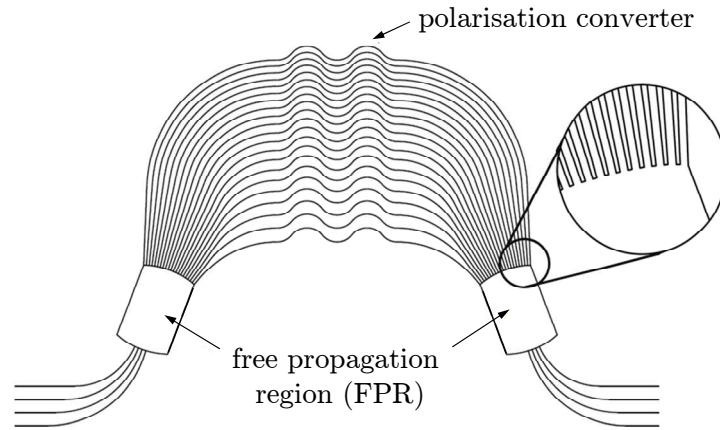


Figure 1-7: Schematic of a polarisation-independent PHASAR demultiplexer with inserted integrated polarisation converters in the centre (after [67, 68]).

1.2.5 Integrated optical isolator

In general, an optical isolator can be considered as the optical counterpart to a diode in the electrical domain. This kind of device provides a nonreciprocal rotation functionality which manifests itself in a way that light is always rotated in the *same direction in relation to the rotator regardless of its direction of propagation*.

Current and next generation photonic integrated circuits necessitate stable, narrow line width integrated optical sources that are free from the injection noise that arises as a consequence of emitted radiation being reflected back into the laser cavity [70-77]. Currently, in order to achieve this stability, bulk optical isolators [78], which conventionally exploit the *magneto-optic* (MO) Faraday effect [38], are incorporated between the laser source and the optical system. Their assembly is a labour- and time intensive process that results in increased cost and reduced throughput. Consequently, the prospect of a monolithically integration of an optical isolator functionality has attracted considerable attention. A possible implementation of this device [79-81] is schematically illustrated in Figure 1-8.

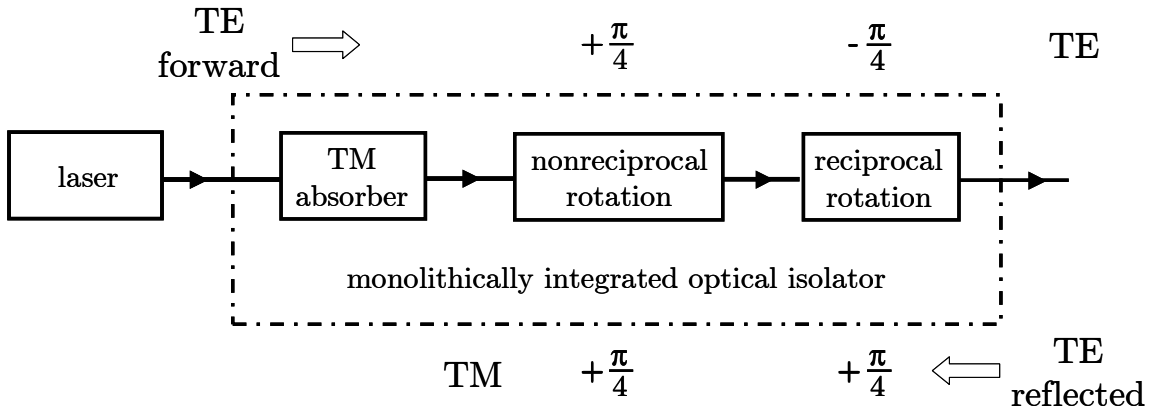


Figure 1-8: Schematic of the functionality of a monolithically integrated optical isolator.

The device consists of a TM absorber [82] followed by a nonreciprocal [83, 84] and reciprocal [85-88] rotation section. Both rotation sections are designed to impart a 45° rotation on the SOP of the incident light.

The predominantly TE polarised emitted light from a semiconductor heterostructure QW laser passes through the TM absorber and the nonreciprocal rotation element where it imparts a 45° rotation of its SOP. The reciprocal rotation section provides another rotation of 45° , but in the opposite direction. Hence, in the forward propagating direction, a TE polarised input will have the imparted polarisation rotation cancelled and be returned into the initial and desired TE polarisation at the output. A reflected backwards propagating TE polarised light will impart a combined rotation of both rotation sections, which results in a TM polarised light. The TM absorber then rejects the TM polarised light. This two-stage rotation principle provides the desired optical isolator functionality.

1.3 Objectives and organisation of the thesis

Considering the potential applications for integrated passive polarisation rotators in the previous section, these kind of devices introduce the opportunity to realise novel optical device- or even optical circuit functionalities that do not exist in the integrated domain yet. The aim of this thesis is the development of novel integrated passive polarisation converter designs and fabrication methods. This includes rigorous theoretical optimisation of the device geometries, the fabrication and characterisation of the devices.

The following second chapter gives an introduction to the basic theory behind the functionality of passive polarisation converters based on structural birefringence. Starting with Maxwell's equations over the vectorial wave equations and Helmholtz equations, birefringence, polarisation and the boundary conditions at dielectric interfaces are defined. This is followed by the definition of optical modes and the characteristics of *transverse electric* (TE) and *transverse magnetic* (TM) modes in dielectric slab- and stripe waveguides. The basic concept of calculating the mode propagation and mode field patterns is discussed upon the *beam propagation method* (BPM). The principle of birefringence in uniaxial crystals is demonstrated upon a waveplate, on which the functionality of the proposed and realised integrated passive polarisation converters in this thesis is based upon.

An overview of the current state of the art integrated passive polarisation converter device designs is given in the third chapter.

The fourth chapter introduces the dry-etch fabrication process utilising a customised in-situ sample holder which allows the converter section waveguides of the developed device designs to be fabricated in a single etch step.

The first device design comprising an asymmetric waveguide structure is introduced in the fifth chapter. The converter section waveguide profile consists of two sloped sidewalls. After a rigorous theoretical optimisation of the device geometries, the device is fabricated on a passive GaAs/AlGaAs material structure and characterised.

The sixth chapter deals with the implementation of this polarisation converter design on an unstrained GaAs/AlGaAs double quantum well heterostructure material system. This device represents one of the building blocks in a monolithically integrated passive polarisation converter incorporated within a Fabry-Perot semiconductor laser diode, which will be introduced in the seventh chapter.

Chapter eight presents the second novel polarisation converter design, which is based on the modification of an already existing stripe waveguide structure.

The thesis is concluded in the ninth chapter where also future perspectives are discussed.

1.4 References

- [1] O'Mahony M. J., Politi C., Klonidis D., Nejabati R. and Simeonidou D., "Future Optical Networks", *IEEE Journal of Lightwave Technology*, vol. **24**, no. 12, pp. 4684 - 4696, (2006).
- [2] Lee C. and Knight D., "Realization of the Next-Generation Network", *IEEE Communications Magazine*, vol. **43**, no. 10, pp. 34 - 41, (2005).
- [3] Sadiku M. N. and Nguyen T. H., "Next generation networks", *IEEE Potentials*, vol. **21**, no. 2, pp. 6 - 9, (2002).
- [4] Wilkinson N., *"Next Generation Network Services"*, John Wiley & Sons, Ltd., Chichester, UK, ISBN 0-471-48667-1, (2002).
- [5] Moore G. E., "Cramming More Components onto Integrated Circuits", *Proceedings of the IEEE*, vol. **86**, no. 1, pp. 82 - 85, (1998).
- [6] Forrest S. R., "Optoelectronic Integrated Circuits", *Proceedings of the IEEE*, vol. **75**, no. 11, pp. 1488 - 1497, (1987).
- [7] Wada O., "Recent progress in optoelectronic integrated circuits (OEICs)", *IEEE Journal of Quantum Electronics*, vol. **22**, no. 6, pp. 805 - 823, (1986).
- [8] Koch T. L., "Semiconductor integrated circuits", *IEEE Journal of Quantum Electronics*, vol. **27**, no. 3, pp. 641 - 653, (1991).
- [9] Nagarajan R., Joyner C. H., Schneider R. P., Jr., Bostak J. S., Butrie T., Dentai A. G., Dominic V. G., Evans P. W., Kato M., Kauffman M., Lambert D. J. H., Mathis S. K., Mathur A., Miles R. H., Mitchell M. L., Missey M. J., Murthy S., Nilsson A. C., Peters F. H., Pennypacker S. C., Pleumeekers J. L., Salvatore R. A., Schlenker R. K., Taylor R. B., Huan-Shang T., Van Leeuwen M. F., Webjorn J., Ziari M., Perkins D., Singh J., Grubb S. G., Reffle M. S., Mehuys D. G., Kish F. A. and Welch D. F., "Large-scale photonic integrated circuits", *IEEE Selected Topics in Quantum Electronics*, vol. **11**, no. 1, pp. 50 - 65, (2005).
- [10] Waynant R. W. and Ediger M. N., *"Electro-Optics Handbook"*, McGraw-Hill, New York, USA, ISBN 0-07-068716-1, (2000).
- [11] Miniscalco W., "Erbium-doped glasses for fiber amplifiers at 1500 nm", *IEEE Journal of Lightwave Technology*, vol. **9**, pp. 234 - 250, (1991).
- [12] Kartalopoulos S. V., *"Introduction to DWDM technology: Data in a Rainbow"*, John Wiley & Sons, New York, USA, ISBN 0-7803-5399-4, (2000).
- [13] ITU-T Recommendation G.694.1, *"Spectral grids for WDM applications: DWDM frequency grid"*, <http://www.itu.int>
- [14] Schoenfelder T., "Polarization Division Multiplexing in Optical Data Transmission Systems", *US patent 6580535*, (2003).

-
- [15] Damask J. N., *"Polarization optics in telecommunications"*, 1st. ed., Springer, New York, USA, ISBN 0-387-22493-9, (2005).
- [16] Poole C. D., Tkach R. W., Chraplyvy A. R. and Fishman D. A., "Fading in Lightwave Systems due to Polarization-Mode Dispersion", *IEEE Photonics Technology Letters*, vol. **3**, no. 1, pp. 68 - 70, (1991).
- [17] Poole C. D. and Wagner R. E., "Phenomenological approach to polarization dispersion in long single-mode fibers", *Electronics Letters*, vol. **22**, no. 19, pp. 1029 - 1030, (1996).
- [18] Bigo S., "Technologies for global telecommunications using undersea cables", in Kaminow I. P., Li T., Willner A. E. (Eds.), *"Optical Fiber Telecommunications V B: Systems and Networks"*, 1st. ed., Academic Press, Oxford, UK, 2008, ch. 14, pp. 561 - 610, ISBN 978-0-12-37-374172-1.
- [19] Kaminow I. P., "Polarization in optical fibers", *IEEE Journal of Quantum Electronics*, vol. **17**, no. 1, pp. 15 - 22, (1981).
- [20] Derickson D., *"Fiber optic test and measurement"*, 1st. ed., Prentice Hall, Upper Saddle River, New Jersey, USA, ISBN 0135343305, (1997).
- [21] Poole C. D. and Nagel J., "Polarization Effects in Lightwave Systems", in Kaminow I. P., Koch T. L. (Eds.), *"Optical Fiber Communications III A"*, 1st. ed., Academic Press, San Diego, USA, 1997, ch. 6, pp. 114 - 264, ISBN 0-12-395170-4.
- [22] Kogelnik H., Jopson R. M. and Nelson N. E., "Polarization-Mode Dispersion", in Kaminow I. P., Li T. (Eds.), *"Optical Fiber Telecommunications IV B: Systems and Impairments"*, 1st. ed., Academic Press, San Diego, USA, 2002, ch. 15, pp. 725 - 861, ISBN 0-12-395173-9.
- [23] Eickhoff W., Yen Y. and Ulrich R., "Wavelength dependence of birefringence in single-mode fiber", *Applied Optics*, vol. **20**, no. 19, pp. 3428 - 3435, (1981).
- [24] Agrawal G. P., *"Fiber-Optic Communication Systems"*, John Wiley & Sons Inc., New York, USA, ISBN 0-471-17540-4, (1997).
- [25] ITU-T Recommendation G.652, *"Characteristics of a single-mode optical fibre and cable"*, <http://www.itu.int>
- [26] Schuh K. and Lach E., "High-bit-rate ETDM transmission systems", in Kaminow I. P., Li T., Willner A. E. (Eds.), *"Optical Fiber telecommunications V B: Systems and Networks"*, 1st. ed., Academic Press, Oxford, UK, 2008, ch. 5, pp. 179 - 200, ISBN 978-0-12-37-374172-1.
- [27] Doerr C. R. and Okamoto K., "Planar Lightwave Circuits in Fiber-Optic Communications", in Kaminow I. P., Li T., Willner A. E. (Eds.), *"Optical Fiber Telecommunications V A: Components and Subsystems"*, 1st. ed., Academic Press, Oxford, UK, 2008, ch. 9, pp. 269 - 342.
- [28] Li M.-J., Chen X., Nolan D. A., Wang J., West J. A. and Koch K. W., "Specialty Fibers for Optical Communication Systems", in Kaminow I. P., Li T., Willner A. E. (Eds.), *"Optical Fiber Telecommunications V A: Components and Subsystems"*, 1st. ed., Academic Press, Oxford, UK, 2008, ch. 15, pp. 523 -592.

- [29] Barwicz T., Watts M. R., Popovic M. A., Rakich P. T., Socci L., Kaerntner F. X., Ippen E. P. and Smith H. I., "Polarization-transparent microphotonic devices in the strong confinement limit", *nature photonics*, vol. **1** no. 1, pp. 57 - 60, (2007).
- [30] Kunz R. E., "Miniature integrated optical modules for chemical and biochemical sensing", *Sensors and Actuators, B: Chemical*, vol. **B38**, no. 1 - 3 pt. 1, pp. 13 - 28, (1997).
- [31] Jung M. H., Hyun H. R., Soon R. P., Jae W. J., Seung G. L., El Hang L., Se-Geun P., Deokha W., Sunho K. and Beom-Hoan O., "Design and fabrication of a significantly shortened multimode interference coupler for polarization splitter application", *IEEE Photonics Technology Letters*, vol. **15**, no. 1, pp. 72 - 74, (2003).
- [32] Rahman B. M. A., Somasiri N., Themistos C. and Grattan K. T. V., "Design of optical polarization splitters in a single-section deeply etched MMI waveguide", *Journal of Applied Physics B: Lasers and Optics*, vol. **73**, no. 5 - 6, pp. 613 - 618, (2001).
- [33] Soldano L. B., de Vreede A. I., Smit M. K., Verbeek B. H., Metaal E. G. and Green F. H., "Mach-Zehnder interferometer polarization splitter in InGaAsP/InP", *IEEE Photonics Technology Letters*, vol. **6**, no. 3, pp. 402 - 405, (1994).
- [34] Burns W. and Milton A., "Mode conversion in planar-dielectric separating waveguides", *IEEE Journal of Quantum Electronics*, vol. **11**, no. 1, pp. 32 - 39, (1975).
- [35] Albrecht P., Hamacher M., Heidrich H., Hoffmann D., Nolting H. P. and Wienert C. M., "TE/TM mode splitters on InGaAsP/InP", *IEEE Photonics Technology Letters*, vol. **2**, no. 2, pp. 114 - 115, (1990).
- [36] Augustin L. M., van der Tol J. J. G. M., Hanfoug R. and Smit M. K., "Design of a single etchstep fabrication-tolerant polarisation splitter", in *Proceedings of the 12th European Conference on Integrated Optics 2005 (ECIO'05)*, Grenoble, France, 6 - 8 April 2005, pp. 125 - 128.
- [37] Mikami O., "LiNbO₃ coupled-waveguide TE/TM mode splitter", *Applied Physics Letters*, vol. **36**, no. 7, pp. 491 - 493, (1980).
- [38] Zvezdin A. K. and Kotov V. A., *Modern Magneto-optics and Magneto-optical Materials*, 1st ed., Institute of Physics Publishing, Bristol, UK, ISBN 0-7503-0362-X, (1997).
- [39] Alferness R. C. and Buhl L. L., "Waveguide electro-optic polarization transformer", *Applied Physics Letters*, vol. **38**, no. 9, pp. 658 - 660, (1981).
- [40] Schlak M., Weinert C. M., Albrecht P. and Nolting H. P., "Tunable TE/TM-mode converter on (001)-InP-substrate", *IEEE Photonics Technology Letters*, vol. **3**, no. 1, pp. 15 - 16, (1991).
- [41] Yamanouchi K., Higuchi K. and Shibayama K., "TE-TM mode conversion by interaction between elastic surface waves and a laser beam on a metal-diffused optical waveguide", *Applied Physics Letters*, vol. **28**, no. 2, pp. 75 - 77, (1976).

- [42] Yamanouchi K., Wakazono K. and Shibayama K., "Optical surface wave mode converters and modulators utilizing static strain-optic effects", *IEEE Journal of Quantum Electronics*, vol. **16**, no. 6, pp. 628 - 634, (1980).
- [43] Agrawal G. P. and Dutta N. K., "*Semiconductor lasers*", 2nd ed., Van Nostrand Reinhold, New York, USA, ISBN 0-442-01102-4, (1993).
- [44] Zory P. S., "*Quantum Well Lasers*", 1st ed., Academic Press, Boston, USA, ISBN 0-12-78189-01, (1993).
- [45] Coldren L. A. and Corzine S. W., "*Diode lasers and photonic integrated circuits*", 1st ed., Wiley, New York, USA, ISBN 0471118753, (1995).
- [46] Reinhart F. K., Hayashi I. and Panish M. B., "Mode Reflectivity and Waveguide Properties of Double-Heterostructure Injection Lasers", *Journal of Applied Physics*, vol. **42**, no. 11, pp. 4466 - 4479, (1971).
- [47] Agahi F., Lau K. M., Choi H. K., Baliga A. and Anderson N. G., "High-Performance 770 nm AlGaAs-GaAsP Tensile-Strained Quantum-Well Laser Diodes", *IEEE Photonics Technology Letters*, vol. **7**, no. 2, pp. 140 - 142, (1995).
- [48] Bour D. P., Treat D. W., Beernink K. J., Thornton R. L., Paoli T. L. and D. B. R., "Tensile-strained AlGaAsP- and InGaAsP-(AlGa)_{0.5}In_{0.5}P Quantum Well Laser Diodes for TM-Mode Emission in the Wavelength Range $650 < \lambda < 850$ nm", *IEEE Photonics Technology Letters*, vol. **6**, no. 11, pp. 1283 - 1285, (1994).
- [49] Sun D. and Treat D. W., "Low-Threshold 833 nm GaAsP-AlGaAs Tensile-Strained Quantum-Well Laser Diodes", *IEEE Photonics Technology Letters*, vol. **8**, no. 1, pp. 13 - 15, (1986).
- [50] Mori Y., Shibata J. and Kajiwara T., "Optical polarization bistability with high switching speed in a TM wave injected buried heterostructure laser", *Applied Physics Letters*, vol. **54**, no. 24, pp. 1971 - 1973, (1987).
- [51] Sapia A., Spano P. and B. D., "Polarization switching in semiconductor lasers driven via injection from an external radiation", *Applied Physics Letters*, vol. **50**, no. 2, pp. 57 - 59, (1987).
- [52] Loh W. H., Ozeki Y. and Tang C. L., "High-frequency polarization self-modulation and chaotic phenomena in external cavity semiconductor lasers", *Applied Physics Letters*, vol. **56**, no. 26, pp. 2613 - 2615, (1990).
- [53] Mitsuhashi Y., "Polarization control of an antireflection-coated GaAlAs laser diode by an external optical feedback", *Journal of Applied Physics*, vol. **53**, no. 12, pp. 9200 - 9201, (1982).
- [54] Syvridis D., Inaudi D. and Guekos G., "Polarization state of the Emission of External Grating Diode Lasers", *IEEE Journal of Quantum Electronics*, vol. **30**, no. 4, pp. 966 - 974, (1994).
- [55] Wakana S., Shirasaki M., Furukawa Y. and Inagaki T., "Polarization and frequency control of a semiconductor laser with a new external cavity structure", *Applied Physics Letters*, vol. **50**, no. 22, pp. 1547 - 1549, (1987).
- [56] Connelly M. J., "*Semiconductor Optical Amplifiers*", Kluwer Academic Publishers, New York, USA, ISBN 0-7923-7657-9, (2002).

-
- [57] Deguet C., Delprat D., Crouzel G., Traynor N. J., P. M., Pearsal T., Lermينياux C., Andreakis N., Caneau C., Favire F., Bhat R. and Zah Z. E., "Homogeneous Buried Ridge Stripe Semiconductor Optical Amplifier with near Polarisation Independence", in *Proceedings of the 25th European Conference on Optical Communications 1999 (ECOC'99)*, Nice, France, 26 - 30 September 1999, pp. 26 - 30.
 - [58] Holtmann C., Besse P.-A., Brenner T. and Melchior H., "Polarisation independent bulk active region SOAs for 1.3 μm wavelengths", *IEEE Photonics Technology Letters*, vol. **8**, no. 3, pp. 343 - 345, (1996).
 - [59] Magari K., Okamoto M. and Noguchi Y., "1.55 μm polarization-insensitive high-gain tensile-strained-barrier MQW optical amplifier", *IEEE Photonics Technology Letters*, vol. **3**, no. 11, pp. 998 - 1000, (1991).
 - [60] Newkirk M. A., Miller B. I., Koren U., Young M. G., Chien M., Jopson R. M. and Burrus C. A., "1.5 μm multiquantum-well semiconductor optical amplifier with tensile and compressively strained wells for polarization-independent gain", *IEEE Photonics Technology Letters*, vol. **5**, no. 4, pp. 406 - 408, (1993).
 - [61] Godefroy A., Le Corre A., Clerot F., Salaun S., Loualiche S., Simon J. C., Henry L., Vaudry C., Keromnes J. C., Joulie G. and Lamouler P., "1.55 μm polarization-insensitive optical amplifier with strain-balanced superlattice active layer", *IEEE Photonics Technology Letters*, vol. **7**, no. 5, pp. 473 - 475, (1995).
 - [62] Joma M., Horikawa H., Xu C. Q., Yamada K., Katoh Y. and Kamijoh T., "Polarization insensitive semiconductor laser amplifiers with tensile strained InGaAsP/InGaAsP multiple quantum well structure", *Applied Physics Letters*, vol. **62**, pp. 121 - 122, (1993).
 - [63] Grosskopf G., Ludwig R., Waarts R. F. G. and Weber H. G., "Optical amplifier configurations with low polarization sensitivity", *Electronics Letters*, vol. **23**, pp. 1387 - 1388, (1987).
 - [64] Koga M. and Matsumoto T., "Polarization Insensitive Optical Amplifier Consisting of Two Semiconductor Laser Amplifiers and a Polarization Insensitive Isolator in Series", *IEEE Photonics Technology Letters*, vol. **1**, no. 12, pp. 431 - 433, (1989).
 - [65] Takahashi H., Hibino Y. and Nishi I., "Polarization-Insensitive Arrayed Waveguide Grating Wavelength Multiplexer On Silicon", *Optics Letters*, vol. **17**, no. 7, pp. 499 - 501, (1992).
 - [66] Takahashi H., Hibino Y., Ohmori Y. and Kawachi M., "Polarization-insensitive arrayed-waveguide wavelength demultiplexer with birefringence compensating film", *IEEE Photonics Technology Letters*, vol. **5**, no. 6, pp. 707 - 709, (1993).
 - [67] van Dam C., "InP-based polarisation independent wavelength demultiplexers", *PhD thesis*, Delft University of Technology, Delft, The Netherlands, (1997).
 - [68] van Dam C., Heidrich H., Hamacher M., Steenbergen C. A. M., Smit M. K. and Weinert C. M., "Integrated optical circuit comprising a polarization converter", *US patent 5838844*, (1998).

- [69] van Dam C., Spiekman L. H., van Ham F. P. G. M., Groen F. H., van der Tol J. J. G. M., Moerman I., Pascher W. W., Hamacher M., Heidrich H., Weinert C. M. and Smit M. K., "Novel compact polarization converters based on ultra short bends", *IEEE Photonics Technology Letters*, vol. **8**, no. 10, pp. 1346 - 1348, (1996).
- [70] Fujiwara M., Kubota K. and Lang R., "Erratum: Low-frequency intensity fluctuation in laser diodes with external optical feedback", *Applied Physics Letters*, vol. **39**, no. 2, pp. 182 - 182, (1981).
- [71] Fujiwara M., Kubota K. and Lang R., "Low-frequency intensity fluctuation in laser diodes with external optical feedback", *Applied Physics Letters*, vol. **38**, no. 4, pp. 217 - 220, (1981).
- [72] Hirota O. and Suematsu Y., "Noise properties of injection lasers due to reflected waves", *IEEE Journal of Quantum Electronics*, vol. **15**, no. 3, pp. 142 - 149, (1979).
- [73] Hirota O., Suematsu Y. and Kin-Sing K., "Properties of intensity noises of laser diodes due to reflected waves from single-mode optical fibers and its reduction", *IEEE Journal of Quantum Electronics*, vol. **17**, no. 6, pp. 1014 - 1020, (1981).
- [74] Ikushima I. and Maeda M., "Self-coupled phenomena of semiconductor lasers caused by an optical fiber", *IEEE Journal of Quantum Electronics*, vol. **14**, no. 5, pp. 331 - 332, (1978).
- [75] Ikushima I. and Maeda M., "Lasing spectra of semiconductor lasers coupled to an optical fiber", *IEEE Journal of Quantum Electronics*, vol. **15**, no. 9, pp. 844 - 845, (1979).
- [76] Lang R. and Kobayashi K., "External Optical Feedback Effects on Semiconductor Injection Laser Properties", *IEEE Journal of Quantum Electronics*, vol. **16**, no. 3, pp. 347 - 355, (1980).
- [77] Stubkjaer K. and Small M., "Noise properties of semiconductor lasers due to optical feedback", *IEEE Journal of Quantum Electronics*, vol. **20**, no. 5, pp. 472 - 478, (1984).
- [78] *IO-F-FFB-980-X Isolator*, OFR Inc., <http://www.ofr.com>
- [79] Holmes B. M., Bregenzer J. J. and Hutchings D. C., "Enabling Technologies for the Monolithic Integration of Semiconductor Lasers and Waveguide Optical Isolators", in *Proceedings of the Conference of Lasers and Electro-Optics 2007 (CLEO '07)*, 8 - 10 May 2007, Baltimore, Maryland, USA, paper CTuH3.
- [80] Holmes B. M. and Hutchings D. C., "Towards the Monolithically Integrated Optical Isolator on a Semiconductor Laser Chip", in *Proceedings of the IEEE Lasers & Electro-Optics Society Annual Meeting 2006 (LEOS '06)*, Montreal, Canada, 29 October - 2 November 2006, pp. 897 - 898.
- [81] Hutchings D. C., "Prospects for the implementation of magneto-optic elements in optoelectronic integrated circuits: A personal perspective", *Journal of Physics D: Applied Physics*, vol. **36**, no. 18, pp. 2222 - 2229, (2003).

-
- [82] Izutsu M. and Wang Z. L., "Propagation Losses of Guided Waves in Metallized Sidewall Waveguides", *Japanese Journal of Applied Physics*, vol. **37**, no. 6B, pp. 3643 - 3646, (1998).
 - [83] Holmes B. M. and Hutchings D. C., "Demonstration of quasi-phase-matched nonreciprocal polarization rotation in III-V semiconductor waveguides incorporating magneto-optic upper claddings", *Applied Physics Letters*, vol. **88**, no. 6, pp. 061116.1 - 0061116.3, (2006).
 - [84] Holmes B. M., Hutchings D. C. and Bregenzer J., "Experiments Towards the Realisation of a Monolithically-Integrated Optical Isolator Incorporating Quasi-Phase Matched Magneto-Optical Effects", in *Proceedings of the Material Research Society (MRS) Fall Meeting 2004*, Boston, USA, 29 November - 03 December 2004, paper J4.4.
 - [85] Bregenzer J. J., Holmes B. M., Sorel M. and Hutchings D. C., "Realization of a single-section passive polarization converter using a single-step etch process", in *Proceedings of the 17th Annual Meeting of the IEEE Lasers & Electro-Optics Society 2004 (LEOS'04)*, Rio Grande, Puerto Rico, 7 - 11 November 2004, paper TuA1, pp. 161 - 162.
 - [86] Holmes B. M., Bregenzer J. J. and Hutchings D. C., "Novel fabrication techniques for the realisation of passive waveguide polarisation converters", in *Proceedings of the Conference on Lasers and Electro-Optics 2005 (CLEO '05)*, Baltimore, Maryland, USA, 22 - 27 May 2005, paper CWD4, pp. 1285 - 1287.
 - [87] Holmes B. M. and Hutchings D. C., "Realization of Novel Low-Loss Monolithically Integrated Passive Waveguide Mode Converters", *IEEE Photonics Technology Letters*, vol. **18**, no. 1, pp. 43 - 45, (2006).
 - [88] Holmes B. M. and Hutchings D. C., "High Efficiency and Low Loss Fully Integrated Passive Waveguide Mode Converters", in *Proceedings of the IEEE Lasers & Electro-Optics Society Annual Meeting 2006 (LEOS '06)*, Montreal, Canada, 29 October - 2 November 2006.

Chapter 2

Theoretical background

2.1 Governing equations

The distribution of electromagnetic fields in dielectric media is governed by the set of macroscopic Maxwell's equations in free space [1]

$$\nabla \times \mathcal{E}(\mathbf{r}, t) = -\frac{\partial \mathcal{B}(\mathbf{r}, t)}{\partial t} \quad (2.1)$$

$$\nabla \times \mathcal{H}(\mathbf{r}, t) = \mathcal{J}(\mathbf{r}, t) + \frac{\partial \mathcal{D}(\mathbf{r}, t)}{\partial t} \quad (2.2)$$

$$\nabla \cdot \mathcal{D}(\mathbf{r}, t) = \rho \quad (2.3)$$

$$\nabla \cdot \mathcal{B}(\mathbf{r}, t) = 0. \quad (2.4)$$

The position vector \mathbf{r} defines a particular location in space, according to the used coordinate system, at which the time-dependent fields are being measured. In a Cartesian coordinate system for example, they can also be expressed in the form

$$\mathcal{A}(\mathbf{r}, t) \equiv \mathcal{A}(x, y, z, t). \quad (2.5)$$

$\mathcal{E}(\mathbf{r}, t)$, $\mathcal{B}(\mathbf{r}, t)$, $\mathcal{H}(\mathbf{r}, t)$ and $\mathcal{D}(\mathbf{r}, t)$ represent the electric field vector (in V/m), magnetic flux density vector (in T), magnetic field vector (in A/m) and electric displacement vector (in C/m²), respectively. The quantity $\mathcal{J}(\mathbf{r}, t)$ is the current density (in A/m²) and ρ represents the volume density of free electric charges (in As/m³). The constitutive equations are

$$\mathcal{D}(\mathbf{r}, t) = \varepsilon_0 \tilde{\varepsilon}_r(\mathbf{r}) \mathcal{E}(\mathbf{r}, t) \quad \text{and} \quad (2.6)$$

$$\mathcal{B}(\mathbf{r}, t) = \mu_0 \tilde{\mu}_r(\mathbf{r}) \mathcal{H}(\mathbf{r}, t). \quad (2.7)$$

The constants ε_0 and μ_0 represent the dielectric permittivity of vacuum ($\varepsilon_0 \cong 8.85 \times 10^{-9}$ F/m) and the magnetic permeability of vacuum ($\mu_0 = 4\pi \times 10^{-7}$ H/m), respectively. Both constants are related to the velocity of light in vacuum c_0

$$c_0 = (\varepsilon_0 \mu_0)^{-\frac{1}{2}} \simeq 299,792,458 \text{ m/s}. \quad (2.8)$$

The quantities $\tilde{\varepsilon}_r(\mathbf{r})$ and $\tilde{\mu}_r(\mathbf{r})$ denote the relative dielectric permittivity and relative magnetic permeability, respectively, of the material. Within this thesis, only linear (both $\tilde{\varepsilon}_r(\mathbf{r})$ and $\tilde{\mu}_r(\mathbf{r})$ are independent of field strengths) and non-magnetic materials ($\tilde{\mu}_r(\mathbf{r})$ is equal to the identity matrix) are considered.

In general, a periodic electromagnetic field can be expanded into a set of harmonic functions according to the Fourier analysis. It is common, that monochromatic fields (oscillating at one definite frequency f (in Hz)) are applied to the dielectric material. The field vectors then become harmonic functions of time. In order to obtain mathematical simplification, it is therefore convenient to express each field vector as a complex exponential function (by applying the Euler identity) in the form

$$\mathcal{A}(\mathbf{r}, t) = \mathbf{A}(\mathbf{r}) \cos(\omega t) = \operatorname{Re} \left\{ \mathbf{A}(\mathbf{r}) e^{j\omega t} \right\} = \frac{1}{2} \left\{ \mathbf{A}(\mathbf{r}) e^{j\omega t} + \mathbf{A}^*(\mathbf{r}) e^{-j\omega t} \right\}, \quad (2.9)$$

with

$$\omega = 2\pi f \quad (\text{in rad/s}). \quad (2.10)$$

The fields $\mathbf{A}(\mathbf{r})$ are called phasors and represent complex functions that depend only on the spatial position. The asterisk indicates the complex conjugate. ω denotes the angular frequency (in rad/s). Considering this representation, one has to bear in mind that only the real part of the vector fields, indicated by the symbol $\operatorname{Re}\{\}$, has a physical significance. Hence, omitting the symbol $\operatorname{Re}\{\}$ as well as the position vector \mathbf{r} (by assuming the use of a Cartesian coordinate system - unless otherwise stated - for the remainder of this thesis) for compactness of notation from the equations, it can simply be written

$$\mathcal{A}(\mathbf{r}) = \mathbf{A} e^{j\omega t}. \quad (2.11)$$

The general differential form of the Maxwell's equations can therefore be expressed (after substituting Equations (2.6) and (2.7)) for the time harmonic case for materials with no current sources or free charges ($\mathbf{j}(\mathbf{r}) = 0$, $\rho = 0$) as

$$\nabla \times \mathbf{E} = -j\omega\mu_0\mu_r\mathbf{H} \quad (2.12)$$

$$\nabla \times \mathbf{H} = j\omega\varepsilon_0\tilde{\varepsilon}_r(\mathbf{r})\mathbf{E} \quad (2.13)$$

$$\nabla \cdot (\varepsilon_0\tilde{\varepsilon}_r(\mathbf{r})\mathbf{E}) = 0 \quad (2.14)$$

$$\nabla \cdot (\mu_0\mu_r\mathbf{H}) = 0. \quad (2.15)$$

One has also to bear in mind that the time dependence, which is given by the factor $e^{j\omega t}$ and occurs as a common factor in all terms, has been factored out.

2.2 Birefringence

In the general case of *loss-less anisotropic* materials, $\tilde{\epsilon}_r(\mathbf{r})$ is a function of the spatial coordinates and can be expressed (in a Cartesian coordinate system) as a real, second rank tensor in the form

$$\tilde{\epsilon}_r(\mathbf{r}) = \begin{bmatrix} \epsilon_{xx} & \epsilon_{xy} & \epsilon_{xz} \\ \epsilon_{yx} & \epsilon_{yy} & \epsilon_{yz} \\ \epsilon_{zx} & \epsilon_{zy} & \epsilon_{zz} \end{bmatrix}. \quad (2.16)$$

This symmetric ($\epsilon_{ji} = \epsilon_{ij}$) matrix [2, 3] is a special case of a Hermitian matrix, resulting in pure real eigenvalues and eigenvectors and therefore consists of a total of six elements. The magnitude of each individual tensor component ϵ_{ij} depends on the relative orientation of the x -, y - and z -axes with respect to the crystal axes of the medium. It is always possible to choose the orientation of the coordinate system in a way that the axes are parallel to the eigenvectors. In this case, the permittivity tensor reduces to diagonal form

$$\epsilon_r(\mathbf{r}) = \begin{bmatrix} \epsilon_x & 0 & 0 \\ 0 & \epsilon_y & 0 \\ 0 & 0 & \epsilon_z \end{bmatrix}, \quad (2.17)$$

where $\epsilon_x = \epsilon_{xx}$ etc.. are the *principal* or *effective dielectric permittivities* along the set of three axes - called the *principal dielectric axes of the crystal* [4]. The dielectric response of the anisotropic material by means of the electric permeability tensor can therefore be defined as

$$D_x = \epsilon_0 \epsilon_{r,x} E_x \quad (2.18)$$

$$D_y = \epsilon_0 \epsilon_{r,y} E_y \quad (2.19)$$

$$D_z = \epsilon_0 \epsilon_{r,z} E_z. \quad (2.20)$$

Each direction of the principal axes imposes a different value of the effective permittivity, and therefore a different phase velocity.

In general, at a given direction of propagation in the medium, there exist *two* independent, *mutually orthogonal*, linearly polarised eigenwaves (with associated eigenphase-velocities and direction of polarisation) [3].

When considering a wave propagating in the z -direction and having its \mathbf{E} field linearly polarised parallel to one of the other principal axes (e.g. the x -direction), then \mathbf{D} is parallel to \mathbf{E} . An anisotropic material can then be considered to be isotropic with a dielectric permittivity equal to the corresponding effective dielectric permittivity (ϵ_x). Its phase velocity will be $c_x = (\mu_0 \epsilon_0 \epsilon_x)^{-1/2}$ [5].

When a wave propagates in the z -direction and its linearly polarised field has equal components in both x - and y -direction, it will split into two components, linearly polarised in x - and y -direction. These two directions impose two different refractive indices on the

incident wave. This is also referred to as *birefringence*. The two components propagate at different phase velocities according to their direction of polarisation.

The two allowed polarisation directions and the corresponding refractive indices for an *arbitrary* propagation direction in the medium is geometrically described by an index ellipsoid, which is also referred to as *indicatrix*. The indicatrix can be constructed from the permittivity tensor and encompasses all possible effective refractive indices of the medium

$$\frac{x^2}{n_x^2} + \frac{y^2}{n_y^2} + \frac{z^2}{n_z^2} = 1. \quad (2.21)$$

The major and minor axes of the indicatrix are aligned to the principal axes. The lengths of the axes represent the refractive indices along the associated lattice axes (n_x, n_y, n_z). The determination of the direction of polarisation and the corresponding refractive indices for a given direction of propagation is demonstrated in the following section for a positive uniaxial crystal.

The dielectric tensor may be further simplified by considering the crystal symmetry of materials. Crystallographic material structures can be categorised into three classes in terms of their optical properties [6] according to their lattice structure:

- In *cubic* (which are optically *isotropic*) crystals the atomic length of the three unit cell dimensions are equal. $\tilde{\epsilon}_r(\mathbf{r})$ is therefore independent from the spatial coordinates and represents itself as a scalar as all off-diagonal elements vanish and all diagonal elements have the same value ($\epsilon_{xx} = \epsilon_{yy} = \epsilon_{zz} = \epsilon_r$).
- *Uniaxial* crystals (which include trigonal, tetragonal, and hexagonal lattice types) have one unique and two identical unit cell dimensions. Subsequently, two of the components ϵ_x, ϵ_y and ϵ_z are equal (e.g. $\epsilon_x = \epsilon_y \neq \epsilon_z$).
- *Biaxial* crystals (which include orthorhombic, monoclinic and triclinic lattice types) have different unit cell dimensions in all three directions. Hence, none of the components ϵ_x, ϵ_y and ϵ_z are equal ($\epsilon_x \neq \epsilon_y \neq \epsilon_z$).

As a consequence of the differences in the unit cell directions, uniaxial and biaxial crystals have two and three different refractive indices, respectively.

2.2.1 Uniaxial crystal

In an uniaxial material, the principal axis that has the unique lattice constant is called the *extraordinary* (*e*-) *axis*, whereas the other two ones are called *ordinary* (*o*-) *axes*. An uniaxial crystal can be categorised in positive uniaxial ($n_e > n_o$) (e.g. quartz) and negative uniaxial ($n_o < n_e$) (e.g. calcite). The equation of the index ellipsoid becomes

$$\frac{x^2}{n_o^2} + \frac{y^2}{n_o^2} + \frac{z^2}{n_e^2} = 1. \quad (2.22)$$

The corresponding indicatrix for a positive uniaxial crystal is illustrated in Figure 2-1(a). The axis of rotational symmetry (*z*-axis) is also referred to as *optical axis*. The direction of propagation \mathbf{n} is at an angle γ to the *z*-axis and, without loss of generality, the projection of \mathbf{n} onto the *x-y* plane coincides with the *y*-axis. The directions of polarisation and the corresponding refractive indices for a given direction of propagation (\mathbf{n}) can be determined by evaluating the ellipse (shaded), which is formed by the intersection of a plane through the origin and perpendicular to the direction of propagation and the index ellipsoid (Figure 2-1(a)). The two allowed directions of polarisation ($\mathbf{D}^{(1)}$ and $\mathbf{D}^{(2)}$) correspond to the direction of the major and minor axis of the formed ellipse (Figure 2-1(b)). The refractive indices corresponding to the two allowed mutually perpendicular directions of polarisation ($n^{(1)}$, $n^{(2)}$) are represented by the lengths of the major- and minor semi-axes of the formed ellipse [4]. As the minor semi-axis (major semi-axis for a negative uniaxial crystal) always lies in the *x-y* plane, its length $n_x = n^{(2)} = n_o$ is *independent* of γ . A ray with this direction of polarisation is also referred to as *ordinary* (*o*-) ray. The length of the other semi-axis ($n^{(1)} = n_e$) is *dependent* on γ . A ray with this direction of polarisation is also referred to as *extraordinary* (*e*-) ray.

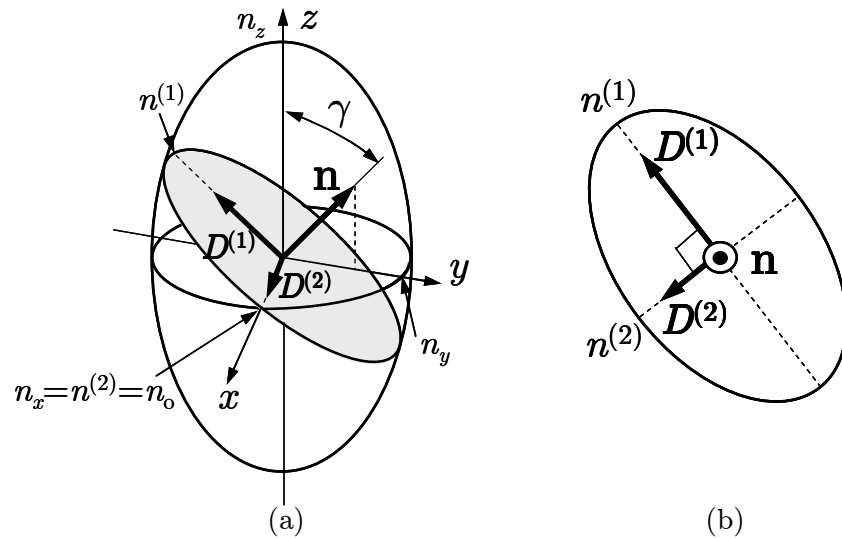


Figure 2-1: (a) Indicatrix for a positive uniaxial crystal ($n_x = n_y = n_o < n_z = n_e$). The inner ellipse (shaded) is the intersection of the indicatrix with the plane perpendicular to \mathbf{n} . (b) Graphical evaluation of the two allowed directions of polarisation and corresponding refractive indices ($n^{(1)}$, $n^{(2)}$) for a given direction \mathbf{n} from the formed ellipse. (after [7])

2.3 Wave equation

By applying the vectorial operator $\nabla \times$ to Equation (2.12) ($\mu_r = 1$)

$$\nabla \times (\nabla \times \mathbf{E}) = -j\omega\mu_0\nabla \times \mathbf{H} \quad (2.23)$$

and using the formula

$$\nabla \times (\nabla \times \mathbf{A}) = \nabla (\nabla \cdot \mathbf{A}) - \nabla^2 \mathbf{A}, \quad (2.24)$$

Equation (2.23) can be written in the form

$$\nabla (\nabla \cdot \mathbf{E}) - \nabla^2 \mathbf{E} = -j\omega\mu_0\nabla \times \mathbf{H}. \quad (2.25)$$

Substituting Equation (2.13)

$$\nabla (\nabla \cdot \mathbf{E}) - \nabla^2 \mathbf{E} = \omega^2\mu_0\varepsilon_0\varepsilon_r(\mathbf{r})\mathbf{E} \quad (2.26)$$

and substituting

$$\nabla \cdot (\varepsilon_r(\mathbf{r})\mathbf{E}) = \nabla\varepsilon_r(\mathbf{r}) \cdot \mathbf{E} + \varepsilon_r(\mathbf{r})\nabla \cdot \mathbf{E} = 0 \quad \longrightarrow \quad \nabla \cdot \mathbf{E} = -\frac{\nabla\varepsilon_r(\mathbf{r}) \cdot \mathbf{E}}{\varepsilon_r(\mathbf{r})}, \quad (2.27)$$

the *vectorial wave equation* for the electric field \mathbf{E} can be obtained in the form

$$\nabla^2 \mathbf{E} + \nabla \left(\frac{\nabla\varepsilon_r(\mathbf{r})}{\varepsilon_r(\mathbf{r})} \cdot \mathbf{E} \right) + \omega^2\mu_0\varepsilon_0\varepsilon_r(\mathbf{r})\mathbf{E} = 0. \quad (2.28)$$

In an analogous way, the vectorial wave equation for the magnetic field \mathbf{H} can be obtained and written as

$$\nabla^2 \mathbf{H} + \frac{\nabla\varepsilon_r(\mathbf{r})}{\varepsilon_r(\mathbf{r})} \times (\nabla \times \mathbf{H}) + \omega^2\mu_0\varepsilon_0\varepsilon_r(\mathbf{r})\mathbf{H} = 0. \quad (2.29)$$

For *homogeneous, isotropic* materials, $\varepsilon_r(\mathbf{r})$ is independent of the spatial coordinates and is therefore represented as a scalar as all off-diagonal elements vanish and all diagonal elements have the same value. The vectorial wave equations for general waveguide problems can therefore be reduced to the so-called *Helmholtz equations* for the electric field \mathbf{E} (by applying Equation (2.14))

$$\nabla^2 \mathbf{E} + \omega^2\mu_0\varepsilon_0\varepsilon_r\mathbf{E} = 0 \quad (2.30)$$

and in an analogous way for the magnetic field \mathbf{H}

$$\nabla^2 \mathbf{H} + \omega^2\mu_0\varepsilon_0\varepsilon_r\mathbf{H} = 0. \quad (2.31)$$

These time-independent vector wave equations are valid for fields oscillating at a single angular frequency ω .

2.4 Plane waves

The basic solution to the Helmholtz equation is represented by a plane wave in a bulk medium. There are no boundaries to the medium in which the field exists. The plane wave's surfaces of constant phase are therefore infinite planes (as the name indicates), perpendicular to the direction of propagation (z -axis). In this case, no field quantities vary in direction of the transverse coordinates x and y ($\partial/\partial x = \partial/\partial y = 0$). The only spatial variation is caused by variations in the z -direction. Considering the electric field to have only one component, e.g. in x -direction, for simplicity, Equation (2.30) reduces to a scalar equation

$$\frac{d^2 E_x}{dz^2} + \omega^2 \mu_0 \varepsilon_0 \varepsilon_r = 0. \quad (2.32)$$

This is a second order differential equation, which has a solution in the form

$$E_x = E_{x+} e^{-jkz} + E_{x-} e^{jkz}, \quad (2.33)$$

where E_{x+} and E_{x-} are constants. The *wave number* k of the plane wave in the specified medium is given by

$$k = \omega(\mu_0 \varepsilon_0 \varepsilon_r)^{1/2}. \quad (2.34)$$

At this stage one can extract the *wave number in vacuum* k_0 , which is defined as

$$k_0 = \omega(\varepsilon_0 \mu_0)^{1/2} = \frac{\omega}{c_0} = \frac{2\pi}{\lambda_0}, \quad (2.35)$$

with λ_0 as the wavelength (in nm) in vacuum. The wave number in the specified medium k can be expressed as

$$k = \omega(\varepsilon_0 \mu_0 \mu_r \varepsilon_r)^{1/2} = k_0(\mu_r \varepsilon_r)^{1/2} = k_0 n = \frac{2\pi}{\lambda}, \quad (2.36)$$

where λ is the *spatial wavelength* (in nm). λ represents the distance that separates planes of equal phase. The *refractive index* n of the material is defined as

$$n = \varepsilon_r^{1/2}. \quad (2.37)$$

The velocity of the wave, also referred to as *phase velocity*, v_p is given by

$$v_p = \frac{\omega}{k} = \frac{1}{(\mu_0 \varepsilon_0 \varepsilon_r)^{1/2}} = \frac{c_0}{n}. \quad (2.38)$$

Considering only the forward propagating waves (within the context of this thesis) including the time dependence, Equation (2.33) becomes

$$E_x = E_{x+} e^{j(\omega t - kz)}. \quad (2.39)$$

The magnetic field component, which accompanies the solution for the x -component of the electric field, has only a component in the y -direction

$$H_y = H_{y+} e^{j(\omega t - kz)}. \quad (2.40)$$

Thus, the direction of the magnetic field amplitude is perpendicular to both the direction of propagation (z -axis) and the electric field (E_x). As there are no longitudinal field components, plane electromagnetic waves are often referred to as *transverse electromagnetic* (TEM) waves [6].

2.5 Polarisation

Considering the electric field of a time-harmonic monochromatic wave in vacuum that propagates in the z -direction (that means no electric field component in the z -direction), the electric field vector has the most general form [6, 8]

$$\mathbf{E}(z, t) = \begin{pmatrix} E_{x+} e^{j\phi_x} \\ E_{y+} e^{j\phi_y} \end{pmatrix} e^{j(\omega t - kz)}, \quad (2.41)$$

where ϕ_x and ϕ_y are arbitrary (but constant) phase factors. The evolution of the resulting electric field, whose two components lie in the x - y plane, governs the polarisation of the wave.

The convention used in this thesis to describe the tracing direction of the electric field vector in the x - y plane is as follows: The observer looks towards the source ($-z$ -direction) and observes the electric field as it propagates in the z -direction.

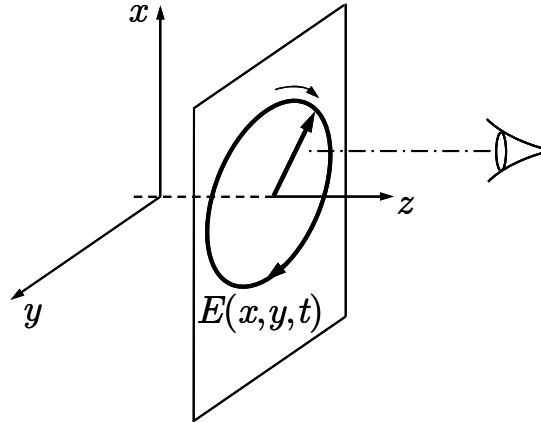


Figure 2-2: Description of polarisation as the trace of the electric field in the plane (x, y) perpendicular to the direction of propagation z . A right-hand elliptically polarised field is illustrated as an example according to the convention that a field is called right handed polarised when the field is looked at as it propagates towards the observer and performs a clockwise rotation (after [8]).

The electric field is called *right (left) hand polarised* when the electric field vector traces an ellipse (the most general case) clockwise (anticlockwise) [9]. The following combinations of E_{x+} , E_{y+} , ϕ_x and ϕ_y are particularly important:

- If $E_{x+} = E_{y+}$ and $\phi_x = \phi_y$, the resulting type of wave is called *linearly polarised*. The direction of the electric field vector represents the direction of polarisation. The plane of polarisation does not change during propagation.

- For $E_{x+} = E_{y+}$ and $\phi_x = \phi_y \pm \pi/2$, the magnitude of the electric field vector remains constant. The direction of polarisation rotates as a function of space and time and describes a *circularly polarised* wave. The sign of the $\pi/2$ phase shift determines a right- or left hand circularity.

2.6 Boundary conditions

Optical waveguides usually consist of different layers with different material constants. The solutions to Maxwell's equations are subject to boundary conditions at the intersections between these media. Figure 2-3 illustrates the boundary between two layers of different media (indices 1 and 2).

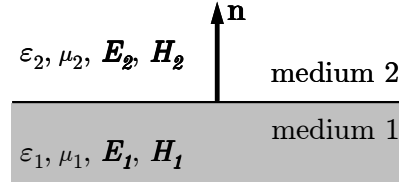


Figure 2-3: Boundary scenario between two media with different material constants. The unit normal vector \mathbf{n} is perpendicular to the surface at the transition point.

In the absence of surface charges ($\rho = 0$) and surface currents ($\mathbf{j}(\mathbf{r}, t) = 0$) the boundary conditions are given as

$$\mathbf{n} \times (\mathbf{E}_1 - \mathbf{E}_2) = 0 \quad (2.42)$$

$$\mathbf{n} \times (\mathbf{H}_1 - \mathbf{H}_2) = 0 \quad (2.43)$$

$$\mathbf{n} \cdot (\varepsilon_1 \mathbf{E} - \varepsilon_2 \mathbf{E}) = 0 \quad (2.44)$$

$$\mathbf{n} \cdot (\mathbf{H}_1 - \mathbf{H}_2) = 0. \quad (2.45)$$

These conditions imply the continuity of all magnetic field components (as $\mu_1 = \mu_2 = \mu_0 = \text{constant}$) as well as the tangential component of the electric field across the boundary. Equation (2.44) states a discontinuity of the normal component of the electric field due to different permittivity values of both media.

2.7 Modal analysis of optical waveguides

In integrated optics, a dielectric waveguide is described by its refractive index profile $n(x, y)$, as schematically shown in Figure 2-4. The coordinate axes have been oriented in a way that the waveguide structure is longitudinal invariant in z -direction, which is also the direction of light propagation. In this thesis, only waveguides that are comprised of homogenous regions, such that $n(x, y)$ is piecewise constant, are considered. The assumed low refractive index contrast between the waveguide layers result in a weakly guiding waveguide.

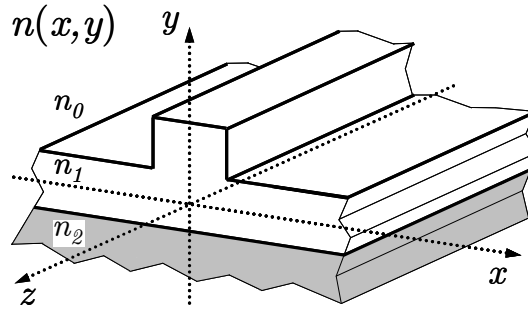


Figure 2-4: Schematic of a longitudinal invariant optical waveguide and the choice of the orientation of the Cartesian coordinate system. The waveguide is described by the refractive index profile $n(x, y)$.

The field solutions to Maxwell's equations of monochromatic light propagating in this longitudinal homogeneous waveguide can be expressed as the product of the transversal field distribution and a term representing the harmonic time and propagation coordinate dependence in the form

$$\mathcal{A}(x, y, z, t) = \mathbf{A}(x, y)e^{j(\omega t - \beta z)}. \quad (2.46)$$

Mathematically, the term $\mathbf{A}(x, y)$ represents the eigensolution, which is uniquely determined by its eigenvalue - the propagation constant β . An optical mode is defined by the electric and magnetic components of the transversal field distribution and its propagation constant β and represents an *independent* solution. It is convenient to define an effective refractive index n_{eff} by the ratio of the propagation constant of the considered mode β_ν to the wave number in vacuum k_0

$$n_{eff} = \frac{\beta_\nu}{k_0}, \quad (2.47)$$

where ν is the mode label that indicates the mode number [10]. By omitting the time-dependence, the electric and magnetic field solutions for a waveguide mode are

$$\mathbf{E}(x, y, z) = \mathbf{E}(x, y)e^{-j\beta z} \quad (2.48)$$

$$\mathbf{H}(x, y, z) = \mathbf{H}(x, y)e^{-j\beta z}. \quad (2.49)$$

For a given device geometry, the discrete set of guided modes and the continuum of radiation modes form a *complete set* that represents all possible field distributions of an incident optical signal in the given waveguide [11, 12].

2.7.1 One dimensional confinement: slab waveguide

Figure 2-5 illustrates a three-layer asymmetric dielectric slab waveguide consisting of a guiding (core) layer (thickness d and refractive index n_2), lower cladding (substrate) layer (refractive index n_3) and upper cladding layer (refractive index n_1), which provide the boundary conditions for the solution of the wave equation.

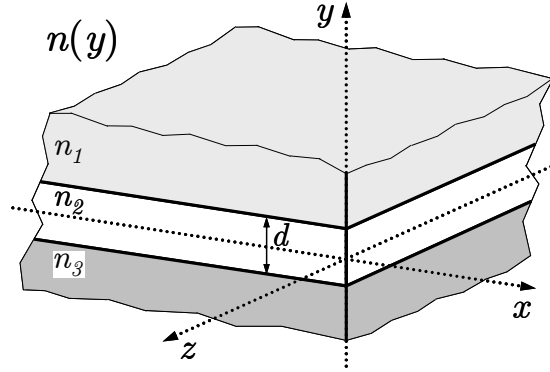


Figure 2-5: Schematic of an asymmetric slab waveguide and the chosen orientation of the Cartesian coordinate system.

The relation between the refractive indices was chosen to be $n_1 < n_3 < n_2$, whereas the refractive index contrast between core- and cladding layers Δn is assumed to be *low* ($\Delta n \ll 1$) and therefore establishing a *weakly guiding waveguide*. The right-handed coordinate system is chosen in a way that the y -axis is perpendicular to the layer plane and the z -axis indicates the direction of propagation. The waveguide structure is uniform in both x - and z -direction which confines the light to only one dimension, the y -direction. The refractive index $n(y)$ and the corresponding modal fields are functions of only this coordinate and *independent* of x . The derivative with respect to the x -coordinate can therefore be set to zero ($\partial/\partial x = 0$). The modes propagate in the z -direction with their corresponding propagation constant β and depend on z as $e^{j\beta z}$. The derivative with respect to the z -coordinate, $\partial/\partial z$, can therefore be replaced by $-j\beta$. Under these conditions Maxwell's equations (2.12) and (2.13) have the components

$$j\beta E_y + \frac{\partial E_z}{\partial y} = -j\omega\mu_0 H_x \quad (2.50)$$

$$j\beta E_x = -j\omega\mu_0 H_y \quad (2.51)$$

$$-\frac{\partial E_x}{\partial y} = -j\omega\mu_0 H_z \quad (2.52)$$

and

$$\frac{\partial H_z}{\partial y} + j\beta H_y = j\omega\varepsilon_0\varepsilon_r E_x \quad (2.53)$$

$$-j\beta H_x = j\omega\varepsilon_0\varepsilon_r E_y \quad (2.54)$$

$$-\frac{\partial H_x}{\partial y} = j\omega\varepsilon_0\varepsilon_r E_z, \quad (2.55)$$

respectively. The general solution of Equations (2.50) to (2.55) splits into *two* self-consistent types of solutions. Both sets, consisting of three equations each, are *independent* from each other, and so are their solutions. The solutions are also referred to as *transverse electric* (TE) and *transverse magnetic* (TM) modes.

Transverse electric (TE) modes

Equations (2.51), (2.52) and (2.53) form a set that contains only the particular field components E_x , H_y and H_z and is referred to as TE modes, since the electric field is restricted to the transverse direction (E_x) and has no component in longitudinal direction ($E_y = E_z = H_x = 0$). The magnetic field components in this set are related to E_x by

$$\mathbf{E} = \begin{pmatrix} E_x \\ 0 \\ 0 \end{pmatrix}, \quad \mathbf{H} = \frac{1}{\omega\mu_0} \begin{pmatrix} 0 \\ \beta E_x \\ -j\frac{\partial E_x}{\partial y} \end{pmatrix}. \quad (2.56)$$

The field component E_x of the mode in each layer obeys the wave equation

$$\nabla^2 E_{x,i}(x, y, z) + \omega^2 \mu_0 \varepsilon_0 n_i^2 E_{x,i} = 0 \quad i = 1, 2, 3. \quad (2.57)$$

Considering the boundary conditions, the solution of the electric field has the form

$$\mathbf{E}(x, y, z, t) = \mathbf{E}(x, y) e^{j(\omega t - \beta z)} \quad (2.58)$$

so that Equation (2.57) becomes

$$\left(\frac{\partial^2}{\partial x^2} + \frac{\partial^2}{\partial y^2} \right) E_x(x, y) + (k_0^2 n_i^2 - \beta^2) E_x = 0 \quad i = 1, 2, 3. \quad (2.59)$$

Setting $\partial/\partial x = 0$ and writing it separately for the different layers in the slab waveguide

$$\frac{\partial}{\partial y^2} E_x(y) = -(k_0^2 n_2^2 - \beta^2) E_x(y) = h^2 E_x(y); \quad \text{core layer} \quad (2.60)$$

$$\frac{\partial}{\partial y^2} E_x(y) = -(k_0^2 n_1^2 - \beta^2) E_x(y) = p^2 E_x(y); \quad \text{upper cladding} \quad (2.61)$$

$$\frac{\partial}{\partial y^2} E_x(y) = -(k_0^2 n_3^2 - \beta^2) E_x(y) = q^2 E_x(y); \quad \text{lower cladding}, \quad (2.62)$$

where the constants h, p, q are defined as

$$h^2 = k_0^2 n_2^2 - \beta^2; \quad p^2 = \beta^2 - k_0^2 n_1^2; \quad q^2 = \beta^2 - k_0^2 n_3^2. \quad (2.63)$$

Depending on the relative values of n_1, n_2, n_3 and k_0 there are different regimes for the mode solutions as a function of β at a fixed ω (Figure 2-6(top)).

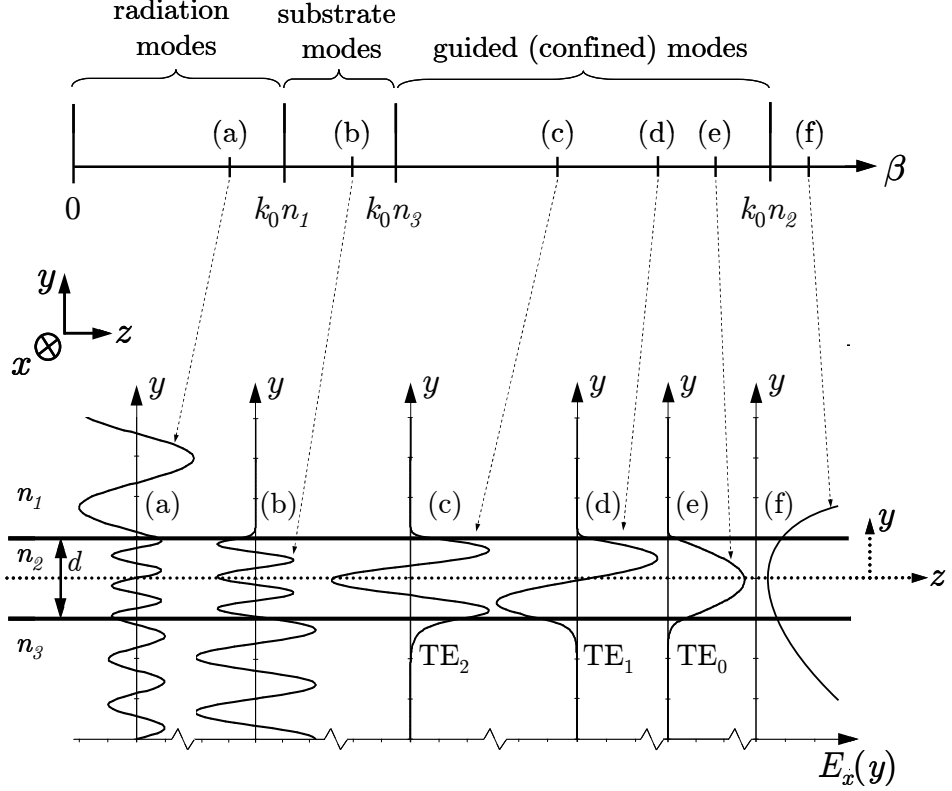


Figure 2-6: (Top) Illustration of the distribution of the different regimes of the propagation constant β - and therefore the types of modes - of the dielectric slab waveguide. (Bottom) Illustration of the $E_x(y)$ field distributions to the corresponding regime of β . (after [4])

Guided modes of the waveguide are represented by sinusoidal oscillations restricted to the core layer and an exponentially decaying electric field in the cladding layers. This limits the values for β to the region $k_0 n_3 < \beta < k_0 n_2$ (h^2, p^2, q^2 are positive) (Figure 2-6).

For the TE mode, $E_x(y)$ takes the form in the core layer as

$$E_x(y) = A \cos(hy) + B \sin(hy). \quad (2.64)$$

The characteristic equation for the guided TE modes is then given as

$$\tan(hd) = \frac{(p+q)h}{h^2 - pq}. \quad (2.65)$$

This transcendental equation manifests itself in a way that the allowed values for β in the guiding regime $k_0 n_3 < \beta < k_0 n_2$ are *discrete* (β_v), while in other regimes β is continuous. The number of confined modes depends on ω, d and the refractive indices of the layers n_1, n_2 and n_3 . The mode cut-off condition [13] is given by

$$\beta_v = k_0 n_2 \quad \text{or} \quad n_{eff,v} = n_2. \quad (2.66)$$

An illustration of the electric and magnetic field components of the fundamental TE mode (TE_0) in a slab waveguide (Figure 2-5) is given in Figure 2-7 and Figure 2-8, respectively. The operating wavelength was set to $\lambda = 1064 \text{ nm}$, which corresponds to the emitting wavelength of an available *diode pumped solid state* (DPSS) Nd:YAG laser that was used as a signal source. Figure 2-7(b) shows the simulated slab waveguide layer structure and the computational window Ω_W . A $0.5 \mu\text{m}$ thick core ($n_2 = 3.476$, equivalent to n_{GaAs}) was positioned above a lower cladding layer ($n_3 = 3.306$, equivalent to n of $\text{Al}_{0.27}\text{Ga}_{0.73}\text{As}$) ($\rightarrow \Delta n = 0.17$) and topped by a $1 \mu\text{m}$ thick air layer. The refractive index contrast

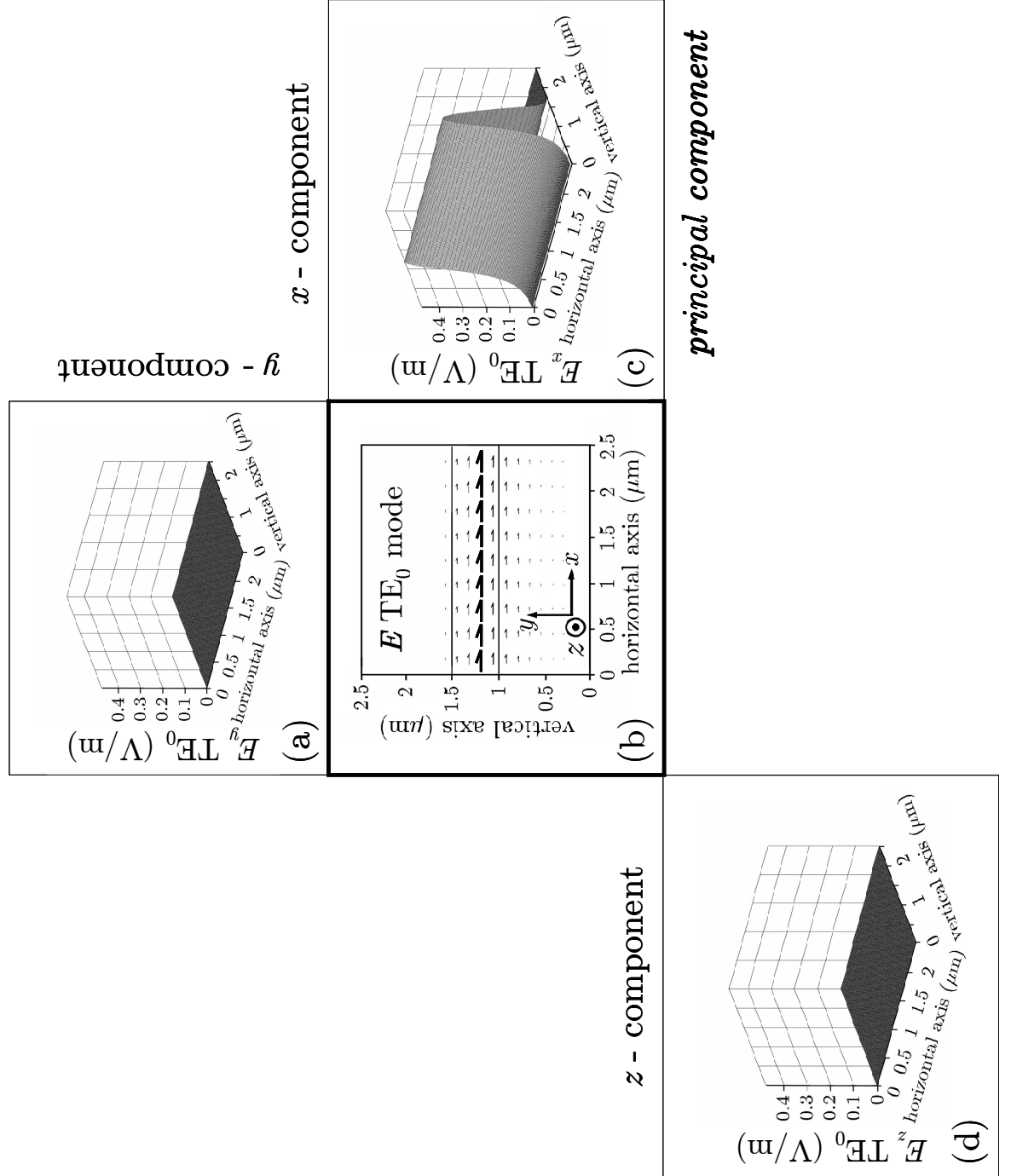


Figure 2-7: (a)-(d) Illustration of the electric vector field with corresponding profile plots of the fundamental TE mode (TE_0) components in a dielectric slab waveguide. The principal electric field component of the TE_0 mode is E_x .

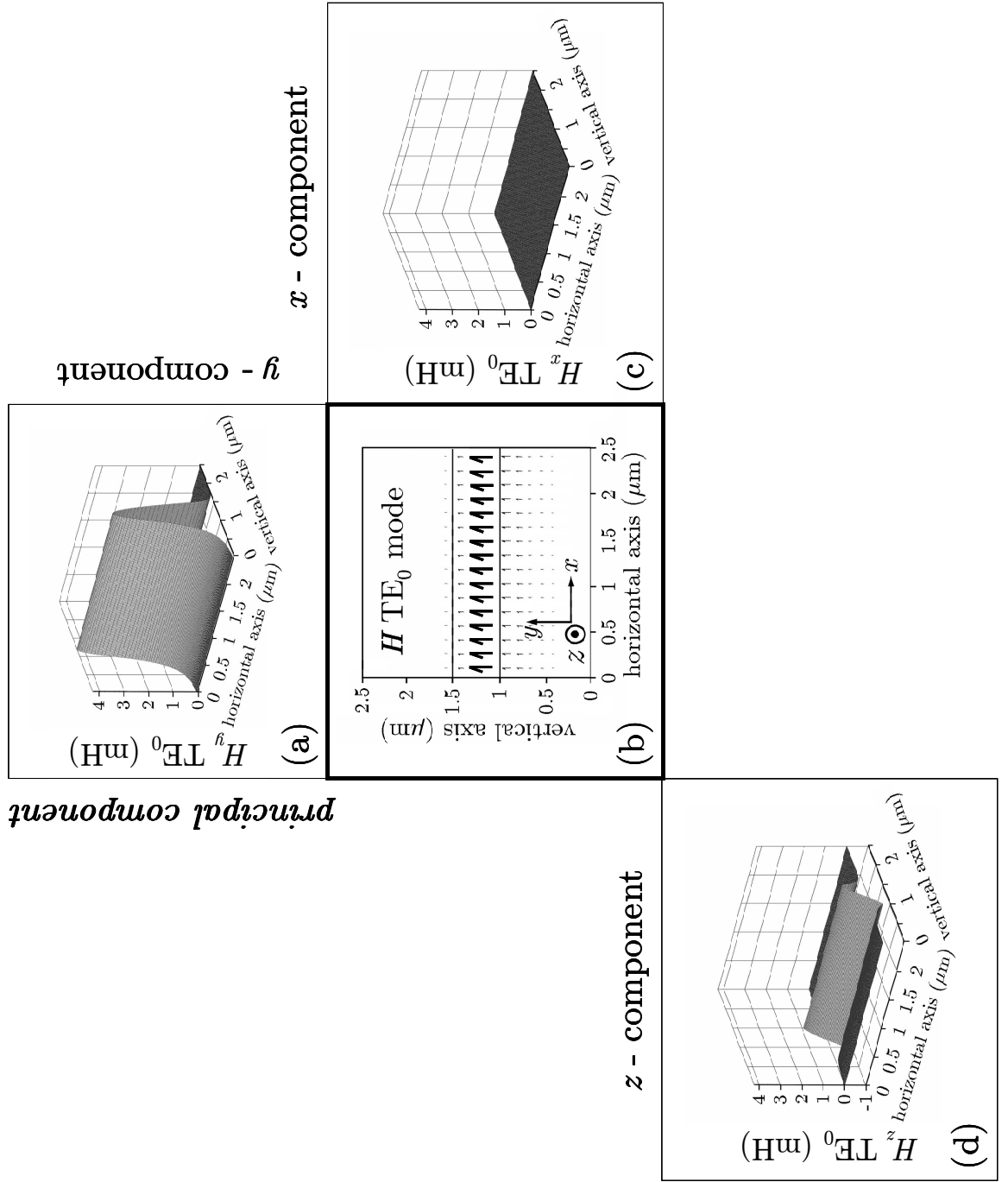


Figure 2-8: (a)-(d) Illustration of the magnetic vector field with corresponding profile plots of the fundamental TE_0 mode components in a dielectric slab waveguide. The principal magnetic field component of the TE_0 mode is H_y .

between core- and lower cladding layer Δn is assumed to be *low* ($\Delta n \ll 1$) and therefore establishing a *weakly guiding waveguide*. The refractive index of the lower cladding layer was set to $n_3 = 3.306$ (equivalent to n of $\text{Al}_{0.27}\text{Ga}_{0.73}\text{As}$), which results in a value for Δn of 0.17. A commercial available *finite element method* (FEM) based mode solver [14] was used to calculate the propagation constant β_{TE0} of $20.074 \mu\text{m}^{-1}$ (equivalent to $n_{\text{eff,TE0}} = 3.399$). For the remainder of this thesis, the imposed boundary conditions of the computational window were set by default to *electric wall* on the right- and left hand side and *magnetic wall* on the top and bottom. Also, the mesh densities were set to the default values of 60 triangles in both x - and y -direction. It can be noted that there is *no* electric field component in longitudinal (z) direction. The electric (magnetic) field in transverse direction consists of only *one* component (E_x (H_y)), which is also referred to as the *principal* component.

Transverse magnetic (TM) modes

The second set formed by Equations (2.50), (2.54) and (2.55) contains only the particular components H_x , E_y and E_z . This set is also referred to as TM modes as the magnetic field contains only a transverse component (H_x) and no longitudinal component ($E_x = H_y = H_z = 0$). The electric field components in this set are related to H_x by

$$\mathbf{E} = \frac{1}{\omega\epsilon_0\epsilon_r} \begin{pmatrix} 0 \\ -\beta H_x \\ j \frac{\partial H_x}{\partial y} \end{pmatrix}, \quad \mathbf{H} = \begin{pmatrix} H_x \\ 0 \\ 0 \end{pmatrix}. \quad (2.67)$$

The transcendental eigenvalue equation for the guided TM modes can be obtained in analogous form to the TE mode:

$$\tan(hd) = \frac{h \left(\frac{n_2^2}{n_3^2} p + \frac{n_2^2}{n_1^2} q \right)}{h^2 - \frac{n_2^4}{n_3^2} \frac{qp}{n_1^2}}. \quad (2.68)$$

An illustration of the electric and magnetic field components of the fundamental TM mode (TM_0) in a slab waveguide is given in Figure 2-9 and Figure 2-10, respectively. The slab waveguide layer composition is the same as for the TE_0 mode investigation. The resulting propagation constant β_{TM0} is $19.996 \mu\text{m}^{-1}$ (equivalent to $n_{\text{eff,TM0}} = 3.386$). It can be noted that there is *no* magnetic field component in longitudinal (z -) direction. The electric (magnetic) field in the transverse direction consists of only *one* (the principal) component (E_y (H_x)).

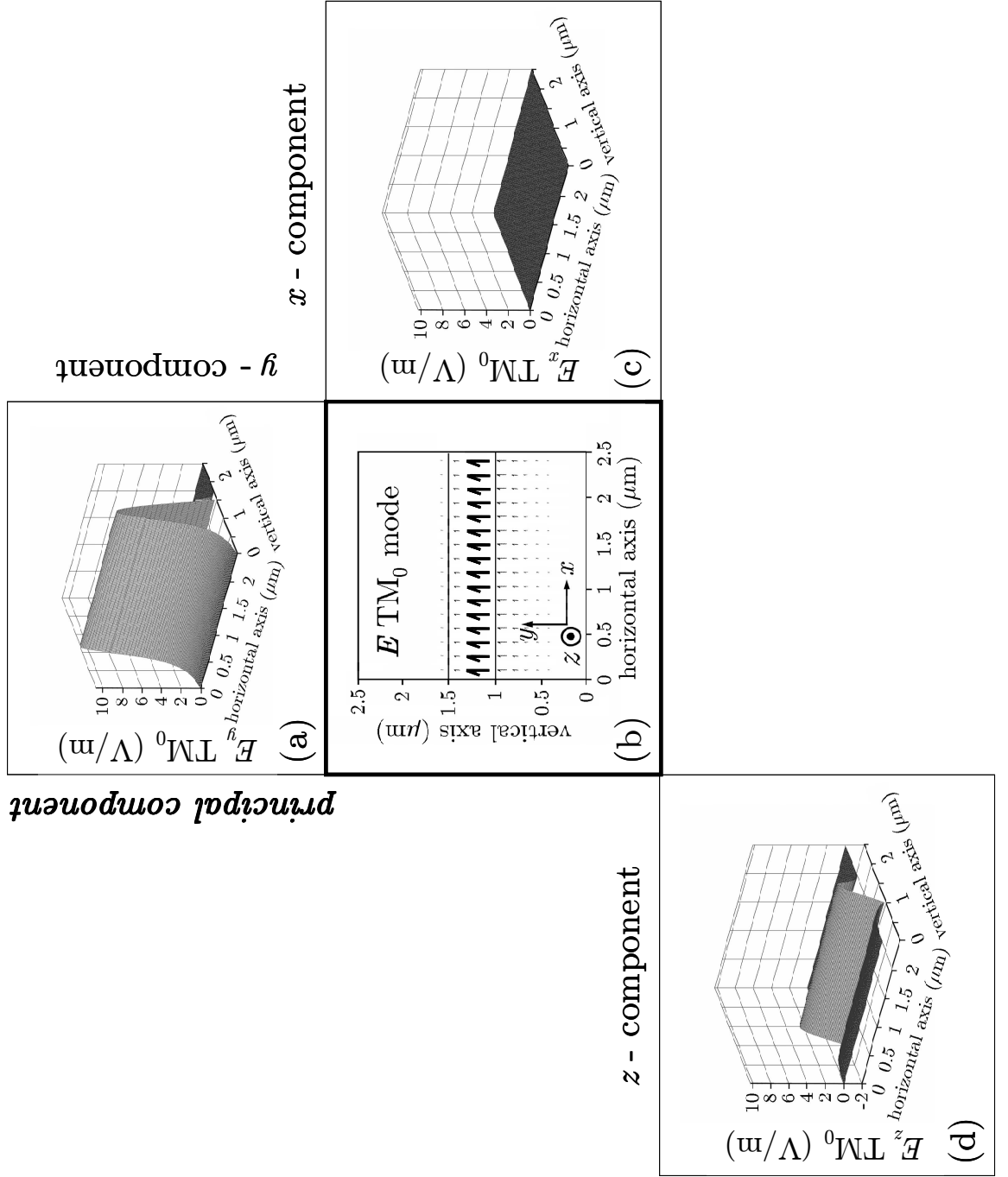


Figure 2-9: (a)-(d) Illustration of the electric vector field with corresponding profile plots of the fundamental TM mode (TM_0) components in a dielectric slab waveguide. The principal electric field component of the TM_0 mode is E_y .

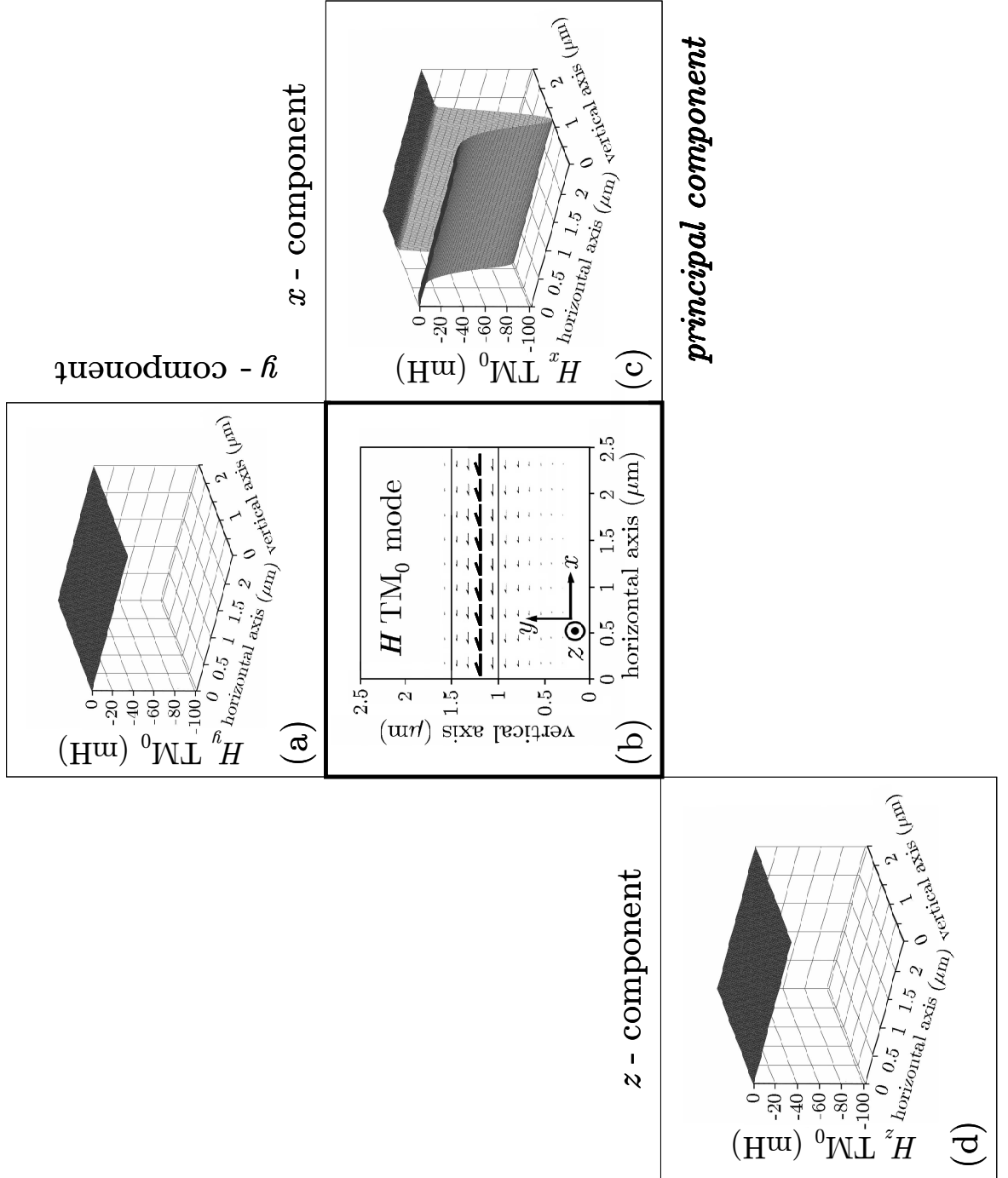


Figure 2-10: (a)-(d) Illustration of the magnetic vector field with corresponding profile plots of the fundamental TM mode (TM_0) components in a dielectric slab waveguide. The principal magnetic field component of the TM_0 mode is H_x .

2.7.2 Two dimensional confined waveguides

As planar waveguides confine light in only one transversal direction, their application in integrated optics is rare. Two dimensional confined waveguide structures such as stripe- or rib waveguides (Figure 2-4) are commonly used in integrated optics. They can be considered as longitudinally invariant optical waveguides that are comprised of homogenous refractive index regions. The transverse refractive index distribution $n(x,y)$ is piecewise constant and $\partial n/\partial z = 0$. Due to the longitudinal invariance, the field components can be separated into transversal and longitudinal components. It is common practice in dealing with waveguide problems to focus on the transversal components as they are related to the longitudinal components via Equations (2.12) and (2.13). The total field can therefore be derived from the two transverse components of the electric (E_x, E_y) or magnetic (H_x, H_y) field. As $\varepsilon_r(\mathbf{r}) = n^2(x,y)$ and $\partial \varepsilon_r(\mathbf{r})/\partial z = 0$, the transverse electric field components in the vectorial wave equation (2.28) are given by

$$\frac{\partial^2 E_x}{\partial x^2} + \frac{\partial^2 E_x}{\partial y^2} + \frac{\partial^2 E_x}{\partial z^2} + \frac{\partial}{\partial x} \left(\frac{1}{\varepsilon_r(\mathbf{r})} \frac{\partial \varepsilon_r(\mathbf{r})}{\partial x} E_x \right) + k_0^2 \varepsilon_r(\mathbf{r}) E_x = -\frac{\partial}{\partial x} \left(\frac{1}{\varepsilon_r(\mathbf{r})} \frac{\partial \varepsilon_r(\mathbf{r})}{\partial y} E_y \right) \quad (2.69)$$

and

$$\frac{\partial^2 E_y}{\partial x^2} + \frac{\partial^2 E_y}{\partial y^2} + \frac{\partial^2 E_y}{\partial z^2} + \frac{\partial}{\partial y} \left(\frac{1}{\varepsilon_r(\mathbf{r})} \frac{\partial \varepsilon_r(\mathbf{r})}{\partial y} E_y \right) + k_0^2 \varepsilon_r(\mathbf{r}) E_y = -\frac{\partial}{\partial y} \left(\frac{1}{\varepsilon_r(\mathbf{r})} \frac{\partial \varepsilon_r(\mathbf{r})}{\partial x} E_x \right). \quad (2.70)$$

Likewise, the transverse magnetic field components in Equation (2.29) can be written as

$$\frac{\partial^2 H_x}{\partial x^2} + \frac{\partial^2 H_x}{\partial y^2} + \frac{\partial^2 H_x}{\partial z^2} - \frac{1}{\varepsilon_r(\mathbf{r})} \frac{\partial \varepsilon_r(\mathbf{r})}{\partial y} \frac{\partial H_x}{\partial y} + k_0^2 \varepsilon_r(\mathbf{r}) H_x = -\frac{1}{\varepsilon_r(\mathbf{r})} \frac{\partial \varepsilon_r(\mathbf{r})}{\partial y} \frac{\partial H_y}{\partial x} \quad (2.71)$$

$$\frac{\partial^2 H_y}{\partial x^2} + \frac{\partial^2 H_y}{\partial y^2} + \frac{\partial^2 H_y}{\partial z^2} - \frac{1}{\varepsilon_r(\mathbf{r})} \frac{\partial \varepsilon_r(\mathbf{r})}{\partial x} \frac{\partial H_y}{\partial x} + k_0^2 \varepsilon_r(\mathbf{r}) H_y = -\frac{1}{\varepsilon_r(\mathbf{r})} \frac{\partial \varepsilon_r(\mathbf{r})}{\partial x} \frac{\partial H_x}{\partial y}. \quad (2.72)$$

As there is only the transverse cross section considered, the first derivatives of the electric and magnetic fields with respect to z are constant

$$\frac{\partial}{\partial z} = -j\beta. \quad (2.73)$$

Substituting (2.73) in Equations (2.69) and (2.70), the transverse electric field components can be expressed as

$$\frac{\partial^2 E_x}{\partial x^2} + \frac{\partial}{\partial x} \left(\frac{\partial \varepsilon_r(\mathbf{r})}{\partial x} E_x \right) + \frac{\partial^2 E_x}{\partial y^2} + (k_0^2 \varepsilon_r(\mathbf{r}) - \beta^2) E_x = -\frac{\partial}{\partial x} \left(\frac{1}{\varepsilon_r(\mathbf{r})} \frac{\partial \varepsilon_r(\mathbf{r})}{\partial y} E_y \right) \quad (2.74)$$

and

$$\frac{\partial^2 E_y}{\partial x^2} + \frac{\partial^2 E_y}{\partial y^2} + \frac{\partial}{\partial y} \left(\frac{1}{\varepsilon_r(\mathbf{r})} \frac{\partial \varepsilon_r(\mathbf{r})}{\partial y} E_y \right) + (k_0^2 \varepsilon_r(\mathbf{r}) - \beta^2) E_y = -\frac{\partial}{\partial y} \left(\frac{1}{\varepsilon_r(\mathbf{r})} \frac{\partial \varepsilon_r(\mathbf{r})}{\partial x} E_x \right). \quad (2.75)$$

The magnetic field components can be obtained in an analogous way by substituting Equation (2.73) into Equations (2.71) and (2.72)

$$\frac{\partial^2 H_x}{\partial x^2} + \frac{\partial^2 H_x}{\partial y^2} - \frac{1}{\varepsilon_r(\mathbf{r})} \frac{\partial \varepsilon_r(\mathbf{r})}{\partial y} \frac{\partial H_x}{\partial y} + (k_0^2 \varepsilon_r(\mathbf{r}) - \beta^2) H_x = -\frac{1}{\varepsilon_r(\mathbf{r})} \frac{\partial \varepsilon_r(\mathbf{r})}{\partial y} \frac{\partial H_y}{\partial x} \quad (2.76)$$

$$\frac{\partial^2 H_y}{\partial x^2} - \frac{1}{\varepsilon_r(\mathbf{r})} \frac{\partial \varepsilon_r(\mathbf{r})}{\partial x} \frac{\partial H_y}{\partial x} + \frac{\partial^2 H_y}{\partial y^2} + (k_0^2 \varepsilon_r(\mathbf{r}) - \beta^2) H_y = -\frac{1}{\varepsilon_r(\mathbf{r})} \frac{\partial \varepsilon_r(\mathbf{r})}{\partial x} \frac{\partial H_x}{\partial y}. \quad (2.77)$$

Equations (2.69) to (2.72) and (2.74) to (2.77) represent *coupled partial differential equations* [15]. The solutions are subject to the appropriate boundary conditions given by the waveguide geometry. The right hand side expressions are referred to as *coupling terms* as they couple the x - and y -components of the associated field. The appearance of significant magnitudes of the coupling terms manifests itself in a way that *both* transverse components contribute to the composition of the overall \mathbf{E} (\mathbf{H}) field. The resulting modes are therefore not purely TE or TM polarised.

Although the formulations for both the \mathbf{E} and \mathbf{H} field are equivalent, the \mathbf{H} field formulation is the preferred one for numerical simulations. This is due to the continuity of the \mathbf{H} field components at dielectric interfaces (Equation (2.45)), which is in contrast to their \mathbf{E} field counterparts (Equation (2.44)).

As these coupled partial differential equations can not be solved analytically, numerical methods need to be applied.

2.7.2.1 Semi-vectorial approximation

In general weakly-guiding waveguide geometries (e.g. rib- or stripe waveguides) the magnitude of the coupling terms is small. These coupling terms are usually neglected, if the coupling between the x - and y -directed field components is not a factor to be considered in the design and functionality of the waveguide. The vectorial wave equations become decoupled and reduce to *semi-vectorial wave equations* [16, 17]. The polarisation dependent continuity relations for the transverse field components are maintained. The guided modes can be classified into two sets as in the case for planar waveguides, depending on whether the predominant electric field component lies in the x - or y -direction. The mode that has the predominant electric field component in the x -direction (E_x) resembles the TE mode in a slab waveguide configuration. This mode is called *quasi-TE* (or *TE-like*) mode. Similarly, the quasi-TM mode has its dominant electric field component in y -direction [18]. Although the eigenmodes of these optical dielectric waveguides are not purely TE or TM polarised, it is common practice to refer to them as TE or TM modes, as one (the predominant) of the transverse field components is orders of magnitude larger than the other one.

TE mode

The predominant electric (magnetic) field component of the TE mode in the waveguide structure given in Figure 2-4 is orientated in x - (y -) direction. The semi-vectorial wave equations for the TE mode are given by the E_x component

$$\frac{\partial^2 E_x}{\partial x^2} + \frac{\partial}{\partial x} \left(\frac{\partial \varepsilon_r(\mathbf{r})}{\partial x} E_x \right) + \frac{\partial^2 E_x}{\partial y^2} + (k_0^2 \varepsilon_r(\mathbf{r}) - \beta^2) E_x = 0 \quad (2.78)$$

and H_y component

$$\frac{\partial^2 H_y}{\partial x^2} - \frac{1}{\varepsilon_r(\mathbf{r})} \frac{\partial \varepsilon_r(\mathbf{r})}{\partial x} \frac{\partial H_y}{\partial x} + \frac{\partial^2 H_y}{\partial y^2} + (k_0^2 \varepsilon_r(\mathbf{r}) - \beta^2) H_y = 0. \quad (2.79)$$

An illustration of the predominant electric and magnetic field components of the fundamental TE mode (TE_0) in a stripe waveguide is given in Figure 2-11 and Figure 2-12, respectively. The considered operating wavelength was $\lambda = 1064$ nm. A $0.5 \mu\text{m}$ thick and $1 \mu\text{m}$ wide rectangular-shaped core ($n_2 = 3.476$, equivalent to n_{GaAs}) was positioned above a lower cladding layer ($n_3 = 3.306$, equivalent to n of $\text{Al}_{0.27}\text{Ga}_{0.73}\text{As}$) ($\rightarrow \Delta n = 0.17$) and topped by air. The resulting propagation constant β_{TE_0} is $19.841 \mu\text{m}^{-1}$ (equivalent to $n_{\text{eff,TE}_0} = 3.359$). It can be noted that the predominant transverse field components E_x and H_y are orders of magnitude larger than the non-dominant components E_y and H_x . The occurring longitudinal components E_z and H_z are negligible.

TM mode

The dominant electric (magnetic) field component of the TM mode in the waveguide structure given in Figure 2-4 is orientated in y - (x -) direction. The semi-vectorial wave equations for the TM mode are given by the E_y component

$$\frac{\partial^2 E_y}{\partial x^2} + \frac{\partial^2 E_y}{\partial y^2} + \frac{\partial}{\partial y} \left(\frac{1}{\varepsilon_r(\mathbf{r})} \frac{\partial \varepsilon_r(\mathbf{r})}{\partial y} E_y \right) + (k_0^2 \varepsilon_r(\mathbf{r}) - \beta^2) E_y = 0 \quad (2.80)$$

and H_x component

$$\frac{\partial^2 H_x}{\partial x^2} + \frac{\partial^2 H_x}{\partial y^2} - \frac{1}{\varepsilon_r(\mathbf{r})} \frac{\partial \varepsilon_r(\mathbf{r})}{\partial y} \frac{\partial H_x}{\partial y} + (k_0^2 \varepsilon_r(\mathbf{r}) - \beta^2) H_x = 0. \quad (2.81)$$

An illustration of the dominant electric and magnetic field components of the fundamental TM mode (TM_0) in a stripe waveguide is given in Figure 2-13 and Figure 2-14, respectively. The stripe waveguide layer composition is the same as for the TE_0 mode investigation. The resulting propagation constant β_{TM_0} is $19.799 \mu\text{m}^{-1}$ (equivalent to $n_{\text{eff,TM}_0} = 3.353$). It can be noted that the predominant transverse field components E_y and H_x are orders of magnitude larger than the non-dominant components E_x and H_y . The occurring longitudinal components E_z and H_z are negligible.

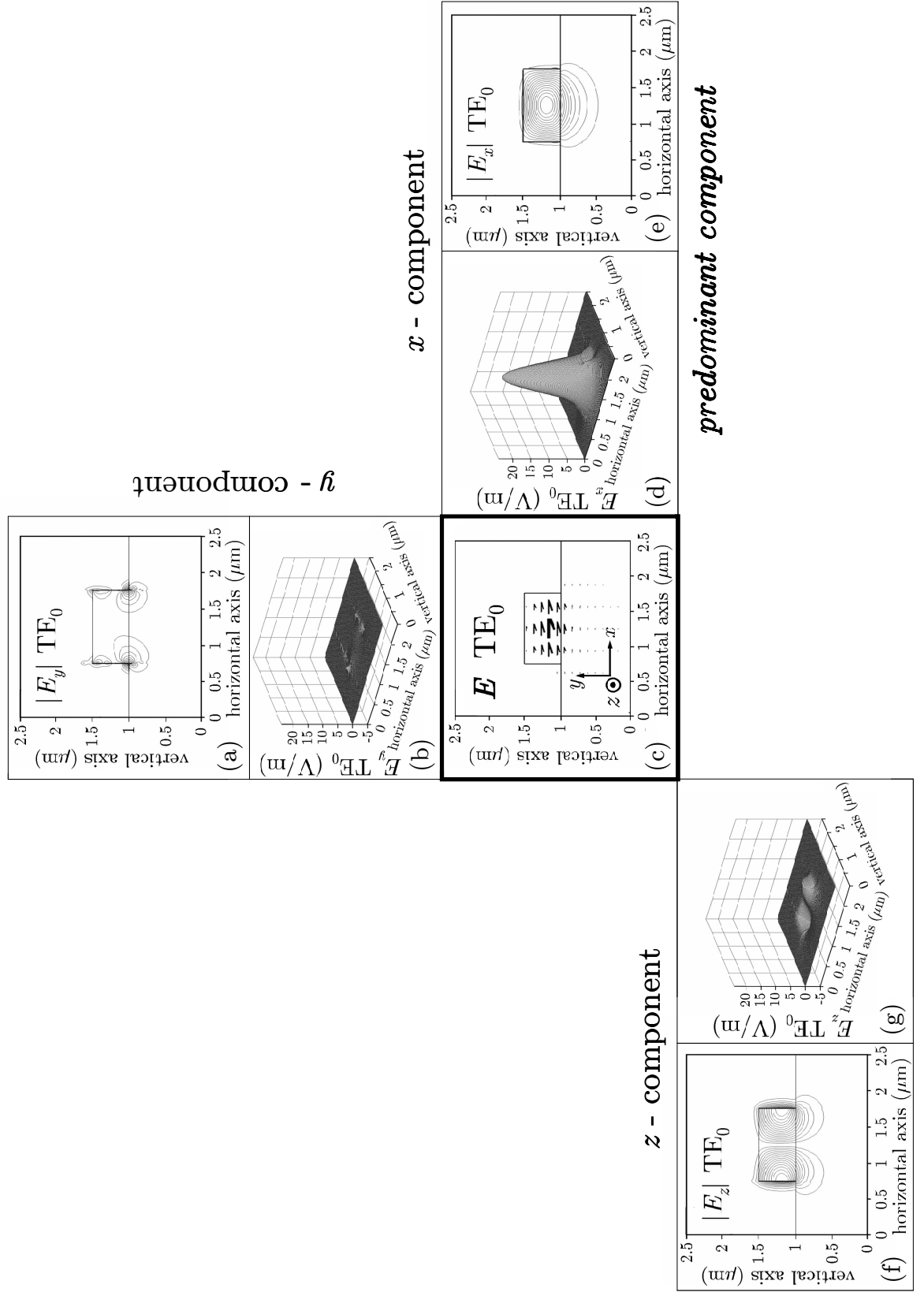


Figure 2-11: (a)-(g) Illustration of the electric vector field with corresponding profile plots of the fundamental TE mode (TE_0) components in a dielectric stripe waveguide. The predominant electric field component of the TE_0 mode is given by the E_x component.

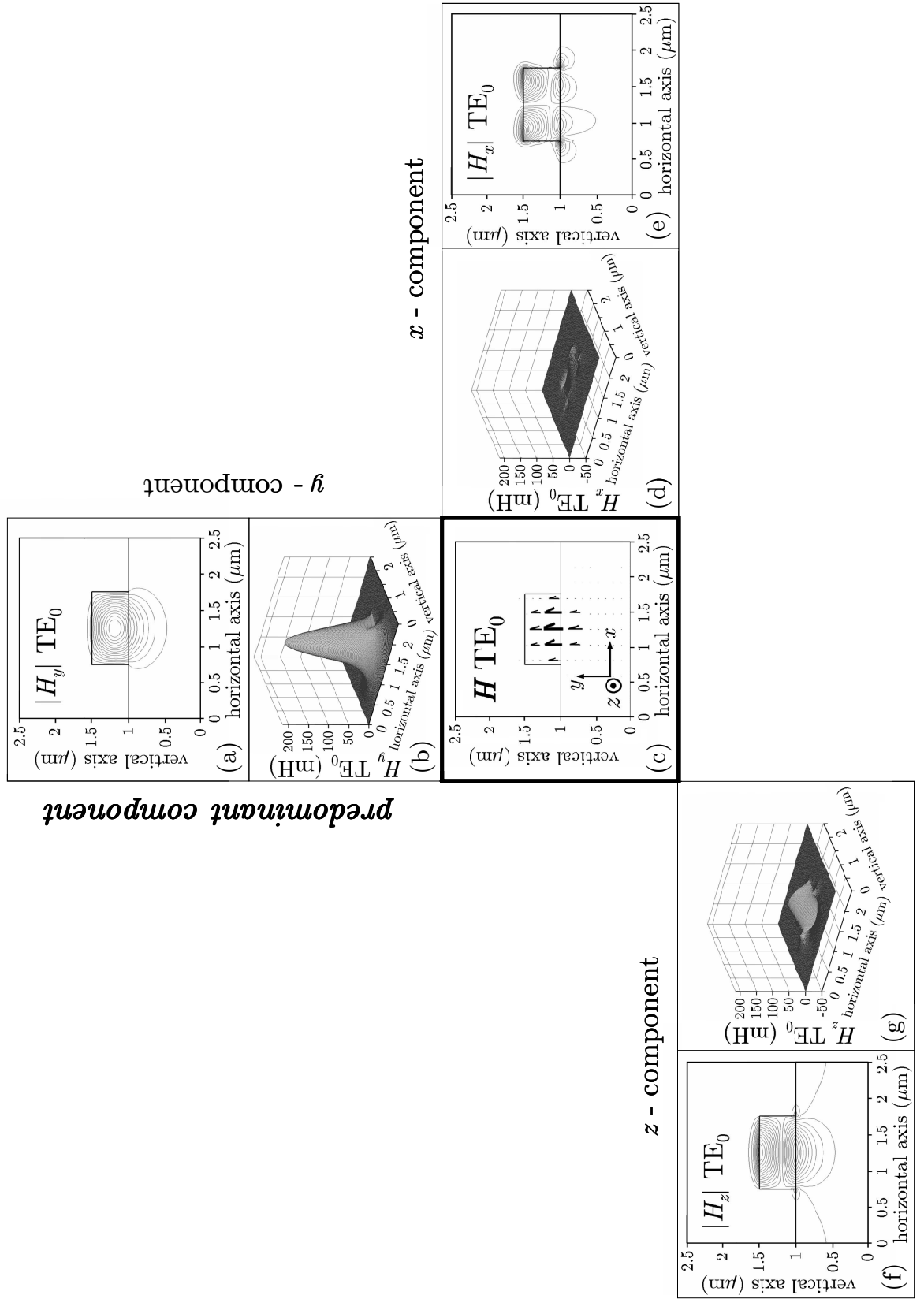


Figure 2-12: (a)-(g) Illustration of the magnetic vector field with corresponding profile plots of the fundamental TE mode (TE_0) components in a dielectric stripe waveguide. The predominant magnetic field component of the TE_0 mode is given by the H_y component.

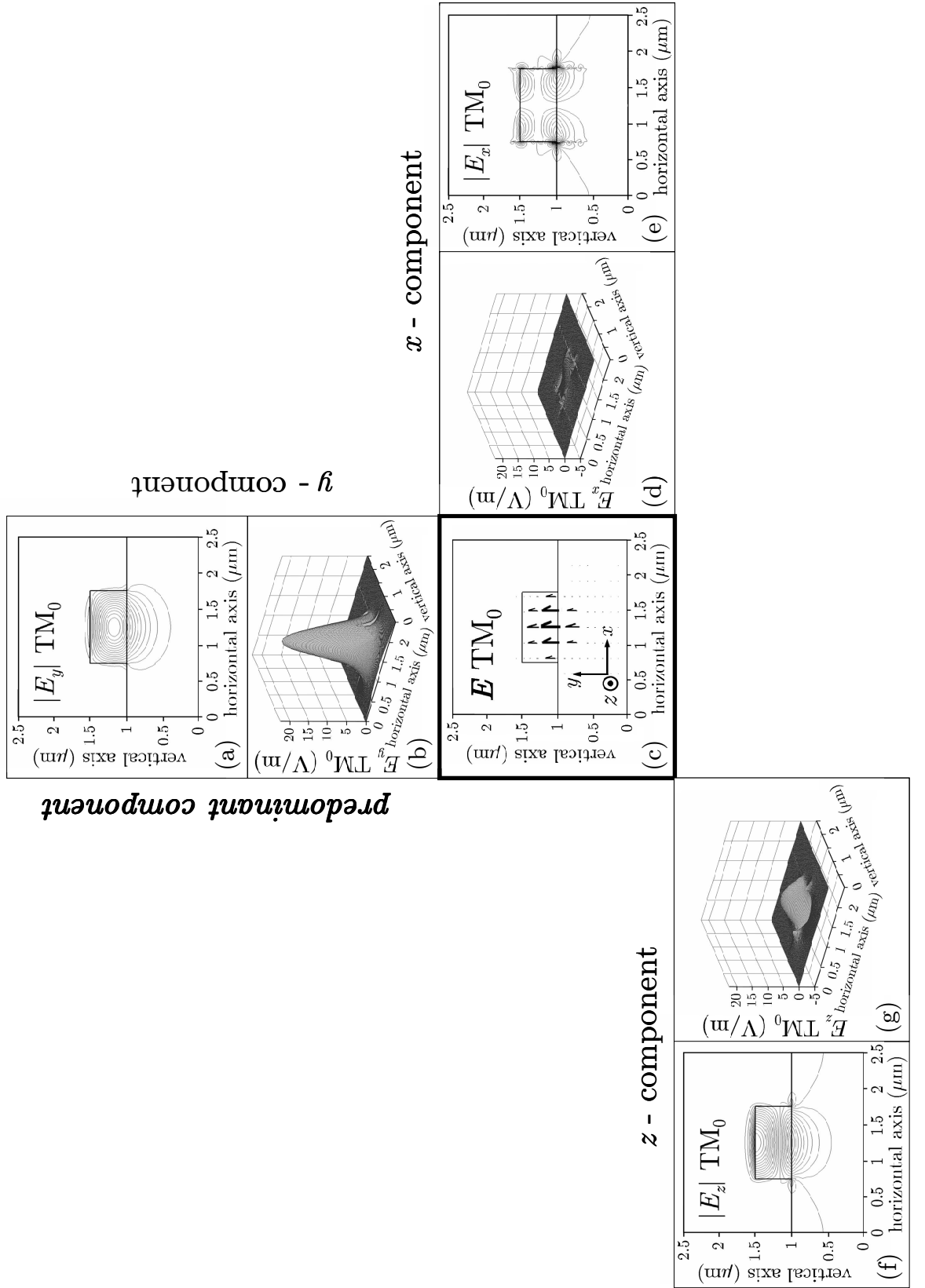


Figure 2-13: (a)-(g) Illustration of the electric vector field with corresponding profile plots of the fundamental TM mode (TM_0) components in a dielectric stripe waveguide. The predominant electric field component of the TM_0 mode is given by the E_y component.

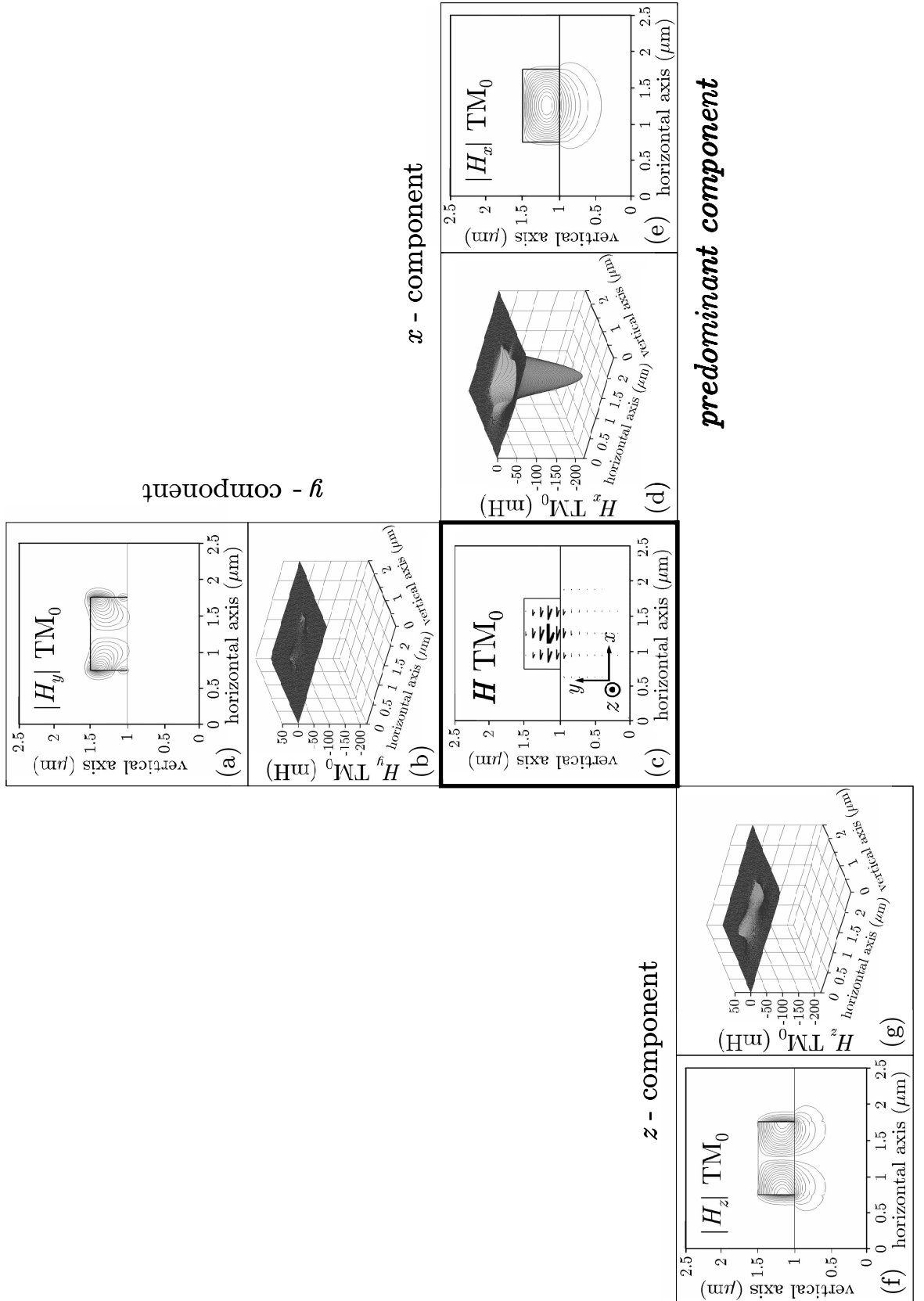


Figure 2-14: (a)-(g) Illustration of the magnetic vector field with corresponding profile plots of the fundamental TM mode (TM_0) components in a dielectric stripe waveguide. The predominant magnetic field component of the TM_0 mode is given by the H_x component.

2.7.2.2 Scalar approximation

If the weakly guiding waveguide medium consists of piecewise isotropic regions (e.g. bulk media), the first derivatives of the relative permittivity $\varepsilon_r(\mathbf{r})$ with respect to x and y (and already z) are zero

$$\frac{\partial \varepsilon_r(\mathbf{r})}{\partial x} = \frac{\partial \varepsilon_r(\mathbf{r})}{\partial y} = 0. \quad (2.82)$$

The wave equations can therefore be reduced to *scalar wave equations*. These are expressed for the electric field in the form

$$\frac{\partial^2 E_x}{\partial x^2} + \frac{\partial^2 E_x}{\partial y^2} + (k_0^2 \varepsilon_r - \beta^2) E_x = 0 \quad (2.83)$$

and

$$\frac{\partial^2 E_y}{\partial x^2} + \frac{\partial^2 E_y}{\partial y^2} + (k_0^2 \varepsilon_r - \beta^2) E_y = 0. \quad (2.84)$$

Similarly, the transversal magnetic field components are expressed as

$$\frac{\partial^2 H_x}{\partial x^2} + \frac{\partial^2 H_x}{\partial y^2} + (k_0^2 \varepsilon_r - \beta^2) H_x = 0 \quad (2.85)$$

and

$$\frac{\partial^2 H_y}{\partial x^2} + \frac{\partial^2 H_y}{\partial y^2} + (k_0^2 \varepsilon_r - \beta^2) H_y = 0. \quad (2.86)$$

The scalar wave equations do not distinguish between TE and TM polarised modes as the equations do not account for any polarisation dependence of the modes.

2.7.3 Beam propagation method

The *beam propagation method* (BPM) [19] is an effective method for the analysis of electromagnetic wave propagation in optical waveguides. BPM applies the *slowly varying envelope approximation* (SVEA) in order to approximate the light propagating in $+z$ -direction. It is also assumed that the light propagates paraxial (or at least approximately), so that the wavefronts of the propagating waves are approximately planar [20] (paraxial approximation). The SVEA involves the replacement of the wave functions (e.g. for the electric field) $E_x(x, y, z)$ and $E_y(x, y, z)$, which propagate in the z -direction, with the slowly varying envelope functions $\tilde{E}_x(x, y, z)$ and $\tilde{E}_y(x, y, z)$ and the rapidly oscillating phase term $e^{-j\beta z}$

$$E_x(x, y, z) = \tilde{E}_x(x, y, z) e^{-j\beta z} \quad (2.87)$$

$$E_y(x, y, z) = \tilde{E}_y(x, y, z) e^{-j\beta z}, \quad (2.88)$$

where $\beta = k_0 n_{REF}$. n_{REF} is referred to as *reference index*. Usually, the refractive index of the cladding- or substrate layer is used for n_{REF} . If $\tilde{\mathbf{E}}(x, y, z)$ varies slowly (especially in z -direction), then it is possible to choose fewer mesh points and therefore improve the calculation speed without compromising the accuracy too much. The paraxial approximation allows the second derivative of the wave function $\tilde{\mathbf{E}}(x, y, z)$ with respect to z to be neglected ($\partial^2 \tilde{\mathbf{E}}(x, y, z) / \partial z^2 \approx 0$). As the conventional BPM assumes only forward propagating waves, a *bidirectional* BPM [21] has to be applied in order to analyse backward propagating waves (which are not considered here).

After substituting the second derivatives of the SVEA approximated wave functions with respect to z into Equations (2.69) and (2.70), dividing the result by the phase term $e^{j\beta z}$ and applying the paraxial approximation, the paraxial wave equations for the electric field are then given by

$$2j\beta \frac{\partial \tilde{E}_x}{\partial z} = P_{xx} \tilde{E}_x + P_{xy} \tilde{E}_y \quad (2.89)$$

$$2j\beta \frac{\partial \tilde{E}_y}{\partial z} = P_{yy} \tilde{E}_y + P_{yx} \tilde{E}_x, \quad (2.90)$$

where the components involving the operator P are defined as [22]

$$P_{xx} \tilde{E}_x = \frac{\partial}{\partial x} \left(\frac{1}{\varepsilon_r(\mathbf{r})} \frac{\partial}{\partial x} (\varepsilon_r(\mathbf{r}) \tilde{E}_x) \right) + \frac{\partial^2 \tilde{E}_x}{\partial y^2} + (k_0^2 \varepsilon_r(\mathbf{r}) - \beta^2) \tilde{E}_x \quad (2.91)$$

$$P_{xy} \tilde{E}_y = \frac{\partial}{\partial x} \left(\frac{1}{\varepsilon_r(\mathbf{r})} \frac{\partial}{\partial y} (\varepsilon_r(\mathbf{r}) \tilde{E}_y) \right) - \frac{\partial^2 \tilde{E}_y}{\partial x \partial y} \quad (2.92)$$

$$P_{yy} \tilde{E}_y = \frac{\partial^2 \tilde{E}_y}{\partial x^2} + \frac{\partial}{\partial y} \left(\frac{1}{\varepsilon_r(\mathbf{r})} \frac{\partial}{\partial y} (\varepsilon_r(\mathbf{r}) \tilde{E}_y) \right) + (k_0^2 \varepsilon_r(\mathbf{r}) - \beta^2) \tilde{E}_y \quad (2.93)$$

$$P_{yx} \tilde{E}_x = \frac{\partial}{\partial y} \left(\frac{1}{\varepsilon_r(\mathbf{r})} \frac{\partial}{\partial x} (\varepsilon_r(\mathbf{r}) \tilde{E}_x) \right) - \frac{\partial^2 \tilde{E}_x}{\partial y \partial x}. \quad (2.94)$$

The paraxial wave equation is valid for wave propagation limited to small angles with respect to the z -axis [12]. The matrix expression of the paraxial wave equation for the electric field can be written as

$$2j\beta \frac{\partial}{\partial z} \begin{pmatrix} \tilde{E}_x \\ \tilde{E}_y \end{pmatrix} = \begin{bmatrix} P_{xx} & P_{xy} \\ P_{yx} & P_{yy} \end{bmatrix} \begin{pmatrix} \tilde{E}_x \\ \tilde{E}_y \end{pmatrix}. \quad (2.95)$$

In an analogous way, the SVEA can be applied to the magnetic field by setting

$$H_x(x, y, z) = \tilde{H}_x(x, y, z) e^{-j\beta z} \quad \text{and} \quad (2.96)$$

$$H_y(x, y, z) = \tilde{H}_y(x, y, z) e^{-j\beta z}. \quad (2.97)$$

The matrix expression of the paraxial wave equation for the magnetic field can be written in the form

$$2j\beta \frac{\partial}{\partial z} \begin{pmatrix} \tilde{H}_x \\ \tilde{H}_y \end{pmatrix} = \begin{bmatrix} Q_{xx} & Q_{xy} \\ Q_{yx} & Q_{yy} \end{bmatrix} \begin{pmatrix} \tilde{H}_x \\ \tilde{H}_y \end{pmatrix}, \quad (2.98)$$

where the components involving the operator Q are defined as [23]

$$Q_{xx}\tilde{H}_x = \frac{\partial^2 \tilde{H}_x}{\partial x^2} + \varepsilon_r(\mathbf{r}) \frac{\partial}{\partial y} \left(\frac{1}{\varepsilon_r(\mathbf{r})} \frac{\partial \tilde{H}_x}{\partial y} \right) + (k_0^2 \varepsilon_r(\mathbf{r}) - \beta^2) \tilde{H}_x \quad (2.99)$$

$$Q_{xy}\tilde{H}_y = \frac{\partial^2 \tilde{H}_y}{\partial y \partial x} - \varepsilon_r(\mathbf{r}) \frac{\partial}{\partial y} \left(\frac{1}{\varepsilon_r(\mathbf{r})} \frac{\partial \tilde{H}_y}{\partial x} \right) \quad (2.100)$$

$$Q_{yy}\tilde{H}_y = \varepsilon_r(\mathbf{r}) + \frac{\partial}{\partial x} \left(\frac{1}{\varepsilon_r(\mathbf{r})} \frac{\partial \tilde{H}_y}{\partial x} \right) + \frac{\partial^2 \tilde{H}_y}{\partial y^2} + (k_0^2 \varepsilon_r(\mathbf{r}) - \beta^2) \tilde{H}_y \quad (2.101)$$

$$Q_{yx}\tilde{H}_x = \frac{\partial^2 \tilde{H}_x}{\partial x \partial y} - \varepsilon_r(\mathbf{r}) \frac{\partial}{\partial x} \left(\frac{1}{\varepsilon_r(\mathbf{r})} \frac{\partial \tilde{H}_x}{\partial y} \right). \quad (2.102)$$

The parabolic partial differential equations in the matrix expressions (2.95) and (2.98) represent the basic BPM equations for two dimensions (x, y). Given an (e.g. electric) input field, $\tilde{\mathbf{E}}(x, y, z=0)$, Equation (2.95) determines the field evolution in direction of propagation (here: z -direction). Various kinds of BPM implementations based on for instance the *fast Fourier transform* (FFT-BPM) [19], *finite differences* (FD-BPM) [24] or *finite elements* (FEM-BPM) [25, 26] have been developed, which are also used in commercially available photonics simulation software packages.

2.7.4 Mode solver

Mode solvers provide the solutions for (e.g. the electrical field) $\tilde{\mathbf{E}}(x, y)$ in (2.95) by setting $\partial \tilde{\mathbf{E}}(x, y) / \partial z = 0$, which leads to Equations (2.74) to (2.77). This results in the determination of the values of β and the corresponding modal pattern for each desired mode in a given waveguide cross section geometry at a specified operating wavelength λ . Mode solvers can be categorised in scalar wave equation solvers, semi-vectorial wave equation solvers and full-vectorial wave equation solvers [27]. Similar to BPM, a number of numerical implementations based on either finite elements [28], finite differences [16, 17] and other methods, which are introduced in review papers such as [29] and [30], have been developed.

The device functionalities of the developed optical devices in this thesis are based on structural birefringence, which manifests itself as intentionally introduced waveguide cross section profile asymmetries. The electric and magnetic field components of the guiding waveguide modes will therefore have components of significant magnitude in both horizontal and vertical direction. As will be seen later in this chapter, it is even desired that the field components are equally distributed over both the horizontal and vertical direction. The waveguide cross sectional profiles will consist of slanted sidewalls. As the FEM discretises the waveguide cross section into a number of rectangular or triangular shaped elements, it allows the analysis of arbitrary cross section geometries. A FEM based full vectorial mode solver [14] together with a full-vectorial BPM solver were therefore required for the theoretical optimisations of the waveguide geometry dimensions of the proposed devices in this thesis. The wave propagation module integrated with [14] uses an *eigenmode expansion* (EME) algorithm [31], which characterises the optical properties of a

longitudinal structure by local modes. The different local modes are coupled with each other via matrices, which results in short calculation times.

2.7.5 Optimisation of a passive optical stripe waveguide

The waveguide structure was based on the GaAs/AlGaAs material system. As a rule of thumb, the refractive index difference between the core and cladding layers in a weakly guiding dielectric waveguide is about $\Delta n < 0.2$. Figure 2-15 illustrates the wavelength dependence of the refractive index for GaAs and different ternary $\text{Al}_x\text{Ga}_{1-x}\text{As}$ compositions [32]. The considered operating wavelength is $\lambda = 1064$ nm (indicated by a vertical line in Figure 2-15). This corresponds to the emitting wavelength of a *diode pumped solid state* (DPSS) Nd:YAG laser, which was used as a signal source. GaAs was the chosen material for the waveguide core. For fabrication simplification purposes, *no* upper cladding semiconductor layer was introduced. The refractive index of GaAs at $\lambda = 1064$ nm is $n_{\text{GaAs}} = 3.476$. In order to fulfil the requirement of $\Delta n < 0.2$, an $\text{Al}_x\text{Ga}_{1-x}\text{As}$ material composition of $x = 0.27$ was chosen for the lower cladding ($n_{\text{LOWER CLADDING}} = 3.306$), which corresponds to a Δn of 0.17.

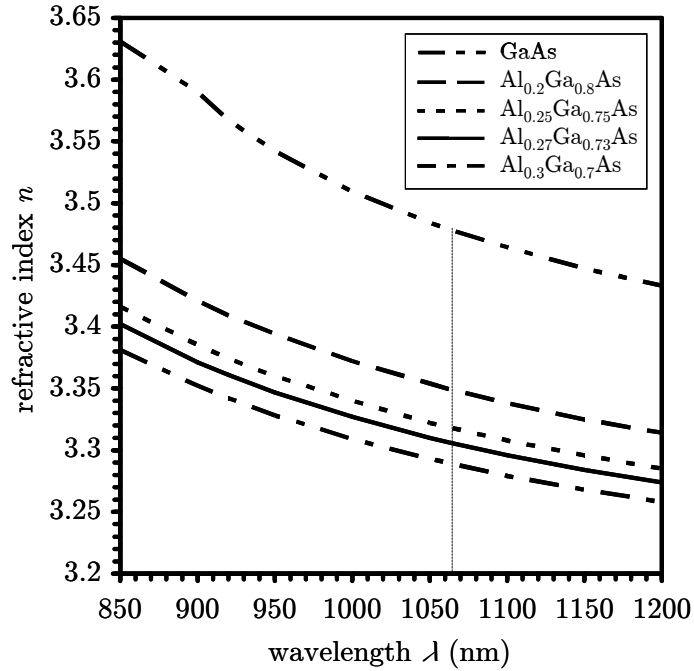


Figure 2-15: Wavelength dependence of the refractive index of GaAs and different AlGaAs compositions.

Single mode operation of dielectric optical waveguides is typically needed in PICs, although in many cases the functionality requires multimode operation (e.g. *multi mode interference* (MMI) coupler). Here, the emphasis is given on single mode operation. Single mode operation involves the excitation of only the two fundamental modes (TE_0 and TM_0) in the given waveguide. The single mode regime for a certain stripe waveguide height h_{stripe} ($0.3 \mu\text{m} < h_{\text{stripe}} < 1 \mu\text{m}$) and stripe waveguide width w_{stripe} ($w_{\text{stripe}} < 1 \mu\text{m}$) can be depicted in Figure 2-16. The boundaries for single mode operation are given by the cut off conditions for the highest fundamental (dashed line) and lowest first order (chain-dotted

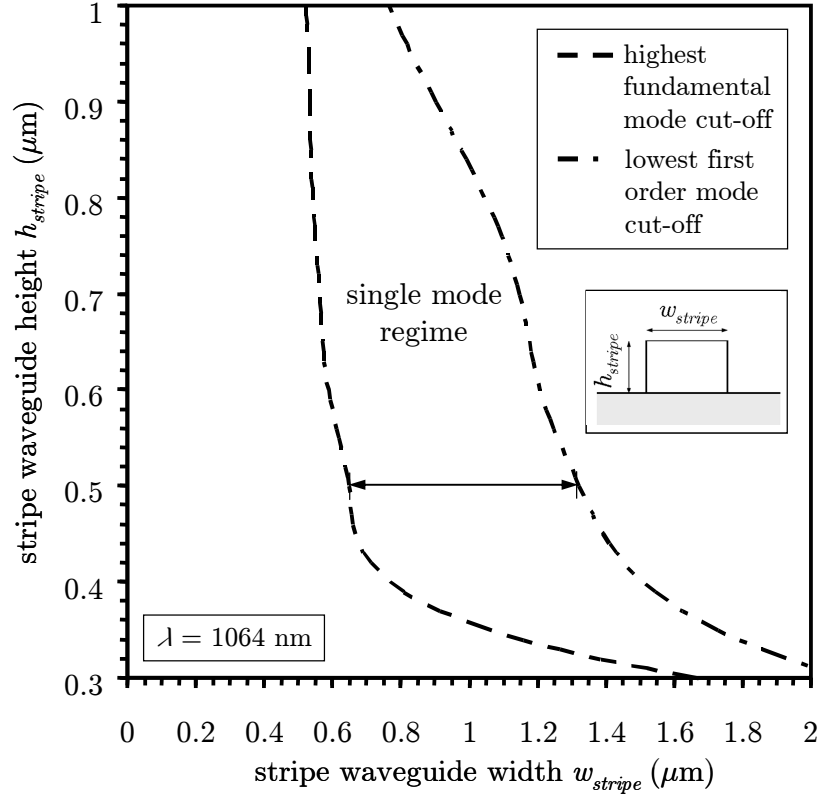


Figure 2-16: Single mode regime for different stripe waveguide geometries.

line) mode in the waveguide. The largest w_{stripe} interval for single mode operation is given for $h_{\text{stripe}} = 0.5 \mu\text{m}$, which is indicated by the horizontal arrow in Figure 2-16. The chosen wafer layer structure was that of an already available wafer, which was initially designed for another application. The structure consists of a GaAs core layer thickness of $0.5 \mu\text{m}$ and a $4.7 \mu\text{m}$ $\text{Al}_{0.27}\text{Ga}_{0.73}\text{As}$ lower cladding, grown using *metal-organic chemical-vapour deposition* (MOCVD) upon a n-doped GaAs substrate.

2.8 Waveplates

Waveplates, also referred to as *retardation plates*, convert the SOP of an incident light beam. A waveplate is made of birefringent material, which is typically a uniaxial crystal. The crystal is cut in a way that its extraordinary axis lies in the plane of the input crystal face, and the input and output crystal faces are parallel to each other. A light beam normally incident on the input crystal plane is decomposed into an ordinary and extraordinary ray according to the relative orientation of the extraordinary axis and the plane of polarisation of the input beam (Figure 2-18(a)). The axis that has the lower refractive index is also referred to as the *fast* (f) axis, whereas the other one is referred to as the *slow* (s) axis. The electric field vector of the decomposed linearly polarised input beam has the form (omitting the time dependence)

$$\mathbf{E}(x, y, z) = \begin{pmatrix} E_s e^{-j\beta_s z} \\ E_f e^{-j\beta_f z} \end{pmatrix}, \quad (2.103)$$

which is illustrated in Figure 2-17.

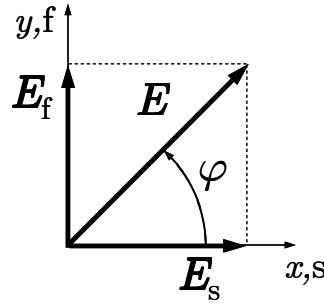


Figure 2-17: Decomposition of the incident \mathbf{E} field vector.

The different phase velocities of the two linearly polarised independently propagating components (v_s , v_f) result in a phase difference Ψ (Figure 2-18(b)). The phase difference Ψ between the two orthogonally polarised rays is defined as

$$\Psi = (-\beta_s z) - (-\beta_f z). \quad (2.104)$$

The phase difference varies as the two rays propagate along the waveguide. The *relative* phase difference Ψ_{REL} within the waveplate causes the resulting SOP to evolve periodically from an initially linear SOP through various elliptical SOP as the two components propagate in the longitudinal (z -) direction. The interference pattern between the two orthogonally polarised rays projected onto the plane of the input SOP results in a beating pattern between these two rays.

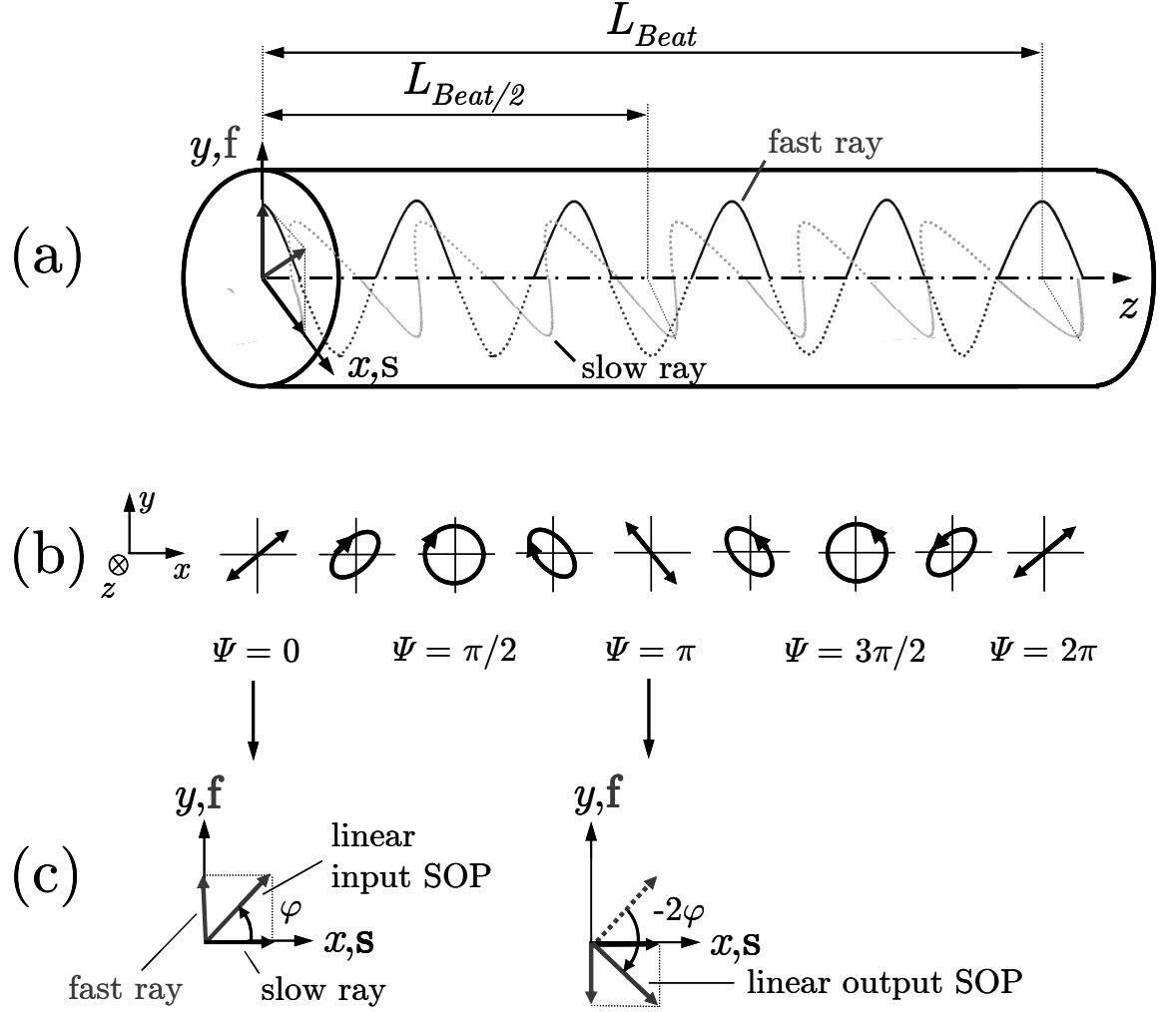


Figure 2-18: Illustration of the functionality of a waveplate consisting of a uniaxial crystal. (a) Independent propagation of fast and slow ray within the waveplate. (b) Evolution of the SOP of a linearly polarised input beam through various elliptical SOP over one beat length L_{Beat} . (c) Comparison between input- and output SOP of a half-wave plate.

For $z = L_{Beat}$, the phase difference Ψ equals 2π

$$\Psi = 2\pi = (-\beta_s \cdot L_{Beat}) - (-\beta_f \cdot L_{Beat}), \quad (2.105)$$

hence

$$L_{Beat} = \frac{2\pi}{(\beta_f - \beta_s)} = \frac{\lambda}{(n_{eff,f} - n_{eff,s})}. \quad (2.106)$$

It can be noted that after a propagation distance of the *half beat length* $L_{Beat}/2$, which equals to a phase difference of $\Psi = \pi$, the input SOP imparts a rotation of 90° . $L_{Beat}/2$ is defined as

$$L_{Beat}/2 = \frac{\pi}{(\beta_f - \beta_s)} = \frac{\lambda}{2(n_{eff,f} - n_{eff,s})}. \quad (2.107)$$

By rewriting Equation (2.107) it can be noted that at a crystal thickness equal to $L_{Beat/2}$, the difference in optical path length between the fast and slow ray is half the wavelength

$$(n_{eff,s} - n_{eff,f})L_{Beat/2} = \frac{\lambda}{2}. \quad (2.108)$$

A crystal of this thickness is also referred to as *half-wave plate*. An input wave, which is linearly polarised at an angle φ to the optical axis still emerges linearly polarised. Its plane of polarisation, however, is flipped (or mirror imaged) about the optical axis with its direction now $-\varphi$ to the optical axis. This corresponds to an effective rotation of 2φ (Figure 2-18(c)). In particular for $\varphi = 45^\circ$, the linear output polarisation is perpendicular to the linear input polarisation. *This is the main principle on which the proposed devices in this thesis are based on.* In the case of incident circularly polarised light, a half-wave plate converts a right-hand circularly polarised light (regardless of φ) into a left-hand circularly polarised light and vice versa [33].

A crystal thickness equal to a *quarter beat length* $L_{Beat/4}$ imposes an optical path length difference between the fast and slow ray of a quarter wavelength. A crystal of this thickness is also referred to as *quarter-wave plate*. At the output of the crystal, the fast and slow rays will be $\pi/2$ out of phase with each other. This manifests itself in a conversion of a linearly polarised input signal into a circularly polarised signal or vice versa.

The half-wave plate functionality is of particular interest in both discrete and integrated optics. The perpendicularity between the linearly polarised input- and output beam in the bulk half-wave plate is equivalent to the characteristic of an integrated TE \leftrightarrow TM polarisation converter. As the \mathbf{E} field of an incident TE (TM) polarised mode in integrated optics lies in the horizontal (vertical) direction (x - (y -) direction), the optical axis of a TE \leftrightarrow TM polarisation converter is desired to be at an angle of $\varphi = 45^\circ$ with respect to the coordinate axis (here: e.g. horizontal axis). In contrast to the bulk half-wave plate example given in Figure 2-18, the optical axis in integrated TE \leftrightarrow TM converters is not oriented parallel to the Cartesian coordinate system (Figure 2-19).

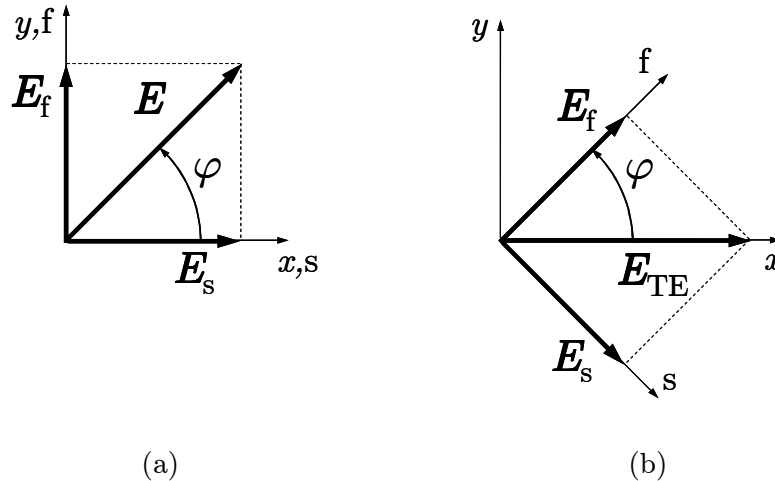


Figure 2-19: Illustration of equivalent optical axes orientation in both (a) general bulk half-wave plate and (b) integrated TE \rightarrow TM polarisation converter. The SOP of the electric fields corresponds to linearly polarised input signals.

Assuming a TE polarised input signal, for $\varphi = 45^\circ$ a complete TE \rightarrow TM polarisation conversion takes place after a converter length of $L_{Beat}/2$. The desired *TM polarisation purity* P_C equals 100%. P_C is defined at the output of the device for a TE polarised input signal

$$P_C = \frac{P_{TM}}{P_{TE} + P_{TM}} \Big|_{\text{@ output}}^{\text{for TE input}} \cdot 100 \quad (\text{in } \%), \quad (2.109)$$

where P_{TE} and P_{TM} are the TE and TM polarised output powers, respectively. In this case, the accumulated relative phase difference Ψ_{REL} is π (Figure 2-20(a)).

In order to achieve a P_C of 100% at the output for $\varphi \neq 45^\circ$, half-wave plates of alternating equal tilts of the optical axis have to be cascaded. The related tilt angles of the optical axis with respect to the horizontal x -axis are

$$\varphi_m = (-1)^m \varphi \quad \text{for } m = 0 \dots (N-1), \quad (2.110)$$

with N representing the number of half-wave plates and φ is typically chosen as

$$\varphi = \frac{\pi}{4N} \quad (2.111)$$

in order to achieve a P_C value of 100%. The scenarios for $N = 1$ to 4 are illustrated in Figure 2-20. This technique, similar to the quasi phase matching technique [4], was already implemented in bulk form as a folded Solc-filter [3, 34] and in integrated form. Integrated implementations can be depicted in the next chapter.

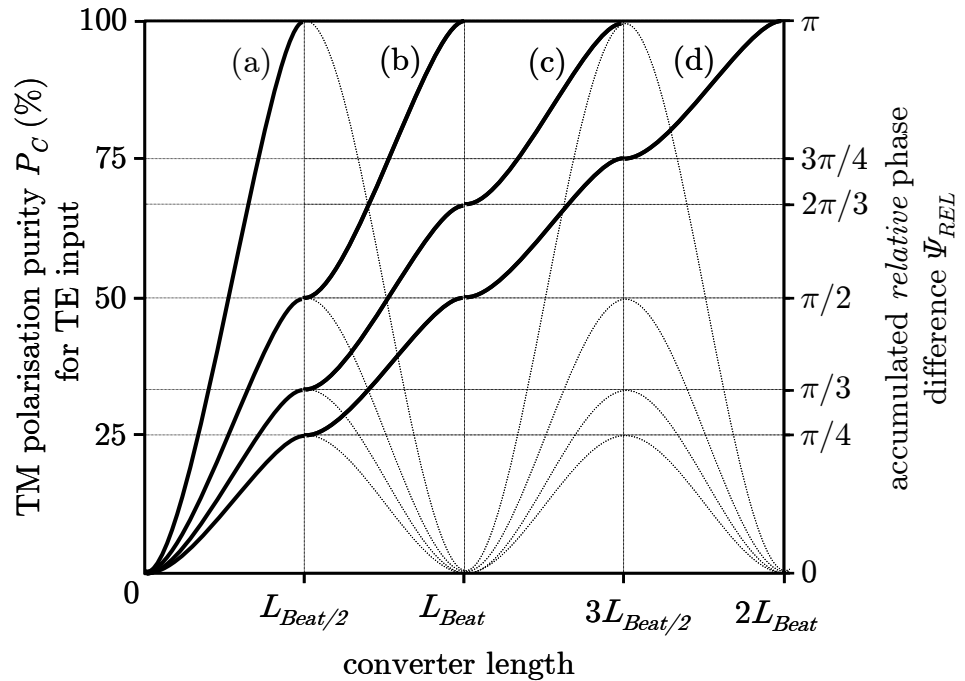


Figure 2-20: Principle of cascading half-wave plates of alternating equal tilts of the optical axis in order to achieve an accumulated relative phase difference Ψ_{REL} of π between the two propagating rays. (a) $N = 1$ ($\varphi = 45^\circ$), (b) $N = 2$ ($\varphi = 22.5^\circ$), (c) $N = 3$, ($\varphi = 15^\circ$) and (d) $N = 4$ ($\varphi = 11.25^\circ$)

The material structures in integrated optics are based on isotropic materials such as GaAs, InP or Si. In general, an isotropic material becomes anisotropic by applying an electric- or magnetic field, mechanical stress or change of the waveguide cross section geometry, which results in a change in the permittivity [3, 35]. Therefore, in order to realise a *passive* polarisation converter in integrated form, *form* birefringence [36], which is also referred to as *geometrical*- or *shape*-birefringence, has to be introduced. This is achieved by an asymmetry in the waveguide cross section profile in terms of slanted- or stepped sidewalls or sub-wavelength air trench gratings. An overview on several asymmetric waveguide cross section designs is given in the next chapter.

Two criteria for the evaluation of the intentionally introduced asymmetry of the waveguide cross section profile in the polarisation converter designs proposed in this thesis were used:

The *angle of rotation of the optical axis* δ was defined with respect to the vertical axis and equals to

$$\delta = \tan^{-1} \left(\frac{\iint_{\Omega_W} n^2(x, y) \cdot E_x^2(x, y) dx dy}{\iint_{\Omega_W} n^2(x, y) \cdot E_y^2(x, y) dx dy} \right) \quad (\text{in } ^\circ). \quad (2.112)$$

$E_x(x, y)$, $E_y(x, y)$ and $n(x, y)$ represent the distribution of the electric field components of the specified excited mode in the waveguide and the refractive index distribution in lateral and transverse direction, respectively, within the computational window Ω_W . An equal power distribution between both components in an excited mode results in a value of $\delta = 45^\circ$, which represents the optimum. Both δ and φ are complementary angles ($\delta + \varphi = 90^\circ$).

A criterion of the distribution of the launched power in an excited waveguide mode was defined as the *power overlap* κ

$$\kappa = \frac{\iint_{\Omega_W} n^2(x, y) \cdot E_y^2(x, y) dx dy}{\iint_{\Omega_W} n^2(x, y) \cdot E_x^2(x, y) dx dy + \iint_{\Omega_W} n^2(x, y) \cdot E_y^2(x, y) dx dy}. \quad (2.113)$$

$E_x(x, y)$, $E_y(x, y)$ and $n(x, y)$ represent the distribution of the electric field components of the specified excited mode and the refractive index distribution in lateral and transverse direction, respectively, within the computational window Ω_W . An equal power distribution between both components in an excited mode results in a value of $\kappa = 0.5$, which represents the optimum.

2.9 References

- [1] Landau L. D. and Lifshitz E. M., "*Electrodynamics of continuous media*", 2nd ed., Pergamon Press, Oxford, United Kingdom, ISBN 0-08030276-9, (1964).
- [2] Born M. and Wolf E., "*Principles of Optics*", 6th ed., Pergamon Press, Oxford, United Kingdom, ISBN 0-08-026482-4, (1986).
- [3] Yariv A. and Yeh P., "*Optical Waves in Crystals*", 1st ed., John Wiley & Sons, New York, USA, ISBN 0-471-09142-1, (1984).
- [4] Yariv A., "*Optical Electronics in Modern Communications*", 1st ed., Oxford University Press, New York, USA, ISBN 0-19-510626-1, (1997).
- [5] Yariv A., "*Introduction to Optical Electronics*", 2nd ed., Holt, Rinehart and Winston, New York, USA, ISBN 0-03-089892-7, (1976).
- [6] Syms R. R. A. and Cozens J. R., "*Optical Guided Waves and Devices*", 1st ed., McGraw-Hill, London, United Kingdom, ISBN 0-07-707425-4, (1992).
- [7] Reider A. D., "*Photonik*", 1st ed., Springer, Vienna, Austria, ISBN 3-211-21901-3, (2004).
- [8] Damask J. N., "*Polarization optics in telecommunications*", 1st ed., Springer, New York, USA, ISBN 0-387-22493-9, (2005).
- [9] Jenkins F. A. and White H. E., "*Fundamentals of Optics*", 4th ed., McGraw-Hill, New York, USA, ISBN 0-07-032330-5, (1976).
- [10] Kogelnik H., "Theory of Optical Waveguides", in Tamir T. (Ed.), "*Guided-Wave Optoelectronics*", 2nd ed., Springer, New York, USA, ch. 2, pp. 7 - 88, ISBN 0-387-52780-X, (1990).
- [11] Brinkmeyer E., "Optische Fasern: Grundlagen", in Voges E., Petermann K. (Eds.), "*Optische Kommunikationstechnik*", 1st ed., Springer, Berlin, Germany, ch. 3, pp. 56 - 79, ISBN 3-540-67213-3, (2002).
- [12] Hutchings D. C. and Arnold J. M., "Overview of Electromagnetic Solvers for Photonics", in *Newsletter Fall 2004 of the Institute of Physics (IoP) Computational Physics Group*, (<http://groups.iop.org/CP/Newsletter/2004-fall.pdf>), pp. 1 - 9.
- [13] Adams M. J., "*An Introduction to Optical Waveguides*", John Wiley & Sons Ltd., New York, USA, ISBN 0-471-27969-2, (1981).
- [14] *FIMMWAVETM*, Photon Design Ltd., <http://www.photond.com>
- [15] Kawano K. and Kitoh T., "*Introduction to Optical Waveguide Analysis: Solving Maxwell's Equations and the Schroedinger Equation*", John Wiley & Sons Inc., New York, USA, ISBN 0-471-22160-0, (2001).

- [16] Stern M. S., "Semivectorial polarised finite difference method for optical waveguides with arbitrary index profiles", *IEEE Proceedings-Optoelectronics*, vol. **135**, no. 1, pp. 56-63, (1988).
- [17] Stern M. S., "Semivectorial polarised H field solutions for dielectric waveguides with arbitrary index profiles", *IEEE Proceedings-Optoelectronics*, vol. **135**, no. 5, pp. 333-338, (1988).
- [18] Nishihara H., Haruna M. and Suhara T., "Optical Integrated Circuits", in Waynant R. W., Ediger M. N. (Eds.), *"Electro-optics Handbook"*, 2nd ed., McGraw-Hill, Inc., New York, USA, ch. 26, pp. 26.01 - 26.37, ISBN 0-07-068716-1 (2000).
- [19] Feit M. D. and Fleck J. A. J., "Light propagation in graded-index optical fibers", *Applied Optics*, vol. **17**, no. 24, pp. 3990 - 3998, (1978).
- [20] Lee D. L., *"Electromagnetic principles of integrated optics"*, 1st ed., John Wiley & Sons, Inc., New York, USA, ISBN 0-471-85937-0, (1986).
- [21] Kaczmarek P. and Lagasse P. E., "Bidirectional beam propagation method", *Electronics Letters*, vol. **42**, no. 11, pp. 675 - 676, (1988).
- [22] Huang W. P. and Xu C. L., "Simulation of three-dimensional optical waveguides by a full-vector beam propagation method", *IEEE Journal of Quantum Electronics*, vol. **29**, no. 10, pp. 2639-2649, (1993).
- [23] Huang W. P., Xu C. L. and Chaudhuri S. K., "A vector beam propagation method based on H fields", *IEEE Photonics Technology Letters*, vol. **3**, no. 12, pp. 1117-1120, (1991).
- [24] Yamauchi J., Mugita T. and Nakano H., "Implicit Yee-mesh-based finite-difference full-vectorial beam-propagation method", *IEEE Journal of Lightwave Technology*, vol. **23**, no. 5, pp. 1947-1955, (2005).
- [25] Patrocínio da Silva J., Hernandez-Figueroa H. E. and Ferreira Frasson A. M., "Improved Vectorial Finite-Element BPM Analysis for Transverse Anisotropic Media", *IEEE Journal of Lightwave Technology*, vol. **21**, no. 2, pp. 567 - 576, (2003).
- [26] Tsuji Y. and Koshiya M., "Finite element beam propagation method with perfectly matched layer boundary conditions for three-dimensional optical waveguides", *International Journal of Numerical Modelling: electronic Networks, Devices, and Fields*, vol. **13**, pp. 115 - 126, (2000).
- [27] Scarmozzino R., Gopinath A., Pregla R. and Helfert S., "Numerical techniques for modeling guided-wave photonic devices", *IEEE Selected Topics in Quantum Electronics*, vol. **6**, no. 1, pp. 150 - 162, (2000).
- [28] Rahman B. M. A. and Davies J. B., "Finite-Element Analysis of Optical and Microwave Waveguide Problems ", *IEEE Transactions on Microwave Theory and Techniques*, vol. **MTT-32**, no. 1, pp. 20 - 28, (1984).
- [29] Chiang K. S., "Review of numerical and approximate methods for the modal analysis of general optical dielectric waveguides", *Optical and Quantum Electronics*, vol. **26**, pp. 113 - 134, (1994).

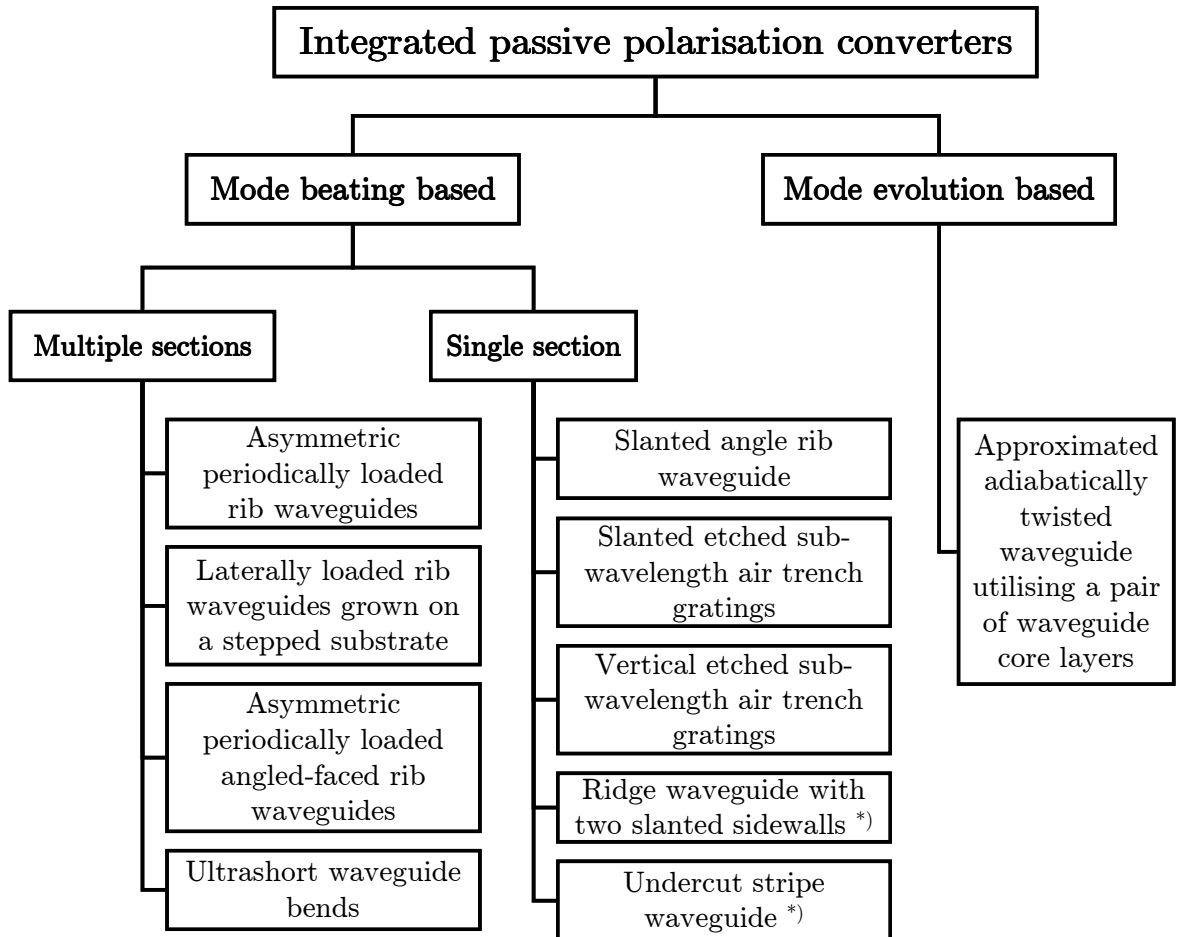
-
- [30] Vassallo C., "1993-1995 Optical mode solvers", *Optical and Quantum Electronics*, vol. **29**, no. 2, pp. 95 - 114, (1997).
 - [31] Gallagher D. F. G. and Felici T., "Eigenmode Expansion Methods for Simulation of Optical Propagation in Photonics - Pros and Cons", in *Proceedings of the SPIE Photonics West Conference 2003*, San Jose, USA, 25 - 31 January 2003, paper 4987-10.
 - [32] Luxpop Inc., <http://www.luxpop.com>
 - [33] Huard S., "*Polarization of Light*", John Wiley & Sons, New York, USA, ISBN 0-471-96536-7, (1997).
 - [34] Solc I., "Birefringent Chain Filters", *Journal of the Optical Society of America*, vol. **55**, no. 6, pp. 621 - 625, (1965).
 - [35] Liu J.-M., "*Photonic Devices*", 1st ed., Cambridge University Press, New York, USA, ISBN 978-0-521-55195-3, (2005).
 - [36] Chen C.-C., "*Foundations for guided-wave optics*", 1st ed., John Wiley & Sons, Hoboken, New Jersey, USA, ISBN 0-471-75687-3, (2006).

Chapter 3

Integrated passive polarisation rotators: State of the art

The following chapter gives an overview of different designs of already realised passive polarisation converters on GaAs/AlGaAs, InP/InGaAsP, SOI (silicon on insulator) and InGaAsP based QW material structures.

Figure 3-1 illustrates technologies of realised passive polarisation converters categorised according to their functionality.



*) proposed in this thesis

Figure 3-1: Overview of realised integrated passive polarisation converter technologies.

Integrated passive polarisation converter functionalities are based on the principle of mode beating or mode evolution. Converters based on mode evolution can be considered as the integrated counterparts to twists that are used in microwave applications. Converters based on mode beating that utilise form birefringence by introducing an asymmetry in the waveguide cross section, can be categorised in single section and multiple section devices.

3.1 Mode beating based device designs

3.1.1 Multiple section beating

- ***Asymmetric periodically loaded rib waveguides***

One of the first passive polarisation converter designs to be introduced was based on a rotation of the optical axis of a rib waveguide due to asymmetric transverse cross sections. The device consists of periodically butt-coupled and asymmetrically-loaded rib waveguide sections as illustrated in Figure 3-2.

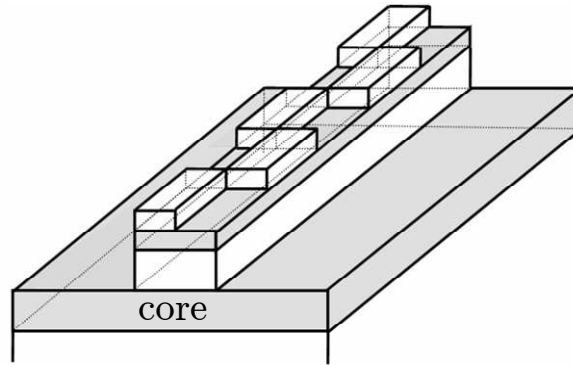


Figure 3-2: Schematic of the device configuration of an asymmetrically-loaded rib waveguide polarisation converter (after [1]).

A publication overview of proposed and realised integrated passive polarisation converters based on this design is given in Table 3-1.

author	art of proposal	year	material	λ	P_C	device length	losses
Shani <i>et al.</i> [1]	experiment	1991	InP	$1.5 \mu\text{m}$	90-100 %	$3700 \mu\text{m}$	insertion loss = 13 dB* excess loss = 2 dB (for TE input) excess loss = 3 dB (for TM input)
Huang <i>et al.</i> [2]	theory	1992	n/a	n/a	n/a	n/a	n/a
Alferness [3]	experiment	1993	n/a	n/a	n/a	n/a	n/a
Mustieles <i>et al.</i> [4]	theory	1993	InP/ InGaAsP	n/a	n/a	$824 \mu\text{m}$	7.6 dB
Gustavsson [5]	theory	n/a	n/a	n/a	n/a	n/a	n/a
Obayya <i>et al.</i> [6]	theory	2000	n/a	$1.55 \mu\text{m}$	98%	$740 \mu\text{m}$	insertion loss = 0.13dB

*including input and output waveguide coupling losses

Table 3-1: Overview of proposed and realised passive polarisation rotators based on asymmetric periodically loaded rib waveguides (λ ...operating wavelength, P_C ...Polarisation conversion).

• **Passive polarisation converters based on laterally tilted rib waveguides grown on a stepped substrate**

In order to achieve a rotation of the optical waveguide axis relative to the surface of the substrate, this approach modifies the surface of the substrate underneath the core area [7]. Figure 3-3 illustrates the schematic of a passive polarisation converter based on laterally tilted rib waveguides grown on a stepped substrate.

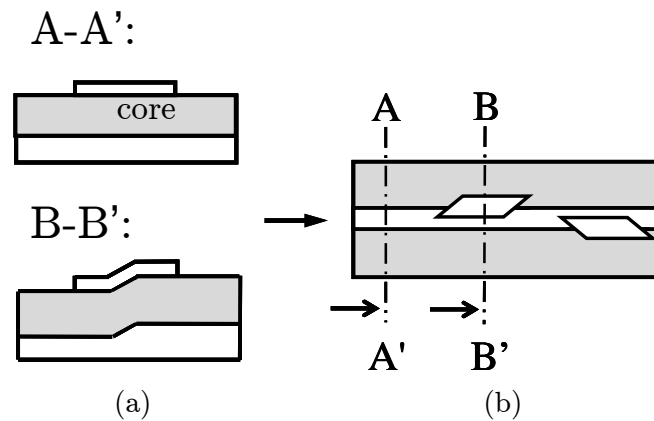


Figure 3-3: (a) Schematic cross section of the feeding waveguide (A-A') and the converter section (B-B'). (b) Top view of the passive 45° polarisation rotator based on periodically tilted rib waveguides (after [7]).

After grooves being dry-etched into the substrate, the buffer- and waveguide layer were grown onto the modified substrate. In order to minimise reflections from the stepped substrate section back into the unmodified sections, the input and output interfaces of the grooves have an angle of 45° relative to the waveguides. A subsequent dry-etch process

forms the rib waveguide. Alternating tilted sections with lengths corresponding to the half-beat-length are cascaded in order to establish a sufficient polarisation rotation. So far, only a 45° polarisation rotator has been realised using this technology. An overview on the device parameters of a realised device is given in Table 3-2.

author	art of proposal	year	material	wavelength	polarisation conversion**	converter length	loss
Heidrich <i>et al.</i> [7]	experiment	1992	InP/InGaAsP	$1.56 \mu\text{m}$	n/a	$7025 \mu\text{m}$	excess loss = 3 dB

** 45° rotation of SOP

Table 3-2: Device parameter overview of a realised passive polarisation rotator based on laterally tilted rib waveguides grown on a stepped substrate structure.

Due to the critical preparation of the stepped substrate in terms of exact transversal position and depth of the recessed area, it is quite difficult and time consuming to integrate this type of polarisation converter together with other components onto a single chip. Moreover, the required regrowth process introduces additional efforts not only into the fabrication process but also in financial terms. A converter length of about 7 mm makes this kind of device unattractive for an application in integrated optical circuits [7].

- ***Asymmetric periodically loaded angled-facet rib waveguides***

This design introduces a modification of the shape of the loaded elements in the previously introduced asymmetric periodically loaded rib waveguide structure. A schematic illustration of this design is given in Figure 3-4.

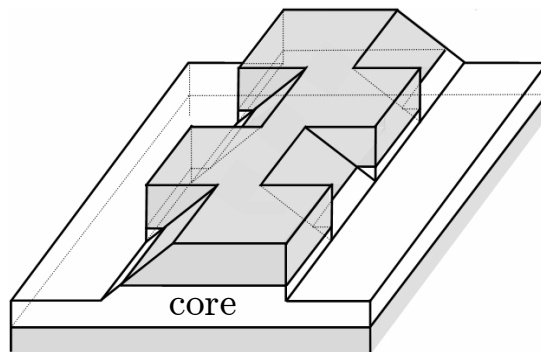


Figure 3-4: Schematic illustration of a passive polarisation converter design incorporating asymmetric periodically loaded angled-facet rib waveguides (after [8]).

In general, the disadvantage of longitudinally-periodic polarisation converters is the section-to-section coupling loss that occurs at each junction of the periodic structure and the difficulty of fabricating the multisection devices. In addition, the required device lengths are relatively long because multiple sections are needed to achieve a significant

polarisation conversion [8]. An overview on the device parameters of a realised device is given in Table 3-3.

author	art of proposal	year	material	wavelength	polarisation conversion	converter length	loss
van der Tol [8]	theory/ experiment	1995	InP/InGaAsP	1.5 μm	>90%	900 μm	excess loss = 0.25 dB

Table 3-3: Device parameter overview of a realised passive polarisation rotator based on asymmetric periodically loaded angled-facet rib waveguides.

• ***Polarisation converters based on ultrashort bends***

This type of passive polarisation converter design is based on deeply etched narrow ridge waveguide bends with small radii [9, 10], which is schematically illustrated in Figure 3-5.

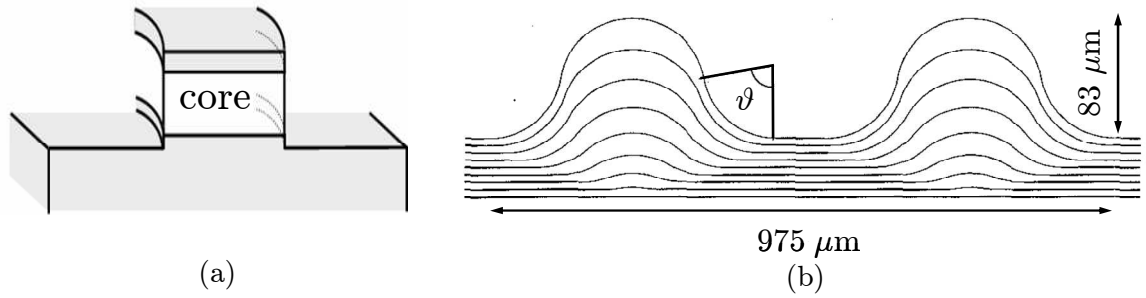


Figure 3-5: (a) Schematic of a deeply etched bended ridge waveguide structure. (b) Top view of the schematic layout of the polarisation converter device (the segment angle is depicted as ϑ). (after [10])

The fabricated device, based on an InP/InGaAsP wafer structure, consisted of a bending radius of 50 μm and a segment angle ϑ of 70°. The device achieved a polarisation conversion of about 85% at an operating wavelength of 1508 nm. An excess loss of about 2.7 dB and a beat length of 120 μm were achieved. The sidewall angle was about 13°. The overall size of this device was about 975 \times 83 μm [10].

3.1.2 Single section beating

- ***Passive polarisation converter comprising a slanted angle rib waveguide***

In order to overcome the necessity of periodically loaded asymmetric waveguides, single-section polarisation converter free of longitudinally-periodic structures were proposed and realised. A schematic of the device design is illustrated in Figure 3-6.

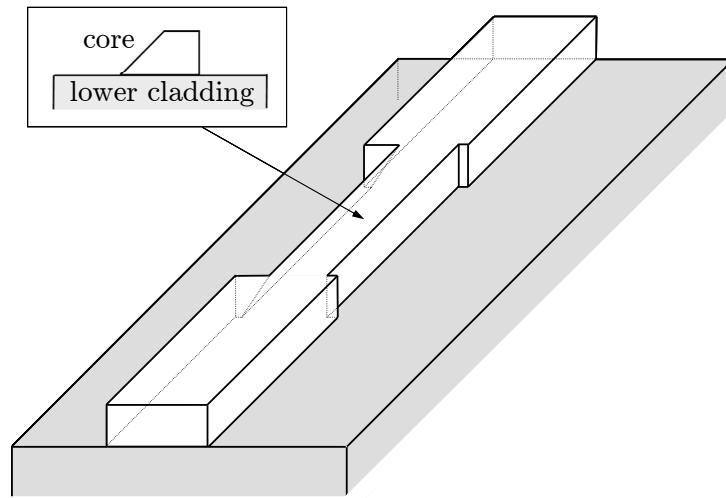


Figure 3-6: 3D schematic of a longitudinally-invariant passive polarisation converter comprising a slanted angle rib waveguide (including input and output rib waveguides). (Insert) Waveguide profile of the converter section.

In order to establish both the vertical and tilted sidewall of the converter section, *two* separate etch processes are necessary. A dry-etch fabrication step is performed to realise the vertical sidewall and a crystallographic wet-etch step is performed to establish the slanted sidewall. This requires an accurate re-masking alignment between these two etch process steps. Another drawback of this design are optical losses due to mode size mismatching at the converter section interface with a regular symmetric waveguide, which can prove to be significant.

Based on this design, a passive polarisation converter was realised on a material structure, which can be used for active device functionalities [11, 12].

An overview on the device parameters of realised devices is given in Table 3-4.

author	art of proposal	year	material	wavelength	polarisation conversion	converter length	losses
Tzolov <i>et al.</i> [13]	theoretical	1996	InP/ InGaAsP	n/a	92 - 93%	250 μm	coupling loss = 2.5 dB
Fontaine [14]	theoretical	1997	n/a	n/a	95%	2800 μm	n/a
Fontaine [15]	theoretical	1999	AlGaAs	1.55 μm	n/a		n/a
Huang [16] & Huang <i>et al.</i> [17]	experiment	2000	GaAs/ AlGaAs	1.55 μm	96%	720 μm	propagation loss of converter section = 1.25 dB/mm propagation loss of input waveguides = 0.65 dB/mm
Rahman <i>et al.</i> [18, 19]	theoretical	2001	GaAs/ AlGaAs	1.55 μm	> 99%	320 μm	insertion loss = 0.4 dB
Somasiri [20] & Somasiri <i>et al.</i> [21]	theoretical	2002/ 2003	InP/ InGaAsP	1.55 μm	99.8%	403 μm	insertion loss = 0.6 dB polarisation crosstalk = -20 dB
Yamauchi <i>et al.</i> [22]	theoretical	2003	n/a	1.55 μm	n/a	75 μm	reflection loss = 0.08 dB radiation loss = 1.5 dB
Correia <i>et al.</i> [23, 24]	theoretical	2003	n/a	n/a	99%	90 μm	insertion loss = 1.16 dB
El-Refaei <i>et al.</i> [25]	theoretical	2003	InP/ InGaAsP	1.55 μm	> 99.98%	226 μm	n/a
El-Refaei <i>et al.</i> [26]	experiment	2004	InP/ InGaAsP	1.55 μm	n/a	330 μm	excess loss = 0.02 dB
Zhu <i>et al.</i> [27-30]	experiment	2000- 2005	InP/ InGaAsP	1.55 μm	99%	112 μm	excess loss < 2 dB
Khalique <i>et al.</i> [31, 32]	experiment	2004/ 2005	InP/ InGaAsP	1.55 μm	> 95%	125 μm	excess loss < 1 dB
Groen <i>et al.</i> [33]	experiment	2003	InP/ InGaAsP	1.55 μm	> 80%	150 μm	insertion loss = 2 dB
Deng [34] & Deng <i>et al.</i> [35, 36]	theoretical	2004/ 2005	SOI	1.55 μm	99.98%	< 100 μm	coupling loss = 0.2 dB
Brooks <i>et al.</i> [37]	experiment	2004	SOI	1.55 μm	52%	2605 μm	n/a
Augustin <i>et al.</i> [12]	experiment	2007	InP/ InGaAsP	1.55 μm	97%	131 μm	excess loss = 2.4 dB (for TE polarisation)

Table 3-4: Overview of proposed and realised longitudinally-invariant passive polarisation converter using a slanted angle rib waveguide. (The converter length denoted in the table equals the half beat length of the converter section.)

- ***Slanted etched sub-wavelength air trench gratings***

This passive polarisation converter device design is based on sub-wavelength air trench gratings, which are angled-etched across a ridge waveguide. A schematic of the device design is illustrated in Figure 3-7.

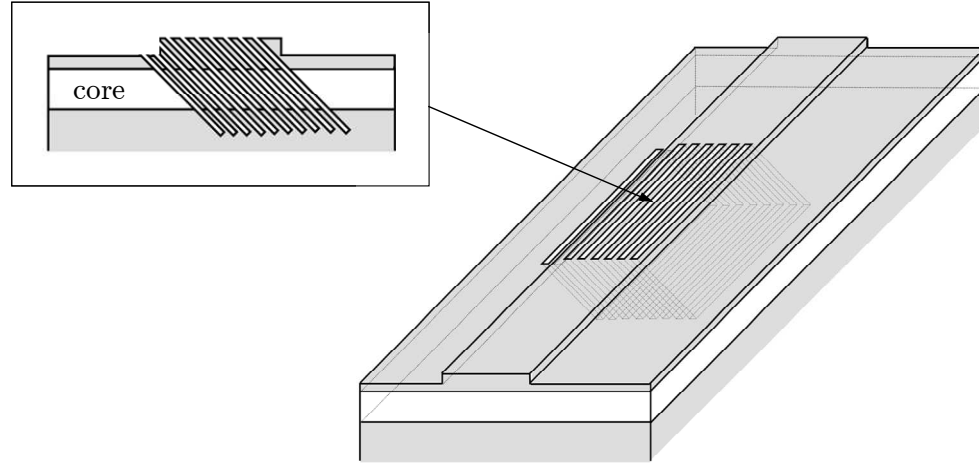


Figure 3-7: 3D schematic of a passive polarisation converter based on deep angled-etched air trenches. (Insert) Waveguide profile of the converter section.

The converter section design is based on the principle that an incident linearly polarised mode is forced by the device structure to degenerate into two components, which are orthogonally polarised to each other. One component is polarised in direction of the etched air trench, whilst the other one is orthogonal to it. The component polarised along the air trenches experiences a lower refractive index, and therefore a higher phase velocity than the other one. As the air trenches introduce a high form birefringence, the resulting converter section lengths are quite short [38-40].

An overview on the device parameters of passive polarisation converters based on this design is given in Table 3-5.

author	art of proposal	year	material	wavelength	polarisation conversion	converter length	losses
Cai <i>et al.</i> [41]	theoretical	2004	n/a	1.28 - 1.4 μm	> 98%	4.3 μm	insertion loss ≤ 0.04 dB
Kotlyar <i>et al.</i> [38-40]	theoretical / experimental	2005	InP/ InGaAsP	1.29 - 1.33 μm	96%	1.5 μm	extinction ratio = 14 dB

Table 3-5: Overview of proposed and realised passive polarisation rotators based on deep angled-etched sub-wavelength air trenches.

- ***Vertical etched sub-wavelength air trench gratings***

This polarisation converter design utilises the *aspect-ratio dependent etching* (ARDE), also called *reactive ion-etch lag* (RIE lag), phenomenon [42] in order to establish an asymmetry in the core geometry of a stripe waveguide cross section. A schematic of the device design is illustrated in Figure 3-8.

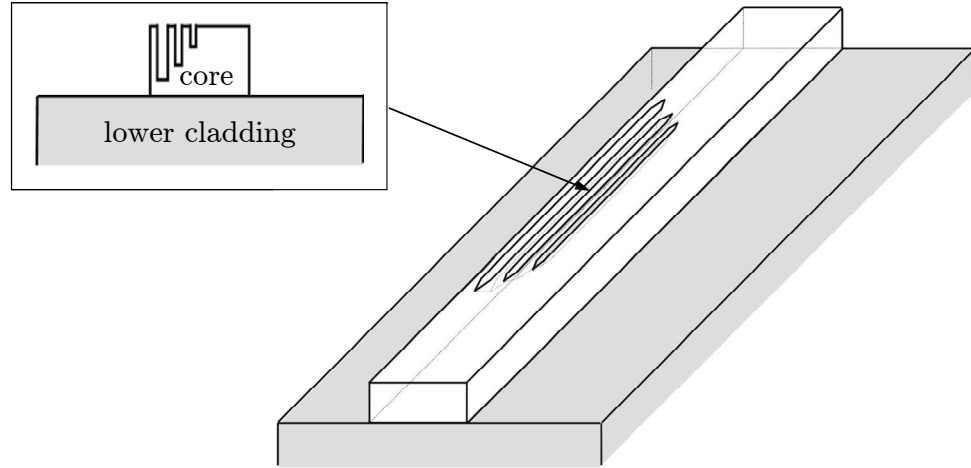


Figure 3-8: 3D schematic of a passive polarisation converter based on vertical etched sub-wavelength air trenches utilising the RIE lag phenomenon. (Insert) Waveguide profile of the cross section (here: three vertical etched air trenches).

The RIE lag phenomenon manifests itself in the way that small features with an aspect ratio (depth/width) much bigger than 1 (narrow trenches, small diameter holes) etch slower than large features (wide trenches, large diameter holes) in the submicron domain [43]. Whereas usually seen as an undesirable phenomenon in dry-etch processes, in this application it simplifies the fabrication of the device structure. The entire device can be fabricated in a single dry-etch process. This minimises the risk of potential fabrication errors due to the avoidance of mask realignment at subsequent fabrication steps. An overview on the device parameters of realised devices consisting of a single [44] or multiple [45-47] vertical air trenches is given in Table 3-6.

author	art of proposal	year	material	wavelength	P_c	converter length	losses
Holmes <i>et al.</i> [45-47]	experimental	2005/2006	GaAs/AlGaAs	900-940 nm	96%	150 μm	n/a
Kim <i>et al.</i> [44]	experimental	2009	GaInAsP/InP	1.55 μm	95%	210 μm	excess loss = 1.38 dB (for TE polarisation)

Table 3-6: Overview of realised passive polarisation rotators based on vertical etched sub-wavelength air trenches utilising the RIE lag phenomenon. The converter length denotes the half beat length of the converter section. (P_c ...polarisation conversion)

3.2 Mode evolution based device designs

This polarisation converter design introduces an adiabatic change to the geometry of the waveguide cross section. It basically represents a twisted waveguide in analogy to a twister, which is used in microwave applications. By twisting the waveguide, a rotation of the principal axis of the waveguide takes place. This imparts a rotation of the SOP of the excited modes within the waveguide. But, the evolution of the waveguide structure also induces a mode-coupling. While on mode beating based polarisation converters exploit mode-coupling, it is not desired in this device design and needs to be suppressed. This can be established by a slow evolution of the waveguide structure.

In order to approximate the form of a twisted waveguide, a pair of asymmetrically and oppositely tapered waveguide core layers is being used. Two possible configurations are illustrated in Figure 3-9. The upper core layer is either tapered and stays on the lower core layer (Figure 3-9(a)), or its width stays constant (or just being slightly tapered) and it is separated from the lower core layer (Figure 3-9(b)) [48-50].

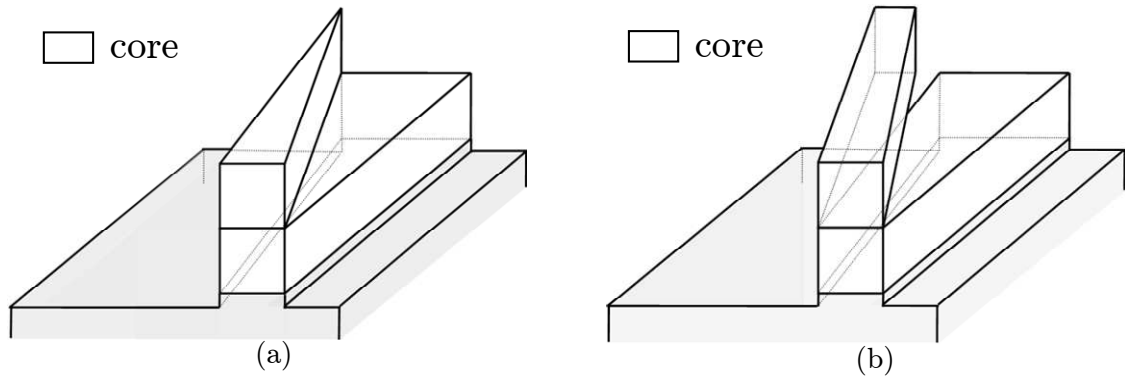


Figure 3-9: Passive polarisation converter based on mode-evolution consisting of (a) tapered upper and lower core layers and (b) tapered and separated upper and lower core layers (after [48-50]).

This passive polarisation converter design is largely insensitive to wavelength changes, which makes it quite attractive for the usage in multi-wavelength applications.

An overview on the theoretical device parameters for this passive polarisation converter design is given in Table 3-7.

author	art of proposal	year	material	wavelength	polarisation conversion	converter length	loss
Watts <i>et al.</i> [48-50]	theoretical	2005/2007	n/a	1.55 μm	>98%	100 - 200 μm	< 0.1 dB

Table 3-7: Device parameter of a theoretically proposed passive polarisation converter based on the principle of mode evolution.

3.3 Concluding remarks

An overview of different designs of already realised passive polarisation converters on GaAs/AlGaAs, InP/InGaAsP, SOI and InGaAsP based QW material structures was given. The achievable polarisation conversion P_C is quite high for polarisation converters based on both mode beating and -evolution. However, the converter section lengths, especially in multiple section, mode beating based designs, are quite long. In addition, the drawback of almost all introduced designs is the required accurate re-masking between two subsequent etch process steps. Optical losses due to mode-mismatching at the converter section periphery with a regular, symmetric rib waveguide can also prove to be significant. Also, an implementation of certain designs, such as vertically etched sub-wavelength gratings on material structures designed for active device functionalities, can prove to be difficult in terms of optimisation of the dry-etch process.

3.4 References

- [1] Shani Y., Alferness R., Koch T., Koren U., Oron M., Miller B. I. and Young M. G., "Polarization rotation in asymmetric periodic loaded rib waveguides", *Applied Physics Letters*, vol. **59**, no. 11, pp. 1278 - 1280, (1991).
- [2] Huang W. and Mao Z. M., "Polarization rotation in periodic loaded rib waveguides", *IEEE Journal of Lightwave Technology*, vol. **10**, no. 12, pp. 1825 - 1831, (1992).
- [3] Alferness R. C., Koch T. L. and Shani Y., "Asymmetric, periodically loaded waveguide for polarization rotation", *US patent 5243669*, (1993).
- [4] Mustieles F. J., Ballesteros E. and Hernandez-Gil F., "Multimodal Analysis Method for the Design of Passive TE/TM Converters in Integrated Waveguides", *IEEE Photonics Technology Letters*, vol. **5**, no. 7, pp. 809 - 811, (1993).
- [5] Gustavsson M., "Analysis of polarization independent optical amplifiers and filters based on polarization rotation in periodically asymmetric waveguides", *IEEE Journal of Quantum Electronics*, vol. **29**, no. 4, pp. 1168 - 1178, (1993).
- [6] Obayya S. S. A., Rahman B. M. A. and El-Mikati H. A., "Vector Beam Propagation Analysis of Polarization Conversion in Periodically Loaded Waveguides", *IEEE Photonics Technology Letters*, vol. **12**, no. 10, pp. 1346 - 1348, (2000).
- [7] Heidrich H., Albrecht P., Hamacher M., Nolting H. P., Schroeter-Janssen H. and Weinert C. M., "Passive mode converter with a periodically tilted InP/GaInAsP rib waveguide", *IEEE Photonics Technology Letters*, vol. **4**, no. 1, pp. 34 - 36, (1992).

- [8] van der Tol J. J. G. M., Hakimzadeh F., Pedersen J. W., Li D. and van Brug H., "A new short and low-loss passive polarization converter on InP", *IEEE Photonics Technology Letters*, vol. **7**, no. 1, pp. 32 - 34, (1995).
- [9] van Dam C., Heidrich H., Hamacher M., Steenbergen C. A. M., Smit M. K. and Weinert C. M., "Integrated optical circuit comprising a polarization converter", *US patent 5838844*, (1998).
- [10] van Dam C., Spiekman L. H., van Ham F. P. G. M., Groen F. H., van der Tol J. J. G. M., Moerman I., Pascher W. W., Hamacher M., Heidrich H., Weinert C. M. and Smit M. K., "Novel compact polarization converters based on ultra short bends", *IEEE Photonics Technology Letters*, vol. **8**, no. 10, pp. 1346 - 1348, (1996).
- [11] Augustin L. M., "Polarization Handling in Photonic Integrated Circuits", *PhD thesis*, Eindhoven University of Technology, Eindhoven, The Netherlands, (2008).
- [12] Augustin L. M., Van der Tol J. J. G. M., Geluk E. J. and Smit M. K., "Short Polarization Converter Optimized for Active-Passive Integration in InGaAsP-InP", *IEEE Photonics Technology Letters*, vol. **19**, no. 20, pp. 1673 - 1675, (2007).
- [13] Tzolov V. P. and Fontaine M., "A passive polarization converter free of longitudinally-periodic structure", *Optics Communications*, vol. **127**, no. 1 - 3, pp. 7 - 13, (1996).
- [14] Fontaine M., "Theoretical approach to investigating cross-phase modulation phenomena in waveguides with arbitrary cross sections", *Journal of the Optical Society of America B (Optical Physics)*, vol. **14**, no. 6, pp. 1444 - 1452, (1997).
- [15] Fontaine M., "Integrated optical wave plate", *Journal of Modern Optics*, vol. **46**, no. 6, pp. 973 - 980, (1999).
- [16] Huang J. Z., "Design and Fabrication of Integrated Optical Waveguide Devices", *PhD thesis*, Columbia University, USA, (1999).
- [17] Huang J. Z., Scarmozzino R., Nagy G., Steel M. J. and Osgood R. M. J., "Realization of a compact and single-mode optical passive polarization converter", *IEEE Photonics Technology Letters*, vol. **12**, no. 3, pp. 317 - 319, (2000).
- [18] Rahman B. M. A., Obayya S. S. A., Somasiri N., Rajarajan M., Grattan K. T. V. and El Mikathi H. A., "Design and characterization of compact single-section passive polarization rotator", *IEEE Journal of Lightwave Technology*, vol. **19**, no. 4, pp. 512 - 519, (2001).
- [19] Rahman B. M. A., Wongcharoen T., Obayya S. S. A., Rajarajan M., Themistos C., Somasiri N., Anwar N., El Mikati H. A. and Grattan K. T. V., "Rigorous analysis of photonic devices by using the finite element method", in *Proceedings of the 8th IEEE International Symposium on High Performance Electron Devices for Microwave and Optoelectronic Applications 2000 (EDMO2000)*, Glasgow, UK, 13 - 14 November 2000, Glasgow, UK, pp. 173 - 178.
- [20] Somasiri N., "Finite Element Modelling of Polarization Issues in Optoelectronic Systems", *PhD thesis*, City University, London, UK, (2003).

- [21] Somasiri N., Rahman B. M. A. and Obayya S. S. A., "Fabrication tolerance study of a compact passive polarization rotator", *IEEE Journal of Lightwave Technology*, vol. **20**, no. 4, pp. 751 - 757, (2002).
- [22] Yamauchi J., Ohba I., Ando T. and Nakano H., "FDTD Analysis of a Polarization Conversion Waveguide with a Single Sloped Sidewall", in *Proceedings of OSA Topical Meetings: Integrated Photonics Research and Applications 2003 (IPRA 2003)*, Washington, DC, USA, 16 -20 June 2003, paper ITuH1-1, pp. 198 - 200.
- [23] Correia D., Da Silva J. P. and Hernandez-Figueroa H. E., "Efficient Design of Polarization Rotators by Genetic Algorithm and Vectorial Finite-Element BPM", in *Proceedings of the IEEE International Microwave and Optoelectronics Conference 2003 (IMOC 2003)*, Foz do Iguacu, Brazil, 20 - 23 September 2003, pp. 595 - 598.
- [24] Correia D., Da Silva J. P. and Hernandez-Figueroa H. E., "Genetic algorithm and finite-element design of short single-section passive polarization converter", *IEEE Photonics Technology Letters*, vol. **15**, no. 7, pp. 915 - 917, (2003).
- [25] El-Refaei H. and Yevick D., "An optimized InGaAsP/InP polarization converter employing asymmetric rib waveguides", *IEEE Journal of Lightwave Technology*, vol. **21**, no. 6, pp. 1544 - 1548, (2003).
- [26] El-Refaei H., Yevick D. and Jones T., "Slanted-rib waveguide InGaAsP-InP polarization converters", *IEEE Journal of Lightwave Technology*, vol. **22**, no. 5, pp. 1352 - 1357, (2004).
- [27] Zhu Y. C., Groen F. H., Leijtens X. J. M. and van der Tol J. J. G. M., "Single-section polarisation converter on InP/InGaAsP using asymmetrical waveguides", in *Proceedings of the 6th Annual Symposium of the IEEE Lasers & Electro-Optics Society (LEOS) BENELUX Chapter 2001*, Brussels, Belgium, 3 December 2001, pp. 209 - 213.
- [28] Zhu Y. C., Groen F. H., Maat D. H. P., Leijtens X. J. M. and Smit M. K., "Design of a short polarization converter on InP/InGaAsP using asymmetrical waveguides", in *Proceedings of the 5th Annual Symposium of the IEEE Laser & Electro-Optics Society (LEOS) BENELUX Chapter 2000*, Delft, The Netherlands, 30 October 2000, pp. 227 - 230.
- [29] Zhu Y. C., Khalique U., van der Tol J. J. G. M., Geluk E. J., Groen F., Karouta F. and Smit M. K., "Ultrashort, highly efficient integrated optical polarization converter", in *Proceedings of the 12th European Conference on Integrated Optics 2005 (ECIO '05)*, Grenoble, France, 6 - 8 April 2005, pp. 96 - 99.
- [30] Zhu Y. C., Khalique U., Van der Tol J. J. G. M., Geluk F. E. J., Groen F. H., Karouta F. and Smit M. K., "Ultrashort Polarization Converter on InP/InGaAsP", in *Proceedings of the 9th Annual Symposium of the IEEE Laser & Electro-Optics Society (LEOS) BENELUX Chapter 2004*, Gent, Belgium, 2 - 3 December 2004, pp. 115 - 118.
- [31] Khalique U., Zhu Y., van der Tol J. J. G. M., Augustin L. M., Hanfoug R., Groen F. H., van de Moosdijk M., de Laat W., Simon K., van Veldhoven P. J. and Smit M. K., "Polarization converter on InP/InGaAsP fabricated with optical reduction

- wafer stepper", in *Proceedings of the 9th Annual Symposium of the IEEE Laser & Electro-Optics Society (LEOS) BENELUX Chapter 2004*, Ghent, Belgium, 2 - 3 December 2004, pp. 131 - 135.
- [32] Khalique U., Zhu Y., van der Tol J. J. G. M., Augustin L. M., Hanfoug R., Groen F. H., van Veldhoven P. J. and Smit M. K., "Ultrashort polarization converter on InP/InGaAsP fabricated by optical lithography", in *Proceedings of OSA Topical Meetings : Integrated Photonics Research and Applications Nanophotonics for Information Systems 2005 (IPRA 2005)*, San Diego, CA, USA, 11 - 15 April 2005, paper IWA3, pp. 1 - 3.
- [33] Groen F. H., Zhu Y. C. and van der Tol J. J. G. M., "Compact polarization converter on InP/InPGaAs using an asymmetrical waveguide", in *Proceedings of the 11th European Conference on Integrated Optics 2003 (ECIO'03)*, Prague, Czech Republic, 2 - 4 April 2003, pp. 141 - 144.
- [34] Deng H., "Design and Characterization of Silicon-on-Insulator Passive Polarization Converter with Finite-Element Analysis", *PhD thesis*, University of Waterloo, Ontario, Canada, (2005).
- [35] Deng H., Yevick D. O., Brooks C. and Jessop P. E., "Design procedures for slanted-angle SOI polarization rotators", in *Proceedings of the Optical Fiber Communication Conference and Exposition 2004 (OFC 2004)*, Los Angeles, CA, USA, 22 - 27 February 2004, paper MF41.
- [36] Deng H., Yevick D. O., Brooks C. and Jessop P. E., "Design Rules for Slanted-Angle Polarization Rotators", *IEEE Journal of Lightwave Technology*, vol. **23**, no. 1, pp. 432-445, (2005).
- [37] Brooks C., Jessop P. E., Deng H. and Yevick D., "Polarization rotating waveguides in silicon on insulator", in *Proceedings of OSA Topical Meetings: Integrated Photonics Research and Applications 2004 (IPRA 2004)*, San Francisco, CA, USA, 30 June - 2 July 2004, paper IFG4.
- [38] Kotlyar M. V., "Ultra-short InP-based polarization rotator", in *Proceedings of the International Symposium on Photonic and Electromagnetic Crystal Structures (PECS-VI)*, Crete, Greece, 19 - 24 June 2005.
- [39] Kotlyar M. V., Bolla L., Midrio M., O'Faolain L. and Krauss T. F., "Compact polarization converter in InP-based material", *Optics Express*, vol. **13**, no. 13, pp. 5040 - 5045, (2005).
- [40] Kotlyar M. V., O'Faolain L., Wilson R. and Krauss T. F., "High-aspect-ratio chemically assisted ion-beam etching for photonic crystals using a high beam voltage-current ratio", *Journal of Vacuum Science & Technology B: Microelectronics and Nanometer Structures*, vol. **22**, no. 4, pp. 1788 - 1791, (2004).
- [41] Cai J., Jiang J. and Nordin G. P., "Ultra-short waveguide polarization converter using a sub-wavelength grating", in *Proceedings of OSA Topical Meetings: Integrated Photonics Research and Applications 2004 (IPRA 2004)*, San Francisco, CA, USA, 27 June - 2 July 2004, paper IFG2.

- [42] Hedlund C., Blom H.-O. and Berg S., "Microloading effect in reactive ion etching", *Journal of Vacuum Science and Technology A*, vol. **12**, no. 4, pp. 1962 - 1965, (1994).
- [43] Gottscho R. A. and Jurgensen C. W., "Microscopic uniformity in plasma etching", *Journal of Vacuum Science and Technology B*, vol. **10**, no. 5, pp. 2133 - 2147, (1992).
- [44] Kim S.-H., Takei R., Shoji Y. and Mizumoto T., "Single-trench waveguide TE-TM mode converter", *Optics Express*, vol. **19**, no. 14, pp. 11267 - 11273, (2009).
- [45] Holmes B. M., Bregenzler J. J. and Hutchings D. C., "Novel fabrication techniques for the realisation of passive waveguide polarisation converters", in *Proceedings of the Conference on Lasers and Electro-Optics 2005 (CLEO '05)*, Baltimore, Maryland, USA, 22 - 27 May 2005, paper CWD4, pp. 1285 - 1287.
- [46] Holmes B. M. and Hutchings D. C., "Realization of Novel Low-Loss Monolithically Integrated Passive Waveguide Mode Converters", *IEEE Photonics Technology Letters*, vol. **18**, no. 1, pp. 43 - 45, (2006).
- [47] Holmes B. M. and Hutchings D. C., "High Efficiency and Low Loss Fully Integrated Passive Waveguide Mode Converters", in *Proceedings of the IEEE Lasers & Electro-Optics Society Annual Meeting 2006 (LEOS '06)*, Montreal, Canada, 29 October - 2 November 2006.
- [48] Watts M. R., "Polarization Independent Microphotonic Circuits", *PhD thesis*, Massachusetts Institute of Technology, USA, (2005).
- [49] Watts M. R. and Haus H. A., "Integrated mode-evolution-based polarization rotators", *Optics Letters*, vol. **30**, no. 2, pp. 138 - 140, (2005).
- [50] Watts M. R., Haus H. A., Haus E. L. and Cherchi M., "Integrated optic polarization converter based on structural chirality", *US patent 7228015 B2*, (2007).

Chapter 4

Fabrication method and measurement setup

4.1 Dry-etch fabrication process utilising an in-situ sloped sampleholder

4.1.1 Background

Single section passive polarisation converters based on the principle of mode beating represent the most compact and efficient converter devices. Mode beating based designs introduce intentionally an asymmetric waveguide core cross section profile in order to increase the form birefringence of the waveguide. One method of fabricating such an asymmetric waveguide profile in the converter section is to use a combination of crystallographic wet-etch and dry-etch processing, which results in a ridge waveguide consisting of a sloped sidewall. The required accurate (re-)mask alignments between these two separate etch steps represent a drawback of this method. Therefore, it is desirable to fabricate an asymmetric waveguide cross section profile in a *single* fabrication step.

The magnitude of the achievable sidewall slope angle in wet-etch fabrication processes is determined by the crystallographic structure of the wafer material [1, 2]. This introduces restrictions in device designs.

In the dry-etch fabrication technology, however, several methods to fabricate sloped waveguide sidewalls have been reported. Amongst the utilisation of an in-situ conductive shadow mask [3] or an in-situ Faraday cage [4], which were placed above the horizontally mounted sample during the dry-etch process, configurations involving the mounting of the substrate at a tilting angle with respect to the cathode of the reaction chamber were also introduced [5, 6]. The utilisation of a specially designed sample holder incorporating a recessed slanted groove [6], where the sample is positioned, demonstrated very reproducible and controllable sloped smooth waveguide sidewalls in conjunction with a *reactive ion etch* (RIE) [7-12] process.

This fabrication method not only allows the realisation of novel single section passive polarisation converter designs based on mode beating but also enables the fabrication of an asymmetric waveguide profile cross section in a *single* dry-etch process.

4.1.2 Principle

The RIE machine used is an *Oxford Instruments System 100™* (S100) [13]. The S100 machine consists of an integrated loadlock chamber with the main chamber evacuated by a Leybold turbomolecular pump to a typical base pressure of $10 \mu\text{Torr}$. The *radio frequency* (RF) signal generator, operating at 13.56 MHz, is capacitively coupled to the bottom electrode of a parallel plate reactor. The height of the chamber is 135 mm and the chamber diameter is 370 mm. A photograph of this machine is given in Figure 4-1. The



Figure 4-1: Photograph of the *Oxford Instruments System 100™* (S100) RIE machine in the James Watt Nanofabrication Centre (JWNC) at the University of Glasgow, which was used in order to fabricate the asymmetric waveguide profile structures (in conjunction with the specially designed sampleholder).

RF generator drives a current through a low-pressured gas between the two electrodes (Figure 4-2). The discharge causes the gas to form a plasma, which is basically a collection of freely moving charged particles (positive ions and electrons) that are, on the average, electrically neutral. The region, where both the plasma and the electrodes meet, is called *sheath*, which is a thin positively charged layer. Reactive ions are accelerated across the

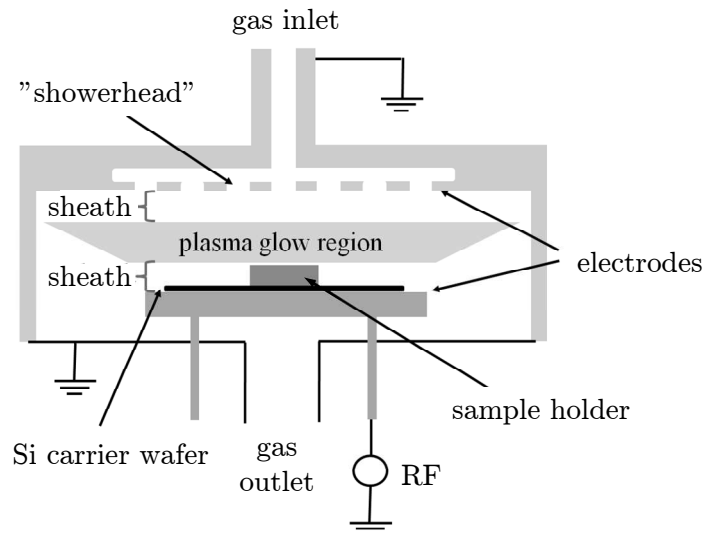


Figure 4-2: Schematic diagram of a conventional parallel plate type RIE machine.

plasma sheath in the vicinity of the substrate in the direction of the electric field. The reactive ions arrive at normal incidence to the surface of the sample [8]. If the sample is positioned at an angle with respect to the cathode, the sample would protrude into the plasma sheath. In this case, the electric charge would distribute itself in a manner that the net field distribution is still perpendicular to the surface of the sample [6]. In order to reduce this field bending effect around the sample, and therefore establish an angled incidence of the reactive ions onto the surface of the sample, a special designed sample holder with a recessed groove was used (Figure 4-3). The sample holder consists of anodised aluminium.

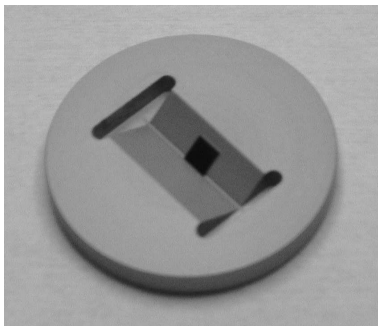


Figure 4-3: Customised sample holder incorporating a recessed slanted groove.

The sample holder was placed on a 4" Si carrier wafer in order to be loaded into the etch chamber. Figure 4-4 shows the manually loaded load lock. The carrier wafer is loaded together with the sample holder through the slit valve onto the lower electrode. The headroom of the slit valve determines the maximum possible sample holder height of 5 mm. This subsequently limits the maximum geometrical width of the sample to 5 - 7 mm, depending on the angle of the sample holder slope.

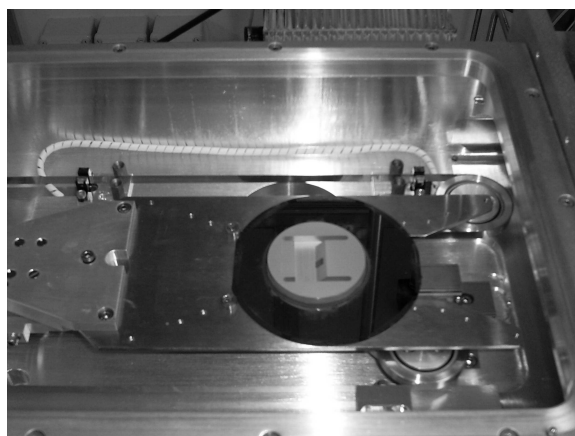


Figure 4-4: Sample holder placed on a 4" Si carrier wafer in the manually loaded load lock of the *Oxford Instruments System 100™* RIE machine.

4.1.3 Realisation

A standard RIE process parameter recipe for GaAs material *at room temperature* was used in the fabrication of angled sidewall waveguides. The parameters are given in Table 4-1.

parameter	value
process gas	SiCl ₄
forward RF power	100 W
process pressure	9 mTorr
corrected gas flow	9 sccm
BIAS	-345 V
table temperature	35 ° C

Table 4-1: Standard RIE process recipe for GaAs material at room temperature.

After PECVD (*plasma enhanced chemical vapour deposition*) of a 200 nm SiO₂ layer, the bulk GaAs test samples were patterned with a 200 nm spin-coated layer of SHIPLEYTM S1818 photoresist using photolithography (HTG2 mask aligner, exposure time: 12 seconds). The subsequent development of the waveguide pattern was conducted by applying a developer solution (1:1 MICROPOSIT[®] Concentrate Developer : *reverse osmosis* (RO) water) for 75 seconds. The waveguide pattern was then transferred onto the GaAs surface by dry-etching the SiO₂ layer using CHF₃ as a reactive gas in the BP80 machine (BP80 parameter settings: process gas: CHF₃, corrected gas flow: 20 sccm, process pressure: 17 mTorr, forward RF power: 100 W, temperature: 25 ° C, BIAS: -280 V, process time: 13 minutes). Sample holders with different slope angles were used for the angled GaAs etch test series. An overview on the etch profile result of the test series is given in Figure 4-5. It can be noted that the etched front slope angles ζ and undercut slope angles α do not necessarily correspond with the slope angle on the sample holder at the given process parameters. By adjusting the process parameters it should be possible to achieve a correspondence. This investigation was not conducted due to a shortage of wafer material.

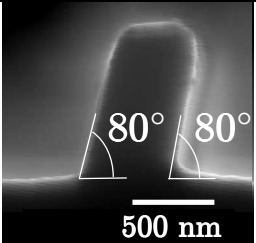
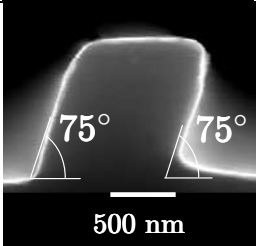
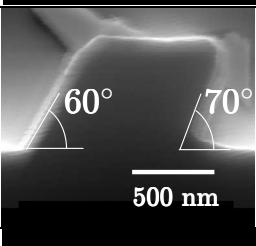
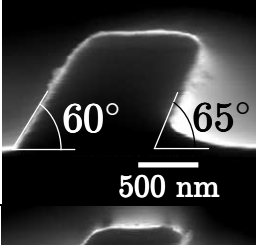
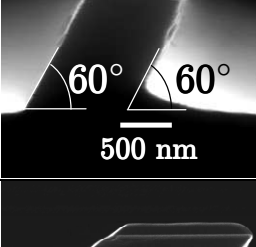
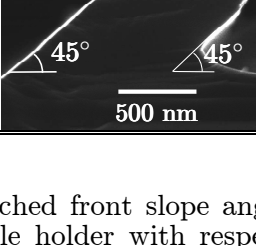
tilt of the slope on the sample holder with respect to the horizontal axis	SEM cross view of the fabricated waveguide	etched front slope angle ξ and undercut slope angle α of the waveguide with respect to the horizontal axis
10°		front angle $\xi = 80^\circ$ undercut angle $\alpha = 80^\circ$
20°		front angle $\xi = 75^\circ$ undercut angle $\alpha = 75^\circ$
30°		front angle $\xi = 60^\circ$ undercut angle $\alpha = 70^\circ$
40°		front angle $\xi = 60^\circ$ undercut angle $\alpha = 65^\circ$
45°		front angle $\xi = 60^\circ$ undercut angle $\alpha = 60^\circ$
75°		front angle $\xi = 45^\circ$ undercut angle $\alpha = 45^\circ$

Figure 4-5: Dependence of the etched front slope angle ξ and undercut slope angle α on the tilt of the slope of the sample holder with respect to the horizontal axis. The used GaAs RIE process parameters were: process gas: SiCl_4 , forward RF power = 100 W, process pressure = 9 mTorr, corrected gas flow = 9 sccm, BIAS = -345 V, table temperature = 35 °C.

4.2 Measurement setup

The devices were characterised at an operating wavelength λ of 1064 nm, which was provided by an available diode pumped solid state Nd:YAG laser. The device measurement setup is schematically illustrated in Figure 4-6. TE polarised radiation, which was established by the polarising cube beam splitter on the positioning stage, was coupled into the waveguides (device under test) with a 40 \times magnification objective lens using the end-fire coupling technique [14]. The output passed again through a polarising beam-splitting cube in order to separate the TE and TM components. The transmitted TE- and TM polarised signals were then individually detected by a photodetector and evaluated by a lock-in amplifier, which is synchronised to a reference signal obtained from an optical chopper. The TM polarisation purity P_C was determined from the corresponding output signals of the lock-in amplifier.

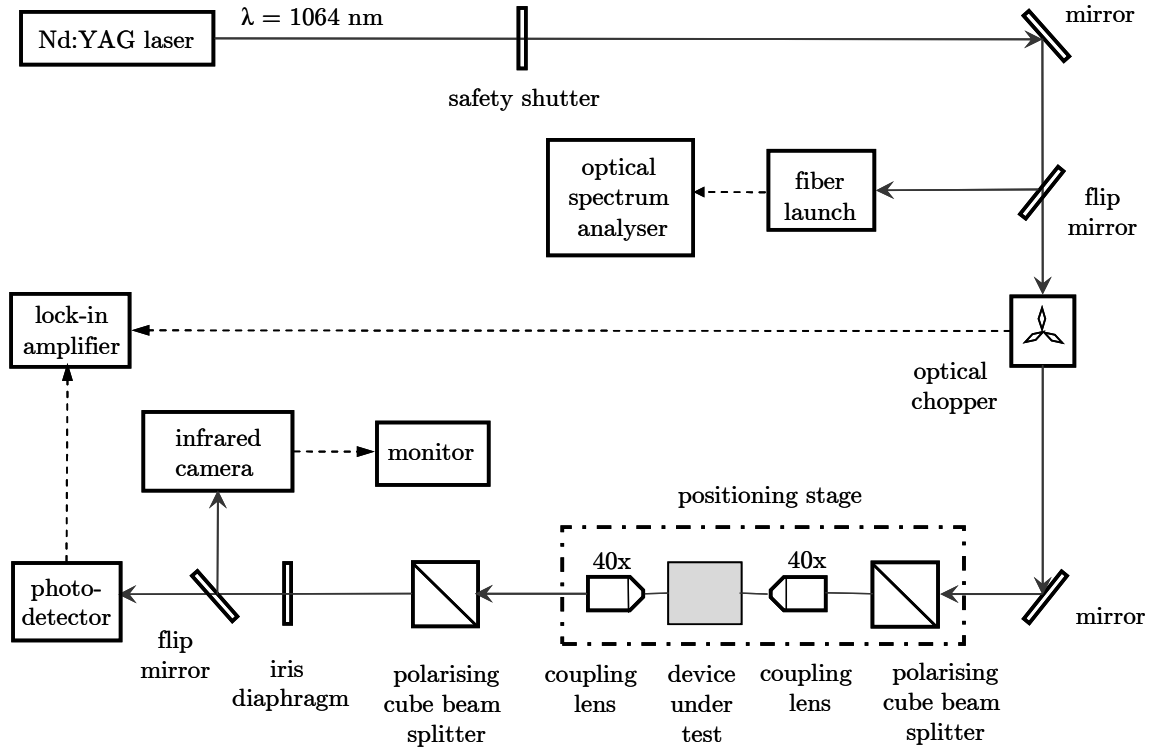


Figure 4-6: Schematic of the device measurement setup comprising a Nd:YAG laser and utilising the end-fire coupling technique.

4.2.1 Evaluation of waveguide losses

The cut-back method [14-16] was used in order to determine the optical waveguide losses. The wafer sample contained devices of overall constant length, but the length of the converter section on the devices was different. The devices were measured using the end-fire coupling technique. It is quite important to carefully align the laser beam onto the waveguide in order to ensure an optimum coupling before conducting each waveguide measurement. The output power P_1 for a waveguide containing a converter section of length L_1 and the input power P_{INPUT} were recorded. Whilst P_{INPUT} was kept constant, the measurement was repeated for a waveguide containing a converter section of length L_2 in order to obtain the corresponding output power P_2 . The propagation loss of a certain converter section length, defined by $L_2 - L_1$, is therefore related to the difference of the output powers from each measurement. It is common practice to fit a straight line to the measured data that are plotted on a semilog paper. The degree of scatter of the data points from the fitted straight line can be considered as coupling errors under the assumption of no fabrication inconsistencies on the waveguides. The slope of the ideal straight line represents the dependence of the transmitted power on the converter section length and determines the propagation loss coefficient Ω (in dB/mm), which can be evaluated from the relation

$$\Omega = -\frac{10 \cdot \log_{10}(P_2 / P_1)}{L_2 - L_1} \quad \text{for } L_2 > L_1 \quad (\text{in dB/mm}), \quad (4.1)$$

where P_1 and P_2 denote the transmitted measured power of two waveguides with different converter section lengths L_1 and L_2 .

As the straight line is evaluated by the linear interpolation of the measured data over a certain range of converter section lengths, the actual number of measured data points is significant.

The insertion loss coefficient Λ can be determined from the ratio

$$\Lambda = -10 \log_{10}(P_1 / P_0) \quad (\text{in dB}), \quad (4.2)$$

where P_0 denotes the measured output power of a waveguide without a converter section.

4.3 References

- [1] Howes M. J. and Morgan D. V., "*Gallium Arsenide*", 1st. ed., John Wiley & Sons, New York, USA, ISBN 0-471-90048-6, (1985).
- [2] Kern D. P., Houzgo P. J., Coane P. J. and Chang T. H. P., "Practical aspects of microfabrication in the 100 nm regime", *Journal of Vacuum Science & Technology B*, vol. **1**, no. 4, pp. 1096 - 1100, (1983).
- [3] Jacobs B. and Zengerle R., "Reactive ion etching of sloped sidewalls for surface emitting structures using a shadow mask technique", *Journal of Vacuum Science and Technology B*, vol. **14**, no. 4, pp. 2537 - 2542, (1996).
- [4] Cho B.-O., Hwang S.-W., Ryu J.-H., Kim I.-W. and Moon S. H., "Fabrication Method for Surface Gratings Using a Faraday Cage in a Conventional Plasma Etching Apparatus", *Electrochemical and Solid-State Letters*, vol. **2**, no. 3, pp. 129 - 130, (1999).
- [5] Coldren L. A. and Rentschler J. A., "Directional reactive-ion-etching of InP with Cl₂ containing gases", *Journal of Vacuum Science and Technology*, vol. **19**, no. 2, pp. 225 - 230, (1981).
- [6] Takamori T., Coldren L. A. and Merz J. L., "Angled etching of GaAs/AlGaAs by conventional Cl₂ reactive ion etching", *Applied Physics Letters*, vol. **53**, no. 25, pp. 2549 - 2551, (1988).
- [7] Coburn J. W. and Winters H. F., "Plasma etching - A discussion of mechanisms", *Journal of Vacuum Science and Technology*, vol. **16**, no. 2, pp. 391 - 403, (1979).
- [8] Lieberman M. A. and Lichtenberg A. J., "*Principles of Plasma Discharges and Materials Processing*", 1st. ed., John Wiley & Sons, New York, USA, ISBN 0-471-00577-0, (1994).
- [9] May G. S. and Sze S. M., "*Fundamentals of Semiconductor Fabrication*", 1st. ed., John Wiley & Sons, Hoboken, NJ, USA, ISBN 0-471-23279-3, (2004).
- [10] Widman D., Mader H. and Friedrich H., "*Technologie hochintegrierter Schaltungen*", Springer, Berlin, Germany, ISBN 3-540-59357-8, (1996).
- [11] Wilkinson C. D. W. and Rahman M., "Dry etching and sputtering", *Philosophical Transactions of the Royal Society A*, vol. **362**, pp. 125 - 138, (2004).
- [12] Williams R., "*Modern GaAs processing techniques*", 1st. ed., Artech House, Norwood, MA, USA, ISBN 0-89006-343-5, (1990).
- [13] Oxford Instruments, <http://www.oxford-instruments.com>
- [14] Hunsperger R. G., "*Integrated Optics: Theory and Technology*", 3rd. ed., Springer, Berlin, Germany, ISBN 0-387-53305-2, (1991).
- [15] Zappe H. P., "*Introduction to Semiconductor Integrated Optics*", Artech House, Boston, USA, ISBN 0-89006-789-9, (1995).

-
- [16] Reed G. T. and Knights A. P., "*Silicon Photonics*", 1st. ed., John Wiley & Sons Ltd., Chichester, United Kingdom, ISBN 0470870346, (2004).

Chapter 5

Passive polarisation converter comprising an asymmetric waveguide structure

5.1 Introduction

As summarised in chapter 3, various designs of integrated passive polarisation converters based on the principles of mode evolution [1-3] and mode beating have already been introduced. Examples include longitudinal waveguide bends [4], longitudinal periodically loaded waveguide sections [5], single ridge waveguide sections consisting of a sloped sidewall [6-9] and sub-wavelength air trenches [10-12]. These designs have already been realised on GaAs/AlGaAs, InP/InGaAsP or silicon on insulator (SOI) material structures. Mode beating based designs intentionally introduce an asymmetric waveguide core cross section profile in order to increase the propagation constant difference between the two lowest order excited modes. One method of fabricating such an asymmetric waveguide profile is to use a combination of crystallographic wet-etch and dry-etch processing [8]. The drawback of such a method is the required accurate re-masking between the two etch process steps. In addition, optical losses due to mode-mismatching at the converter section periphery with a regular, symmetric waveguide can prove to be significant.

This chapter presents a mode beating based passive converter design that bypasses accurate re-masking requirements for the realisation of the asymmetric waveguide core profile. The converter section was fabricated in a *single* dry-etch process. The resulting asymmetric stripe waveguide structure consists of two slanted sidewalls in the waveguide core profile (Figure 5-1(Insert)). Figure 5-1(b) illustrates the proposed passive polarisation converter design. The wafer structure is composed of a $4.7\ \mu\text{m}$ $\text{Al}_{0.27}\text{Ga}_{0.73}\text{As}$ lower cladding and a $0.5\ \mu\text{m}$ GaAs core layer, grown using metal-organic chemical-vapour deposition (MOCVD) upon a n-doped GaAs substrate. The device comprises both an asymmetric and symmetric stripe waveguide section. Light is coupled into the device via a $3\ \mu\text{m}$ wide symmetric stripe waveguide, which is referred to as the input waveguide section. A width of $3\ \mu\text{m}$ not only simplifies to couple light into the device but also provides mechanical strength in order to prevent the waveguide from collapse during fabrication or at cleaving. A following adiabatic linear taper between the input waveguide section and the intermediate waveguide section of width w establishes a close match of the mode profiles

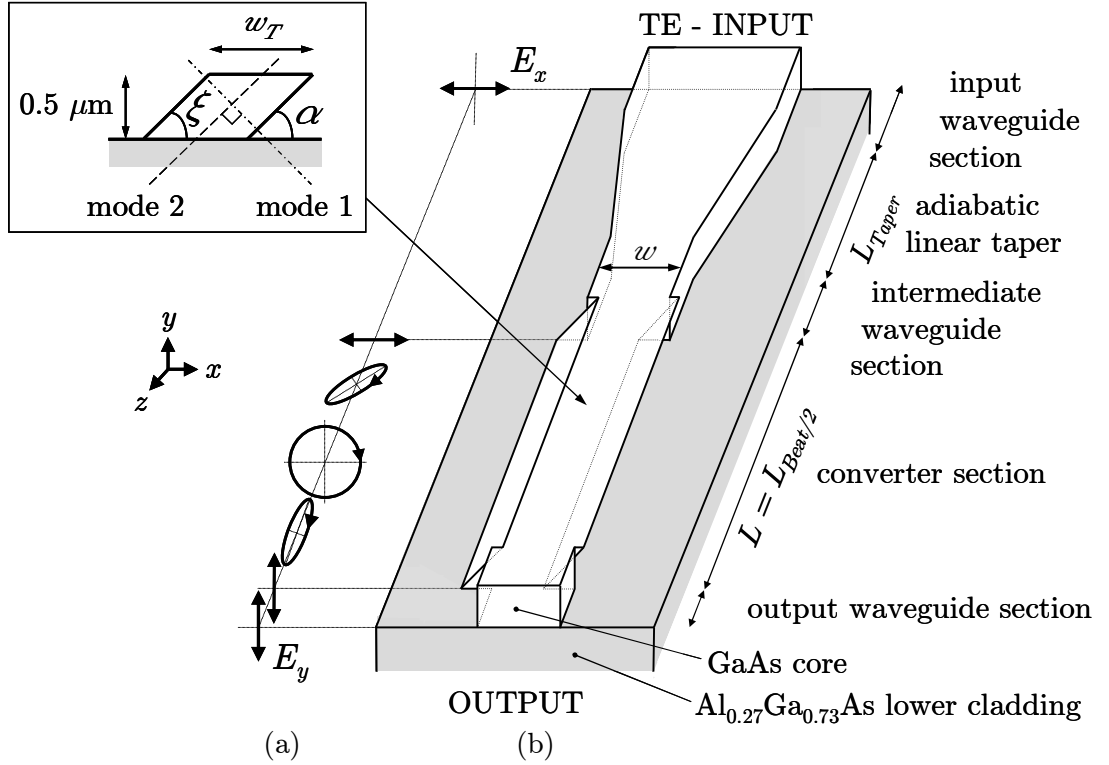


Figure 5-1: Schematic of the design and functionality of the integrated polarisation converter (a) Evolution of the polarisation state of a TE polarised input signal in the device. (b) Device configuration (not to scale). (Insert) Waveguide profile of the converter section defined by the front slope angle ξ , undercut slope angle α and waveguide top width w_T . The orientations of the optical axes, which determine the orientation of the excited lowest order modes (mode 1 and mode 2), are indicated by the chain dotted line (mode 1) and dashed line (mode 2).

and minimises coupling losses. The length of the symmetric intermediate waveguide section was chosen to be $20 \mu\text{m}$. This is a long enough distance not only for the field distributions to level off in the waveguide, but also to avoid the converter section mask alignment to overlap onto the taper section. The asymmetry of the converter section waveguide core profile is characterised by the angles of the sloped sidewalls (front slope angle ξ and undercut slope angle α) and the waveguide top width w_T . The resulting excited optical modes in the converter section waveguide have both significant TE- and TM polarised components. Hence, a TE (or TM) polarised optical signal launched from the symmetric intermediate waveguide excites two (or more - depending on the dimension of the core profile geometry) modes in the asymmetric converter section waveguide (Figure 5-1(Insert)). (For the demonstration of the concept and functionality of the device, only the case of a TE polarised input signal was considered. A TM polarised signal would have an analogous effect on the device functionality.) These two modes propagate with different phase velocities within the asymmetric core according to their different propagation constants (for example $\beta_{\text{mode 1}}$ and $\beta_{\text{mode 2}}$). The *relative* phase difference between these two modes causes the resulting state of polarisation to evolve periodically from an initial linear state through various elliptical states of polarisation as these two modes propagate in the longitudinal direction (Figure 5-1(a)). For two-mode excitation, the maximum orthogonally polarised component - with respect to the input polarisation state - will be developed at odd multiples of the half beat length $L_{\text{Beat}/2}$. This corresponds to the length

over which a *relative* phase difference of 180° between the two excited modes accumulated. The length of the converter section - and therefore $L_{Beat/2}$ - is defined by the intermediate- and output waveguide section. The length of the output waveguide section is determined by the cleaving process and is about $100\ \mu\text{m}$.

5.2 Device optimisation

The crucial core profile parameters in the design of this device are the waveguide width w of the intermediate- and output waveguide sections as well as both sidewall slope angles ζ and α and the waveguide top width w_T of the converter section. At this stage it has to be mentioned that, unless otherwise stated in this chapter, the operating wavelength was set to $\lambda = 1064\ \text{nm}$. This value was chosen according to the emitting wavelength of an available *diode pumped solid state* (DPSS) Nd:YAG laser, which was used as a signal source (see chapter 4). The modelled waveguide layer dimensions of the symmetric stripe waveguide and the asymmetric converter section waveguide as well as the corresponding computational window Ω_W are shown in Figure 5-10. The calculations were conducted with a commercially available FEM based mode solver of which the computational settings were introduced in chapter 2.

5.2.1 Optimisation of the waveguide width w

The width w of the symmetric stripe waveguide in the intermediate- and output waveguide section determines the excitation of guided modes in the waveguide core. The cut-off condition for a certain guided mode is given in good approximation by the one for slab waveguides. In general, the refractive index of the waveguide core material is much closer in value to that of the lower cladding than to the upper cladding (here: air). Cut-off therefore occurs when the effective refractive index n of the guided mode in the waveguide core approaches the value of the refractive index of the lower cladding material at a given wavelength. Figure 5-2 illustrates the w - dependence of the effective refractive indices of the *excited guided modes* in a symmetric stripe waveguide. The horizontal dashed line indicates the refractive index n of the lower cladding material ($\text{Al}_{0.27}\text{Ga}_{0.73}\text{As}$) at the given wavelength ($\lambda = 1064\ \text{nm}$) (here: $n = 3.306$) and represents the cut-off condition for the excited guided modes in the waveguide. Single mode propagation in the symmetric intermediate- and output waveguide section is given in the range of $0.65\ \mu\text{m} < w < 1.32\ \mu\text{m}$. Within this range, a fundamental TE (TE_0) or TM (TM_0) mode is launched from the intermediate waveguide section into the converter section. This wide range allows an optimisation of the overlap of the mode profile distribution at the intersection to and from the converter waveguide section in order to minimise the optical coupling loss.

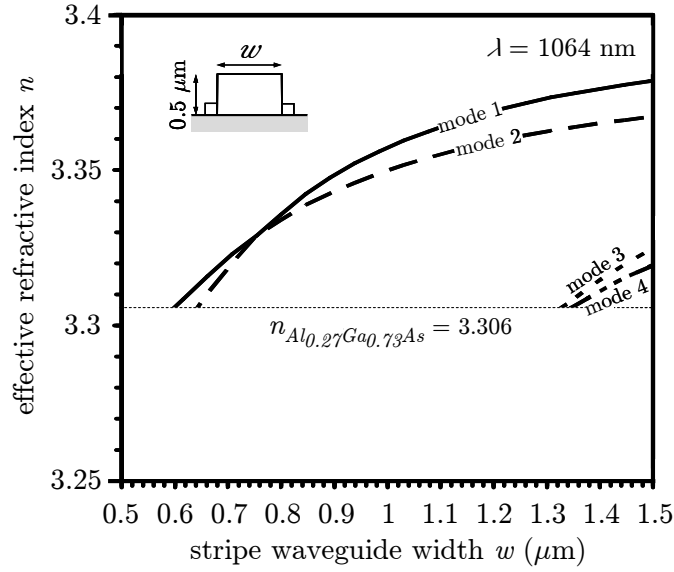


Figure 5-2: Effective refractive index of the excited guided modes in a symmetric stripe waveguide versus the waveguide width w for an operating wavelength $\lambda = 1064$ nm.

5.2.2 Optimisation of the waveguide top width w_T

At first, the influence of w_T on the device parameters such as $L_{Beat/2}$, κ , δ and P_C was investigated. This is shown in Figure 5-3. Figure 5-3(a) illustrates the w_T - dependence of the effective refractive indices of the excited modes in asymmetric stripe waveguides. In order to obtain an overall trend, the two considered waveguide profile geometries consisted of equal values for both ξ and α ($\xi = \alpha = 60^\circ$ (solid line) and $\xi = \alpha = 45^\circ$ (dashed line)). The horizontal dashed line indicates the refractive index of the lower cladding material ($\text{Al}_{0.27}\text{Ga}_{0.73}\text{As}$) at the given wavelength ($\lambda = 1064$ nm) (here: $n = 3.306$) and represents the cut-off condition for the excited guided modes in the waveguide. An excitement of the two lowest order modes (mode 1 and mode 2) in the asymmetric converter section (single mode propagation) is initiated for $w_T > 0.7 \mu\text{m}$ (for $\xi = \alpha = 60^\circ$) and $w_T > 0.8 \mu\text{m}$ (for $\xi = \alpha = 45^\circ$). These cut-off limits are indicated by dotted vertical lines in Figure 5-3(a)-(c).

Considering the dependence of $L_{Beat/2}$ and κ on w_T , as shown in Figure 5-3(b), it can be noted that, for $\xi = \alpha = 60^\circ$, $L_{Beat/2}$ increases as w_T decreases from large values. However, as the decrease of w_T approaches the cut-off limit, $L_{Beat/2}$ decreases as well. For $\xi = \alpha = 45^\circ$, $L_{Beat/2}$ decreases as w_T decreases and approaches the cut-off limit. The power overlap κ on the other hand increases for both waveguide geometries as the w_T - decrease approaches the cut-off condition. In the case for $\xi = \alpha = 60^\circ$, κ almost approaches its optimum value of 0.5 ($\kappa = 0.44$) closely above the cut-off limit ($w_T = 0.7 \mu\text{m}$).

A similar behaviour for both δ and P_C can be depicted in Figure 5-3(c). Again, as the w_T - decrease approaches the cut-off limit, δ and P_C tend towards their optimum of 45° and 100%, respectively. In the case for $\xi = \alpha = 45^\circ$, P_C reaches its best possible value of 85% with $\delta = 78^\circ$ at $w_T = 0.8 \mu\text{m}$. For $\xi = \alpha = 60^\circ$ and $w_T = 0.72 \mu\text{m}$, however, P_C even achieves 98% with a corresponding δ of 49° .

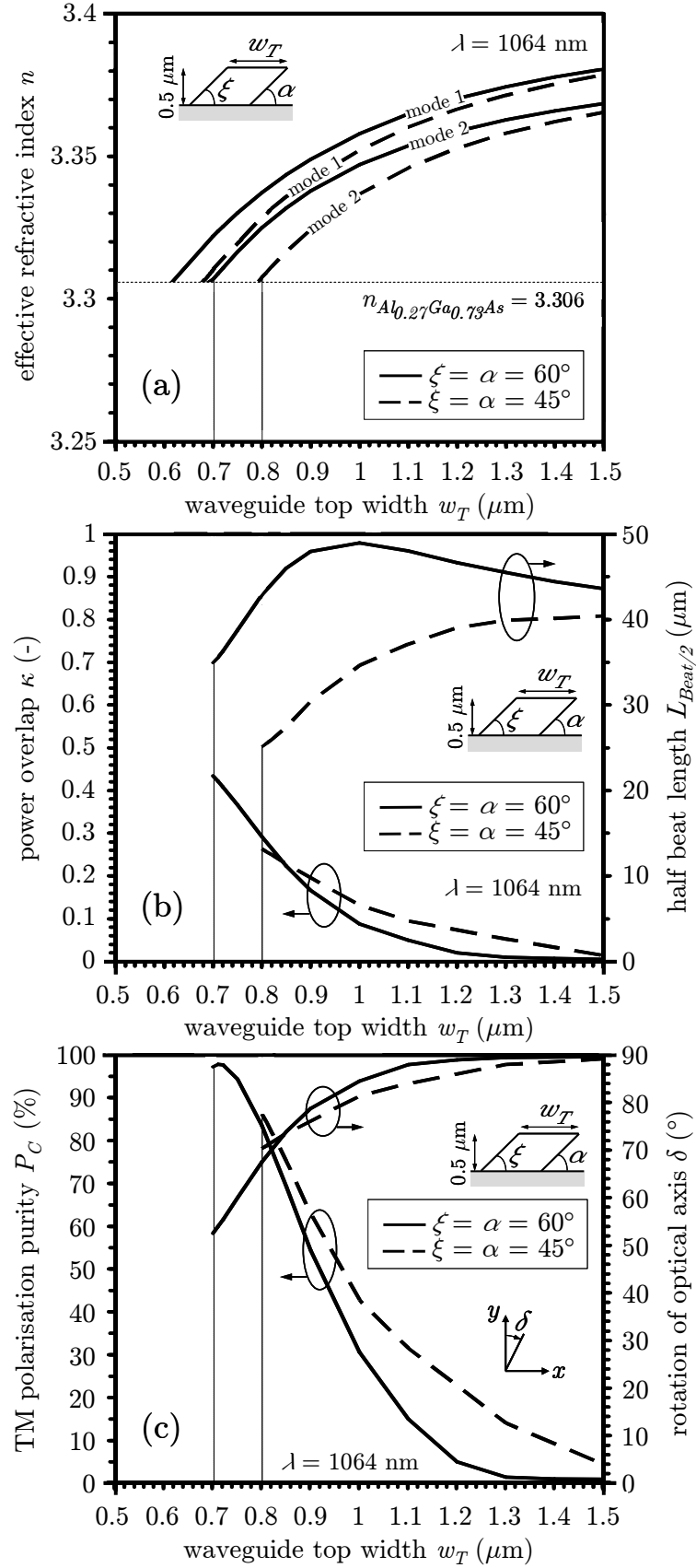


Figure 5-3: (a) Effective refractive index of the excited guided modes in an asymmetric ($\xi = \alpha = 60^\circ$ and $\xi = \alpha = 45^\circ$) stripe waveguide versus the waveguide top width w_T . (b) Power overlap κ and half beat length $L_{\text{Beat}/2}$ of an asymmetric ($\xi = \alpha = 60^\circ$ and $\xi = \alpha = 45^\circ$) stripe waveguide versus the waveguide top width w_T . (c) Rotation of optical axis δ with respect to the vertical axis and TM polarisation purity P_C of an asymmetric ($\xi = \alpha = 60^\circ$ and $\xi = \alpha = 45^\circ$) stripe waveguide versus w_T . ($\lambda = 1064 \text{ nm}$).

The overall trend of these performance influencing parameters is that they obtain their best possible values for w_T - dimensions closely above the second lowest order mode cut-off limit - determined by the refractive index of the (in this case only lower) cladding material. This indicates that the excited higher order modes in the asymmetric waveguide structure are not contributing to the functionality of the device at all.

As the optimum operating point (maximum P_C) of this device design is close to the mode-cut-off dimension of the waveguide, the mode field distribution will be close to the waveguide sidewalls. That can make this design very vulnerable to occurring waveguide sidewall roughness - resulting in an optical power loss.

Figure 5-4 illustrates an overview of the optimised converter waveguide top width w_T - dependence on both ξ ($30^\circ < \xi < 90^\circ$) and α ($30^\circ < \alpha < 90^\circ$) for an operating wavelength of $\lambda = 1064$ nm. The optimised w_T values range from $0.25 \mu\text{m}$ (for $\xi = 30^\circ$, $\alpha = 90^\circ$) to about $1.35 \mu\text{m}$ (for $\xi = 90^\circ$, $\alpha = 30^\circ$).

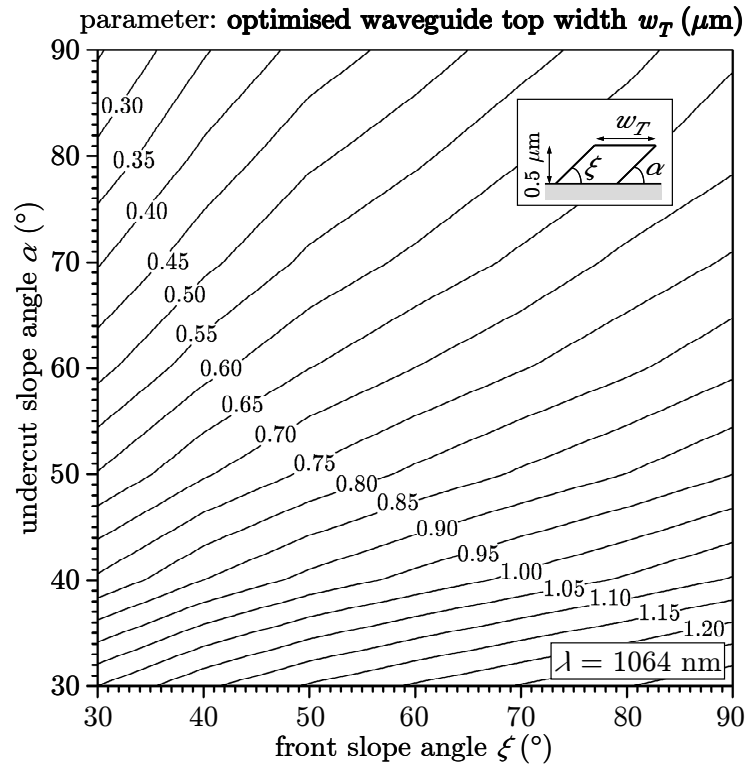


Figure 5-4: Simulated dependence of the optimised waveguide top width w_T on both the front slope angle ξ and undercut slope angle α for an operating wavelength $\lambda = 1064$ nm.

5.2.3 Optimisation of the front slope angle ξ and undercut slope angle α

Based on the evaluated optimum values of w_T for both ξ and α within a range of 30° to 90° , the examined device performance influencing parameters are shown in Figure 5-5 to Figure 5-8. Figure 5-5 displays the evaluated optimum w_T and corresponding $L_{Beat/2}$ values for best possible device performance at given values for both ξ and α . The optimum values for both κ and δ (0.5 and 45° , respectively) occur in a hyperbolic-shaped “corridor”. ξ and α values span from $\xi = 43^\circ$ & $\alpha = 90^\circ$ over $\xi = 62^\circ$ & $\alpha = 62^\circ$ to $\xi = 90^\circ$ & $\alpha = 58^\circ$, as indicated by the chain-dotted line in Figure 5-6 and Figure 5-7, respectively. This corridor is also observed in the contour plot of the P_C dependence on both ξ and α at optimised w_T values (Figure 5-8). P_C values of up to 99% are achieved.

From the fabrication tolerance point of view it can also be noted that at a deviation of both ξ and α by $\pm 10^\circ$ from their optimum values occurs a maximum P_C - degradation of about 10%.

Certain applications, such as an integrated optical isolator [13], require passive polarisation rotators that provide a P_C of only 50%. This device functionality can be realised by considering the contour line for $P_C = 99\%$ and selecting the corresponding values for both ξ and α in Figure 5-8 and determining - in this case - the required $L_{Beat/4}$ from Figure 5-5.

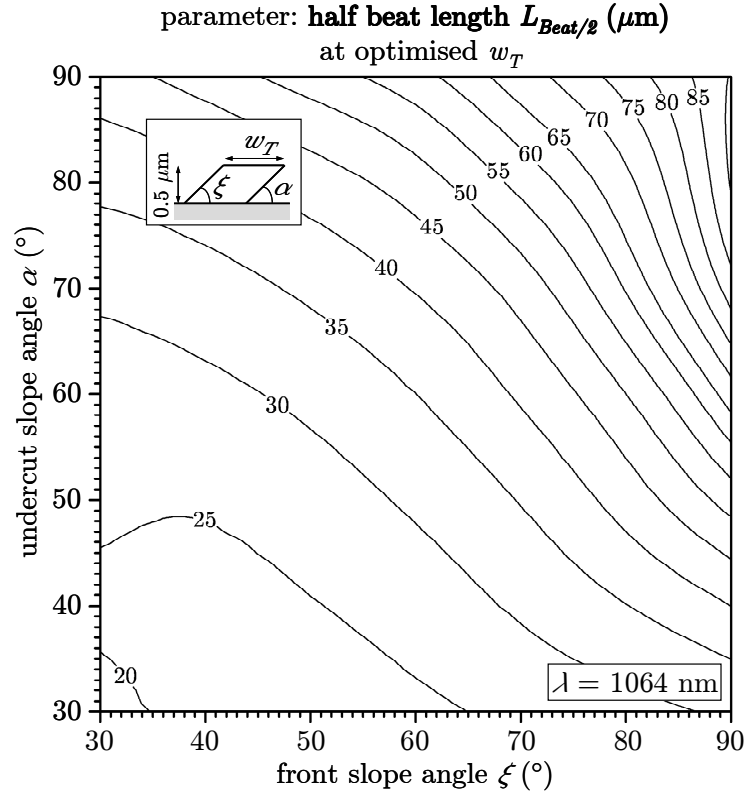


Figure 5-5: Simulated corresponding half beat length $L_{Beat/2}$ for the optimised waveguide top width w_T dependent on both the front slope angle ξ and undercut slope angle α for an operating wavelength of $\lambda = 1064 \text{ nm}$.

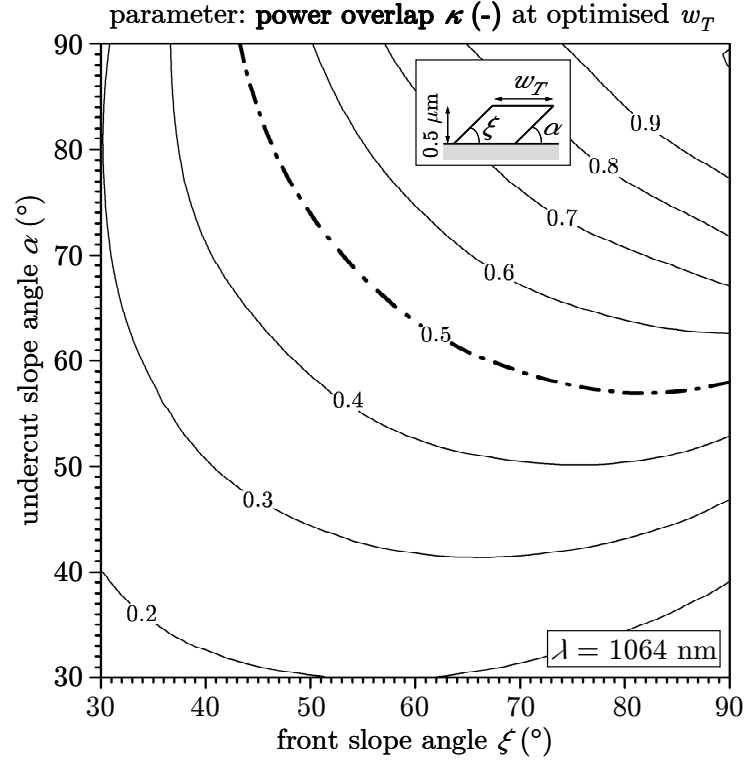


Figure 5-6: Simulated dependence of the power overlap at optimised w_T on both the front slope angle ξ and undercut slope angle α for an operating wavelength $\lambda = 1064 \text{ nm}$.

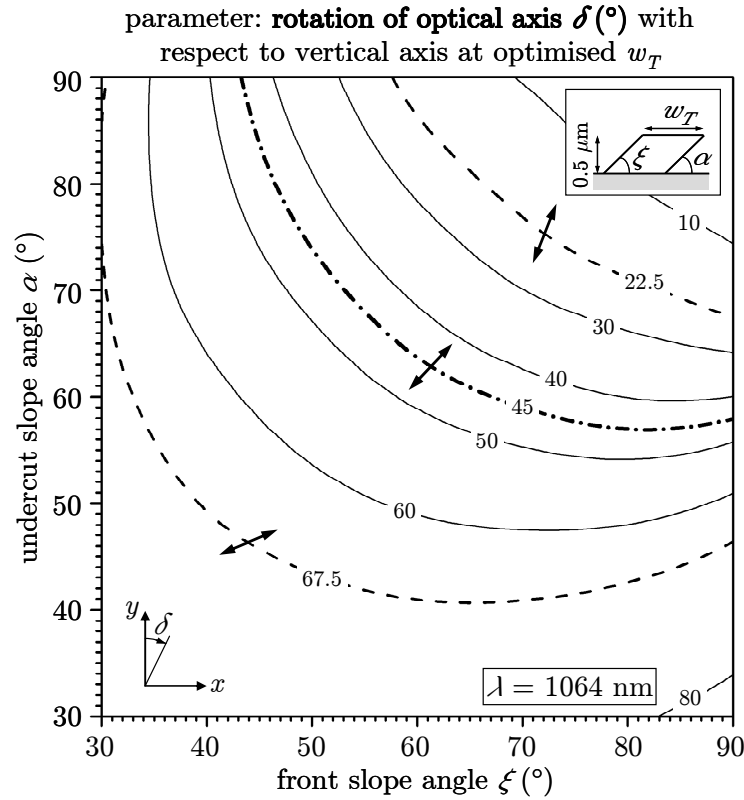


Figure 5-7: Simulated rotation of the optical axis δ with respect to the vertical axis at optimised waveguide top width w_T dependent on both the front slope angle ξ and undercut slope angle α for an operating wavelength of $\lambda = 1064 \text{ nm}$.

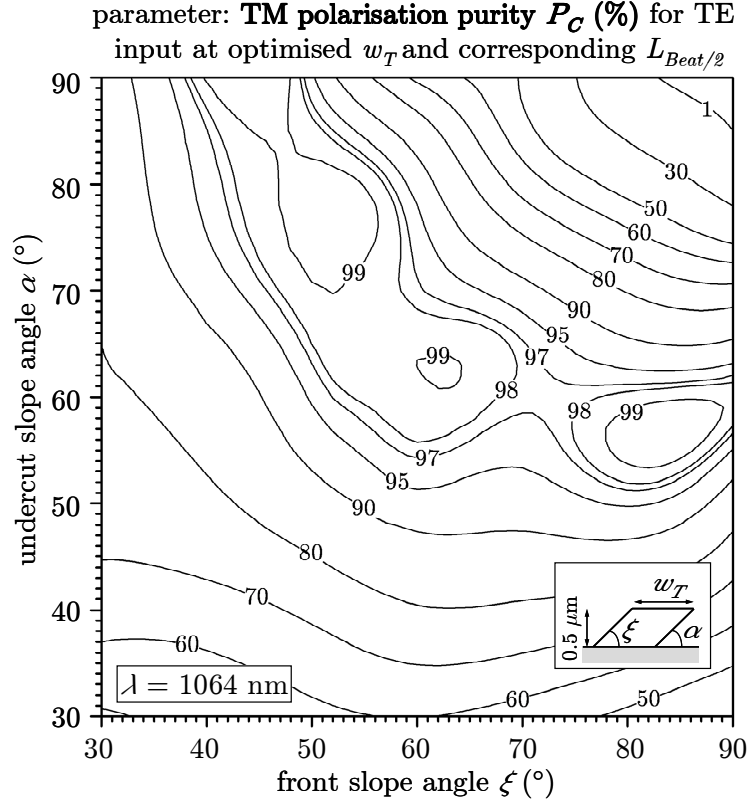


Figure 5-8: Dependence of the simulated TM polarisation purity for a TE polarised input signal at optimised w_T and device length of corresponding $L_{Beat/2}$ on both the front slope angle ξ and undercut slope angle α for an operating wavelength of $\lambda = 1064 \text{ nm}$.

5.2.4 Optimisation of the taper section length L_{Taper}

The length of the taper between the input waveguide ($w = 3 \mu\text{m}$) and the intermediate waveguide has to be optimised for minimum power loss through the taper sidewalls. In section 5.2.1, the minimum width w of the intermediate waveguide - for providing single mode propagation - was determined to be $w = 0.65 \mu\text{m}$. The taper becomes effectively loss-less, or “adiabatic“, as the power lost through the sidewalls decreases as the taper length increases [14].

The optimisation was conducted by utilising the wave propagation calculation module that comes with the commercially available mode solver mentioned above. As the TE polarised input power was kept constant, the transmitted TE_0 mode power - depending on the length of the linear taper L_{Taper} - was monitored and normalised to the TE_0 mode power at the input (Figure 5-9). The insert in Figure 5-9 illustrates the top view of the modelled taper configuration.

The linear taper shows an almost adiabatic behaviour for $L_{Taper} \geq 60 \mu\text{m}$ as the loss is $\leq 0.05 \text{ dB}$. Hence, in order to assure an almost loss-less coupling of the launched input signal from the input waveguide section through the taper section into the intermediate waveguide section, a taper length of $L_{Taper} = 70 \mu\text{m}$ was chosen.

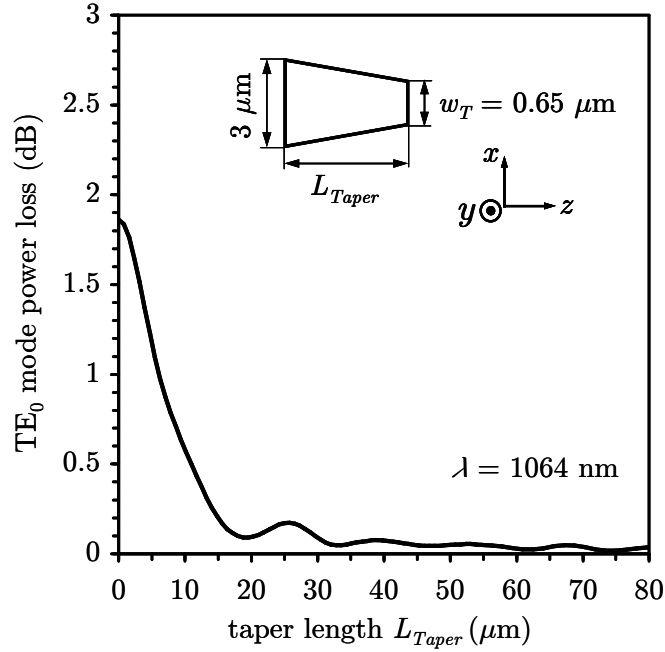


Figure 5-9: Optical power loss of the fundamental TE mode (TE_0) versus the taper length L_{Taper} ($\lambda = 1064$ nm).

5.2.5 Optimisation of the transversal offset τ

Figure 5-10 displays the contour plots of the mode profile (magnitude of the E_x component) at both the end of the intermediate waveguide section ($L = 0^-$ (grey line)) and the beginning of the converter waveguide section ($L = 0^+$ (dashed line)). The unoptimised overlap of both mode profiles due to different waveguide cross section geometries causes an optical loss at the intersection. In order to optimise the mode profile overlap, a transversal converter section offset τ was introduced. A zero-offset corresponds to the lateral alignment of the top edge of the sloped converter section sidewall (defined by the front slope angle ξ) with the vertical sidewall of the intermediate- (or output-) waveguide section. The cross-sectional view of the intersection at $\tau = 0$ is also illustrated in Figure 5-10. A positive value for τ corresponds to a shift of the converter section towards the positive x -direction, whereas the intermediate- (or output-) waveguide section remains in place. There are various combinations of ξ and α to achieve P_C values close to the optimum (100%) - especially the one for $\xi = \alpha = 62^\circ$, as shown in Figure 5-8. This converter section profile geometry was depicted in order to investigate the impact of τ on the intersection loss at different values for the intermediate- (or output-) waveguide width w . While the corresponding optimised w_T for $\xi = \alpha = 62^\circ$ was kept constant at $w_T = 0.71$ μm , both τ and w ($w \geq 0.65$ μm - in order to provide single mode propagation) were varied (Figure 5-10).

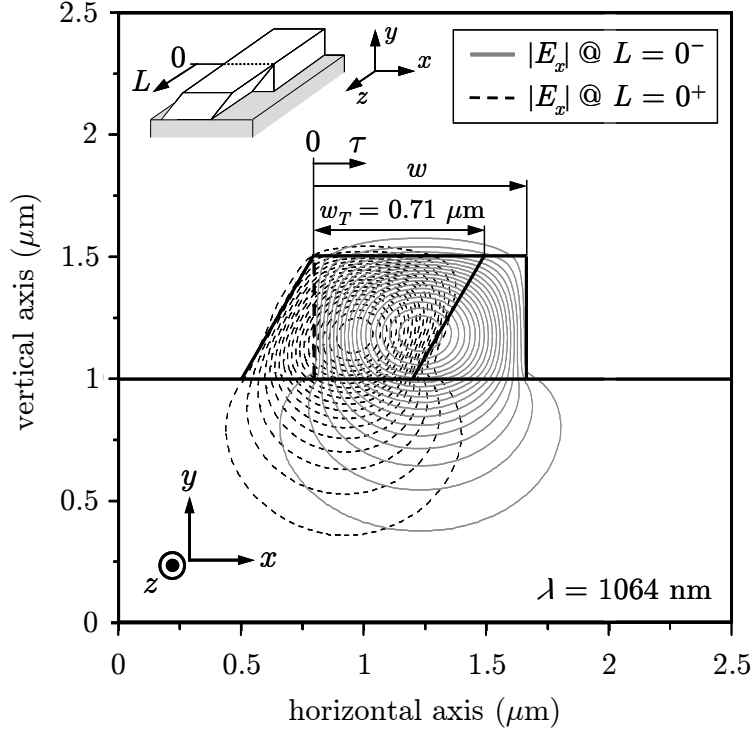


Figure 5-10: Illustration of the overlap of the mode profile contour plots (here: magnitude of the E_x component for the case of a TE polarised input signal) directly before ($L = 0^-$ (grey line)) and directly after ($L = 0^+$ (dashed line)) the intersection between converter- and intermediate- (or output-) waveguide section.

The optimisation was conducted in the same manner as the taper length L_{Taper} optimisation by utilising the wave propagation calculation module that comes with the commercially available mode solver. The modelled waveguide section configuration is illustrated in Figure 5-10(Insert). As the TE polarised input power (P_{INPUT}) was kept constant, the transmitted power (P_{OUTPUT}) - depending on both the transversal offset τ and the intermediate- (or output-) waveguide width w - was monitored and normalised to the input power. The intersection loss was defined as $-10 \times \log_{10}(P_{OUTPUT}/P_{INPUT})$ (in dB). The contour plot in Figure 5-11 illustrates the dependence of the intersection loss on both the transversal offset of the converter section and the intermediate- (or output-) waveguide width w . Without an introduction of τ , intersection loss values > 1.5 dB would occur. At an offset τ of about $0.23 \mu\text{m}$ and $w = 0.65 \mu\text{m}$, however, intersection loss values < 0.16 dB can be achieved. Considering the scenario for $w = 0.9 \mu\text{m}$, the intersection loss decreases by more than 3 dB at an offset of $\tau = 0.3 \mu\text{m}$ in comparison to the zero-offset configuration. This demonstrates the necessity of the introduction of a transversal offset of the converter section waveguide in order to optimise the mode profile overlap and therefore minimise the optical loss at the intersections.

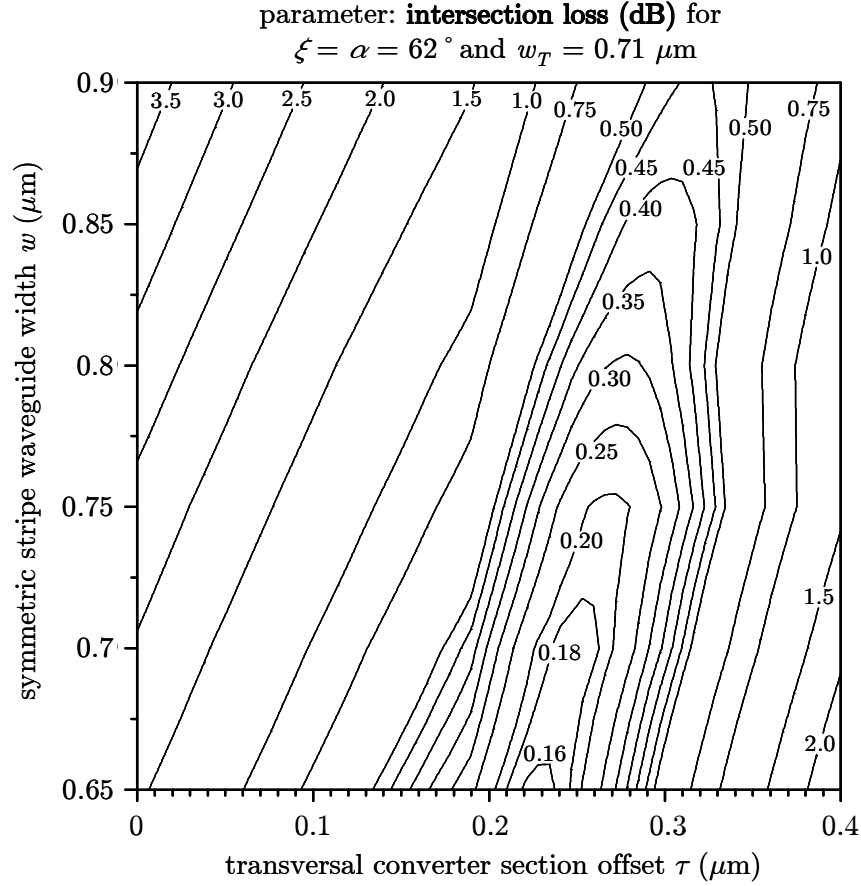


Figure 5-11: Dependence of the intersection loss on the symmetric stripe waveguide width w and the transversal converter section offset τ at the intersection between intermediate- (or output-) waveguide section and converter waveguide section at an operating wavelength of $\lambda = 1064 \text{ nm}$.

5.3 Analysis of the optimised converter section

One of the optimised device dimensions at the given wafer material structure for a maximum achievable TM polarisation purity P_C of $> 99\%$ at the output are $w_T = 0.71 \mu\text{m}$, $L_{\text{Beat}/2} = 37 \mu\text{m}$ and $\xi = \alpha = 62^\circ$ for an operating wavelength $\lambda = 1064 \text{ nm}$. Figure 5-12 to Figure 5-15 illustrate the electric and magnetic, respectively, vector field plots and their corresponding mode profile and contour plot of the transverse (x, y) components of both fundamental modes (mode 1, mode 2) for the optimised waveguide cross section profile. As the relations of the magnetic field are analogous to the electric field, only the electric field was considered for analysis. The electric field vectors of both orthogonal modes in the waveguide core area, which are parallel to the optical axes, are, as desired, at an angle of 45° with respect to the vertical axis (Figure 5-12(c) and Figure 5-13(c)). Each mode has a similar profile of their horizontal (E_x (TE)) (Figure 5-12(d) and Figure 5-13(d)) and vertical (E_y (TM)) (Figure 5-12(b) and Figure 5-13(b)) component as well as an approximately equal field distribution between them. It can be noted from the contour plots, that the evanescent tails of the E_x (Figure 5-12(e) and

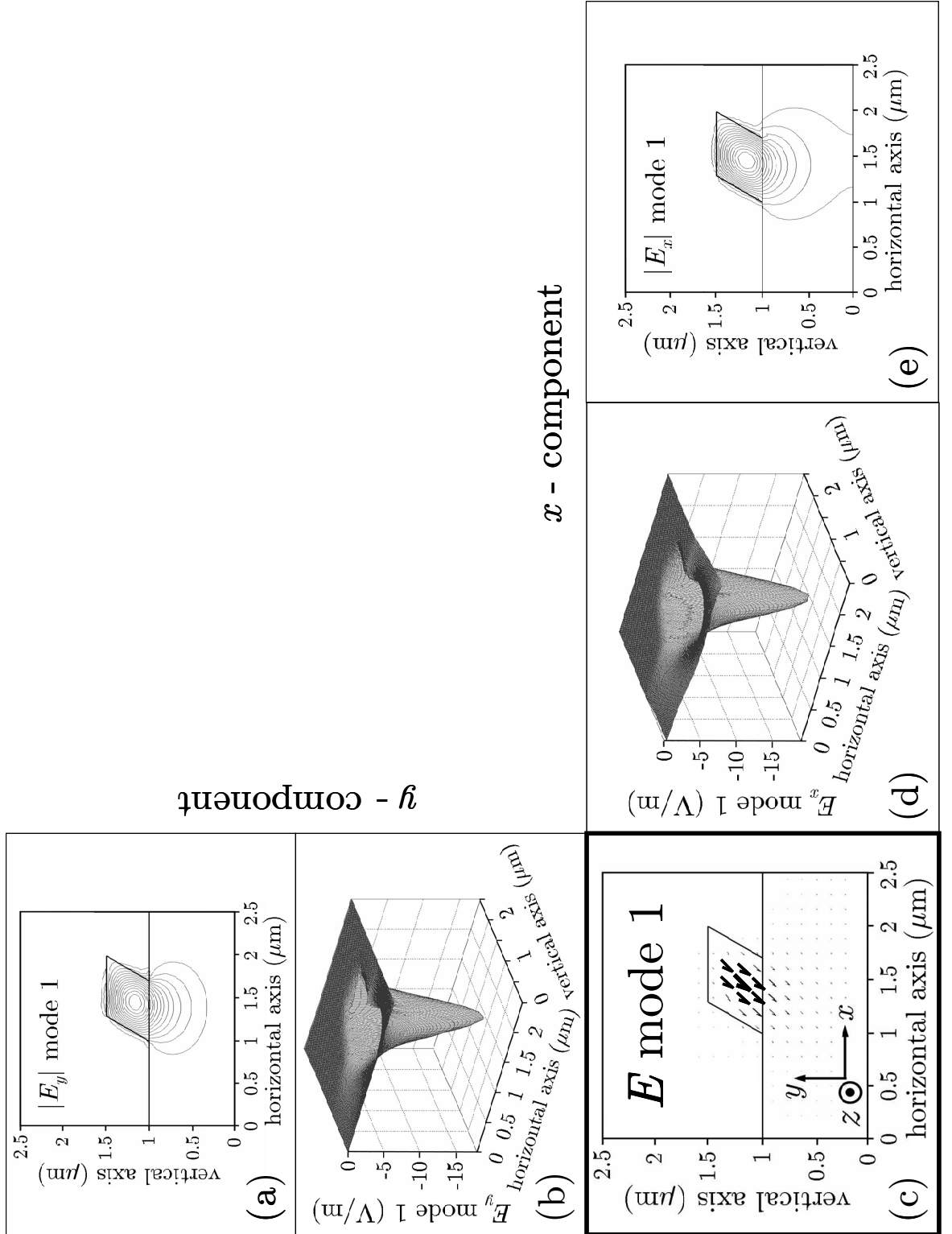


Figure 5-12: (a)-(e) Electric vector field plot and corresponding mode profile and contour plot of the transverse (x, y) components of fundamental mode 1 in the optimised asymmetric waveguide. The structure comprises a front slope angle ξ and an undercut slope angle α of both 62° with respect to the horizontal axis and a waveguide top width w_T of 710 nm in the core profile for an operating wavelength $\lambda = 1064$ nm.

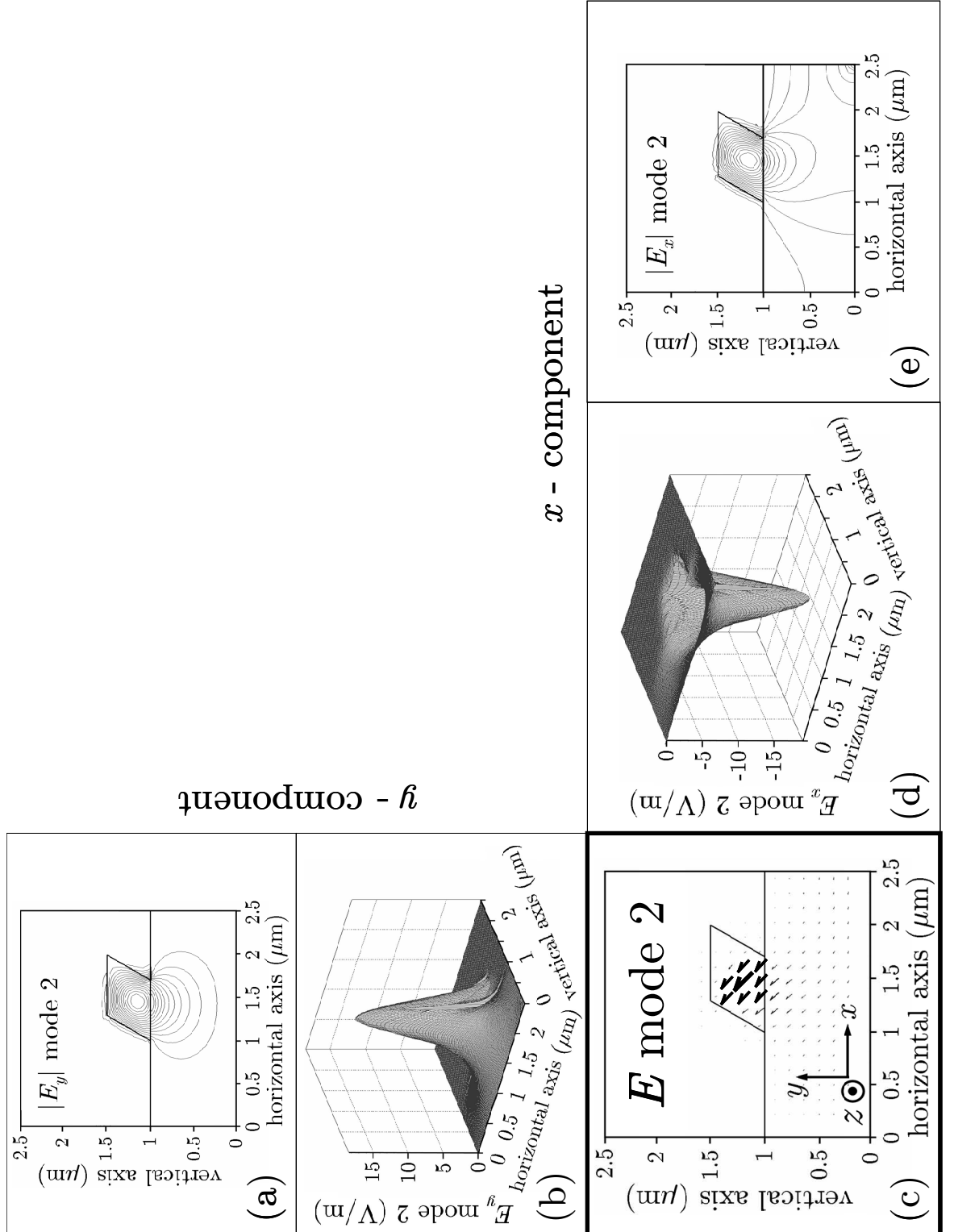


Figure 5-13: (a)-(e) Electric vector field plot and corresponding mode profile and contour plot of the transverse (x , y) components of fundamental mode 2 in the optimised asymmetric waveguide. The structure comprises a front slope angle ζ and an undercut slope angle α of both 62° with respect to the horizontal axis and a waveguide top width w_T of 710 nm in the core profile for an operating wavelength $\lambda = 1064$ nm.

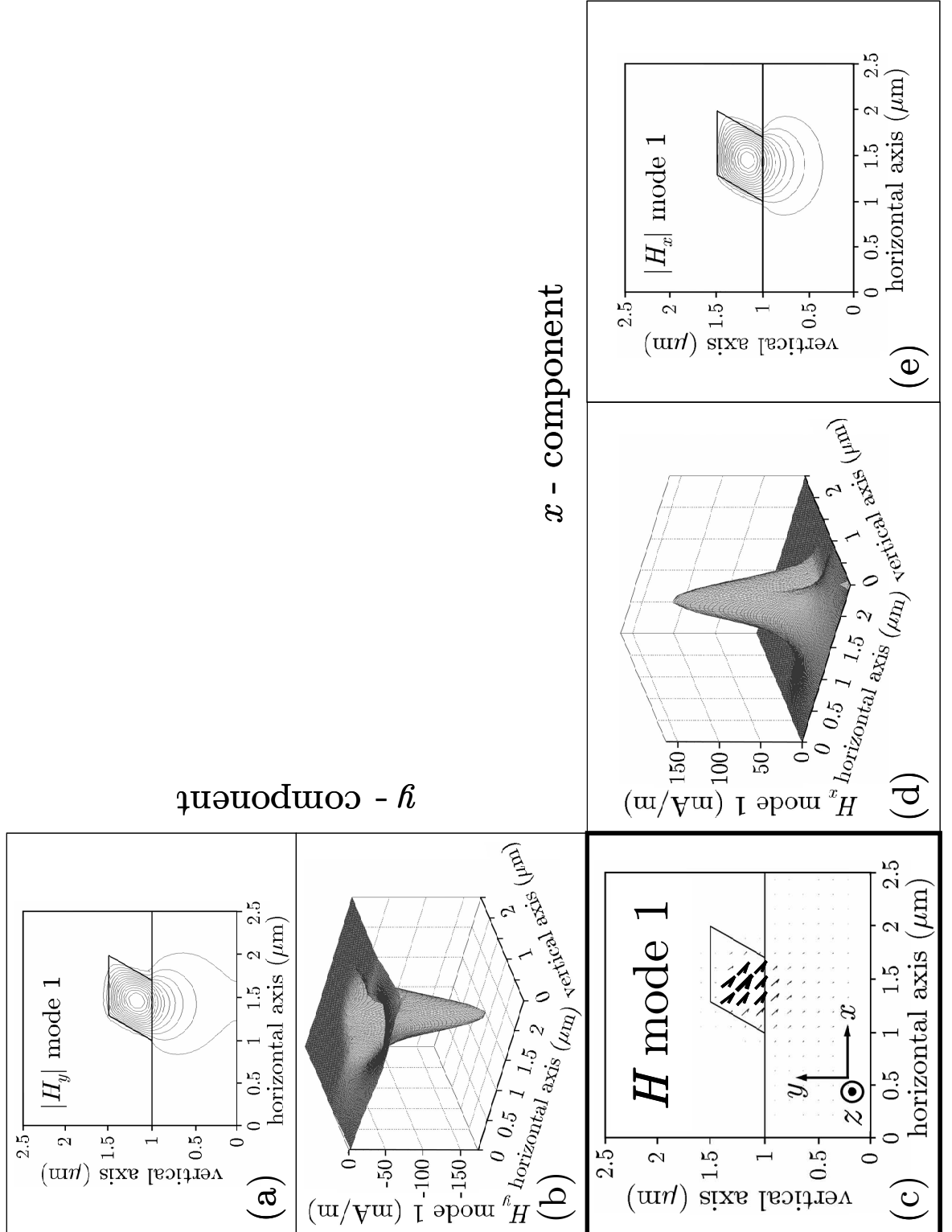


Figure 5-14: (a)-(e) Magnetic vector field plot and corresponding mode profile and contour plot of the transverse (x, y) components of fundamental mode 1 in the optimised asymmetric waveguide. The structure comprises a front slope angle ξ and an undercut slope angle α of both 62° with respect to the horizontal axis and a waveguide top width w_T of 710 nm in the core profile for an operating wavelength $\lambda = 1064$ nm.

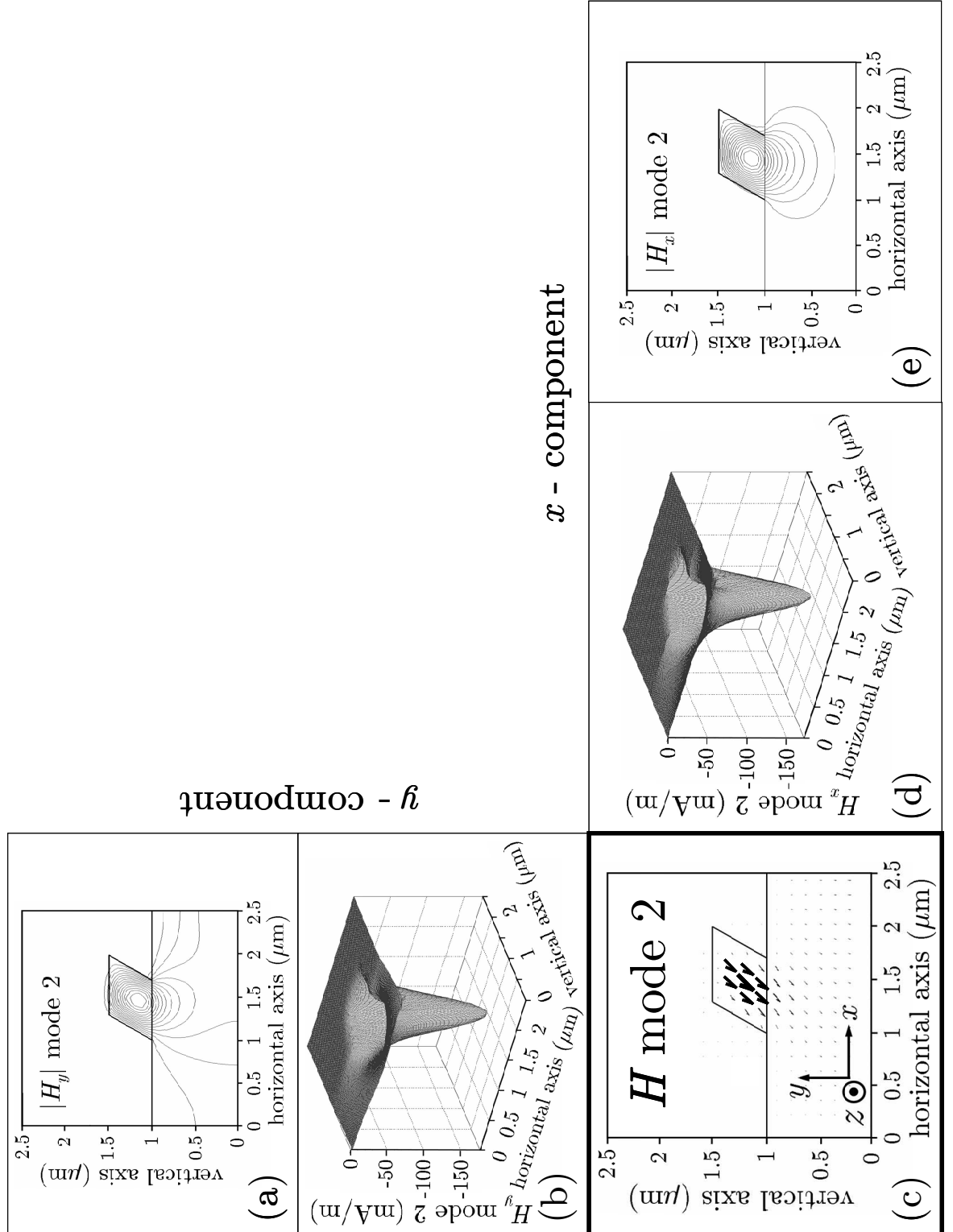


Figure 5-15: (a)-(e) Magnetic vector field plot and corresponding mode profile and contour plot of the transverse (x , y) components of fundamental mode 2 in the optimised asymmetric waveguide. The structure comprises a front slope angle ζ and an undercut slope angle α of both 62° with respect to the horizontal axis and a waveguide top width w_T of 710 nm in the core profile for an operating wavelength $\lambda = 1064$ nm.

Figure 5-13 (e)) (and H_y (Figure 5-12(a) and Figure 5-13(a))) components of both modes penetrate relatively deep into the lower cladding. This indicates that the waveguide profile is close to the cut-off dimensions for both modes. Figure 5-12 to Figure 5-15 show that most of the optical power launched into the converter waveguide section is confined within both lowest order modes in the core area. Only an insignificant amount penetrates into the lower cladding or radiates.

An illustration of the functionality of the optimised converter section is represented in Figure 5-16. It displays the contour plots of the magnitude of both the E_x (TE)- and E_y (TM) components in the converter section as a TE (in this case TE_0 , given by the dimension of w_T) polarised input signal propagates down the device. The interference between the two excited modes (mode 1 and mode 2) results in a harmonic beating pattern of the transversal components with the periodicity of $L_{Beat/2}$. The inserts show the magnitude profiles of both components at the characteristic converter section distances $L = 0 \mu\text{m}$, $L = L_{Beat/4} = 17.5 \mu\text{m}$ and $L = L_{Beat/2} = 35 \mu\text{m}$.

- At $L = 0 \mu\text{m}$, the electric field distribution equals the one of the launched TE polarised signal. Almost all the electric field is contained within the E_x component, whereas the E_y component is insignificant.
- At $L = L_{Beat/4} = 17.5 \mu\text{m}$, the electric field is equally distributed in both components.
- At $L = L_{Beat/2} = 35 \mu\text{m}$, almost all the electric field is contained within the E_y component, whereas the E_x component is insignificant. This corresponds to a TM polarised signal, which is, with the converter length being equal to $L_{Beat/2}$, the desired output characteristic of the device.

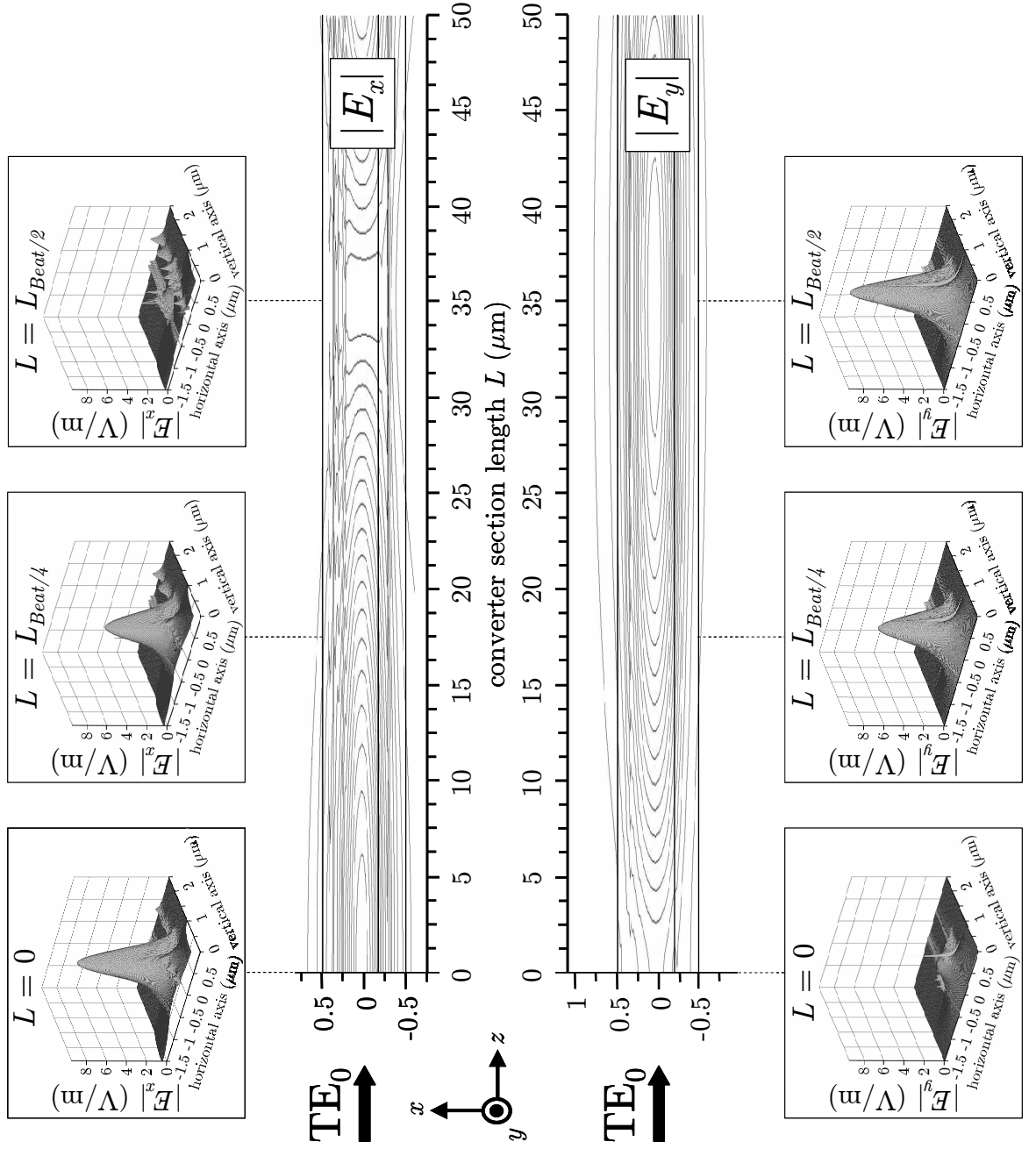


Figure 5-16: Top view of the simulated contour plot of both the E_x (TE) and E_y (TM) component of a TE_0 mode launched from the intermediate waveguide section into the optimised converter section. Inserts: Magnitude of both E_x and E_y components at $L = 0 \mu\text{m}$, $L = L_{Beat}/4 = 17.5 \mu\text{m}$ and $L = L_{Beat}/2 = 35 \mu\text{m}$.

5.4 Device fabrication

5.4.1 Fabrication process steps

Step 1: Creation of e-beam position calibration markers

The standard calibration marker shape is a square with a side length of 20 μm . The marker usually consists of a 100 nm gold (Au) layer on top of a 10 nm titanium (Ti) layer, which acts as a buffer layer to increase the adhesion to the semiconductor surface. The Au surface increases the level of backscattered electrons into the electron detectors in the ebeam-writer and therefore improves the marker detection. The lift-off technique was used to fabricate the marker pattern: The Ti/Au layer was evaporated over a bi-layer of exposed and developed *polymethyl methacrylate* (PMMA) resist mask pattern and the substrate. The PMMA bi-layer thickness had to be greater (600 nm) than that of the deposited Ti/Au layer (110 nm). By selectively dissolving the PMMA bi-layer in acetone, the overlying Ti/Au layer was lifted off and removed, whereas the parts of the Ti/Au layer, which were in contact with the wafer, were left behind. The reason for the PMMA bi-layer is the desire for an undercut resist edge profile in order to establish a successful lift-off process. The two spin-coated resist layers had different molecular weight in their polymer structure. The lower the molecular weight of the polymer, the higher the sensitivity to high energy electron bombardment. Thus, the lower resist layer (500 nm) consisted of lower molecular weight than the upper layer (100 nm) - creating an undercut resist edge profile after the development process.

1. Cleave sample to a suitable size (12 mm \times 10 mm).
2. Clean sample in acetone and *isopropyl alcohol* (IPA) utilising ultrasonic bath for 10 minutes each; Blow dry with nitrogen.
3. Spin-coat 1st. (lower) layer of positive e-beam resist (PMMA 12% ELVACITE® ELV 2010) (low molecular weight) at 5000 rpm for 60 seconds (Figure 5-17(a)).
4. Clean backside of sample with in acetone soaked cotton bud before a 15 minutes bake in the oven @ 180 ° C.
5. Spin-coat 2nd. (upper) layer of positive e-beam resist (PMMA 4% ELV 2041) (higher molecular weight) at 5000 rpm for 60 seconds.
6. Clean backside of sample with in acetone soaked cotton bud before a 2 hours bake in the oven @ 180 ° C.
7. Exposure of e-beam position marker pattern. EBP 5 e-beamwriter control file parameters: resolution: 100 nm, proximity correction file: gaas700-50t.pec, prox min: 1, prox grid: 0.2, dose: 250 $\mu\text{C}/\text{cm}^2$, spot size: 160 nm, job type: simple.
8. Development of e-beam position marker pattern using 2:1 IPA:MIBK (*methyl isobutyl ketone*) developer solution for 75 seconds @ 23.1 ° C; Dip in IPA for 10 seconds; Blow dry with nitrogen (Figure 5-17(b)).

9. Evaporation of 20 nm titanium and 100 nm gold layers using Metal Evaporator Plassys 1 (Figure 5-17(c)).
10. Lift-off Ti-Au layer using acetone in a hot water bath (65 ° C) for 2 hours (Figure 5-17(d)).
11. Clean sample subsequent in acetone and IPA using ultrasonic bath for 5 minutes each; Blow dry with nitrogen.

Step2: Creation of the waveguide outline pattern

12. Deposition of 200 nm PECVD SiO₂ (Figure 5-17(e)).
13. Spin-coat positive e-beam resist (PMMA 4% ELV 2041) at 5000 rpm for 60 seconds.
14. Clean backside of sample with in Acetone soaked cotton bud before a 15 minutes bake in oven @ 180 ° C.
15. Spin-coat second positive e-beam resist layer (PMMA 4% ELV 2041) at 5000 rpm for 60 seconds (Figure 5-17(f)).
16. Clean backside of sample with in Acetone soaked cotton bud before a 90 minutes bake in oven @ 180 ° C.
17. Exposure of waveguide outline pattern. EBPG 5 e-beam-writer control file parameters: resolution: 25 nm (high) / 250 nm (low), proximity correction file: gaas200-50b.pec, prox min: 0.1, prox grid: 0.025, dose: 136 $\mu\text{C}/\text{cm}^2$ (high resolution) / 390 $\mu\text{C}/\text{cm}^2$ (low resolution), spot size: 56 nm (high resolution) / 400 nm (low resolution), job type: registration (Figure 5-17(g)).
18. Development of waveguide pattern using 2:1 IPA:MIBK developer solution for 75 seconds @ 23.1 ° C. Dip in IPA for 10 seconds; Blow dry with nitrogen.
19. SiO₂ dry-etch of waveguide pattern using CHF₃ as a reactive gas in the BP80 machine BP80 parameter settings: process gas: CHF₃, corrected gas flow: 20 sccm, process pressure: 17 mTorr, forward RF power: 100 W, temperature: 25 ° C, BIAS: -280 V, process time: 13 minutes (Figure 5-17(h)).
20. Removal of e-beam resist mask via an O₂ ash process using the BP80 machine. BP80 parameter settings: process gas: O₂, corrected gas flow: 20 sccm, process pressure: 20 mTorr, forward RF power: 100 W, temperature: 25 ° C, BIAS: -320 V, process time: 25 minutes (Figure 5-17(i)).

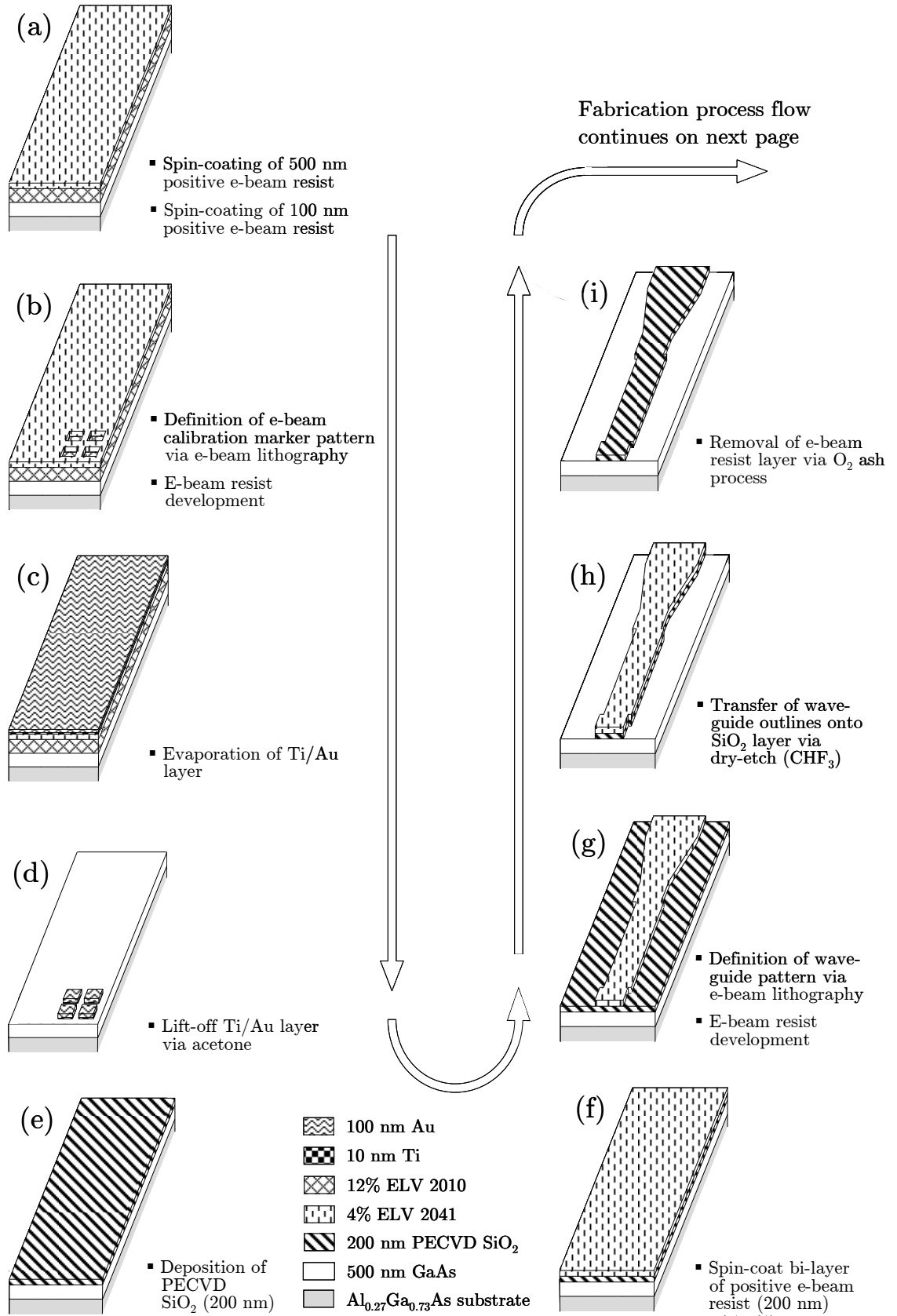


Figure 5-17: (a)-(i) Schematic process flow diagram of the realised polarisation converter device (part 1).

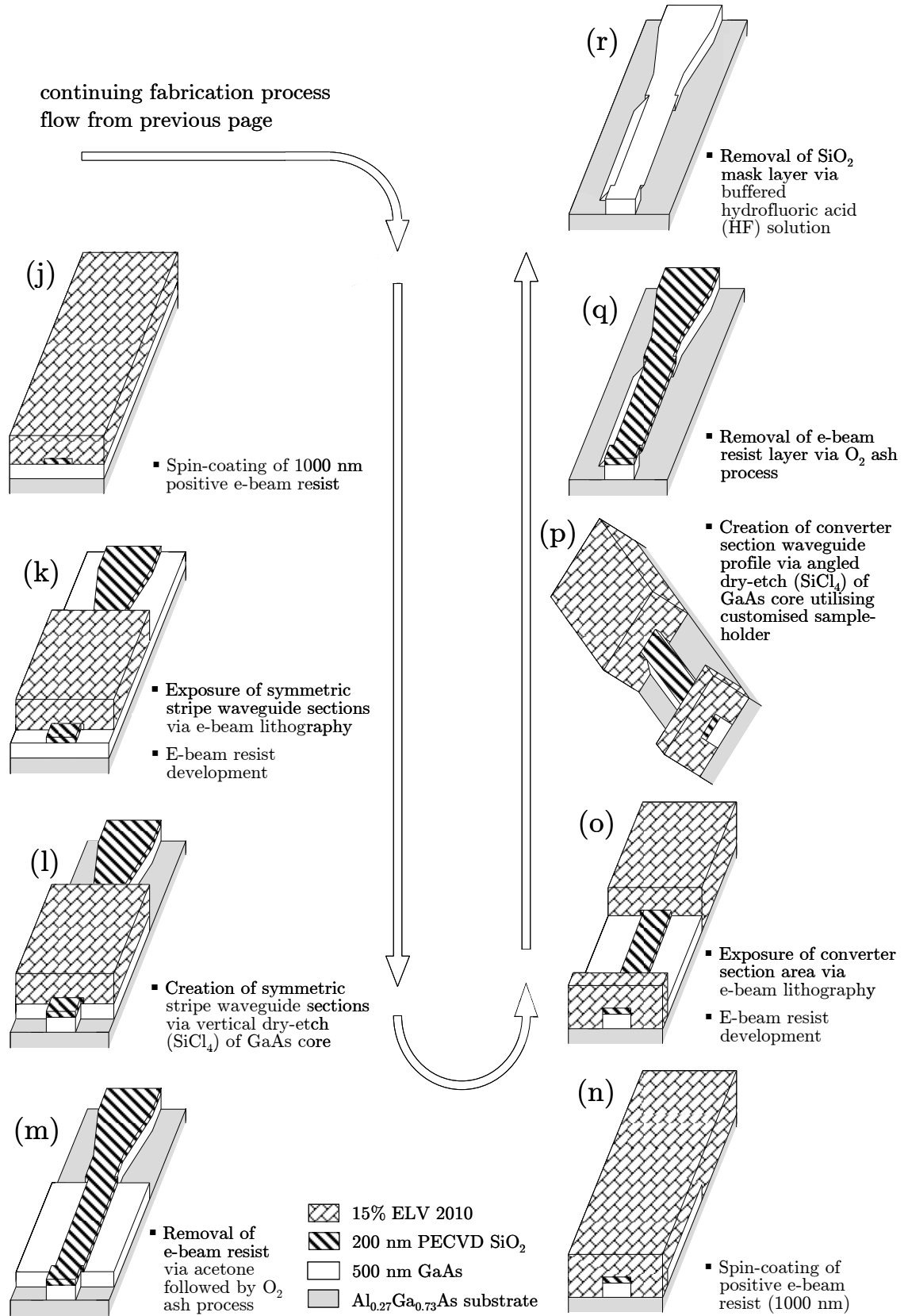


Figure 5-18: (j)-(r) Schematic process flow diagram of the realised polarisation converter device (part 2).

Step3: Realisation of the rib waveguide structure which forms the input waveguide, the adiabatic linear taper, the intermediate waveguide and the output waveguide

21. Spin-coat positive e-beam resist (PMMA 15% ELV 2010) at 5000 rpm for 60 seconds.
22. Clean backside of sample with in acetone soaked cotton bud before a 90 minutes bake in oven @ 180 ° C (Figure 5-18(j)).
23. Exposure of rib waveguide section areas. EBPG 5 e-beam-writer control file parameters: resolution: 25 nm (high) / 250 nm (low), proximity correction file: gaas200-50b.pec, prox min: 0.1, prox grid: 0.025, dose: 270 $\mu\text{C}/\text{cm}^2$ (high resolution) / 490 $\mu\text{C}/\text{cm}^2$ (low resolution), spot size: 56 nm (high resolution) / 400 nm (low resolution), job type: registration (Figure 5-18(k)).
24. Development of waveguide pattern using 2:1 IPA:MIBK developer solution for 75 seconds @ 23.1 ° C. Dip in IPA for 10 seconds; Blow dry with nitrogen.
25. Vertical GaAs dry-etch of the rib waveguide pattern using SiCl_4 as a reactive gas in the S100 machine (Figure 5-18(l)).
S100 chamber clean process parameters: step 1: process gas: H_2 , corrected gas flow: 50 sccm, process pressure: 50 mTorr, forward RF power: 200 W, temperature: 25 ° C, BIAS: -350 V, process time: 20 minutes; step 2: process gas: O_2 , corrected gas flow: 50 sccm, process pressure: 50 mTorr, forward RF power: 100 W, temperature: 25 ° C, BIAS: -200 V, process time: 20 minutes.
Vertical waveguide etch S100 process parameters: process gas: SiCl_4 , corrected gas flow: 18 sccm, process pressure: 9 mTorr, forward RF power: 250 W, temperature: 25 ° C, process time: 5:30 minutes, quartz carrier wafer used.
26. Removal of e-beam resist mask via using acetone in a hot water bath (65 ° C) for 2 hours followed by an O_2 ash process using the BP80 machine (Figure 5-18(m)). BP80 parameter settings: process gas: O_2 , corrected gas flow: 20 sccm, process pressure: 20 mTorr, forward RF power: 100 W, temperature: 25 ° C, BIAS: -320 V, process time: 25 minutes.

Step 4: Realisation of the converter section waveguide structure

27. Spin-coating of positive e-beam resist (PMMA 15% ELV 2010) at 5000 rpm for 60 seconds (Figure 5-18(n)).
28. Clean backside of sample with in acetone soaked cotton bud before a 90 minutes bake in oven @ 180 ° C.
29. Exposure of converter section area (Figure 5-18(o)). EBPG 5 e-beam-writer control file parameters: resolution: 25 nm, proximity correction file: gaas200-50b.pec, prox min: 0.1, prox grid: 0.025, dose: 270 $\mu\text{C}/\text{cm}^2$, spot size: 56 nm, job type: registration.
30. Development of converter waveguide section using 2.5:1 IPA:MIBK developer solution for 30 seconds @ 23.1 ° C and subsequent dip in IPA for 10 seconds; Blow dry with nitrogen.

31. Angled GaAs dry-etch of converter waveguide section using SiCl_4 as a reactive gas in the S100 T-Gate machine (Figure 5-18(p)).
Angled waveguide-etch S100 T-Gate process parameters: process gas: SiCl_4 , corrected gas flow: 9 sccm, process pressure: 9 mTorr, forward RF power: 100 W, temperature: 25°C , BIAS: -346 V, process time: 4:20 minutes, customised anodised aluminium sample holder used (slope angle of sample holder is 65° with respect to the horizontal plane).
32. Removal of e-beam resist dry-etch mask via an O_2 ash process using the BP80 machine (Figure 5-18(q)). BP80 process parameter settings: process gas: O_2 , corrected gas flow: 20 sccm, process pressure: 20 mTorr, forward RF power: 100 W, BIAS: -320 V, temperature: 25°C , process time: 35 minutes.
33. Removal of SiO_2 layer via wet chemical etching using a buffered (hydrofluoric acid) HF:RO (reverse osmosis) water solution (ratio 5:1) for 45 seconds; Rinse thoroughly in RO water for 10 minutes; Blow dry using nitrogen (Figure 5-18(r)).

5.4.2 Fabrication hurdle: mask misalignment

As the proposed device contains both rib waveguide- and asymmetric waveguide sections, attention has to be paid at their intersection during the fabrication process. Both sections are fabricated at different etch steps. This makes a high demand on the accuracy of the (re-)masking alignment in order to prevent unwanted etch-overlaps into these adjacent waveguide sections. A 1000 nm thick layer of e-beam resist was used as the covering mask. This thickness is sufficient in order to cover the waveguide sections which impose a maximum thickness of 500 nm. An e-beam resist thickness of 1000 nm, however, decreases the achievable resolution of the exposed feature patterns in comparison to the 200 nm thick resist layer on which the waveguide outlines were defined (Figure 5-17(g)). On the other hand, a thicker resist layer offers a higher resistance to plasma etching than a thinner one. Usually, a redesign of the etch mask boundary coordinates of the written e-beam pattern - after considering the degradation of the achievable resolution - is conducted. In addition, e-beam position calibration markers are used in order to place the feature pattern, which is supposed to be exposed, at the desired coordinates.

Even by taking all these facts and possible options into consideration at the periphery of the converter section, unwanted etch-overlaps into adjacent waveguide sections due to mask misalignments occurred (Figure 5-19). A vertical etch overlap of about 250 nm from the intermediate waveguide section into the converter section can be depicted in Figure 5-19(b).

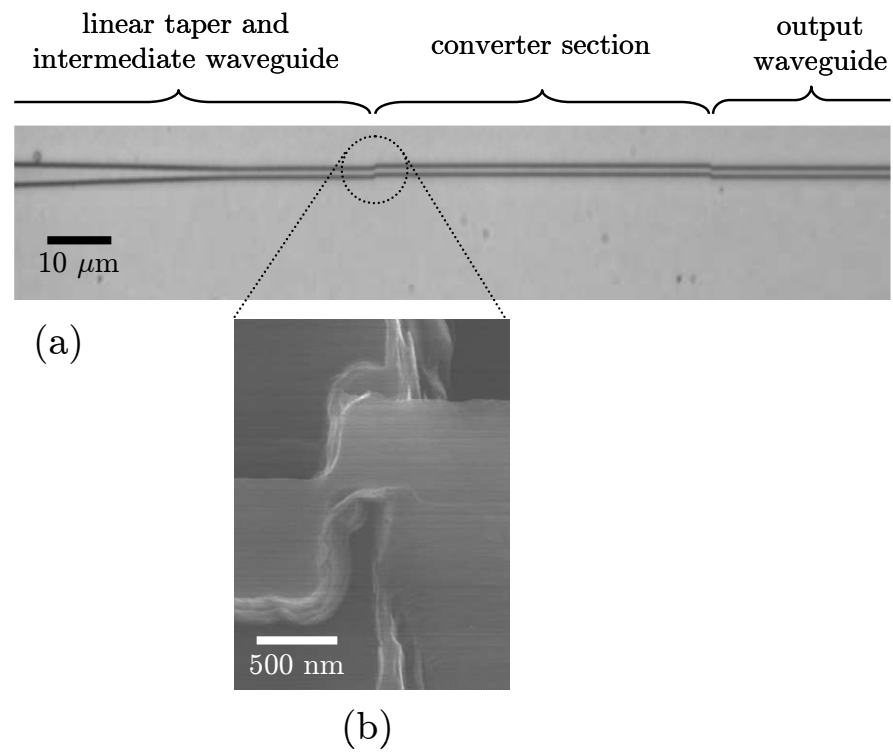


Figure 5-19: Remasking misalignment at the converter section periphery. (a) Optical micrograph of the top view of the device after definition of the waveguide outlines before conducting an etch-step in the fabrication process. (b) SEM micrograph of the top view of the misaligned intersection between the intermediate waveguide section and the converter section of the fabricated device.

5.4.3 Solution to mask misalignment

In order to overcome an unwanted etch overlap into adjacent waveguide sections due to mask misalignments, as shown in the previous section, transversal rib waveguide stripes at the converter section were introduced to the device design (Figure 5-20).

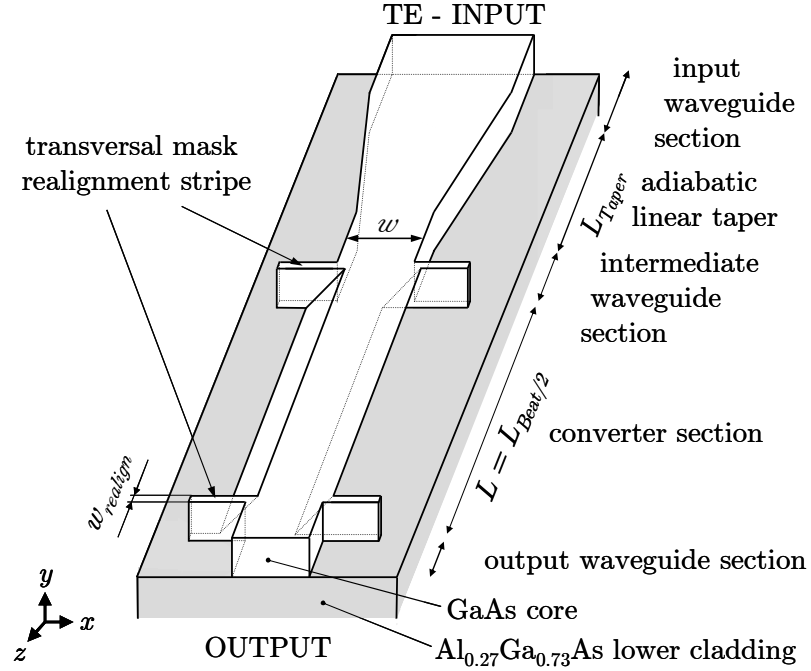


Figure 5-20: Introduction of transversal rib waveguide mask realignment stripes at the converter section periphery in the device design.

The width w_{realign} of the transversal mask realignment stripes at the converter section periphery should provide a buffer-zone to overcome mask (re-)alignment problems on the one hand, but on the other hand not introduce a too high insertion loss. The theoretical optimisation was conducted in an analogous manner to the optimisation of the taper section length L_{Taper} , as described earlier in this chapter. Figure 5-21 illustrates the calculated dependence of the introduced insertion loss on the width w_{realign} of a mask realignment stripe. A stripe width w_{realign} of 250 nm, which would compensate the occurring mask (re-) alignment displayed in the previous section, imposes an insertion loss of about 0.01 dB. In order to allow bigger fabrication tolerances, a stripe width of $w_{\text{realign}} = 500$ nm, which introduces an insertion loss of about 0.04 dB, was chosen in the design of the device.

The fabricated device with an introduced transversal mask (re-)alignment stripe is displayed in Figure 5-22. Figure 5-22(b) shows the SEM micrograph top view of the introduced transversal mask (re-)alignment stripe with a w_{realign} of 500 nm. Both the rib waveguide structure on the left side (which forms the intermediate waveguide section) and the angled etched converter section on the right side were created without etch overlaps. On top of the right half of the (re-)alignment stripe, a vertical remaining mask resist stripe with a width of about 250 nm - resulting from misalignment - can be depicted.

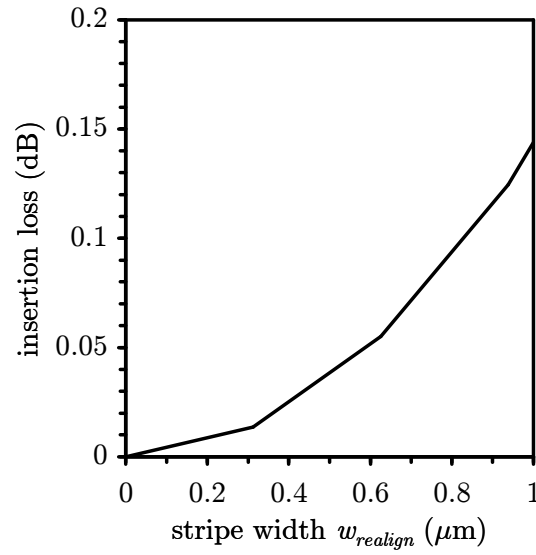


Figure 5-21: Calculated dependence of the occurring insertion loss on the width $w_{realign}$ of the introduced transversal mask realignment stripes.

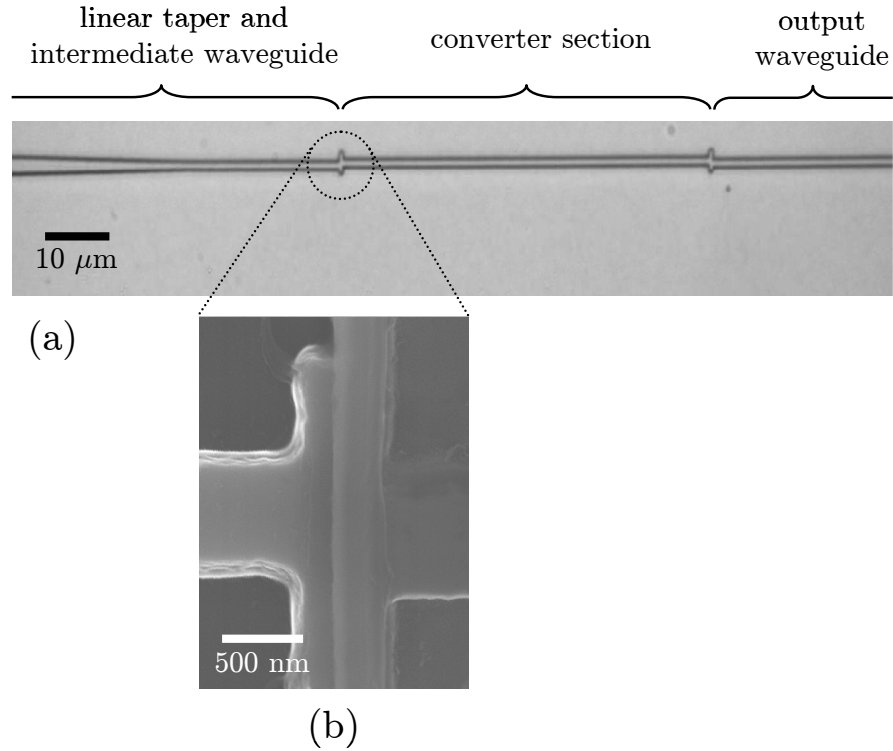


Figure 5-22: Impact of the introduced transversal stripes at the converter section periphery on the mask realignment. (a) Optical micrograph of the top view of the device after definition of the waveguide outlines and before a conducted etch-step in the fabrication process. (b) SEM micrograph of the top view of the intersection between the intermediate waveguide section and converter section of the fabricated device. The introduced transversal mask realignment stripe width $w_{realign}$ is 500 nm.

5.4.4 Realised device

The fabricated waveguide cross section profile of the converter section is shown in Figure 5-23. The profile consists of a front slope angle of $\zeta = 32^\circ$, an undercut angle of $\alpha = 52^\circ$ and a waveguide top width of $w_T = 570$ nm.

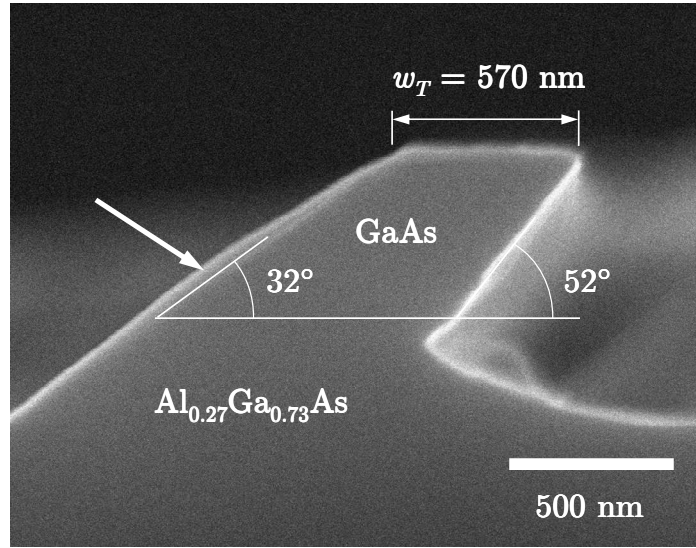


Figure 5-23: SEM micrograph of the fabricated polarisation converter cross section consisting of two slanted sidewalls. The realised front slope angle ζ and undercut slope angle α are about 32° and 52° , respectively, with respect to the horizontal plane. The defined waveguide top width w_T is about 570 nm.

5.5 Device characterisation

5.5.1 Converted TM polarisation purity

Devices consisting of different converter section lengths were fabricated and characterised via the measurement method described in chapter 4. Figure 5-24 displays the dependence of the TM polarisation purity P_C on the converter section length L . The diamond - shaped data points correspond to the measured P_C of the fabricated device. With the fabricated waveguide profile dimensions of $\zeta = 32^\circ$, $\alpha = 52^\circ$ and $w_T = 570$ nm (Figure 5-23), a maximum P_C of 81.4% for a converter section length of $30 \mu\text{m}$ (encircled data point) was achieved. This is in fairly good agreement to a predicted P_C of 74.8% (Figure 5-8) and $L_{Beat/2}$ of $27 \mu\text{m}$ (Figure 5-5) from simulations of a waveguide with the fabricated core profile dimensions (dotted line).

It is believed that the P_C - deviation of 6.6% is due to the 320 nm deep etch of the lower cladding, which increases the mode power overlap in the waveguide cross section and consequently results in an increase of P_C .

The remained e-beam resist layer ($n_{PMMA} < 1.5$ @ $\lambda = 1064$ nm [15]) on the waveguide front slope (defined by ξ), which is indicated by the arrow in Figure 5-23, has no substantial effect on the profile geometry and therefore no impact on the device performance as it is too thin (~ 46 nm).

In general, deviations of data points from theoretically predicted values can occur due to inaccuracies of refractive index models for semiconductor materials [16, 17] used in the simulation, as well as due to possible slight thickness deviations of the deposited semiconductor layers from the modelled wafer structure.

Badly cleaved input- and/or output waveguide facets also contribute to deviations from theoretically predicted values, as coupling errors occur due to the use of the end-fire coupling technique. This can be noticed for data points corresponding to fabricated devices that contain converter section lengths ≥ 55 μm . These are scattered or nonexistent (around L_{Beat} of about 60 μm), as shown in Figure 5-24.

In comparison, simulations for a device comprising of one of the theoretically optimised waveguide cross section geometries ($\xi = \alpha = 62^\circ$, $w_T = 0.71$ μm , $L_{Beat/2} = 37$ μm) predict a P_C of 99%, which is indicated by the dashed line in Figure 5-24.

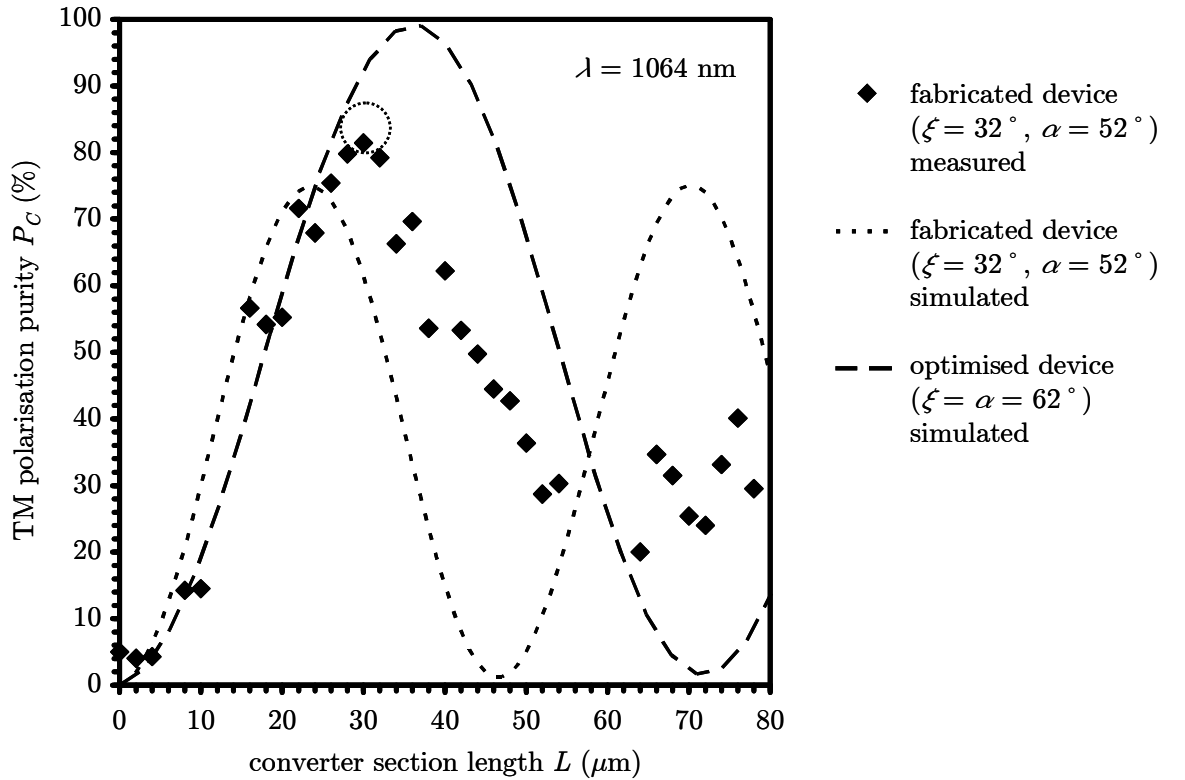


Figure 5-24: TM polarisation purity versus converter section length of the fabricated device (simulated and measured) and the theoretical optimised device for an operational wavelength of $\lambda = 1064$ nm.

5.5.2 Losses

The insertion loss and propagation loss of the realised devices were evaluated via the cut-back method as described in chapter 4. The trend line of the linear extrapolated normalised measured total power, expressed by the linear function $y = -0.0055x + 0.58$, yielded an insertion loss of 2.3 dB and a propagation loss of 2.9 dB / 100 μm - caused by the converter section. The encircled data point corresponds to the fabricated device with a converter section length of 30 μm ($\xi = 32^\circ$, $\alpha = 52^\circ$, $w_T = 570$ nm), imposing a total device loss (including propagation- and insertion/exit losses) of 1.72 dB. The scattering of the data points from the trend line is a result of coupling errors that occur due to the application of the end-fire coupling technique.

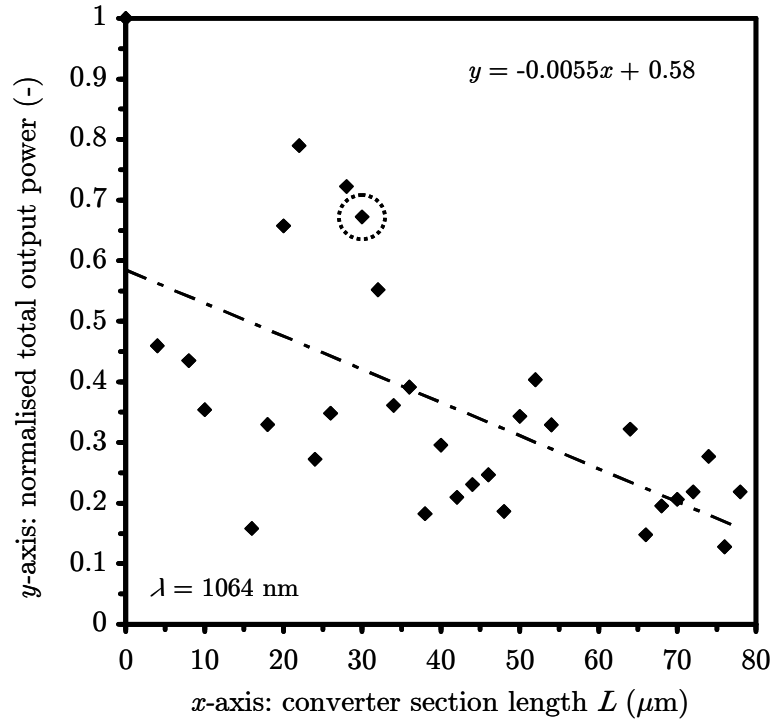


Figure 5-25: Measured normalised total output power versus different converter section lengths of the device for an operating wavelength of $\lambda = 1064$ nm. The extrapolation of the measured data is indicated by the chain-dotted line governed by the equation $y = -0.0055x + 0.58$.

5.5.3 Wavelength dependence

The device was optimised for a designated wavelength ($\lambda = 1064$ nm). Figure 5-26 illustrates the simulated wavelength dependence of the TM polarisation purity of both the theoretically optimised device ($\xi = \alpha = 62^\circ$, $w_T = 0.71 \mu\text{m}$ and $L_{Beat/2} = 37 \mu\text{m}$) and the fabricated device ($\xi = 32^\circ$, $\alpha = 52^\circ$, $w_T = 0.57 \mu\text{m}$ and $L_{Beat/2} = 27 \mu\text{m}$). As the dimensions of the converter waveguide cross section profile are close to the mode cut-off at the designated wavelength, modes at wavelengths higher than the designated are therefore not excited in the waveguide. The designated wavelength represents the upper limit of the

operational wavelength range of the device. This is indicated by the horizontal line at $\lambda = 1064$ nm. In the wavelength range from 900 nm to 1064 nm, a P_C - decrease of about 7.5%/100 nm (for the theoretically optimised device) and 10%/100 nm (for the fabricated device), with respect to the designated wavelength $\lambda = 1064$ nm, occurs. This is indicated by the chain-dotted triangles in Figure 5-26.

The lower limit of the operational wavelength range of the device is determined by the bandgap energy of GaAs (1.43 eV), which corresponds to a wavelength of 867 nm at room temperature.

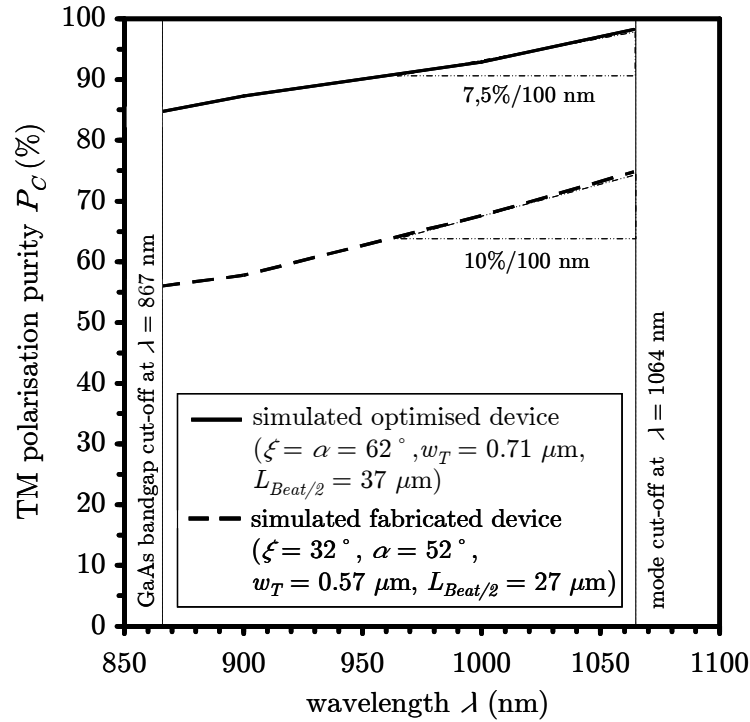


Figure 5-26: Simulated wavelength dependence of the TM polarisation purity P_C for the theoretically optimised device and the fabricated device.

5.6 Summary

A novel integrated reciprocal polarisation converter design, based on the principle of mode beating, was introduced. The waveguide cross section profile of the converter section consists of two parallel slanted sidewalls. This design allows the converter section to be fabricated in a single-step etch process. Before realisation of the device on a GaAs/Al_{0.27}Ga_{0.73}As wafer structure, a rigorous theoretical optimisation of the device geometries was conducted for an operating wavelength of $\lambda = 1064$ nm. A TM polarisation purity of $P_C = 81.4\%$ at a converter section length of $30 \mu\text{m}$ was measured. The total optical loss imposed by the measured device was evaluated to be 1.72 dB. Appearing etch-mask misalignment problems, which cause etch-overlaps into adjacent waveguide sections at the converter section periphery, were solved by introducing transversal rib waveguide stripes at the intersections.

5.7 References

- [1] Watts M. R., "Polarization Independent Microphotonic Circuits", *PhD thesis*, Massachusetts Institute of Technology, USA, (2005).
- [2] Watts M. R. and Haus H. A., "Integrated mode-evolution-based polarization rotators", *Optics Letters*, vol. **30**, no. 2, pp. 138 - 140, (2005).
- [3] Watts M. R., Haus H. A., Haus E. L. and Cherchi M., "Integrated optic polarization converter based on structural chirality", *US patent 7228015 B2*, (2007).
- [4] van Dam C., Spiekman L. H., van Ham F. P. G. M., Groen F. H., van der Tol J. J. G. M., Moerman I., Pascher W. W., Hamacher M., Heidrich H., Weinert C. M. and Smit M. K., "Novel compact polarization converters based on ultra short bends", *IEEE Photonics Technology Letters*, vol. **8**, no. 10, pp. 1346 - 1348, (1996).
- [5] Shani Y., Alferness R., Koch T., Koren U., Oron M., Miller B. I. and Young M. G., "Polarization rotation in asymmetric periodic loaded rib waveguides", *Applied Physics Letters*, vol. **59**, no. 11, pp. 1278 - 1280, (1991).
- [6] Brooks C., Jessop P. E., Deng H. and Yevick D., "Polarization rotating waveguides in silicon on insulator", in *Proceedings of OSA Topical Meetings: Integrated Photonics Research and Applications 2004 (IPRA 2004)*, San Francisco, CA, USA, 30 June - 2 July 2004, paper IFG4.
- [7] El-Refaei H., Yevick D. and Jones T., "Slanted-rib waveguide InGaAsP-InP polarization converters", *IEEE Journal of Lightwave Technology*, vol. **22**, no. 5, pp. 1352 - 1357, (2004).
- [8] Huang J. Z., Scarmozzino R., Nagy G., Steel M. J. and Osgood R. M. J., "Realization of a compact and single-mode optical passive polarization converter", *IEEE Photonics Technology Letters*, vol. **12**, no. 3, pp. 317 - 319, (2000).
- [9] Zhu Y. C., Groen F. H., Leijtens X. J. M. and van der Tol J. J. G. M., "Single-section polarisation converter on InP/InGaAsP using asymmetrical waveguides", in *Proceedings of the 6th Annual Symposium of the IEEE Lasers & Electro-Optics Society (LEOS) BENELUX Chapter 2001*, Brussels, Belgium, 3 December 2001, pp. 209 - 213.
- [10] Holmes B. M. and Hutchings D. C., "Realization of Novel Low-Loss Monolithically Integrated Passive Waveguide Mode Converters", *IEEE Photonics Technology Letters*, vol. **18**, no. 1, pp. 43 - 45, (2006).
- [11] Kim S.-H., Takei R., Shoji Y. and Mizumoto T., "Single-trench waveguide TE-TM mode converter", *Optics Express*, vol. **19**, no. 14, pp. 11267 - 11273, (2009).

- [12] Kotlyar M. V., Bolla L., Midrio M., O'Faolain L. and Krauss T. F., "Compact polarization converter in InP-based material", *Optics Express*, vol. **13**, no. 13, pp. 5040 - 5045, (2005).
- [13] Hutchings D. C., "Prospects for the implementation of magneto-optic elements in optoelectronic integrated circuits: A personal perspective", *Journal of Physics D: Applied Physics*, vol. **36**, no. 18, pp. 2222 - 2229, (2003).
- [14] Felici T., Black R. J. and Gallagher D., "Recent advances and results in waveguide shape optimisation techniques", in *Proceedings of the 15th Annual Meeting of the IEEE Lasers and Electro-Optics Society 2002 (LEOS 2002)*, Glasgow, United Kingdom, 10 - 14 November 2002, vol. **2**, pp. 831 - 832.
- [15] Technical Data Sheet, "NANO PMMA and Copolymer", <http://www.microchem.com>
- [16] Gehrsitz S., Reinhart F. K., Gourgon C., Herres N., Vonlanthen A. and Sigg H., "The refractive index of $\text{Al}_x\text{Ga}_{1-x}\text{As}$ below the band gap: Accurate determination and empirical modeling", *Journal of Applied Physics*, vol. **87**, no. 11, pp. 7825 - 7837, (2000).
- [17] Adachi S., "GaAs, AlAs, and $\text{Al}_x\text{Ga}_{1-x}\text{As}$: Material parameters for use in research and device applications", *Journal of Applied Physics*, vol. **58**, no. 3, pp. R1 - R29, (1985).

Chapter 6

Passive polarisation converter on a double quantum well material structure

6.1 Introduction

Various realised designs of integrated passive reciprocal polarisation converters on GaAs/AlGaAs, InP/InGaAsP and SOI material structures have achieved an analogous functionality to their discrete counterparts in bulk form. These material structures, which are designed for passive devices, are characterised by their guiding layer's energy bandgap being higher than the incident photon energy. This establishes transparency and results in low optical propagation loss.

Towards the development of *photonic integrated circuits* (PICs) it is desirable to monolithically integrate a passive polarisation converter functionality together with other building blocks on a single chip. These blocks, however, are quite often based on material structures designed for active device functionalities (e.g. semiconductor lasers or semiconductor optical amplifiers). Material structures for active devices have - in contrast to the ones for passive devices - an energy bandgap in the active region that is less than the emitted photon energy.

This chapter describes the optimisation, realisation and characterisation of a passive polarisation converter functionality, based on the two sloped sidewalls converter section waveguide profile design (as introduced in the previous chapter), on a material structure for an active device functionality.

6.2 Double quantum well material structure

The material layer structure was adapted from [1] and modified for a theoretically emitting wavelength of $\lambda = 867$ nm (Table 6-1) by co-worker B. Holmes. The wafer contains a *double quantum well* (DQW) GaAs/AlGaAs *separate confinement heterostructure* (SCH), which was lattice-matched to n-doped GaAs. The active region consists of 9 nm thick GaAs wells separated by a 10 nm thick Al_{0.2}Ga_{0.8}As barrier layer, which in turn are sandwiched between two 211 nm thick Al_{0.2}Ga_{0.8}As barrier layers. A 1500 nm thick n-type Al_{0.4}Ga_{0.6}As lower cladding, 1000 nm p-type Al_{0.4}Ga_{0.6}As upper cladding and 100 nm thick highly p-doped GaAs contact layer complete the structure.

material (layers from top)	doping	thickness	comment	
GaAs	p ⁺ -type ($5 \cdot 10^{18} \text{ cm}^{-3}$ (Zn))	100 nm	cap layer	
Al _{0.4} Ga _{0.6} As	p-type ($5 \cdot 10^{17} \text{ cm}^{-3}$ (C))	1000 nm	upper cladding	
Al _{0.2} Ga _{0.8} As	undoped	211 nm	guiding layer	spacer
GaAs	undoped	9 nm		quantum well
Al _{0.2} Ga _{0.8} As	undoped	10 nm		barrier
GaAs	undoped	9 nm		quantum well
Al _{0.2} Ga _{0.8} As	undoped	211 nm		spacer
Al _{0.4} Ga _{0.6} As	n-type ($5 \cdot 10^{17} \text{ cm}^{-3}$ (Si))	1500 nm	lower cladding	
GaAs	n ⁺ -type ($1.5 \cdot 10^{18} \text{ cm}^{-3}$ (Si))	500 nm	growth interface	
(100) GaAs substrate	n ⁺ -type ($2 \cdot 10^{18} \text{ cm}^{-3}$ (Si))	500 μm	substrate	

Table 6-1: Wafer material composition of the double quantum well laser structure.

The material was grown by *metal organic chemical vapour deposition* (MOCVD) at the EPSRC National Centre for III-V Technologies at the University of Sheffield, Sheffield, United Kingdom.

6.3 Double quantum well material evaluation

It is common practice to initially fabricate broad area *oxide stripe lasers* (OSLs) from the semiconductor wafer in order to assess the optical characteristics of the material structure [2]. The structure of an oxide stripe injection laser is shown in Figure 6-1. Its broad-area laser geometry, given by the $75\ \mu\text{m}$ wide current injection stripe, minimises the effect of current spreading from the active region and hence enables an accurate determination of the threshold current density J_{th} in the evaluation of the material structure. This gain-guided laser also offers a fabrication simplification due to its planar structure, as there is only one lithography step required. The laser device geometry represents a Fabry-Perot etalon. The cavity length is defined by cleaved edges at both ends, which form the partially reflecting mirrors of the cavity. These provide a positive optical feedback in order to sustain the laser oscillation inside the resonant cavity. The related theory for semiconductor laser operation is given in [3-11].

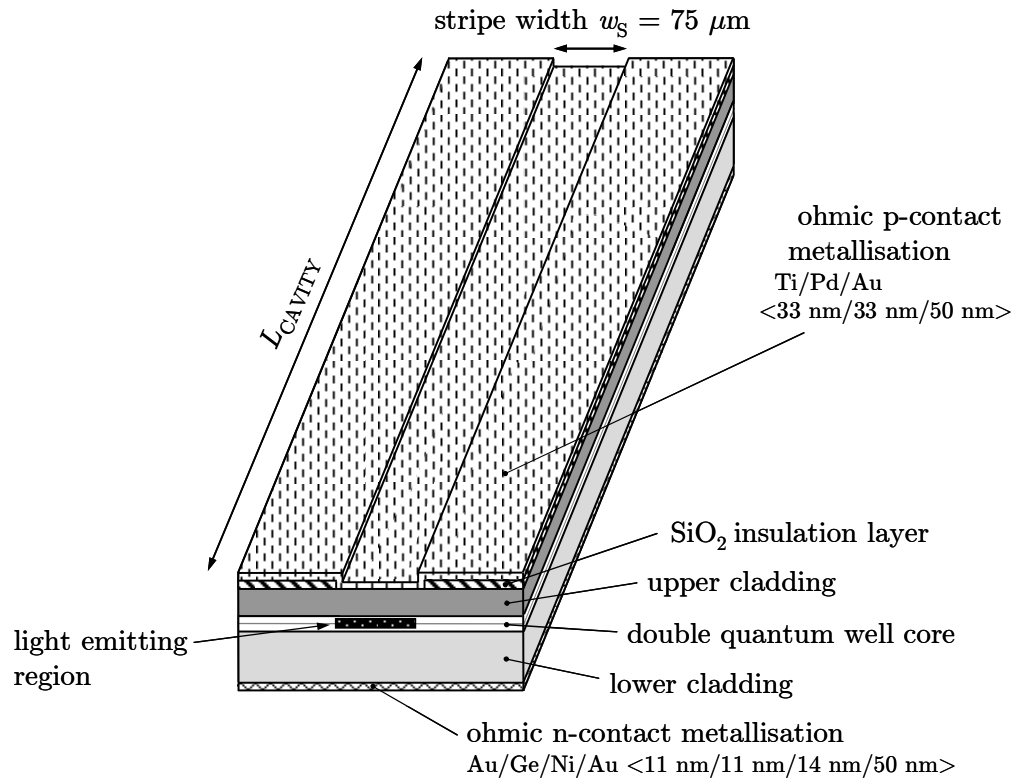


Figure 6-1: Schematic illustration of an oxide stripe injection laser with SiO_2 insulation (not to scale).

OSL of five different cavity lengths L_{CAVITY} (400 , 500 , 600 , 1000 and $2000\ \mu\text{m}$) were fabricated [12] and tested using a Boxcar Averager SystemTM. The measurements were conducted under pulsed current operation (pulse duration: $500\ \text{ns}$, repetition rate: $1\ \text{kHz}$). A Si photodiode was used for the detection of the emitted laser signal. The light output

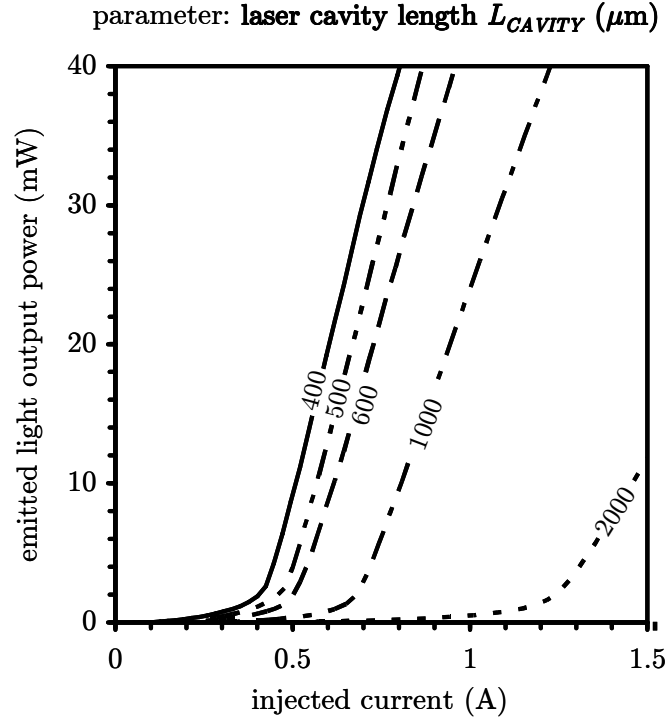


Figure 6-2: Measured dependence of the optical power emission on the injected current of 75 μm wide oxide stripe lasers with different laser cavity lengths L_{CAVITY} at a temperature of 25 °C.

power was measured as the injected current was incrementally increased by an automated computer setup. The measured light output power - current (or L-I) characteristics for different L_{CAVITY} can be depicted in (Figure 6-2). The laser threshold current I_{th} (in A) is defined as the value of the injected current where the gain just matches the optical losses in the laser cavity. At this stage, a round-trip amplification in the cavity is about to occur, but the photon density has not yet built up. The stimulated emission is therefore still small [13].

Another parameter is the *differential external quantum efficiency* η_{EXT} , which indicates how efficient the overall laser device is converting electrical current to light output power above threshold [8, 14]

$$\eta_{EXT} = \frac{\text{increase in output photons}}{\text{increase in number of injected electrons}} = \frac{2e}{hf} \left[\frac{dP_{OUTPUT}}{dI} \right]_{I > I_{th}}, \quad (6.1)$$

where P_{OUTPUT} represents the optical power (in W) emitted from the device, I is the injected current (in A), h the Planck's constant (6.63×10^{-34} Js), f the laser frequency (in Hz) and e the charge of an electron (1.6×10^{-9} C). η_{EXT} is directly related to the gradient of the linear part of the L - I plot ($I > I_{th}$).

Alternatively, the *internal stimulated quantum efficiency* η_{INT} is defined as the ratio of the number of radiative recombinations to the number of injected carriers [14]

$$\eta_{INT} = \frac{\text{number of photons produced in the cavity}}{\text{number of injected electrons}} \quad (6.2)$$

and represents a measure of how efficient electron-hole pairs are converted into photons.

η_{EXT} can also be expressed in the form [4]

$$\eta_{EXT} = \frac{\eta_{INT}}{1 + \frac{2\alpha_{ABS} L_{CAVITY}}{\ln\left(\frac{1}{R_1 R_2}\right)}}, \quad (6.3)$$

where R_1 and R_2 represent the power reflectivity of the laser facets (GaAs QW: $n = 3.636$ @ $\lambda = 867$ nm $\rightarrow R_1 = R_2 = 32\%$), L_{CAVITY} the length of the laser cavity (in μm), and α_{ABS} the *absorption coefficient* (in $1/\text{cm}$). This expression can be rearranged into the form

$$\frac{1}{\eta_{EXT}} = \underbrace{\frac{1}{\frac{\eta_{INT}}{a}}}_{a} + \underbrace{\frac{2\alpha_{ABS}}{\eta_{INT} \ln\left(\frac{1}{R_1 R_2}\right)}}_b L_{CAVITY} = a + bL_{CAVITY}. \quad (6.4)$$

Using Equation (6.1) and plotting $\frac{1}{\eta_{EXT}}$ versus L_{CAVITY} , a straight line in the form

$\frac{1}{\eta_{EXT}} = a + bL_{CAVITY}$ can be obtained (Figure 6-3).

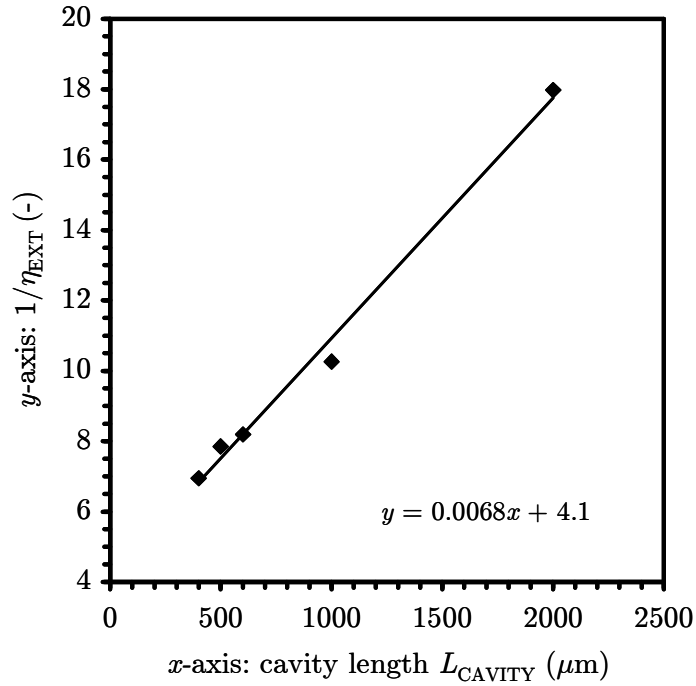


Figure 6-3: Relationship between the inverse of the external quantum efficiency η_{EXT} and the cavity length L_{CAVITY} . The linear solid trendline is governed by the equation $y = 0.0068x + 4.1$.

Estimations for η_{INT} and α_{ABS} can thus be calculated from the y -intercept (a) and the gradient (b) values, respectively, of Figure 6-3 [4]. η_{INT} equals to $1/4.1 = 0.24$ and α_{ABS} equals to $\alpha_{ABS} = b \times \eta_{INT} \times \ln(1/R_1 R_2)/2 = 0.0068 \times 0.24 \times \ln(1/0.32^2)/2 = 18.6$ $1/\text{cm}$.

Another important parameter is the *threshold current density for infinite length* J_{INF} (in A/cm²). This was obtained by plotting $\ln(J_{th})$ versus $1/L_{CAVITY}$ (Figure 6-4) and calculating the y -intersection to give a value for J_{INF} , where J_{th} is the *threshold current density* (threshold current divided by active area) (in A/cm²). J_{INF} was determined to be 727.78 A/cm² ($= e^{6.59}$).

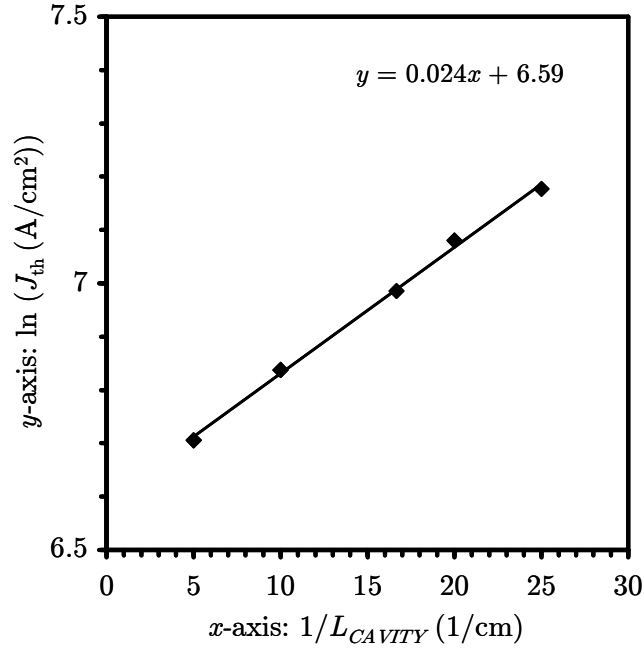


Figure 6-4: Relationship between the natural logarithm of the threshold current density J_{th} and the inverse of the cavity length L_{CAVITY} . The linear solid trendline is governed by the equation $y = 0.024x + 6.59$.

As the evaluated material parameter values were similar to those of previously obtained parameters for similar wafer layer compositions [1], the optical characteristics of the material were acceptable for the further usage of this material.

6.4 Polarisation converter device design

The polarisation converter section design comprising two angled waveguide sidewalls, as introduced in the previous chapter, was chosen for the implementation of the polarisation converter functionality on a DQW SCH material system. The optimum operating point of the polarisation converter functionality in this design is just above the cut-off condition for single mode propagation in the converter section waveguide. This is determined by the waveguide top width w for a given front slope angle ξ , undercut slope angle α , material structure composition and the operating wavelength λ . At this specific waveguide geometry dimension, the maximum power overlap κ between the two excited fundamental modes occurs in the waveguide. This results in a maximum value for the TM polarisation purity P_C for a launched TE-polarised input signal. (For the demonstration of the concept and functionality of the device, only the case of a TE polarised input signal was considered. A TM polarised signal would have an analogous effect on the device functionality.) The power overlap κ decreases with wider waveguide widths w and becomes eventually negligible (see Figure 5-3(b)). For these wide w -dimensions, the asymmetric waveguide structure behaves therefore virtually like a symmetric stripe waveguide structure. This fact not only allows the realisation of an efficient interconnection to other functionality blocks on a PIC, but also enables the waveguide sections of the *entire* device to consist of two angled waveguide sidewalls, which is

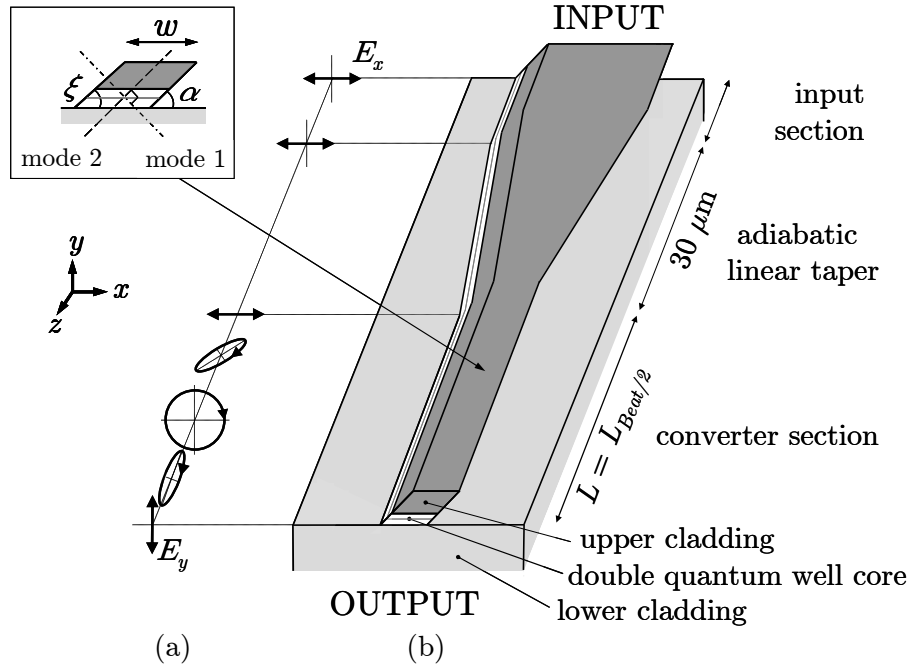


Figure 6-5: Schematic of the design and functionality of the passive linear taper and polarisation converter structure on double quantum well material. (a) Evolution of the polarisation state of a TE polarised signal launched into the device. (b) Device configuration (not to scale). (Insert) Definition of waveguide profile parameters (front slope angle ξ , undercut slope angle α and waveguide top width w) and illustration of the orientations of the optical axes which determine the orientation of the excited lowest order modes (mode 1 (chain dotted line) and mode 2 (dashed line)) in the waveguide.

illustrated in Figure 6-5. The design avoids any mask (re-)alignment problems at the converter section periphery and simplifies the fabrication process as it allows *all* waveguide sections to be fabricated in the *same* etch process step.

Light is coupled into the device via a $3\ \mu\text{m}$ wide waveguide, which is referred to as the input section. A waveguide width w of $3\ \mu\text{m}$ not only simplifies to couple light into the device but also provides mechanical strength in order to prevent the waveguide from collapse during fabrication or at cleaving. A following adiabatic linear taper between the input waveguide section and the converter section establishes a close match of the mode profiles and minimises coupling losses between the two sections. The length of the converter section L , which determines the device functionality, is ideally equal to the half beat length $L_{Beat/2}$ and is defined by the cleaving process.

6.5 Device optimisation

The DQW SCH wafer structure was designed for an emitting wavelength of $\lambda = 867.1\ \text{nm}$. However, for the characterisation of this passive converter device at this specific wavelength, there was no optical source available. As an alternative, a diode pumped solid state (DPSS) Nd:YAG laser, which emits at a wavelength of $\lambda = 1064\ \text{nm}$, was chosen. The device geometries were therefore optimised for both $\lambda = 867.1\ \text{nm}$ and $\lambda = 1064\ \text{nm}$ (Figure 6-6). As the front slope angle ξ and the undercut slope angle α are almost equal in the fabricated converter section waveguide cross section profiles, both angles were chosen to be equal ($\xi = \alpha$) for the sake of simplification of theoretical optimisation efforts. The modelled waveguide layer dimensions of the asymmetric waveguide structure as well as the computational window Ω_W are shown in Figure 6-7(a). The calculations were conducted with a commercially available FEM based mode solver, which computational settings were introduced in chapter 2.

Firstly, the optimum waveguide top width w was determined in the same manner as in chapter 5. Values for w just above the cut-off condition, which establishes the excitation of the two lowest order modes in the waveguide - given by the corresponding cross section geometry parameters, were evaluated (Figure 6-6(a)). The cut-off conditions for single mode propagation were $n_{lower\ cladding} = 3.306 < n_{mode2}$ for $\lambda = 867.1\ \text{nm}$ and $n_{lower\ cladding} = 3.234 < n_{mode2}$ for $\lambda = 1064\ \text{nm}$. The optimised values for the waveguide width w were determined to be within the range of $0.9\ \mu\text{m}$ (@ $\xi = \alpha = 30^\circ$) $\leq w \leq 0.6\ \mu\text{m}$ (@ $\xi = \alpha = 70^\circ$) for $\lambda = 867.1\ \text{nm}$ and within $1.3\ \mu\text{m}$ (@ $\xi = \alpha = 30^\circ$) $\leq w \leq 0.85\ \mu\text{m}$ (@ $\xi = \alpha = 70^\circ$) for $\lambda = 1064\ \text{nm}$. As expected, for any $\xi = \alpha$ -configuration, the mode cut-off at shorter wavelengths takes place at shorter waveguide widths w in comparison to longer wavelengths. The $L_{Beat/2}$ values for the corresponding optimised waveguide top width w of the waveguide cross section are displayed in Figure 6-6(b). These were within the range of $19\ \mu\text{m}$ (@ $\xi = \alpha = 30^\circ$) $\leq w \leq 28\ \mu\text{m}$ (@ $\xi = \alpha = 70^\circ$) for $\lambda = 867.1\ \text{nm}$ and within $41\ \mu\text{m}$ (@ $\xi = \alpha = 30^\circ$) $\leq w \leq 58\ \mu\text{m}$ (@ $\xi = \alpha = 70^\circ$) for $\lambda = 1064\ \text{nm}$.

The optimum values for both κ and δ (0.5 and 45° , respectively) occur for $\xi = \alpha = 52^\circ$ (at optimum waveguide width w and corresponding $L_{Beat/2}$) independent of the operating wavelength. This can be depicted in Figure 6-6(c). This optimum $\xi = \alpha$ - configuration of 52° at *both* operating wavelengths is also observed for the TM polarisation purity P_C in Figure 6-6(d). P_C - values up to 99% were achieved.

From the fabrication tolerance point of view it can also be noted that a deviation of $\pm 5^\circ$ or $\pm 10^\circ$ from the optimum $\xi = \alpha$ - configuration ($\xi = \alpha = 52^\circ$) results in a maximum P_C - degradation of 3% and 10%, respectively.

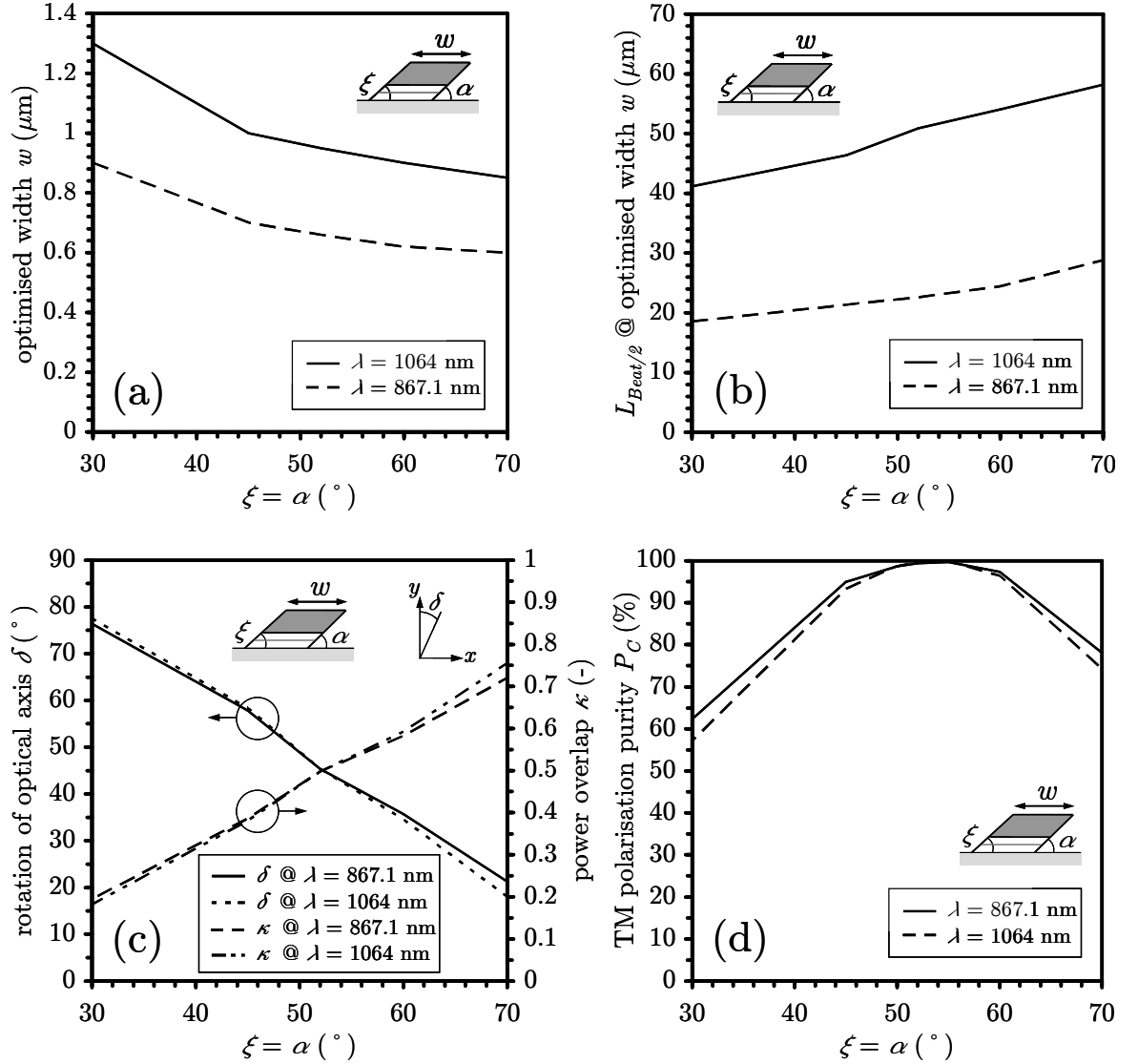


Figure 6-6: Calculated optimum double quantum well converter waveguide cross section profile for equal front slope angle ξ and undercut slope angle α at two different wavelengths ($\lambda = 867$ nm and $\lambda = 1064$ nm). (a) Optimised waveguide width w versus equal angles of the sidewall slopes. (b) Half beat length $L_{Beat/2}$ versus equal angles of the sidewall slopes. (c) Resulting rotation of optical axis δ of the waveguide (with respect to the vertical axis) and power overlap κ versus equal angles of the sidewall slopes. (d) Resulting TM polarisation purity P_C versus equal angles of the sidewall slopes.

6.6 Analysis of the optimised device

The optimised device dimensions for the given wafer material structure to achieve a maximum achievable TM polarisation purity P_C of $> 99\%$ at the output are $w = 670$ nm (960 nm), $L_{Beat/2} = 22$ μm (50 μm) and $\xi = \alpha = 52^\circ$ for an operating wavelength of $\lambda = 867.1$ nm (1064 nm). Figure 6-7 and Figure 6-8 illustrate the electric- and Figure 6-9 and Figure 6-10 the magnetic vector field plots and their corresponding mode profile and contour plot of the transverse (x , y) components of both fundamental modes (mode 1, mode 2) for the optimised waveguide cross section profile for an operating wavelength of $\lambda = 1064$ nm. As the relations of the magnetic field are analogous to the electric field, only the electric field was considered for analysis. It can be noted that the electric field is distributed in the same manner as in a material structure for a passive device (chapter 5). The electric field vectors of both orthogonal modes in the guiding layer, which are parallel to the optical axes, are, as desired, at an angle of 45° with respect to the vertical axis (Figure 6-7(c), Figure 6-8(c)). Each mode has a similar profile of their horizontal (E_x (TE)) (Figure 6-7(d), Figure 6-8(d)) and vertical (E_y (TM)) (Figure 6-7(b), Figure 6-8(b)) components as well as an approximately equal field distribution between them.

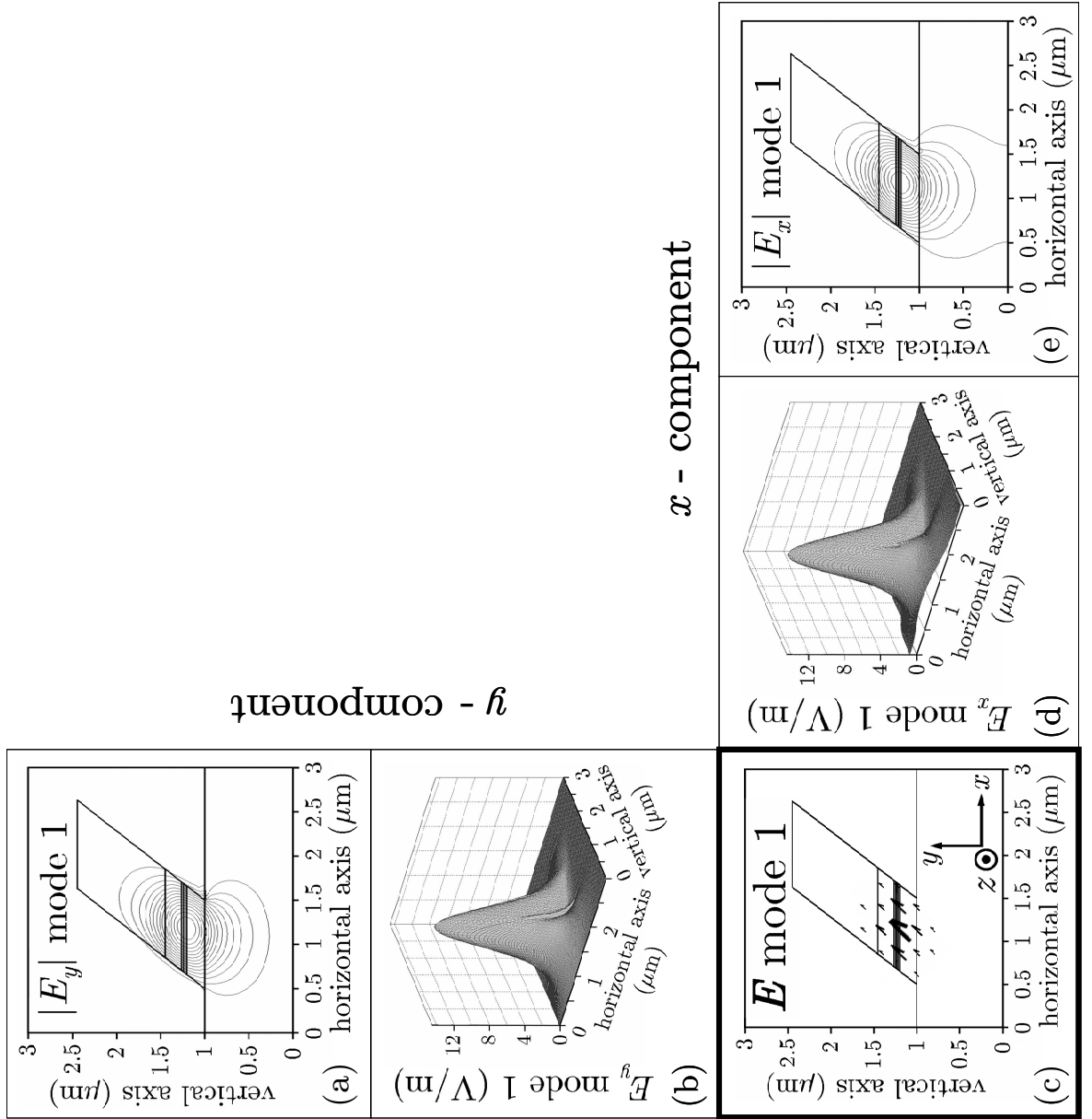


Figure 6-7: (a)-(e) Electric vector field plot and corresponding mode profile and contour plot of the transverse (x , y) components for one (mode 1) of two fundamental modes in the optimised asymmetric waveguide. The structure comprises a front slope angle ξ and an undercut slope angle α of both 52° with respect to the horizontal axis and a waveguide top width w of 960 nm for an operating wavelength of $\lambda = 1064$ nm.

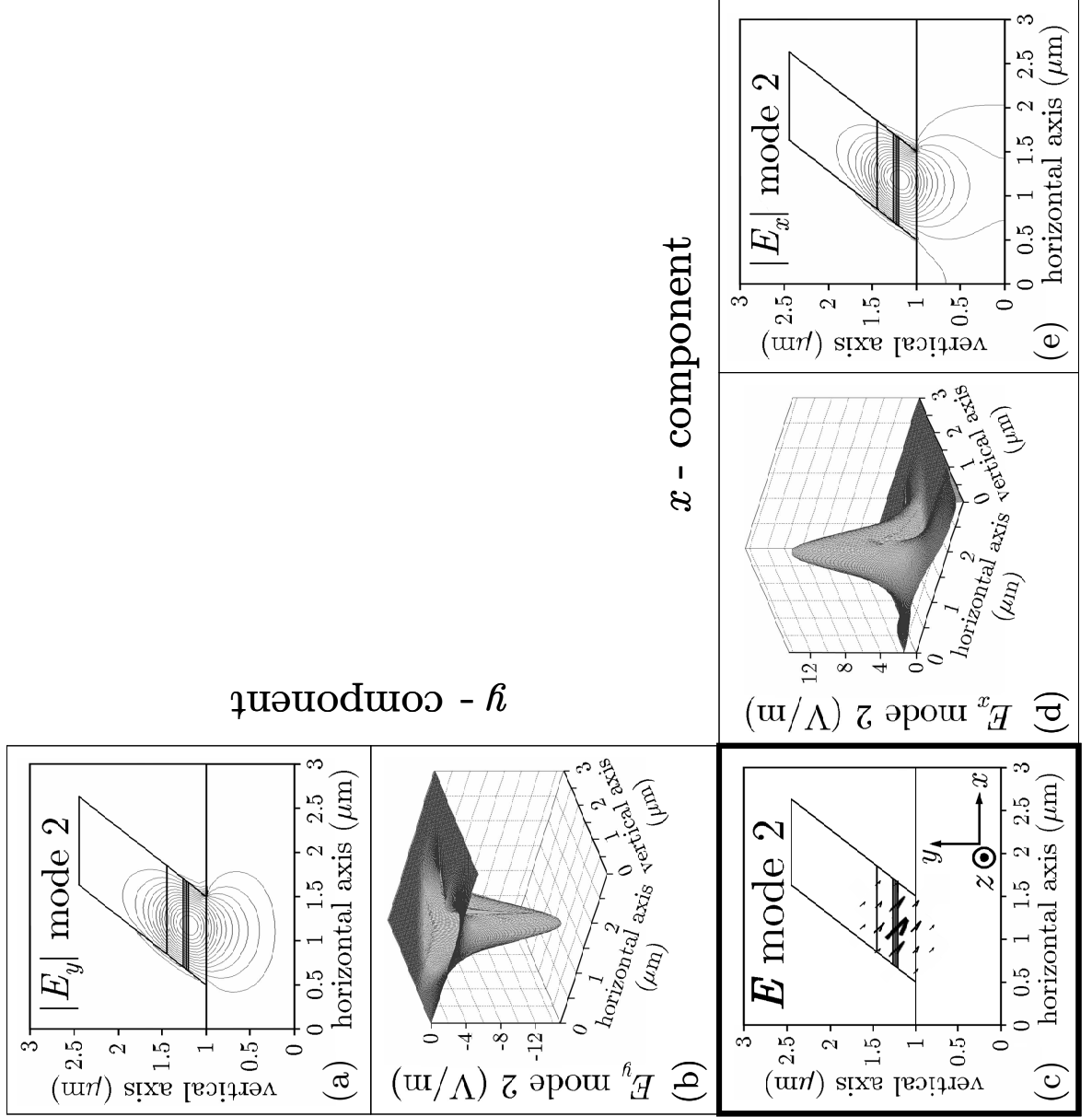
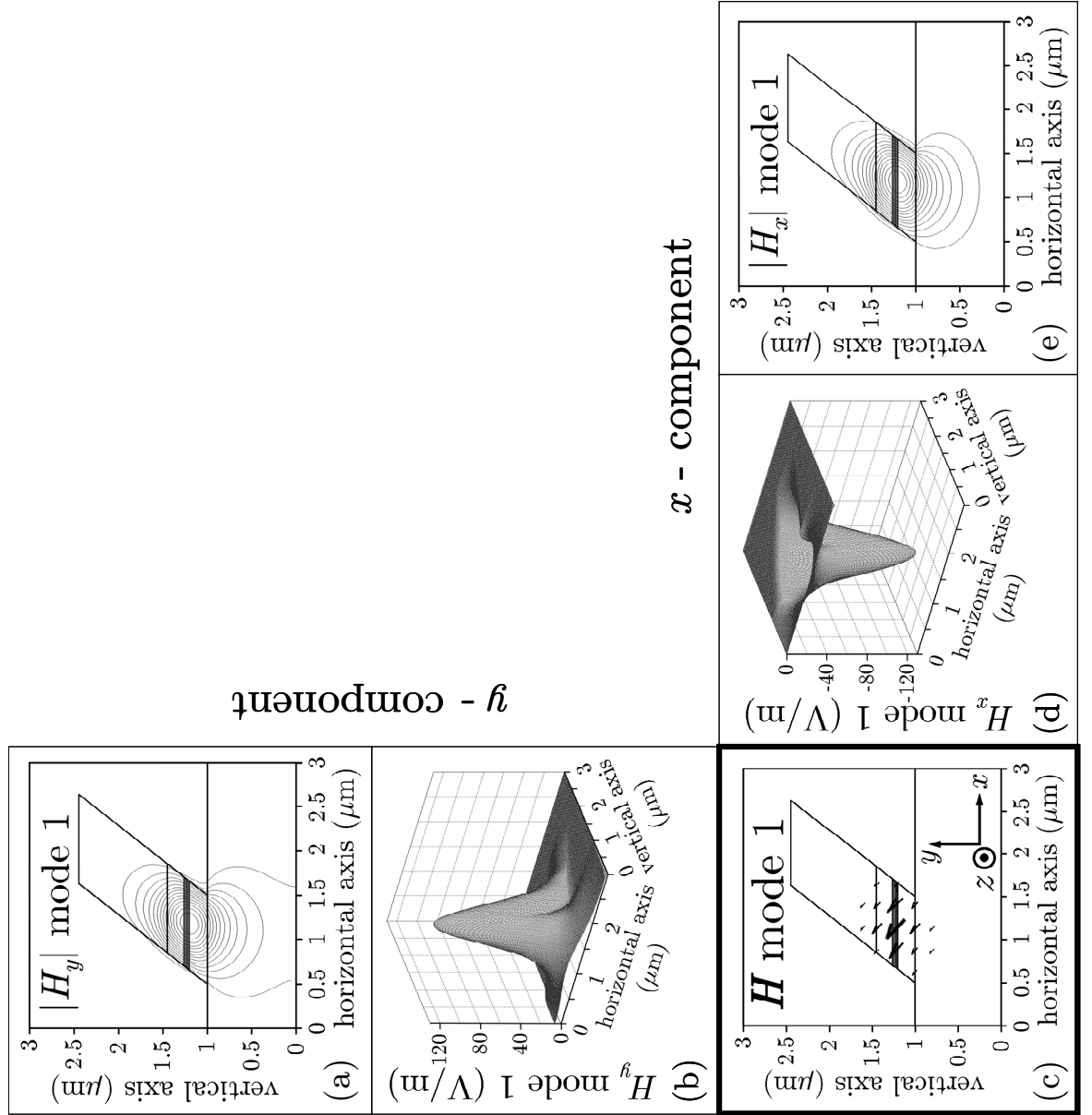


Figure 6-8: (a)-(e) Electric vector field plot and corresponding mode profile and contour plot of the transverse (x , y) components for one (mode 2) of two fundamental modes in the optimised asymmetric waveguide. The structure comprises a front slope angle ξ , and an undercut slope angle α of both 52° with respect to the horizontal axis and a waveguide top width w of 960 nm for an operating wavelength of $\lambda = 1064$ nm.



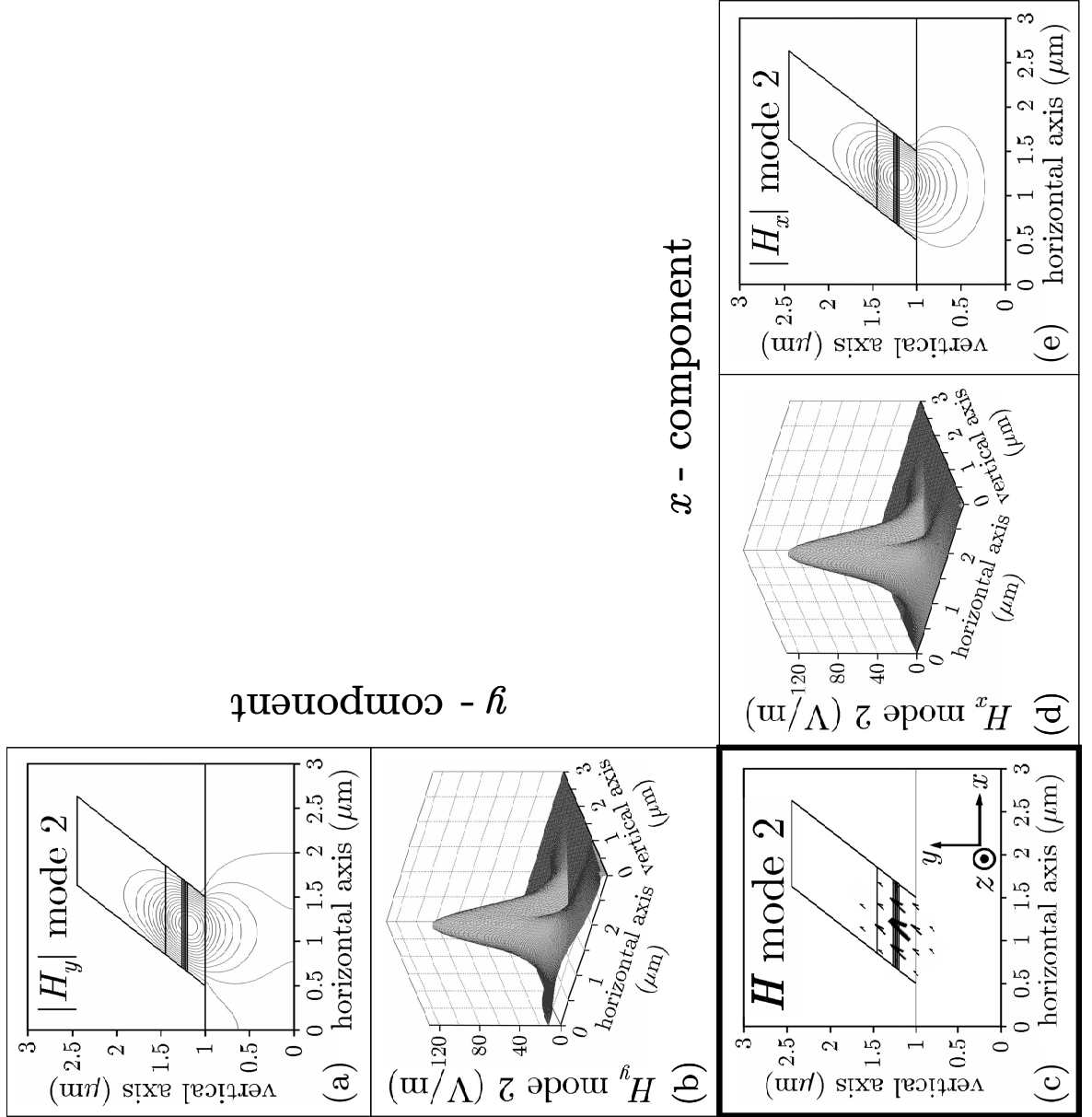


Figure 6-10: (a)-(e) Magnetic vector field plot and corresponding mode profile and contour plot of the transverse (x , y) components for one (mode 2) of two fundamental modes in the optimised asymmetric waveguide. The structure comprises a front slope angle ξ and an undercut slope angle α of both 52° with respect to the horizontal axis and a waveguide top width w of 960 nm for an operating wavelength of $\lambda = 1064$ nm.

An illustration of the functionality of the optimised device for an operating wavelength $\lambda = 1064$ nm is represented in Figure 6-11. It displays the contour plots of the magnitude of both the E_x (TE)- and E_y (TM) components in the taper- and converter section as a TE polarised input signal propagates down the device. The interference between the two excited modes (mode 1 and mode 2) results in a harmonic beating pattern of the transversal components with the periodicity of $50 \mu\text{m}$, which equals $L_{Beat/2}$. It can be noted that the first maximum (minimum) of the TM polarised component, E_y (TE polarised component, E_x) appears at a propagation distance in the converter section of about $44 \mu\text{m}$, shorter than $L_{Beat/2}$ due to an already commencing polarisation evolution towards the end of the linear, $70 \mu\text{m}$ long adiabatic taper section. Simulations indicate that a TM polarisation purity P_C of about 9% occurs at the beginning of the converter section (see Figure 6-15).

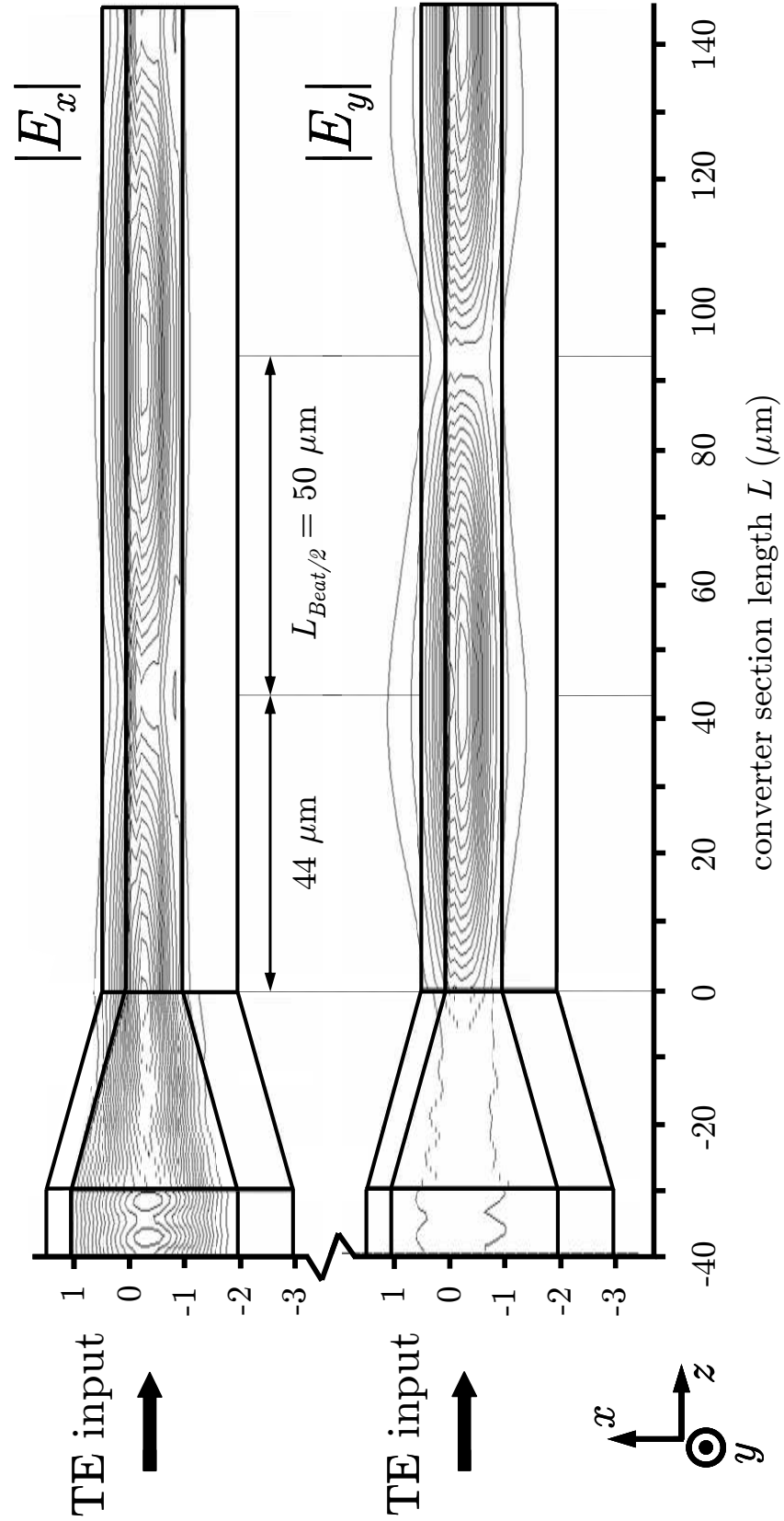


Figure 6-11: Top view of the simulated contour plots of the magnitude of the E_x (TE) and E_y (TM) component of a TE polarised signal launched into the theoretically optimised device ($\zeta = \alpha = 52^\circ$, $w = 960$ nm) at an operating wavelength of $\lambda = 1064$ nm.

6.7 Device fabrication

6.7.1 Fabrication steps

An illustration of the chronology of the fabrication steps is given in Figure 6-12. The initial realisation of the e-beam alignment markers is not included in the schematic as the emphasis is given on the actual fabrication of the device.

Step 1: Creation of e-beam position calibration markers

The e-beam position calibration markers were fabricated according to the description in chapter 5.

Step 2: Realisation of waveguide outline SiO₂ mask pattern

1. Deposition of 200 nm PECVD SiO₂.
2. Spin-coat positive e-beam resist (PMMA 4% ELV 2041) at 5000 rpm for 60 seconds.
3. Clean backside of sample with in acetone soaked cotton bud before a 15 minutes bake in oven @ 180 ° C.
4. Spin-coat second positive e-beam resist layer (PMMA 4% ELV 2041) at 5000 rpm for 60 seconds (Figure 6-12(a)).
5. Clean backside of sample with in acetone soaked cotton bud before a 90 minutes bake in oven @ 180 ° C.
6. Exposure of waveguide outline pattern. EBPG 5 e-beamwriter control file parameters: resolution: 25 nm (high) / 250 nm (low), proximity correction file: gaas200-50b.pec, prox min: 0.1, prox grid: 0.025, dose: 136 $\mu\text{C}/\text{cm}^2$ (high resolution) / 250 $\mu\text{C}/\text{cm}^2$ (low resolution), spot size: 56 nm (high resolution) / 400 nm (low resolution), job type: simple.
7. Development of waveguide pattern using 2:1 IPA:MIBK developer solution for 75 seconds @ 23.1 ° C. Dip in IPA for 10 seconds; Blow dry with nitrogen (Figure 6-12(b)).
8. SiO₂ dry-etch of waveguide pattern using CHF₃ as a reactive gas in the BP80 machine (Figure 6-12(c)). BP80 parameter settings: process gas: CHF₃, corrected gas flow: 20 sccm, process pressure: 17 mTorr, forward RF power: 100 W, temperature: 25 ° C, BIAS: -280 V, process time: 13 minutes.
9. Removal of e-beam resist mask via an O₂ ash process using the BP80 machine (Figure 6-12(d)). BP80 parameter settings: process gas: O₂, corrected gas flow: 20 sccm, process pressure: 20 mTorr, forward RF power: 100 W, temperature: 25 ° C, BIAS: 320 V, process time: 25 minutes.

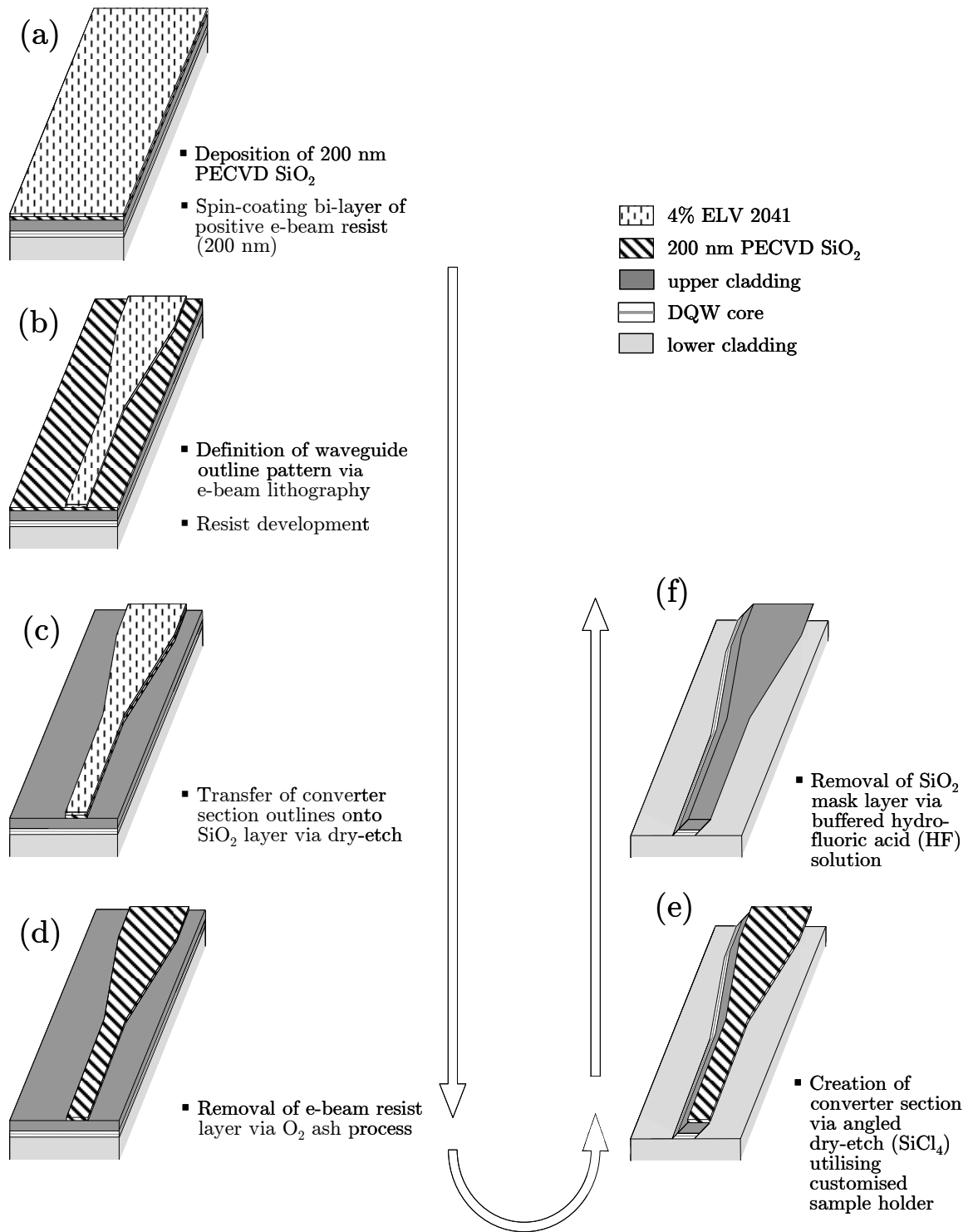


Figure 6-12: (a)-(f) Schematic process flow diagram of the realised polarisation converter device on a double quantum well material structure.

Step 3: Realisation of the entirely angled waveguide structure

10. Angled GaAs dry-etch of converter waveguide section using SiCl_4 as a reactive gas in the S100 T-Gate machine (Figure 6-12(e)). Angled waveguide-etch S100 T-Gate process parameters: process gas: SiCl_4 , corrected gas flow: 9 sccm, process pressure: 9 mTorr, forward RF power: 100 W, temperature: 25°C , BIAS: -346 V, process time: 17 minutes, customised anodised aluminium sample holder used, slope angle of sample holder is 60° with respect to horizontal plane.
11. Removal of SiO_2 layer via wet chemical etching using a buffered (hydrofluoric acid) HF:RO (reverse osmosis) water solution (ratio 5:1) for 45 seconds at a temperature of 45°C ; Rinse thoroughly in RO water for 10 minutes; Blow dry using nitrogen (Figure 6-12(f)).

6.7.2 Realised device

The top view and the converter section waveguide profile of the fabricated device are shown in Figure 6-13. The occurring "grass" (due to micromasking [15]) between the waveguides, as can be noted in Figure 6-13(a,b), has no impact on the device functionality and -performance as it is sufficiently far from the waveguide core. The converter section profile consists of a front slope angle of $\zeta = 50^\circ$, an undercut angle of $\alpha = 55^\circ$ and a waveguide top width w of 980 nm (Figure 6-13(c)). The arrow indicates an e-beam resist layer with a maximum thickness of about 200 nm, which remained from the e-beam removal step during fabrication of the device. But this has no impact on the device functionality. Waveguide sidewall roughness can also be noted at the front slope, which is defined by ζ . The sidewall roughness was caused by the commenced erosion of the SiO_2 mask edges during the tilted dry-etch process. The deviations of the fabricated profile dimensions from the theoretically optimised ones ($\zeta_{\text{OPTIMISED}} = \alpha_{\text{OPTIMISED}} = 52^\circ$ and $w_{\text{OPTIMISED}} = 960\text{ nm}$) are $\Delta\zeta = 2^\circ$, $\Delta\alpha = 3^\circ$ and $\Delta w = 20\text{ nm}$.

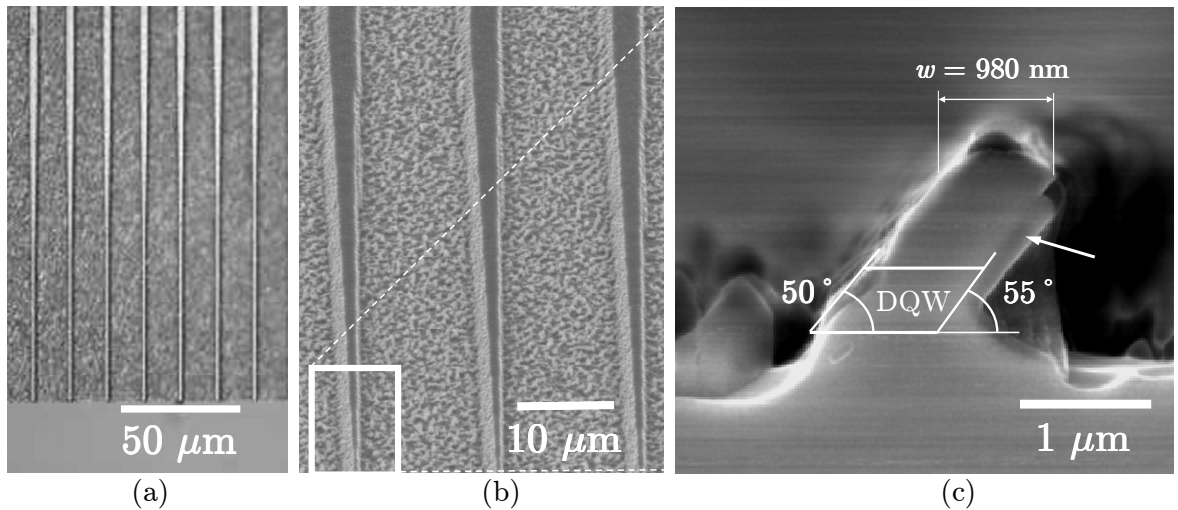


Figure 6-13: (a) Optical micrograph of the fabricated device showing the input waveguide, the linear adiabatic taper and the converter section waveguide. (b) SEM micrograph of the fabricated device showing the linear adiabatic taper and the beginning of the converter section. (c) Magnified SEM view of the deeply etched converter section waveguide cross section profile of the fabricated device.

6.8 Device characterisation

6.8.1 Converted TM polarisation purity

The expected functionality of the fabricated device ($\zeta = 50^\circ$, $\alpha = 55^\circ$ and $w = 980$ nm) for an operating wavelength of $\lambda = 1064$ nm is illustrated in Figure 6-14. It displays the simulated contour plots of the magnitude of both the E_x (TE)- and E_y (TM) components in the taper- and converter section as a TE polarised input signal propagates down the device. The interference between the two excited modes (mode 1 and mode 2) results in a harmonic beating pattern of the transversal components with the periodicity of $55 \mu\text{m}$, which equals $L_{\text{Beat}/2}$. It can be noted that the first maximum (minimum) of the TM polarised component, E_y (TE polarised component, E_x) is expected to appear at a propagation distance in the converter section of about $46 \mu\text{m}$. This distance is shorter than $L_{\text{Beat}/2}$ due to an already commencing polarisation evolution towards the end of the linear, $70 \mu\text{m}$ long adiabatic taper section. Simulations indicate that a TM polarisation purity P_C of about 7% occurs at the beginning of the converter section (Figure 6-15(Insert)).

Devices consisting of different converter section lengths were fabricated and characterised via the measurement method described in chapter 4. Figure 6-15 displays the dependence of the TM polarisation purity P_C on the converter section length L . The diamond - shaped data points correspond to the measured P_C of the fabricated device. With the fabricated waveguide profile dimensions in Figure 6-13(c), a P_C of about 88% (encircled data point) for a converter section length of $80 \mu\text{m}$ (corresponding to $L_{\text{Beat}/2}$) and a P_C of even 92% (double encircled data point) for a converter section length of $166 \mu\text{m}$ (corresponding to $3 \times L_{\text{Beat}/2}$) were achieved. It is believed that this difference results from badly cleaved input- and/or output waveguide facets at $L = L_{\text{Beat}/2}$. Badly cleaved facets also contribute to deviations from theoretical predicted values, as coupling errors occur due to the use of the end-fire coupling technique. In addition, deviations of data points from theoretically predicted values can occur due to inaccuracies of refractive index models for semiconductor materials used in the simulation as well as due to possible slight thickness deviations of the deposited semiconductor layers from the modelled wafer structure. It can also be noted that the measured P_C deviates by 10% (encircled data point) for a converter section length of $80 \mu\text{m}$ (corresponding to $L_{\text{Beat}/2}$) and 6% (double encircled data point) for a converter section length of $166 \mu\text{m}$ (corresponding to $3 \times L_{\text{Beat}/2}$) with an offset in the converter section length from theoretical predicted values. It is believed that this is caused by both the approximately 500 nm deep etch of the lower cladding and the remaining e-beam resist layer of approximately 200 nm at the undercut waveguide sidewall, as indicated in Figure 6-13(c). The actual waveguide cross section width is therefore longer than the theoretically optimised one, which results in lower P_C (see Figure 5-3(c)) and longer $L_{\text{Beat}/2}$ values (see Figure 5-3(b)).

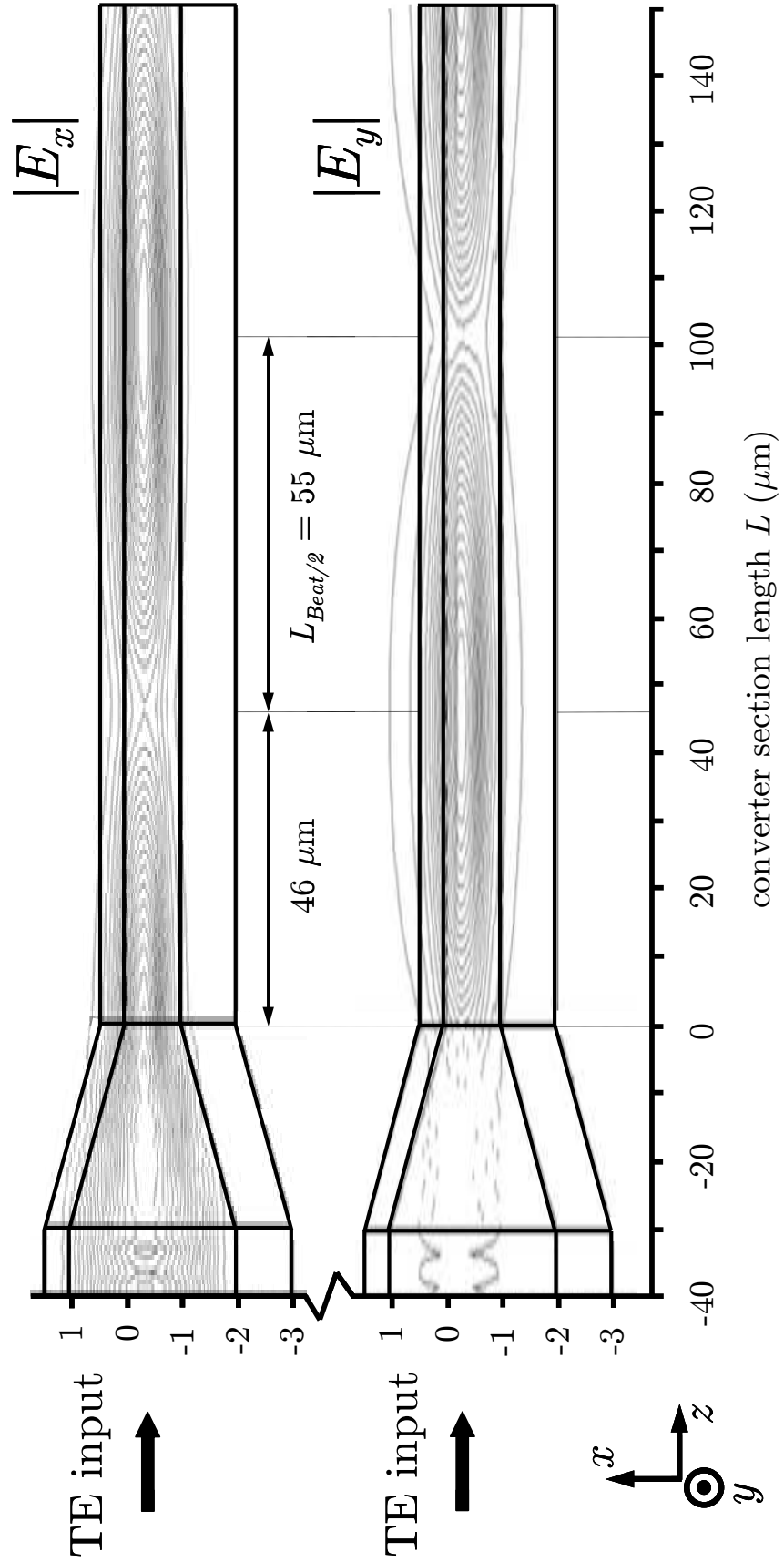


Figure 6-14: Top view of the simulated contour plots of the magnitude of the E_x (TE) and E_y (TM) component of a TE polarised signal launched into the fabricated device ($\xi = 50^\circ$, $\alpha = 55^\circ$, $w = 980$ nm) at an operating wavelength of $\lambda = 1064$ nm.

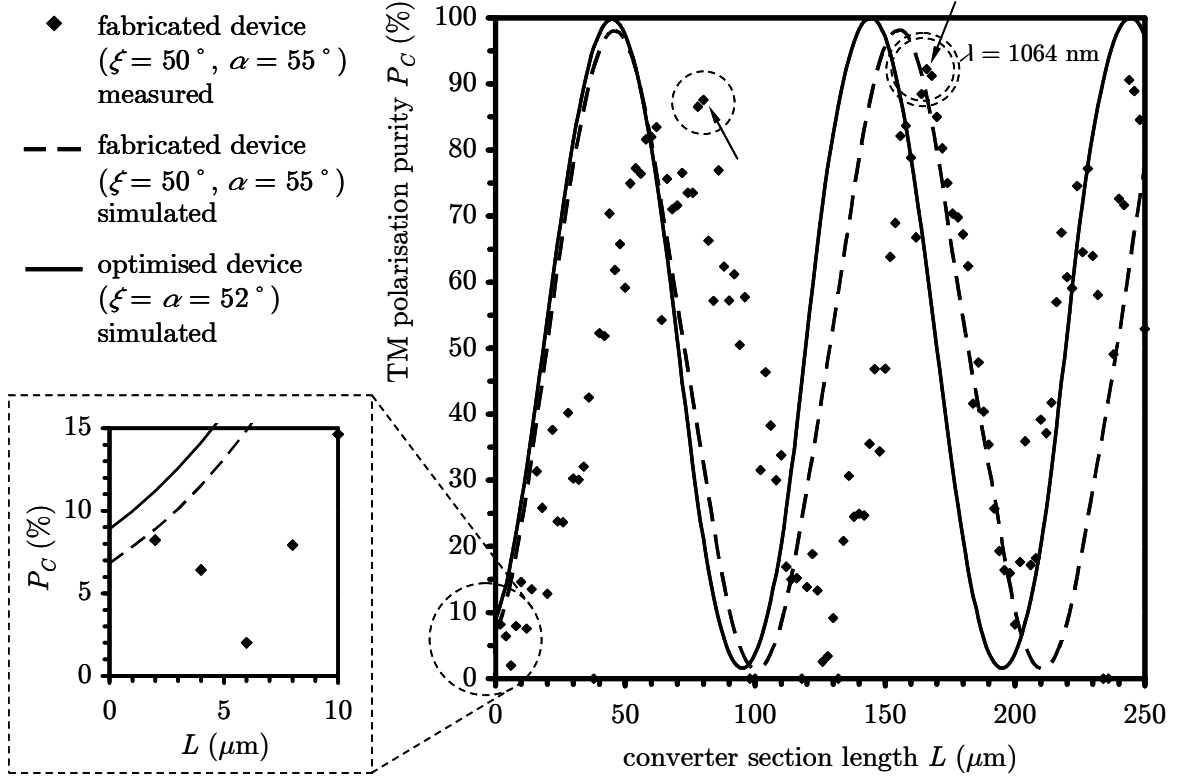


Figure 6-15: TM polarisation purity P_C versus converter section length L of the measured fabricated device and the theoretically optimised device at an operating wavelength of $\lambda = 1064 \text{ nm}$. (Insert) Magnified P_C versus L dependence at the beginning of the converter section.

6.8.2 Losses

The loss characteristics of the fabricated device were evaluated via the cutback-method as described in chapter 4. The insertion loss and propagation loss of the realised device was extracted from Figure 6-16. The trend line of the linear extrapolated normalised measured total power, expressed by the linear function $y = -0.0009x + 0.58$, yielded an insertion loss of 2.37 dB and a propagation loss of 0.73 dB / 100 μm - caused by the converter section. The encircled data point corresponds to the fabricated device achieving a P_C of 88% with a converter section length of 80 μm ($\xi = 50^\circ$, $\alpha = 55^\circ$ and $w = 980 \text{ nm}$), imposing a total device loss (including propagation- and insertion/exit losses) of 0.84 dB. The device achieving a P_C of 92% with a converter section length of 166 μm imposes a total device loss of 2.13 dB (double encircled data point). The scattering of the data points from the trend line is a result of coupling errors that occur due to the application of the end-fire coupling technique under the assumption of no fabrication inconsistencies on the waveguides.

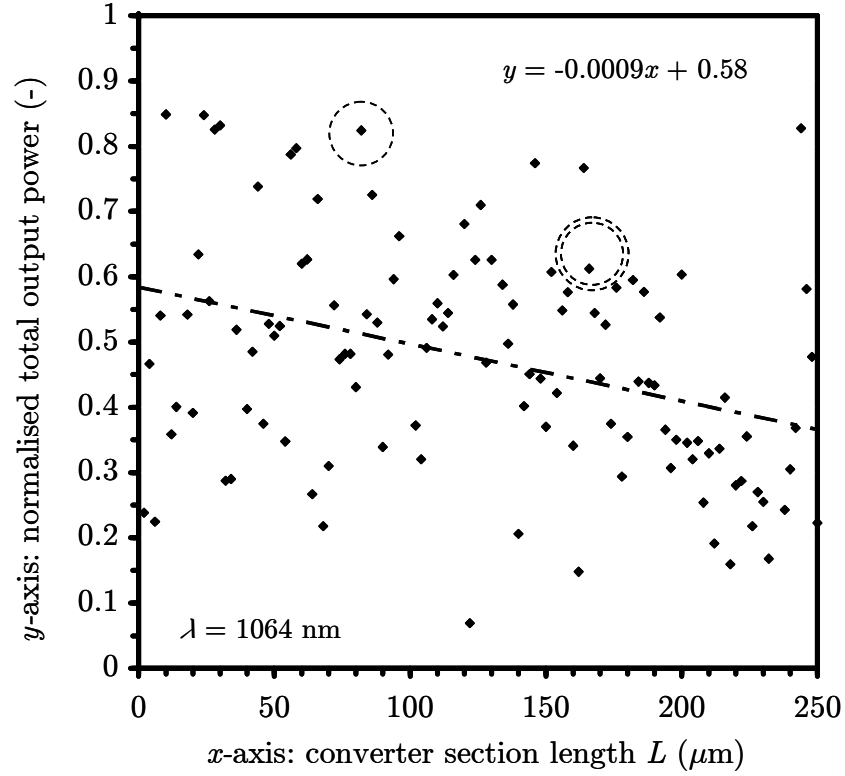


Figure 6-16: Measured normalised total output power versus different converter section lengths of the device for an operating wavelength of $\lambda = 1064 \text{ nm}$. The extrapolation of the measured data is indicated by the chain-dotted line governed by the equation $y = -0.0009x + 0.58$.

6.8.3 Wavelength stability

The considered device was optimised for a designated wavelength of $\lambda = 1064 \text{ nm}$. As the waveguide geometry deviations of the fabricated device from the theoretical optimised one are minimal ($\Delta\zeta = 2^\circ$, $\Delta\alpha = 3^\circ$ and $\Delta w = 20 \text{ nm}$), the wavelength dependence of the TM polarisation purity of only the fabricated device ($\zeta = 50^\circ$, $\alpha = 55^\circ$, $w = 980 \text{ nm}$) was simulated (Figure 6-17). As the dimensions of the converter waveguide cross section profile are close to the mode cut-off at the designed wavelength, modes at wavelengths higher than the designated are therefore not excited in the waveguide. The designated wavelength represents the upper limit of the operational wavelength range of the device. This is indicated by the vertical line at $\lambda = 1064 \text{ nm}$. A P_C -decrease of about 6% / 100 nm, with respect to P_C at the designated wavelength $\lambda = 1064 \text{ nm}$, occurs in the wavelength range from 950 nm to 1064 nm. From $\lambda = 950 \text{ nm}$ towards shorter wavelengths, a P_C -decrease of about 17% / 100 nm, with respect to P_C at $\lambda = 950 \text{ nm}$, occurs. This is indicated by the chain-dotted triangles in Figure 6-17.

The lower limit of the operational wavelength range of the device is determined by the bandgap energy of GaAs (1.43 eV), which corresponds to a wavelength of 867 nm at room temperature.

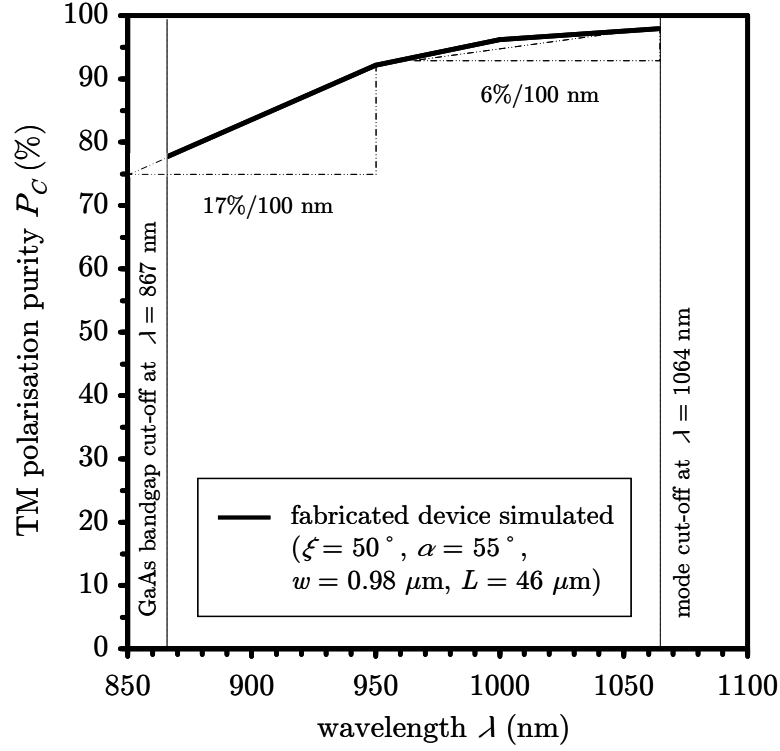


Figure 6-17: Simulated wavelength dependence of the TM polarisation purity P_C for the fabricated device.

6.9 Summary

A passive polarisation converter device functionality on a DQW SCH GaAs/AlGaAs material was demonstrated. The entire device consisted of an asymmetric waveguide structure with two angled waveguide sidewalls. The $3\text{ }\mu\text{m}$ wide input waveguide was mode matched to the converter section waveguide via a $30\text{ }\mu\text{m}$ long adiabatic linear taper. A converted TM polarisation purity P_C of 88% (for a TE polarised input signal) for a converter section length of $80\text{ }\mu\text{m}$ and waveguide width w of 980 nm was achieved for an operating wavelength of $\lambda = 1064\text{ nm}$. The optical loss imposed by this device was evaluated to be 0.84 dB via the cut-back method.

6.10 References

- [1] Walker C. L., "Quantum well intermixing for high brightness semiconductor lasers", *PhD thesis*, University of Glasgow, Glasgow, United Kingdom, (2002).
- [2] Ghafouri-Shiraz H., "*The principles of semiconductor laser diodes and amplifiers*", 1st ed., Imperial College Press, London, UK, ISBN 1-86094-339-X, (2004).
- [3] Zappe H. P., "*Introduction to Semiconductor Integrated Optics*", Artech House, Boston, USA, ISBN 0-89006-789-9, (1995).
- [4] Thompson G. H. B., "*Physics of Semiconductor Laser Devices*", 1st ed., John Wiley & Sons, Ltd., Chichester, UK, ISBN 0-471-27685-5, (1980).
- [5] Singh J., "*Electronic and Optoelectronic Properties of Semiconductor Structures*", 1st ed., Cambridge University Press, Cambridge, UK, ISBN 0-521-82379-X, (2003).
- [6] Rosencher E. and Vinter B., "*Optoelectronics*", 1st ed., Cambridge University Press, New York, USA, ISBN 0-521-77129-3, (2002).
- [7] Liboff R. L., "*Introductory Quantum Mechanics*", 1st ed., Addison-Wesley, Reading, United Kingdom, ISBN 0-201-12221-9, (1980).
- [8] Coldren L. A. and Corzine S. W., "*Diode lasers and photonic integrated circuits*", 1st ed., Wiley, New York, USA, ISBN 0471118753, (1995).
- [9] Casey H. C. and Panish M. B., "*Heterostructure Lasers: Part A, Fundamental Principles*", Academic Press, New York, USA, ISBN 0-12-163101-X, (1978).
- [10] Casey H. C. and Panish M., "*Heterostructure Lasers: Part B, Materials and Operating Characteristics*", Academic Press, New York, USA, ISBN 0-12-163102-8, (1978).
- [11] Bhattacharya P., "*Semiconductor Optoelectronic Devices*", 2nd ed., Prentice-Hall Inc., New Jersey, USA, ISBN 0-13-495656-7, (1997).
- [12] Erwin G., "Compact semiconductor lasers", *PhD thesis*, University of Glasgow, Glasgow, United Kingdom, (2007).
- [13] Blood P., "Evaluation of laser diode performance", in *Proceedings of the International Summer School on Physics of Semiconductor Lasers*, Gregynog, Wales, United Kingdom, 16 - 25 August 2004.
- [14] Senior J. M., "*Optical Fiber Communications*", 2nd ed., Prentice Hall, New York, USA, ISBN 0-13-635426-2, (1992).
- [15] Etrillard J. J.-P., "Reactive Ion Etching of Gallium Arsenide in CCl_2F_2 and SiCl_4 Plasmas: Influence of Chamber Material and Etching Mask", *Japanese Journal of Applied Physics, Part 1*, vol. **7A**, pp. 4126 - 4132, (1994).

Chapter 7

Passive polarisation converter monolithically integrated within a semiconductor laser diode

7.1 Introduction

The ability to control and manipulate the state of polarisation of optical signals is becoming an increasingly desirable feature in numerous applications including integrated optical circuits, *semiconductor optical amplifiers* (SOAs) [1] and optical communication systems based on *dense wavelength division multiplexing* (DWDM) [2-5]. Conventional lattice-matched (i.e. unstrained) III-V semiconductor QW heterostructure edge-emitting lasers based on interband transitions predominantly emit TE polarised light [6]. This polarisation dependence of the optical gain primarily originates from the symmetry of the uppermost, *heavy-hole* (hh), valence band in the quantum well. In addition, the larger TE mode overlap with the optical gain distribution in the waveguide core due to the cross sectional geometry [7] and the higher TE polarised mode reflectivity of the cleaved facets [8], normally yields an overall lower threshold current for TE polarised modes than for TM polarised modes.

In order to obtain TM polarised laser output signals, several techniques to manipulate the SOP on the integrated and discrete level have been applied. In particular on the integrated level, tensile strain in the quantum well structure due to lattice-mismatched core layers has been introduced during the growth process in order to invert the hh and *light-hole* (lh) energy states in the valence band. This results in an emission of either predominantly TM polarised, or a combination of TE- and TM polarised modes [9-11], for example with the goal of implementing polarisation independent gain. In order to manipulate the oscillation properties of semiconductor lasers post growth on the discrete level, structures based on injected light from external pump sources [12, 13] and external optical feedback by means of compound-cavity configurations [14-18] have also been reported.

This chapter introduces the design, fabrication and characterisation of the monolithic integration of a laser source with a passive single-section waveguide polarisation rotator on an unstrained GaAs/AlGaAs DQW heterostructure material.

7.2 Device configuration

The laser cavity consists of a pumped section and a passive polarisation rotating section (Figure 7-1). It is bound in the longitudinal direction by a cleaved facet at a ridge waveguide (back mirror) and a cleaved facet at the end of the passive converter section (front mirror). The shallow-etched pumping section was realised by a $3\ \mu\text{m}$ wide ridge waveguide structure. The passive section comprises two angled waveguide sidewalls, as introduced in the previous chapter, which were deeply etched through the core. It consists of a linear $70\ \mu\text{m}$ long adiabatic taper, a converter section of a certain length and a linear adiabatic output taper. The taper lengths were chosen above the adiabatic limit - as calculated in the previous chapter - in order to ensure a low-loss power transition in the tapers, which are part of the laser cavity. The $70\ \mu\text{m}$ long adiabatic linear taper was introduced for the purpose of matching the radically different lateral size of the fundamental TE polarised mode in the shallow etched pumped section smoothly into that of the two lowest order excited modes (mode 1 and mode 2 (Figure 7-1(Insert))) in the

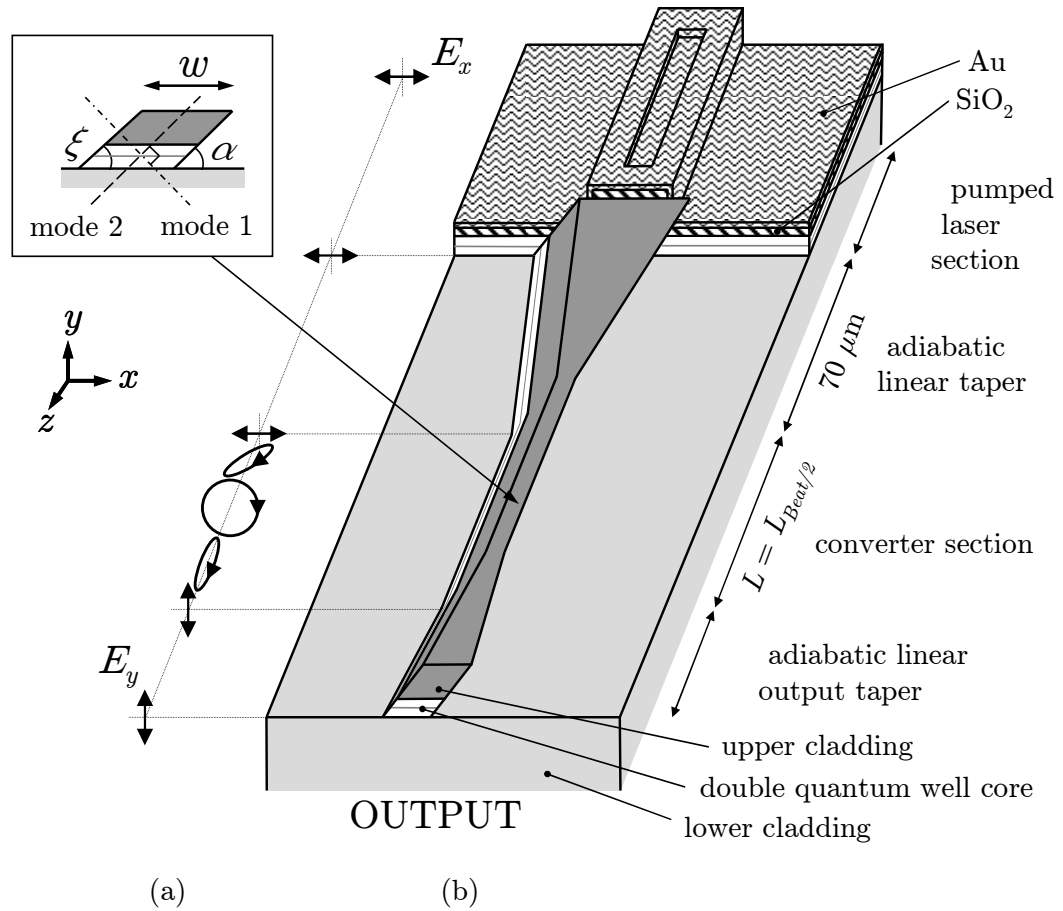


Figure 7-1: Schematic of the design and functionality of the monolithically integrated passive polarisation converter in a Fabry-Perot laser cavity. (a) Evolution of the electric field in the device. (b) Device configuration (not to scale). (Insert) Definition of waveguide profile parameters (front slope angle ξ , undercut slope angle α and waveguide top width w) and illustration of the orientation of the optical axes, which determine the orientation of the excited lowest order modes (mode 1 (chain dotted line) and mode 2 (dashed line)) in the waveguide.

deeply-etched converter section. This avoids large optical losses at the intersection that would occur if these two sections were simply butt-coupled together. The linear adiabatic taper at the output facet was introduced in order to widen the submicron dimensions of the converter section up to a width of $2\ \mu\text{m}$. This output taper does not only define the converter section length, but also facilitates ease of cleaving or, if applicable, provides an interconnection for further monolithically integrated sections with different functionalities. As the total length of the entire device is fixed by the cleaving process, different converter section lengths will have different output taper lengths. The used material structure was introduced in chapter 6.

7.3 Device optimisation

The theoretical optimisation of the converter section waveguide geometry for an operating wavelength of $\lambda = 867\ \text{nm}$ was conducted in chapter 6. For the sake of simplification of theoretical optimisation efforts, both angles were chosen to be equal ($\xi = \alpha$). The optimised device dimensions for the given wafer material structure to achieve a maximum achievable converted polarisation purity P_C of $> 99\%$ at the output are $w = 670\ \text{nm}$, $L_{\text{Beat}/2} = 22\ \mu\text{m}$ and $\xi = \alpha = 52^\circ$.

7.3.1 Optimisation of the transversal offset τ

Figure 7-2 displays the contour plots of the mode profile (magnitude of the E_x component) at both the end of the pumped laser section ($L = 0^-$ (grey line) and the beginning of the passive converter waveguide section ($L = 0^+$ (dashed line)). The not optimised overlap of both mode profiles due to different waveguide cross section geometries causes an optical loss at the intersection. In order to optimise the mode profile overlap, a transversal converter section offset τ was introduced. A zero-offset corresponds to the lateral alignment of the top edge of the shallow-etched pumped laser section sidewall with the top edge of the sloped sidewall (defined by the front slope angle ξ) at the beginning of the taper section. A positive value of τ corresponds to a shift of the pumped laser section towards the positive x -direction, whereas the taper section remains in place. The cross-sectional view of the intersection at $\tau = 0$ is also illustrated in Figure 7-2.

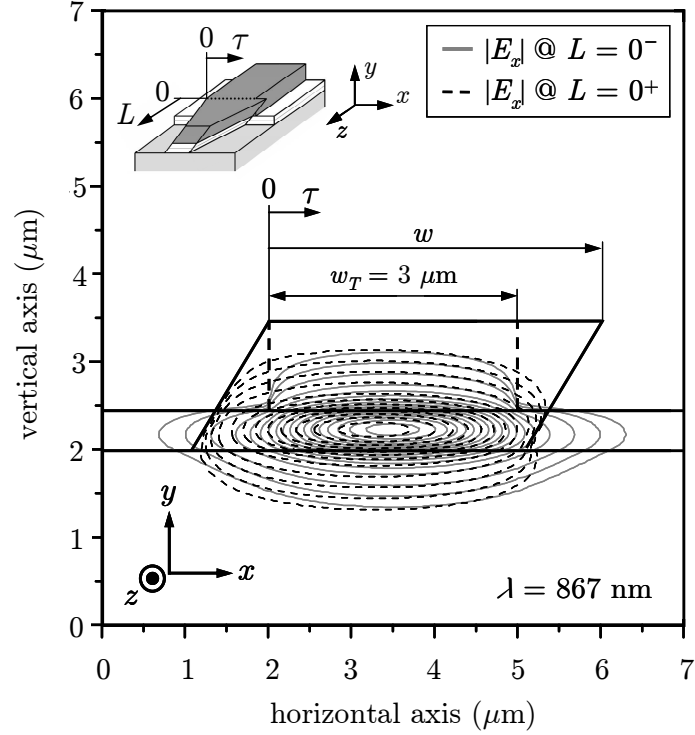


Figure 7-2: Illustration of the overlap of the mode profile contour plots (here: magnitude of the E_x component of a generated TE polarised signal in the pumped laser section) directly before ($L = 0^-$ (grey line)) and directly after ($L = 0^+$ (dashed line)) the intersection between passive converter- and pumped laser section.

The optimisation was conducted by utilising the wave propagation calculation module that comes with the commercially available mode solver mentioned in chapter 2. The modelled layer structure and waveguide section configuration are illustrated in Figure 7-2 and Figure 7-2(Insert), respectively. As the input power (P_{INPUT}) was kept constant, the transmitted power (P_{OUTPUT}) - depending on both the transversal offset τ and the taper width w at the intersection - was monitored. The intersection loss was defined as $-10 \times \log_{10}(P_{\text{OUTPUT}}/P_{\text{INPUT}})$ (in dB). While the waveguide width w_T of the shallow-etched laser section was kept constant ($w_T = 3 \mu\text{m}$), both τ ($0 \leq \tau \leq 2 \mu\text{m}$) and the taper width w at the intersection ($2 \mu\text{m} \leq w \leq 5 \mu\text{m}$) were varied in order to determine the lowest optical loss at the intersection. This is shown in Figure 7-3. Considering a taper width w of $4 \mu\text{m}$ at the intersection, the optical loss at the intersection is lower than 0.06 dB within a range of $0 \leq \tau \leq 0.7 \mu\text{m}$. Taper widths $w > 4 \mu\text{m}$ have a negligible impact on the intersection loss within the taper offset range of $0 \leq \tau \leq 0.7 \mu\text{m}$. The illustration of the mode profile contour plot overlaps at the intersection, which is given in Figure 7-2, shows one of the reasonable configurations ($\tau = 0 \mu\text{m}$, $w = 4 \mu\text{m}$).

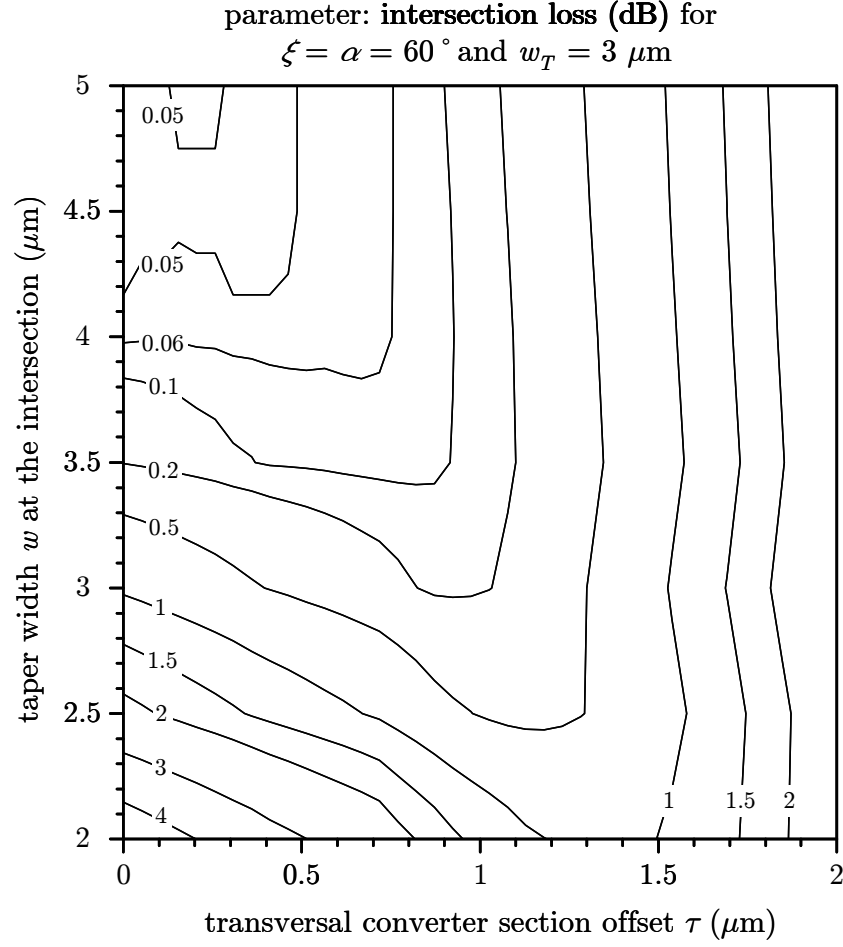


Figure 7-3: Dependence of the intersection loss on the converter section taper width w and the transversal converter section offset τ at the intersection between the pumped laser- and passive converter waveguide section at an operating wavelength of $\lambda = 867 \text{ nm}$.

7.4 Device fabrication

7.4.1 Fabrication process steps

An illustration of the chronology of the fabrication steps is given in Figure 7-4 and Figure 7-5. The initial realisation of the e-beam alignment markers is not included in the schematics as the emphasis is given on the actual fabrication of the device.

Step 1: Creation of e-beam position calibration markers

The e-beam position calibration markers were fabricated according to the description in chapter 5.

Step 2: Realisation of the SiO₂ mask pattern of the converter section waveguide outlines

1. Deposition of 200 nm PECVD SiO₂.
2. Spin-coat positive e-beam resist (PMMA 4% ELV 2041) at 5000 rpm for 60 seconds.
3. Clean backside of sample with in acetone soaked cotton bud before a 15 minutes bake in oven @ 180 ° C.
4. Spin-coat second positive e-beam resist layer (PMMA 4% ELV 2041) at 5000 rpm for 60 seconds (Figure 7-4(a)).
5. Clean backside of sample with in acetone soaked cotton bud before a 90 minutes bake in oven @ 180 ° C.
6. Exposure of converter section waveguide outline pattern. EBPG 5 e-beamwriter control file parameters: resolution: 25 nm (high) / 250 nm (low), proximity correction file: gaas200-50b.pec, prox min: 0.1, prox grid: 0.025, dose: 136 $\mu\text{C}/\text{cm}^2$ (high resolution) / 250 $\mu\text{C}/\text{cm}^2$ (low resolution), spot size: 56 nm (high resolution) / 400 nm (low resolution), job type: simple (Figure 7-4(b)).
7. Development of converter section waveguide pattern using 2:1 IPA:MIBK developer solution for 75 seconds @ 23.1 ° C. Dip in IPA for 10 seconds; Blow dry with nitrogen.
8. SiO₂ dry-etch of waveguide pattern using CHF₃ as a reactive gas in the BP80 machine. BP80 parameter settings: process gas: CHF₃, corrected gas flow: 20 sccm, process pressure: 17 mTorr, forward RF power: 100 W, temperature: 25 ° C, BIAS: -280 V, process time: 13 minutes.
9. Removal of e-beam resist mask via an O₂ ash process using the BP80 machine (Figure 7-4(c)). BP80 parameter settings: process gas: O₂, corrected gas flow: 20 sccm, process pressure: 20 mTorr, forward RF power: 100 W, temperature: 25 ° C, BIAS: 320 V, process time: 25 minutes.

Step 3: Realisation of the angled converter section waveguide structure

10. Angled GaAs dry-etch of converter waveguide section using SiCl₄ as a reactive gas in the S100 T-Gate machine (Figure 7-4(c)).
Angled waveguide-etch S100 T-Gate process parameters: process gas: SiCl₄, corrected gas flow: 9 sccm, process pressure: 9 mTorr, forward RF power: 100 W, temperature: 25 ° C, BIAS: -346 V, process time: 17 minutes, customised anodised aluminium sample holder used, slope angle of sample holder is 75 ° with respect to the horizontal plane.
11. Removal of SiO₂ layer via wet chemical etching using a buffered (hydrofluoric acid) HF:RO (reverse osmosis water) solution (ratio 5:1) for 45 seconds at a temperature of 25 ° C; Rinse thoroughly in RO water for 10 minutes; Blow dry using nitrogen (Figure 7-4(d)).

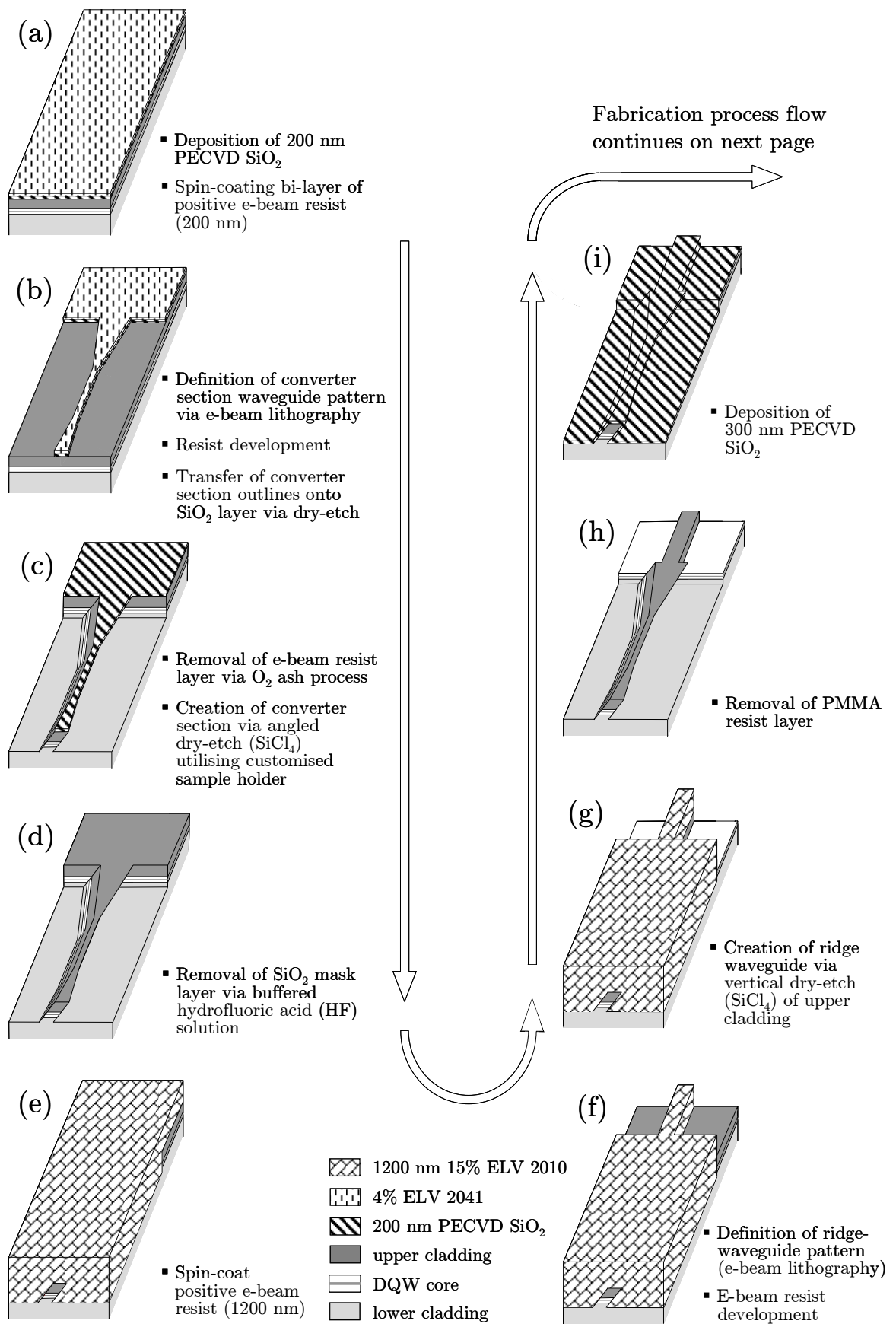


Figure 7-4: (a)-(i) Schematic process flow diagram of the realised monolithically integrated passive polarisation converter within a semiconductor laser diode. (part 1)

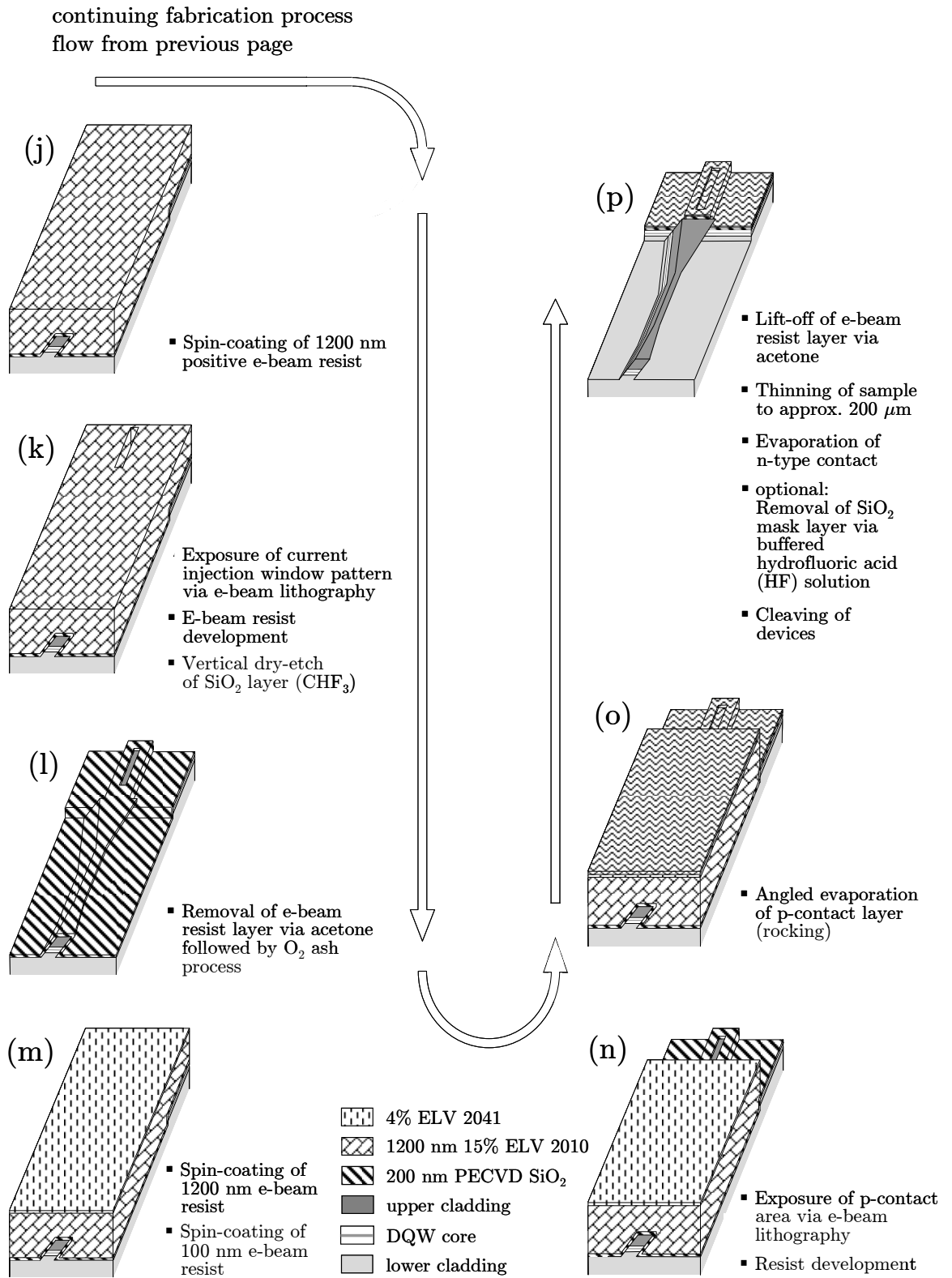


Figure 7-5: (j)-(p) Schematic process flow diagram of the realised monolithically integrated passive polarisation converter within a semiconductor laser diode. (part 2)

Step 4: Realisation of the ridge waveguide structure of the pumped section

12. Spin-coat positive e-beam resist (PMMA 15% ELV 2010) at 5000 rpm for 60 seconds (Figure 7-4(e)).
13. Clean backside of sample with in acetone soaked cotton bud before a 90 minutes bake in oven @ 180 ° C.
14. Exposure of pumped section area. EBPG 5 e-beam-writer control file parameters: resolution: 25 nm (high) / 250 nm (low), proximity correction file: gaas200-50b.pec, prox min: 0.1, prox grid: 0.025, dose: 270 $\mu\text{C}/\text{cm}^2$ (high resolution) / 490 $\mu\text{C}/\text{cm}^2$ (low resolution), spot size: 56 nm (high resolution) / 400 nm (low resolution) (Figure 7-4(f)).
15. Development of pumped section using 2.5:1 IPA:MIBK developer solution for 30 seconds @ 23.1 ° C and subsequent dip in IPA for 10 seconds; Blow dry with nitrogen.
16. Vertical GaAs dry-etch of the rib waveguide pattern using SiCl_4 as a reactive gas in the S100 machine (Figure 7-4(g)).
Vertical waveguide etch S100 process parameters: process gas: SiCl_4 , corrected gas flow: 18 sccm, process pressure: 9 mTorr, forward RF power: 250 W, temperature: 25 ° C, process time: 10:10 minutes, quartz carrier wafer used.
17. Removal of e-beam resist mask via using acetone in a hot water bath (65 ° C) for 2 hours followed by an O_2 ash process using the BP80 machine (Figure 7-4(h)). BP80 parameter settings: process gas: O_2 , corrected gas flow: 20 sccm, process pressure: 20 mTorr, forward RF power: 100 W, temperature: 25 ° C, BIAS: -320 V, process time: 25 minutes.

Step 5: Realisation of the current injection window on top of the ridge waveguide structure

18. Deposition of 300 nm PECVD SiO_2 (Figure 7-4(i)). This ensures sufficient isolation of the etched regions and ridge sidewalls.
19. Spin-coat positive e-beam resist (PMMA 15% ELV 2010) at 5000 rpm for 60 seconds (Figure 7-5(j)).
20. Clean backside of sample with in Acetone soaked cotton bud before a 90 minutes bake in oven @ 180 ° C.
21. Exposure of current injection window. EBPG 5 e-beam-writer control file parameters: resolution: 25 nm (high) / 250 nm (low), proximity correction file: gaas200-50b.pec, prox min: 0.1, prox grid: 0.025, dose: 270 $\mu\text{C}/\text{cm}^2$ (high resolution) / 490 $\mu\text{C}/\text{cm}^2$ (low resolution), spot size: 56 nm (high resolution) / 400 nm (low resolution) (Figure 7-5(k)).
22. Development of pumped section using 2.5:1 IPA:MIBK developer solution for 30 seconds @ 23.1 ° C and subsequent dip in IPA for 10 seconds; Blow dry with nitrogen.

23. SiO₂ dry-etch of waveguide pattern using CHF₃ as a reactive gas in the BP80 machine. BP80 parameter settings: process gas: CHF₃, corrected gas flow: 20 sccm, process pressure: 17 mTorr, forward RF power: 100 W, temperature: 25 ° C, BIAS: -280 V, process time: 13 minutes.
24. Removal of e-beam resist mask via using acetone in a hot water bath (65 ° C) for 2 hours followed by an O₂ ash process using the BP80 machine (Figure 7-5(l)). BP80 parameter settings: process gas: O₂, corrected gas flow: 20 sccm, process pressure: 20 mTorr, forward RF power: 100 W, temperature: 25 ° C, BIAS: -320 V, process time: 25 minutes.

Step 6: Realisation of the p-contact metallisation in the pumped section

This fabrication step was conducted via the lift-off technique as described in chapter 5. Prior to the metal evaporation, a deoxidation process was conducted in order to ensure a GaAs-surface free of native oxides, which would otherwise lead to a bad quality of the metal contact. The directional metal evaporation usually results in a poor coverage of the ridge waveguide sidewalls when the sample is placed horizontally into the evaporation chamber. This can cause difficulties to establish a current injection into the device. The sample is therefore tilted by an angle of 45 ° with respect to the horizontal direction during the evaporation process in order to ensure a satisfying metallisation of the ridge waveguide sidewall. This fabrication step needs to be repeated from the opposite direction for the metallisation of the other ridge waveguide sidewall.

25. Spin-coat positive e-beam resist (PMMA 15% ELV 2010) (low molecular weight) at 5000 rpm for 60 seconds (Figure 7-5(m)).
26. Clean backside of sample with in acetone soaked cotton bud before a 15 minutes bake in the oven @ 180 ° C.
27. Spin-coat positive e-beam resist (PMMA 4% ELV 2041) (higher molecular weight) at 5000 rpm for 60 seconds.
28. Clean backside of sample with in acetone soaked cotton bud before a 2 hours bake in the oven @ 180 ° C.
29. Exposure of p-contact pattern. EBPG 5 e-beam-writer control file parameters: resolution: 100 nm, proximity correction file: gaas700-50t.pec, prox min: 1, prox grid: 0.2, dose: 250 $\mu\text{C}/\text{cm}^2$, spot size: 160 nm, job type: simple (Figure 7-5(n)).
30. Development of p-contact pattern using 2:1 IPA:MIBK (methyl isobutyl ketone) developer solution for 75 seconds @ 23.1 ° C; Dip in IPA for 10 seconds; Blow dry with nitrogen.
31. Deoxidation of GaAs surface by dipping the sample into a buffered (hydrochloric acid) HCl:RO (reverse osmosis water) solution (ratio 1:10) for 30 seconds at a temperature of 25 ° C; Rinse thoroughly in RO water for 10 minutes; Blow dry using nitrogen; Place sample in oven @ 120 ° C for 30 minutes.
32. Sequential angled evaporation (at 45 ° with respect to the horizontal plane) of p-contact metal layers: Ti (33 nm) / Pd (33 nm) / Au (150 nm). This is repeated in opposite direction for covering the other waveguide sidewall (Figure 7-5(o)).
33. Lift-off p-contact layer with acetone in hot water bath (65 ° C) for 2 hours; Rinse sample in IPA; Blow dry with nitrogen.

Step 7: Realisation of the n-contact metallisation

34. Mounting of sample onto a glass coverslip: Spin-coat glass plate with S1818 photoresist at 750 rpm for 5 seconds, place sample *p-side down* onto the photoresist on the glass coverslip, put a little bit of pressure onto the sample, put glass plate onto hotplate @ 90 ° C for 5 minutes and subsequently into the oven @ 90 ° C for 30 minutes.
35. Clear back of sample (which is now on top) and backside of glass coverslip from photoresist with in acetone soaked cotton bud.
36. Mount glass coverslip onto a metal chuck using wax. Glass coverslip is used in order to prevent contact of sample with wax, because wax is difficult to remove from the sample surface.
37. Thinning of sample by lapping the back of the sample with calcium oxide powder (9 μm / 3 μm granules) - water mix on a glass plate. The sample is thinned to a thickness of approximately 200 μm .
38. Clear off wax from glass coverslip with Opticlear in hot water bath (65 ° C) for 30 minutes; Release sample from glass coverslip with acetone in hot water bath (65 ° C) for 30 minutes; Rinse sample in IPA; Blow dry with nitrogen.
39. Mounting of sample onto a glass coverslip: Spin-coat glass plate with S1818 photoresist at 750 rpm for 5 seconds, place sample *p-side down* onto the photoresist on the glass coverslip, put a little bit of pressure onto the sample, put glass plate onto hotplate @ 90 ° C for 5 minutes and subsequently into the oven @ 90 ° C for 30 minutes.
40. Deoxidation of sample surface by dipping the sample into a buffered (hydrochloric acid) HCl:RO (reverse osmosis water) solution (ratio 1:10) for 30 seconds at a temperature of 25 ° C; Rinse thoroughly in RO water for 10 minutes; Blow dry using nitrogen; Place sample in oven @ 120 ° C for 30 minutes.
41. Sequential evaporation of n-contact metal layers: Au (11 nm) / Ge (11 nm) / Ni (11 nm) / Au (140 nm).
42. Release sample from glass coverslip with acetone in hot water bath (65 ° C) for 30 minutes; Rinse sample in IPA; Blow dry with nitrogen.
43. Annealing of sample in *rapid thermal annealer* (RTA) @ 360 ° C for 60 seconds in inert nitrogen atmosphere (recipe 9) in order to form the ohmic contacts.
44. Sample scribed and cleaved into individual devices.

7.4.2 Realised device

A top view of the fabricated device, which shows the pumped laser section - indicated by the gold pad used for p-contact) and the passive polarisation converter section, is given in Figure 7-6(a). The cleaved facet at the laser section end (on the top edge of Figure 7-6(a)

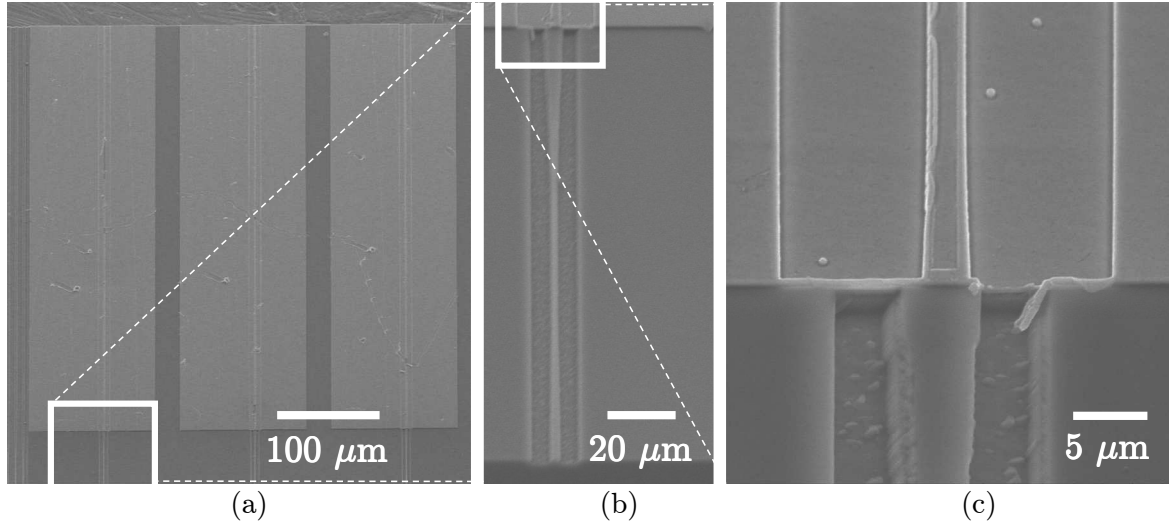


Figure 7-6: (a) SEM micrograph top view of the fabricated device consisting of the pumped laser section (indicated by the gold pad used for p-contact) and the passive polarisation converter section. (b) Magnified SEM micrograph top view of the passive polarisation converter section. (c) Magnified SEM micrograph top view of the intersection between the pumped laser section and the passive polarisation converter section.

defines the pumped laser section to a length of about 1250 μm. Figure 7-6(b) illustrates a magnified view of the passive waveguide section. The converter section length and output taper length of this particular displayed device is 20 μm and 50 μm, respectively. The intersection between the pumped section and passive waveguide section can be depicted in Figure 7-6(c). It also shows the 1 μm wide p-contact window on top of the ridge waveguide structure of the pumped section. Figure 7-7(a) displays the transition from the

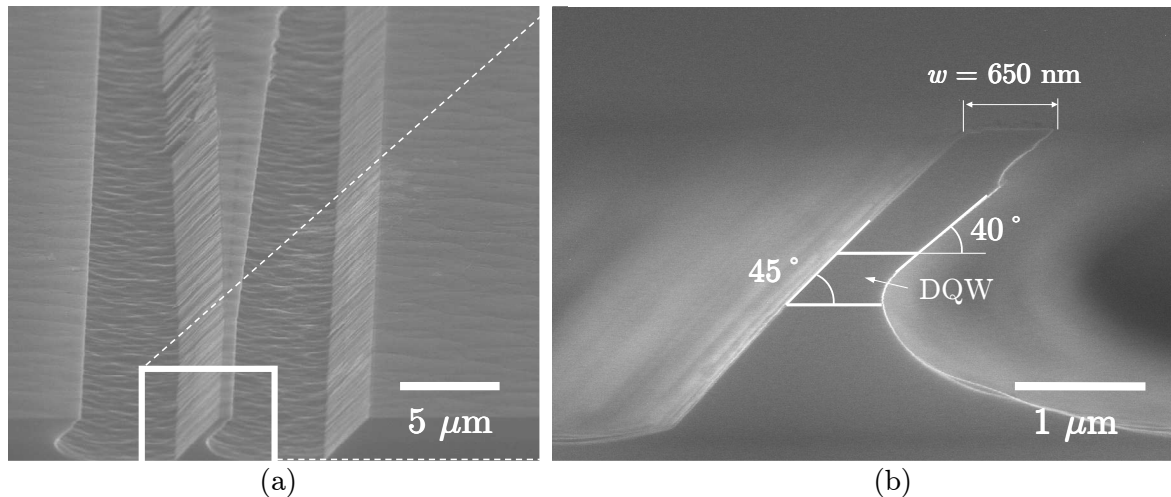


Figure 7-7: (a) SEM micrograph of the deeply etched passive section showing the transition between the linear adiabatic taper and the converter section. (b) SEM micrograph of the waveguide cross section profile of the polarisation converter section.

linear adiabatic input taper to the converter section of the fabricated device. The fabricated waveguide cross section profile of the converter section is shown in Figure 7-7(b). The profile consists of a front slope angle of $\zeta = 45^\circ$, an undercut slope angle of $\alpha = 40^\circ$ and a waveguide top width of $w = 650$ nm.

7.5 Device characterisation

7.5.1 Emitting wavelength

The measured optical spectrum at the output facet of the measured device indicated an emitting wavelength of $\lambda = 867.1$ nm and a line width of 0.1 nm (Figure 7-8). An expression for the description of the spectral purity of a semiconductor laser is given by the *side mode suppression ratio* (SMSR), which is defined as the ratio of the power in the main mode to that of the most intense side mode [7]. The device emitted in a single longitudinal mode with an SMSR of 25 dB. In comparison, SMSR values exceeding 30 dB are generally desirable in telecom applications at a wavelength of $1.55 \mu\text{m}$. The power peak of -49 dBm at $\lambda = 866.5$ nm indicates two sets of optical fringes corresponding to a compound cavity device. These originate from reflections of the double cavity device, which impose a double modulation. Considering the polarisation distribution of the total output power, a substantial TM polarised component can be noted.

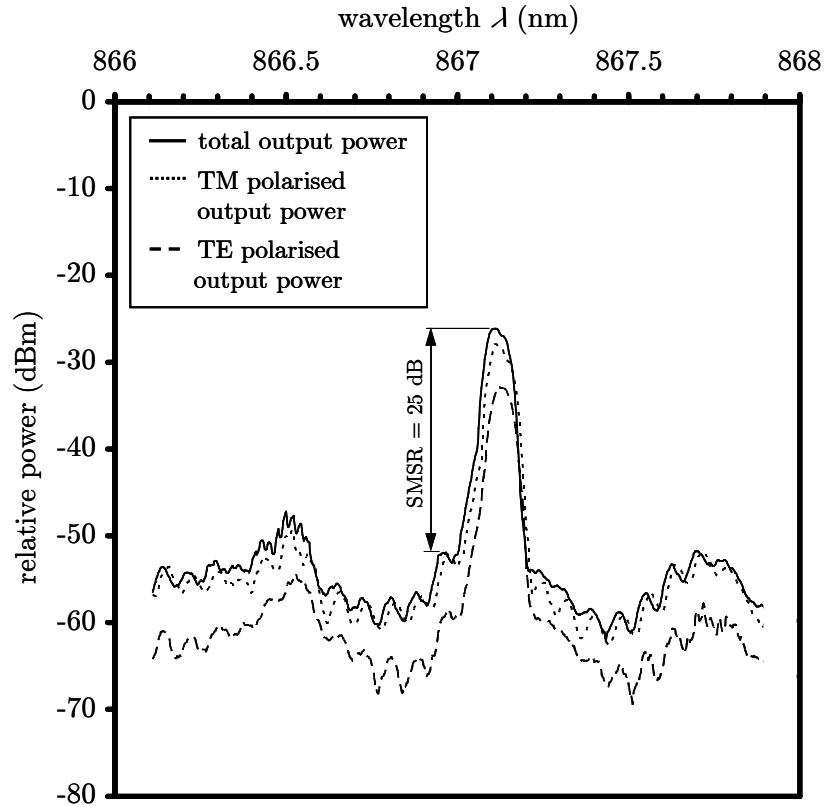


Figure 7-8: Measured optical spectrum at the output facet of the fabricated device, which consists of a converter section length of $20 \mu\text{m}$, at an injected current (continuous wave) of 150 mA (threshold current level = 100 mA). Measurement conducted by S. McMaster.

7.5.2 Converted TM polarisation purity

Figure 7-9 displays the dependence of the measured TM polarisation purity P_C on the converter section length at the polarisation converter facet of the fabricated device. This is

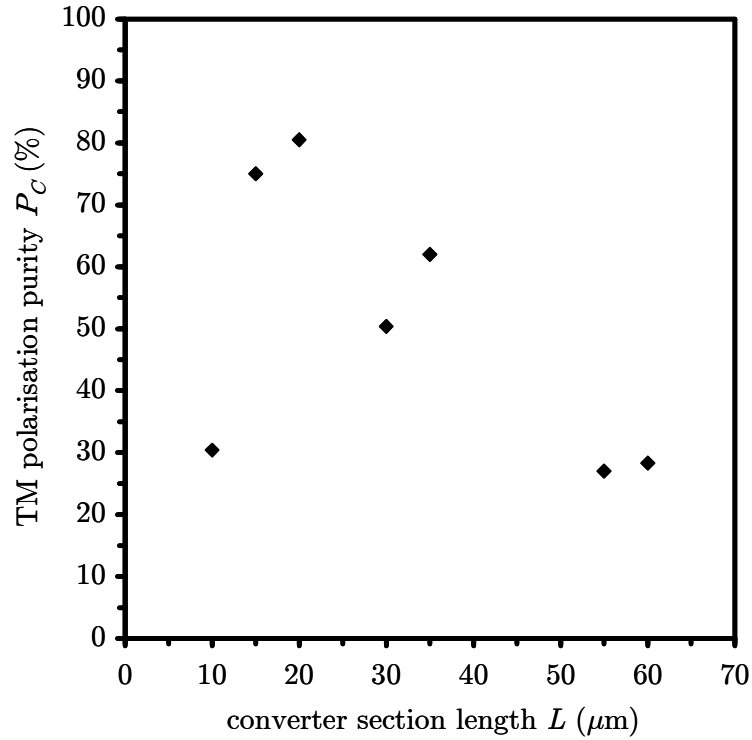


Figure 7-9: Evaluated TM polarisation purity P_C at the converter section facet versus the length of the converter section of the fabricated devices.

indicated by the diamond - shaped data points. With the fabricated converter section waveguide profile dimensions of $\xi = 45^\circ$, $\alpha = 40^\circ$ and $w = 650$ nm (Figure 7-7(b)), a maximum P_C of 80.5% for a converter section length of $20 \mu\text{m}$ was achieved. The resulting linear output taper length after cleaving was $50 \mu\text{m}$. This specific device was selected for the conduction of further characterisations.

The simulated functionality of the passive section of a waveguide with the fabricated converter section waveguide cross profile ($\xi = 45^\circ$, $\alpha = 40^\circ$ and $w = 650$ nm) at an operating wavelength of $\lambda = 867.1$ nm is illustrated in Figure 7-10. The emphasis of this simulation is given on the impact of the linear adiabatic output taper on the converted TM polarisation purity P_C . Figure 7-10(a,b) display the configuration with a $90 \mu\text{m}$ long converter section only, whereas Figure 7-10(c,d) display the configuration with a $20 \mu\text{m}$ long converter section, a $50 \mu\text{m}$ long linear adiabatic output taper and a $20 \mu\text{m}$ long output waveguide section (which corresponds to the fabricated device) instead.

Considering the configuration with the $90 \mu\text{m}$ long converter section only, it can be noted in the contour plot of the magnitude of the E_y (TM) component (Figure 7-10(a)) that the first maximum in the interference pattern of the TM polarised component, which corresponds to a P_C of about 95%, occurs at $16 \mu\text{m}$ - which is shorter than the $L_{\text{Beat}/2}$ of $22 \mu\text{m}$. This is due to the already commencing polarisation evolution towards the end of

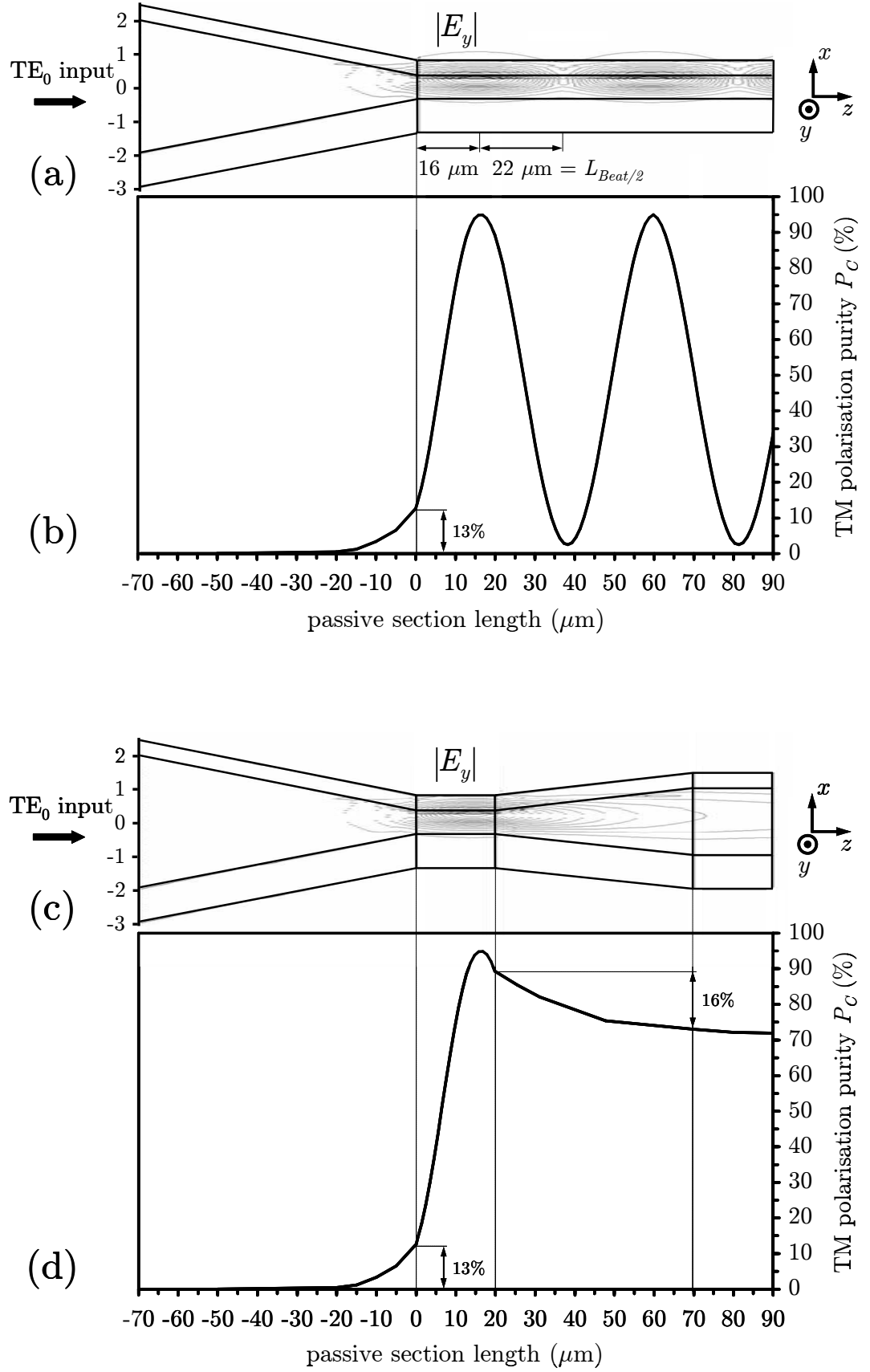


Figure 7-10: Top view of the simulated contour plot of the magnitude of the E_y (TM) component and calculated TM polarisation purity P_C versus the passive section length for a TE₀ polarised signal launched from the gain section into the passive section of the fabricated device ($\xi = 45^\circ$, $\alpha = 40^\circ$, $w = 650$ nm) (a, b) without output taper and -waveguide and (c, d) with a converter section length of 20 μm , 50 μm long linear output taper and 20 μm long output waveguide at an operational wavelength of $\lambda = 867.1$ nm.

the 70 μm long linear, adiabatic input taper which yields to a TM polarisation purity of 13% at the beginning of the converter section. A converter section length of 20 μm would yield a TM polarisation purity of 89% at the output.

The presence of the 50 μm long linear adiabatic output taper after the 20 μm long converter section has the purpose of not only defining the converter section length, but also to facilitate ease of cleaving or, if applicable, to provide an interconnection for further monolithically integrated sections with different functionalities. The output taper, however, imposes an additional polarisation conversion of 16% as it widens the 650 nm wide waveguide up to 2 μm (Figure 7-10(d)). Although its length is 20 μm shorter than the input taper (which narrows the waveguide width from 4 μm to 650 nm), it has a higher (+3%) polarisation conversion. This is due to the exposure of the signal to a narrower waveguide - which imposes a higher polarisation conversion - over an effective longer propagation distance. The output waveguide width of 2 μm is too wide in order to impose a substantial polarisation conversion on the signal. The theoretical TM polarisation purity at the output was expected to be 72% compared to the actual measured value of 80.5%.

7.5.3 Optical power emission versus injected current

The measured total power emission dependence on the injected current of the Fabry-Perot rib waveguide laser structure *without* the converter section is displayed in Figure 7-11. The

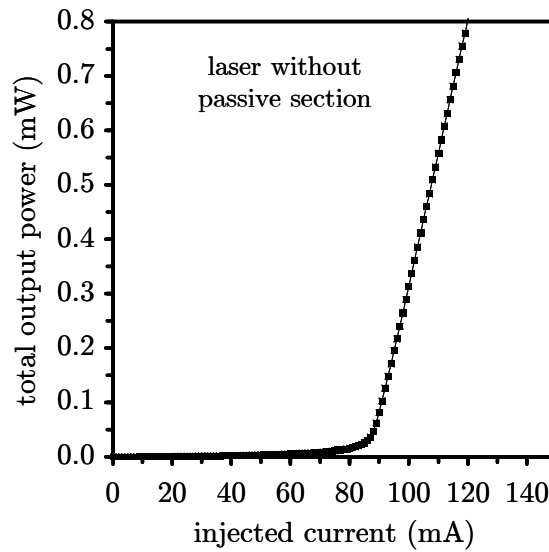


Figure 7-11: Measured total power emission dependence on the injected current of the device without the passive section. Measurement conducted by S. McMaster.

threshold current of this device is 88 mA. In comparison, the power emission dependence on the injected current for the device *including* the passive section is shown in Figure 7-12(a, b). The device - consisting of a converter section length of 20 μm - indicated a threshold current of 100 mA at both the pumped section facet (Figure 7-12(a)) and the polarisation converter facet (Figure 7-12(b)). The passive section therefore increases the threshold current by 14%. At currents of 120 mA or above, the output from the converter section facet consisted predominantly (80%) of TM polarised light (Figure 7-12(c)).

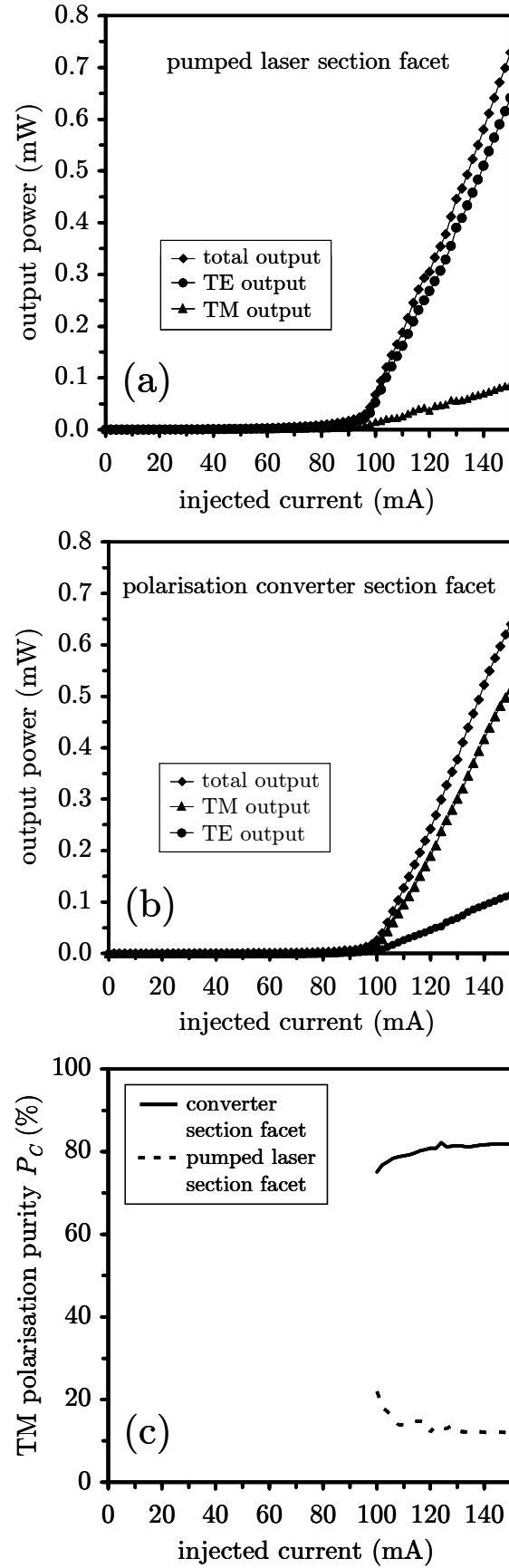


Figure 7-12: Measured power emission dependence on the injected current of the device including the passive section. The total output power and the separated TE and TM output powers at both (a) the pumped laser section facet and (b) the polarisation converter section facet is shown. (c) Resulting TM polarisation purity at both the pumped laser section facet and the polarisation converter section facet above the threshold level. Measurement conducted by S. McMaster.

The pumped section facet predominantly (90%) consisted of TE polarised light (extracted from Figure 7-12(b)). The predominantly (80%) TM polarised light at the converter section facet can also be noted in the wavelength spectrum (Figure 7-13) for an injected current of 150 mA. The emitting wavelength of $\lambda = 867.1$ nm is also shown.

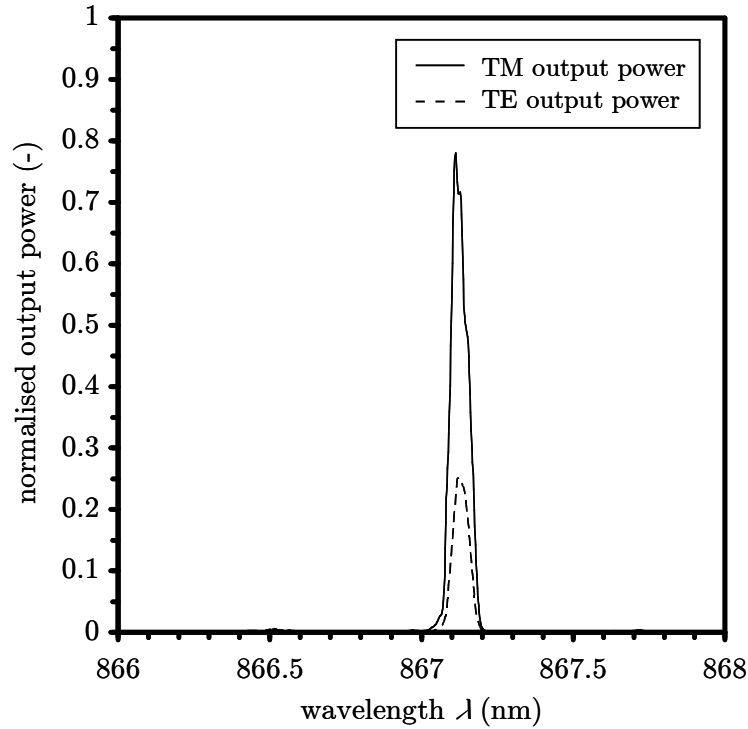


Figure 7-13: Measured TM- and TE polarised components of the output power at the polarisation converter facet for an injection current (continuous wave) of 150 mA (threshold current level = 100 mA). Measurement conducted by S. McMaster.

7.5.4 Mode structure

This compound cavity laser structure consists of basically two cavities (Figure 7-14). The first one is formed by the combination of the pumped section and the passive converter section, defined by its length L_{13} of 1406 μm . The second cavity, which consists of only the passive converter section, is placed within the first cavity. This cavity is defined by its length L_{23} of 156 μm . The examination of the mode structure in this compound cavity

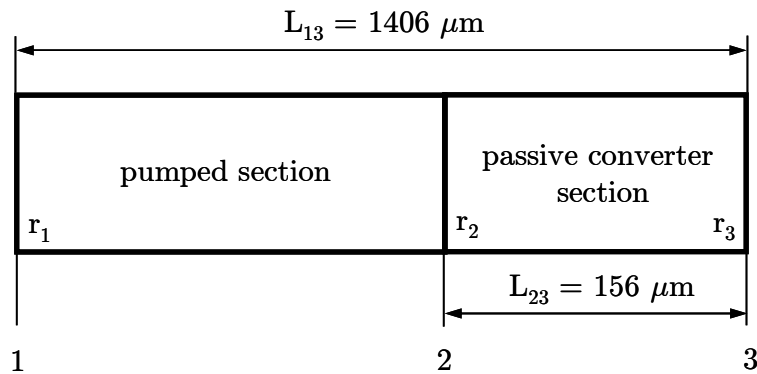


Figure 7-14: Geometry and notation used in the description of the compound cavity configuration of the device.

device was conducted by considering the spontaneous emission spectrum below the threshold level (Figure 7-15). The spectrum indicates two sets of optical fringes corresponding to this compound cavity device. A fringe period $\Delta\lambda$ in the optical spectrum - which represents the longitudinal mode spacing - is caused by a cavity of the length L_{CAVITY} according to the formula [19]

$$\Delta\lambda = \frac{\lambda^2}{2 \cdot n_{eff,group} \cdot L_{CAVITY}}, \quad (7.1)$$

where λ represents the central wavelength (here: $\lambda = 864$ nm) and $n_{eff,group}$ the effective group index (here: $n_{eff,group} = 3.4$) of the semiconductor material.

The modulation associated with the shorter fringe period is not completely resolved, but is commensurate with the width the 0.077 nm period corresponding to the total device length L_{13} of 1406 μm . The longer fringe period is commensurate with the 0.69 nm period corresponding to the passive, angle-etched section length of $L_{23} = 156$ μm .

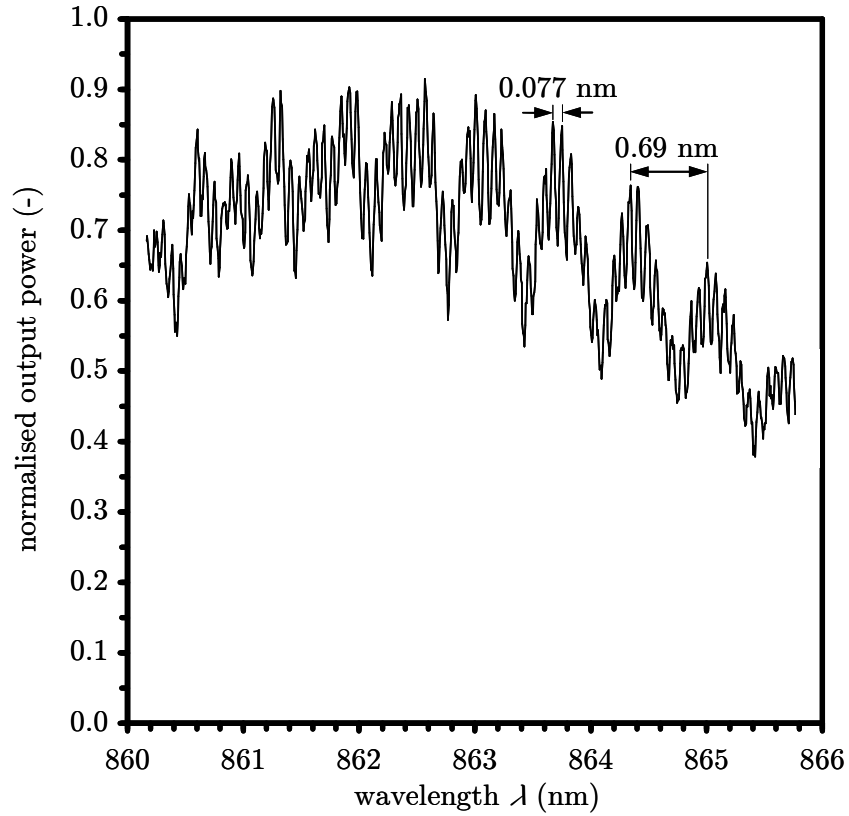


Figure 7-15: Measured spontaneous emission spectrum at sub-threshold level (injected current = 90 mA (continuous wave), threshold current level = 100 mA). Measurement conducted by S. McMaster.

7.6 Summary

The realisation of a Fabry - Perot laser diode comprising a monolithically integrated single-section passive polarisation converter in the cavity based on an unstrained AlGaAs-GaAs material structure for an emitting wavelength of 867.1 nm was introduced. The passive polarisation rotation functionality, based on structural birefringence, was realised by an asymmetric waveguide cross section consisting of two 45 ° sloped sidewalls [20]. The waveguide profile in the converter- and tapered sections was fabricated in a single-step reactive ion etch process utilising a custom designed in-situ sample holder [21]. For a passive polarisation converter section length of 20 μm and waveguide width of 650 nm, the optical emission of the device showed a predominantly TM polarised characteristic from the converter facet. A maximum of just over 80% of the overall output power was observed to be TM polarised for injection currents higher than 120 mA.

7.7 References

- [1] Connelly M. J., *"Semiconductor Optical Amplifiers"*, Kluwer Academic Publishers, New York, USA, ISBN 0-7923-7657-9, (2002).
- [2] Agrawal G. P., *"Fiber-Optic Communication Systems"*, John Wiley & Sons Inc., New York, USA, ISBN 0-471-17540-4, (1997).
- [3] Kartalopoulos S. V., *"Introduction to DWDM technology: Data in a Rainbow"*, John Wiley & Sons, New York, USA, ISBN 0-7803-5399-4, (2000).
- [4] Keiser G., *"Optical Fiber Communications"*, McGraw-Hill, Singapore, ISBN 0-07-236076-3, (2000).
- [5] Keiser G., *"Optical Communications Essentials"*, McGraw-Hill, New York, USA, ISBN 0-07-141204-2, (2003).
- [6] Coldren L. A. and Corzine S. W., *"Diode lasers and photonic integrated circuits"*, 1st. ed., Wiley, New York, USA, ISBN 0471118753, (1995).
- [7] Agrawal G. P. and Dutta N. K., *"Semiconductor lasers"*, 2nd. ed., Van Nostrand Reinhold, New York, USA, ISBN 0-442-01102-4, (1993).
- [8] Reinhart F. K., Hayashi I. and Panish M. B., "Mode Reflectivity and Waveguide Properties of Double-Heterostructure Injection Lasers", *Journal of Applied Physics*, vol. **42**, no. 11, pp. 4466 - 4479, (1971).
- [9] Agahi F., Lau K. M., Choi H. K., Baliga A. and Anderson N. G., "High-Performance 770-nm AlGaAs-GaAsP Tensile-Strained Quantum-Well Laser Diodes", *IEEE Photonics Technology Letters*, vol. **7**, no. 2, pp. 140 - 142, (1995).

- [10] Bour D. P., Treat D. W., Beernink K. J., Thornton R. L., Paoli T. L. and D. B. R., "Tensile-strained AlGaAsP- and InGaAsP-(AlGa)_{0.5}In_{0.5}P Quantum Well Laser Diodes for TM-Mode Emission in the Wavelength Range $650 < \lambda < 850$ nm", *IEEE Photonics Technology Letters*, vol. **6**, no. 11, pp. 1283 - 1285, (1994).
- [11] Sun D. and Treat D. W., "Low-Threshold 833 nm GaAsP-AlGaAs Tensile-Strained Quantum-Well Laser Diodes", *IEEE Photonics Technology Letters*, vol. **8**, no. 1, pp. 13 - 15, (1986).
- [12] Mori Y., Shibata J. and Kajiwarra T., "Optical polarization bistability with high switching speed in a TM wave injected buried heterostructure laser", *Applied Physics Letters*, vol. **54**, no. 24, pp. 1971 - 1973, (1987).
- [13] Sapia A., Spano P. and Daino B., "Polarization switching in semiconductor lasers driven via injection from an external radiation", *Applied Physics Letters*, vol. **50**, no. 2, pp. 57 - 59, (1987).
- [14] Loh W. H., Ozeki Y. and Tang C. L., "High-frequency polarization self-modulation and chaotic phenomena in external cavity semiconductor lasers", *Applied Physics Letters*, vol. **56**, no. 26, pp. 2613 - 2615, (1990).
- [15] Mitsuhashi Y., "Polarization control of an antireflection-coated GaAlAs laser diode by an external optical feedback", *Journal of Applied Physics*, vol. **53**, no. 12, pp. 9200 - 9201, (1982).
- [16] Syvridis D., Inaudi D. and Guekos G., "Polarization state of the Emission of External Grating Diode Lasers", *IEEE Journal of Quantum Electronics*, vol. **30**, no. 4, pp. 966 - 974, (1994).
- [17] Wakana S., Shirasaki M., Furukawa Y. and Inagaki T., "Polarization and frequency control of a semiconductor laser with a new external cavity structure", *Applied Physics Letters*, vol. **50**, no. 22, pp. 1547 - 1549, (1987).
- [18] Fujita T., Schremer A. and Tang C. L., "Polarization bistability in external cavity semiconductor lasers", *Applied Physics Letters*, vol. **51**, no. 6, pp. 392 - 394, (1987).
- [19] Senior J. M., "Optical Fiber Communications", 2nd. ed., Prentice Hall, New York, USA, ISBN 0-13-635426-2, (1992).
- [20] Bregenzer J. J., Holmes B. M., Sorel M. and Hutchings D. C., "Realization of a single-section passive polarization converter using a single-step etch process", in *Proceedings of the 17th Annual Meeting of the IEEE Lasers & Electro-Optics Society 2004 (LEOS'04)*, Rio Grande, Puerto Rico, 7 - 11 November 2004, paper TuA1, pp. 161 - 162.
- [21] Takamori T., Coldren L. A. and Merz J. L., "Angled etching of GaAs/AlGaAs by conventional Cl₂ reactive ion etching", *Applied Physics Letters*, vol. **53**, no. 25, pp. 2549 - 2551, (1988).

Chapter 8

Passive polarisation converter comprising an undercut stripe waveguide

8.1 Introduction

As already mentioned in chapter 3 and chapter 5, various different designs of passive polarisation converters, which are based on the principle of mode beating, inevitably suffer from occurring mask (re-)alignment problems during the fabrication process. The converter section in these designs was realised by one or several dry- and/or wet-etch processes. The mask (re-)alignment was therefore crucial in order to prevent an unwanted etch-overlap into adjacent waveguide sections.

Here in this chapter, a novel polarisation converter design, which *bypasses* these mask (re-)alignment problems, is introduced. The converter section of this design is realised by *modification of an already existing stripe waveguide structure* (Figure 8-1(a)).

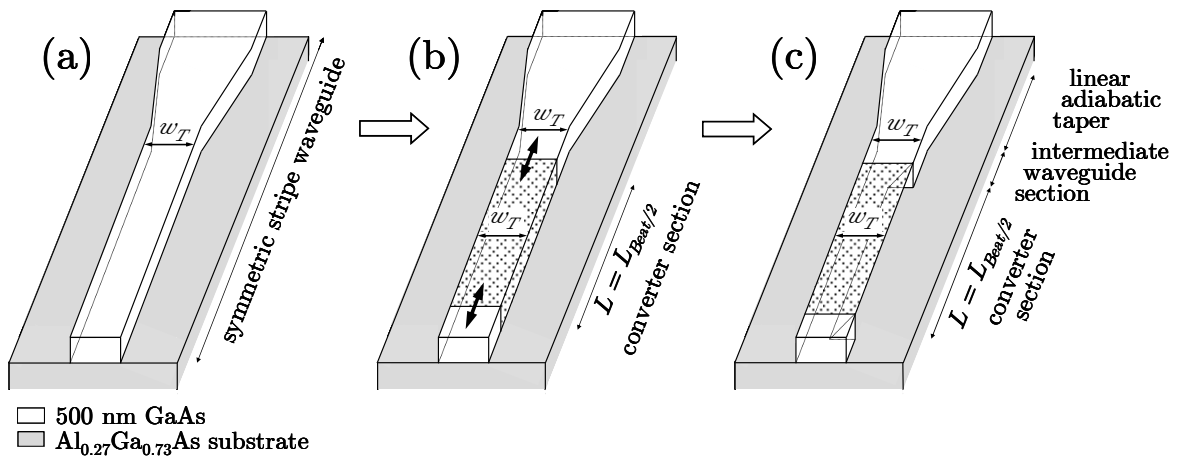


Figure 8-1: Illustration of the simplified converter section mask alignment.

An additional (angled) etch process is applied on a certain length of the stripe waveguide. As the top width w_T of the waveguide in the already existing stripe waveguide structure and the desired converter section are *equal*, the exact position of the converter section can be chosen anywhere along the existing stripe waveguide (Figure 8-1(b)). There are no

requirements for aligning the converter section area to predefined intersection positions as for instance in the previous introduced design. The bypassing of crucial mask alignments offers even the possibility to utilise photolithography for the realisation the entire device. Here, electron beam lithography was used in the fabrication of the entire device. The boundary of the converter section area was positioned about $10\text{ }\mu\text{m}$ apart from the linear adiabatic taper, generating the intermediate waveguide section (Figure 8-1(c)). This is a long enough distance to prevent the converter section mask alignment to overlap onto the taper section.

8.2 Device configuration

The converter design based on waveguide mode beating, as shown in Figure 8-2(b), consists of a stripe waveguide structure comprising a sloped undercut in the core profile (Figure 8-2(Insert)). The wafer structure is composed of a $4.7\text{ }\mu\text{m}$ $\text{Al}_{0.27}\text{Ga}_{0.73}\text{As}$ lower cladding and a $0.5\text{ }\mu\text{m}$ GaAs core layer, grown using *metal-organic chemical-vapor deposition* (MOCVD) upon a n-doped GaAs substrate, as introduced in chapter 2. Light is coupled into the device via a $3\text{ }\mu\text{m}$ wide input waveguide. A following $30\text{ }\mu\text{m}$ long adiabatic linear taper between the input waveguide section and the narrower intermediate waveguide section establishes a close match of the mode profiles and minimises coupling losses. The waveguide top width w_T of the intermediate/output waveguide section and the

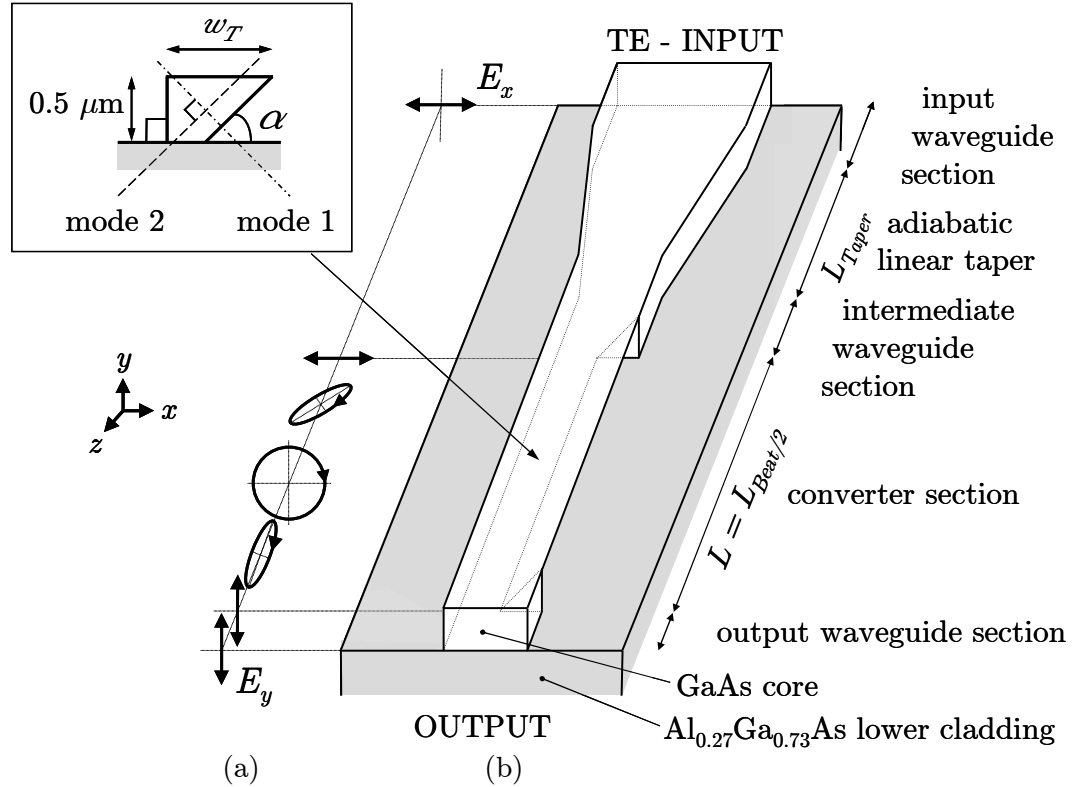


Figure 8-2: Schematic of the design and functionality of the integrated polarisation converter. (a) Evolution of the polarisation state of a TE polarised input signal in the device. (b) Device configuration (not to scale). (Insert) Waveguide profile of converter section and illustration of the optical axes orientations, which determine the orientation of the excited lowest order modes (mode 1 (chain dotted line) and mode 2 (dashed line)).

converter waveguide section was chosen to be *equal*. This choice bypasses mask realignment errors at the beginning and at the end of the converter section at subsequent etch steps during fabrication. The asymmetry in the converter section waveguide core profile results in optical modes with both significant TE- and TM polarised components. Hence, a TE (or TM) polarised optical signal launched from the symmetric intermediate waveguide excites two (or more - depending on the dimension of the core profile geometry) modes in the asymmetric converter section waveguide (Figure 8-2(Insert)). (For the demonstration of the concept and functionality of the device, only the case of a TE polarised input signal was considered. A TM polarised signal would have an analogous effect on the device functionality.) These two modes propagate with different phase velocities within the asymmetric core according to their different propagation constants (for example $\beta_{mode\ 1}$ and $\beta_{mode\ 2}$). The *relative* phase difference between these two modes causes the resulting state of polarisation to evolve periodically from an initial linear state through various elliptical states of polarisation as these two modes propagate in longitudinal direction (Figure 8-2(b)). For two-mode excitation, the maximum orthogonally polarised component - with respect to the input polarisation state - will be developed at odd multiples of the half beat length $L_{Beat/2}$. This corresponds to the length over which a *relative* phase difference of 180° between the two excited modes accumulated. The length of the converter section - and therefore $L_{Beat/2}$ - is defined by the intermediate- and output waveguide section. The length of the symmetric intermediate waveguide section was chosen to be about $10\ \mu\text{m}$. This is a long enough distance not only for the field distributions to level off in the waveguide, but also to avoid the converter section mask alignment to overlap onto the taper section. The length of the output waveguide section is determined by the cleaving process and is about $100\ \mu\text{m}$.

8.3 Device optimisation

Both w_T and α represent the crucial core profile parameters in the design of this device. At this stage it has to be mentioned that, unless otherwise stated in this chapter, the operating wavelength was set to $\lambda = 1064\ \text{nm}$. This value was chosen according to the emitting wavelength of a diode pumped solid state (DPSS) Nd:YAG laser, which was used as a signal source (see chapter 4). The modelled waveguide layer dimensions of the asymmetric converter section waveguide as well as the corresponding computational window Ω_W are shown in Figure 8-8(a). The calculations were conducted with a commercially available FEM based mode solver, which computational settings were introduced in chapter 2.

8.3.1 Optimisation of the waveguide top width w_T

At first, the influence of w_T on the device parameters such as $L_{Beat/2}$, κ , δ and P_C was investigated. This is shown in Figure 8-3. Figure 8-3(a) illustrates the w_T - dependence of the effective refractive indices of the *excited guided modes* in a symmetric ($\alpha = 90^\circ$) (chain

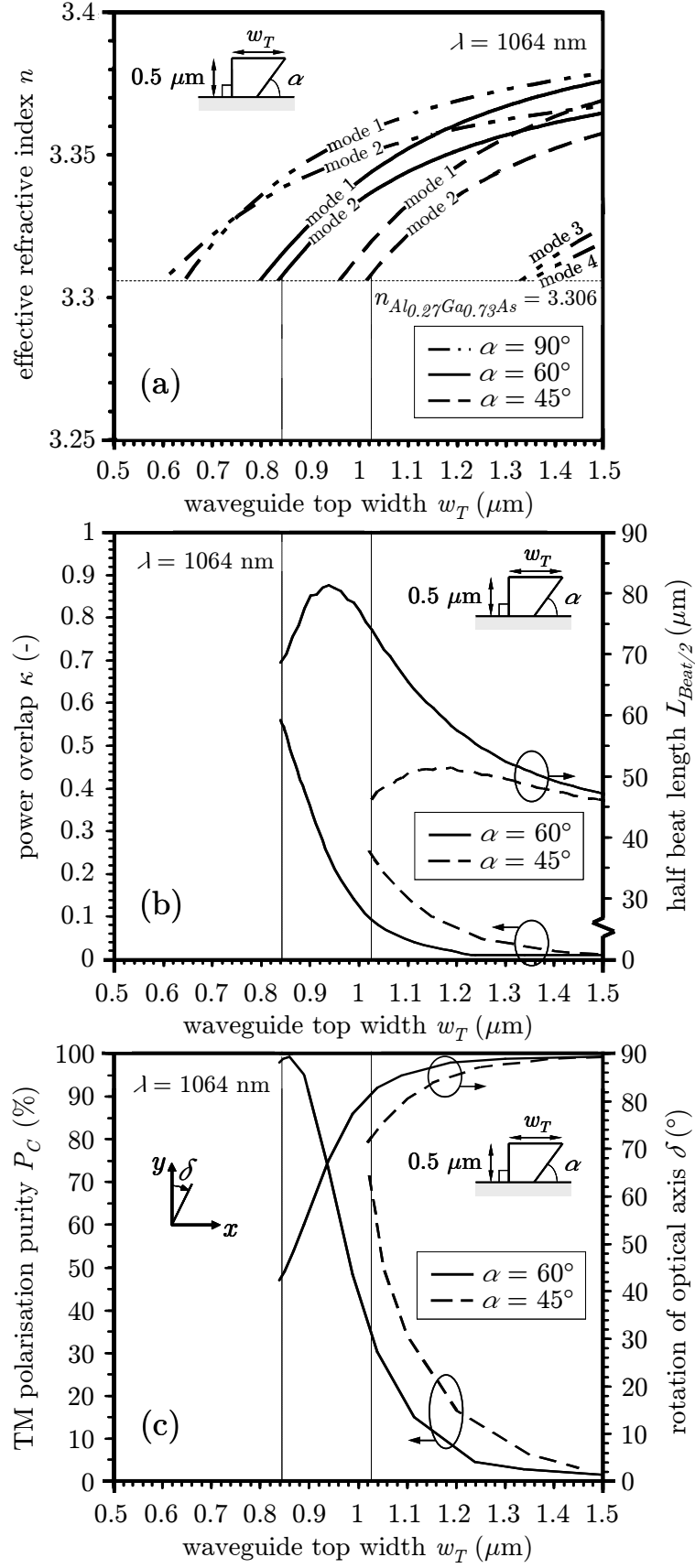


Figure 8-3: (a) Effective refractive index of the excited modes in a symmetric ($\alpha = 90^\circ$) and asymmetric ($\alpha = 60^\circ$ and $\alpha = 45^\circ$) stripe waveguide versus the waveguide top width w_T . (b) Power overlap κ and half beat length $L_{\text{Beat}/2}$ of an asymmetric ($\alpha = 60^\circ$ and $\alpha = 45^\circ$) stripe waveguide versus the waveguide top width w_T . (c) Rotation of optical axis δ with respect to the vertical axis and TM polarisation purity P_C of an asymmetric ($\alpha = 60^\circ$ and $\alpha = 45^\circ$) stripe waveguide versus the waveguide top width w_T . ($\lambda = 1064 \text{ nm}$).

dotted line)) and asymmetric ($\alpha = 60^\circ$ (solid line) and $\alpha = 45^\circ$ (dashed line)) stripe waveguide. The horizontal dashed line indicates the refractive index n of the lower cladding material ($\text{Al}_{0.27}\text{Ga}_{0.73}\text{As}$) at the given wavelength ($\lambda = 1064 \text{ nm}$) (here: $n = 3.306$) and represents the cut-off condition for the excited guiding modes in the waveguide. Single mode propagation in the symmetric ($\alpha = 90^\circ$) intermediate waveguide section is given in the range of $0.62 \mu\text{m} < w_T < 1.32 \mu\text{m}$. Within this range, a fundamental TE (TE_0) or TM (TM_0) mode is launched from the intermediate waveguide section into the converter section. An excitement of the two lowest order modes (mode 1 and mode 2) in the asymmetric converter section is initiated for $w_T > 0.84 \mu\text{m}$ (for $\alpha = 60^\circ$) and $w_T > 1.02 \mu\text{m}$ (for $\alpha = 45^\circ$). These cut-off limits are indicated by dotted vertical lines in Figure 8-3(a)-(c).

Considering the dependence of $L_{\text{Beat}/2}$ and κ on w_T , as shown in Figure 8-3(b), it can be noted that $L_{\text{Beat}/2}$ increases as w_T decreases from large values. However, as the decrease of w_T approaches the cut-off limit, $L_{\text{Beat}/2}$ decreases as well. The power overlap κ on the other hand increases as the w_T -decrease approaches the cut-off condition. In the case for $\alpha = 60^\circ$, κ approaches its optimum value of 0.5 closely above the cut-off limit ($w_T = 0.85 \mu\text{m}$), indicating the desired maximum overlap of the horizontal and vertical optical power components of the lowest order excited mode (mode 1) for an optimum performance of the device.

A similar behaviour for both δ and P_C can be depicted in Figure 8-3(c). Again, as the w_T -decrease approaches the cut-off limit, δ and P_C tend towards their optimum of 45° and 100%, respectively. In the case for $\alpha = 45^\circ$, P_C reaches its best possible value of 70% with $\delta = 72^\circ$ at $w_T = 1.04 \mu\text{m}$. For $\alpha = 60^\circ$ and $w_T = 0.85 \mu\text{m}$, however, P_C even achieves 98% with a corresponding δ of 46° .

The overall trend of these performance influencing parameters is that they obtain their best possible values for w_T -dimensions closely above the second lowest order mode cut-off limit - determined by the refractive index of the (in this case only lower) cladding material. This indicates that the excited higher order modes in the asymmetric waveguide structure are not contributing to the functionality of the device at all.

As the optimum operating point (maximum P_C) of this device design is close to the mode-cut-off dimension of the waveguide, the mode field distribution will be close to the waveguide sidewalls. This can make this design vulnerable to occurring waveguide sidewall roughness, which results in an optical power loss.

8.3.2 Optimisation of the undercut angle α

Based on the evaluated optimum values of w_T for α within a range of $30^\circ < \alpha < 80^\circ$, the examined device performance influencing parameters are shown in Figure 8-4. Figure 8-4(a) displays the evaluated optimum w_T and corresponding $L_{\text{Beat}/2}$ values for best possible device performance at a given value of α . The optimum values for both δ and κ (45° and 0.5, respectively) occur for $\alpha = 58^\circ$ (Figure 8-4(b)) at an evaluated w_T of $0.86 \mu\text{m}$. This results in a P_C of 98.4% (Figure 8-4(c)).

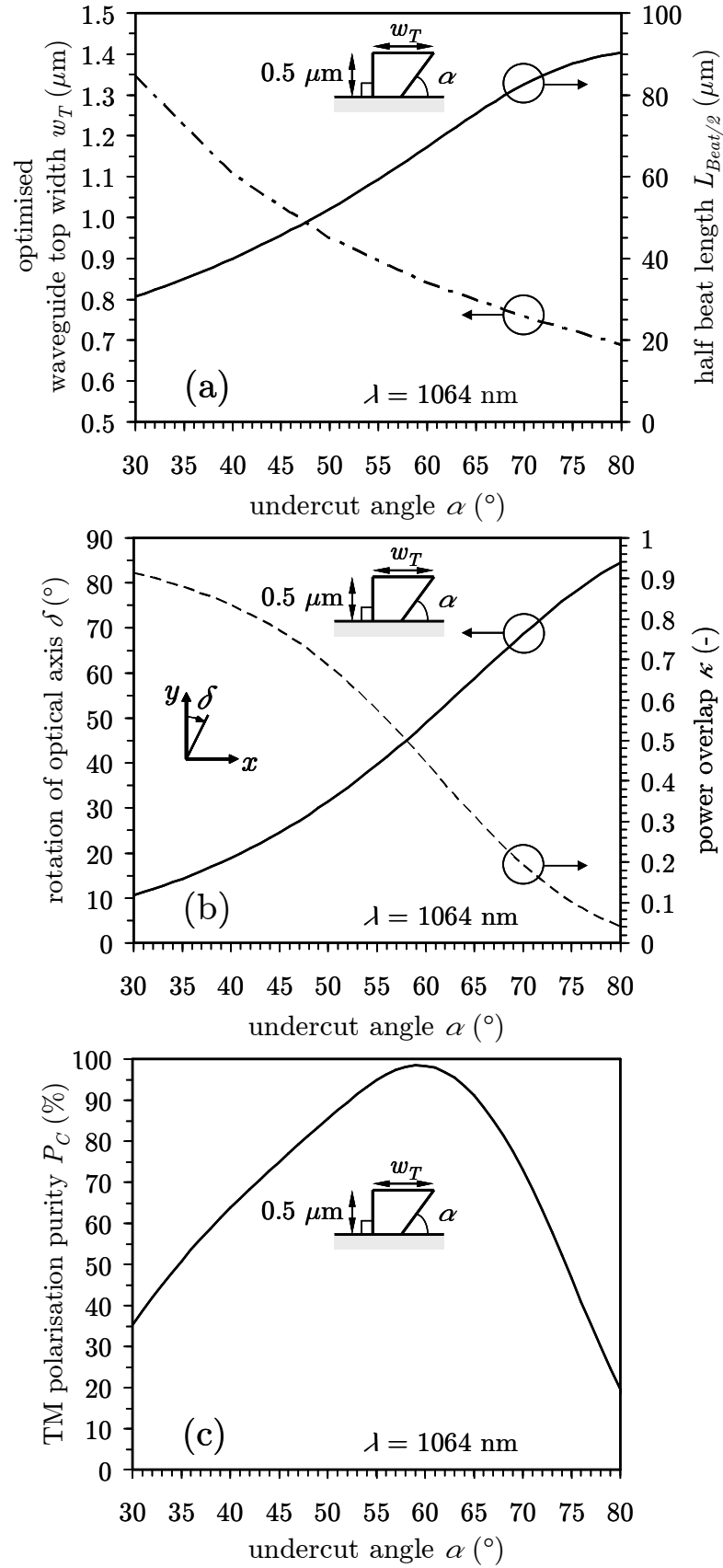


Figure 8-4: (a) Evaluated optimum w_T - dimension closely above single mode cut-off and corresponding $L_{Beat/2}$ versus undercut angle α . (b) Rotation of optical axis δ and power overlap κ versus undercut angle α at optimised w_T . (c) TM polarisation purity P_C versus undercut angle α at optimised w_T . ($\lambda = 1064$ nm).

8.3.3 Converter section fabrication tolerances

Considering a possible α - deviation of $\pm 5^\circ$ from its optimised value of 58° due to fabrication tolerances, a P_C - degradation of up to 10% occurs, assuming that w_T remains constant at $0.86 \mu\text{m}$ (Figure 8-4(c)). Similarly, as can be depicted in Figure 8-3(c), a possible w_T - deviation of about 50 nm (in the case for $\alpha = 60^\circ$) from the optimised value of $w_T = 0.86 \mu\text{m}$ implies a P_C - degradation of 10% as well. These tight tolerances require an accurate fabrication process in order to achieve the best possible performance of the device. Especially an occurring waveguide sidewall roughness, caused by the etch process, can slightly alter the adjusted optimised dimensions and therefore have an impact on the device performance.

8.3.4 Optimisation of the taper section length L_{Taper}

The waveguide top width w_T of the converter section was chosen to be equal to the one of the intermediate waveguide section. The length of the taper between the intermediate waveguide ($w_T = 0.86 \mu\text{m}$) and input waveguide ($w = 3 \mu\text{m}$) has to be optimised for minimum power loss through the taper sidewalls. The taper becomes effectively loss-less, or “adiabatic”, as the power lost through the sidewalls decreases as the taper length increases. The optimisation was conducted by utilising the wave propagation calculation module that comes with the commercially available mode solver mentioned above. As the TE polarised input power was kept constant, the transmitted TE_0 mode power - depending on the length of the linear taper L_{Taper} - was monitored and normalised to the

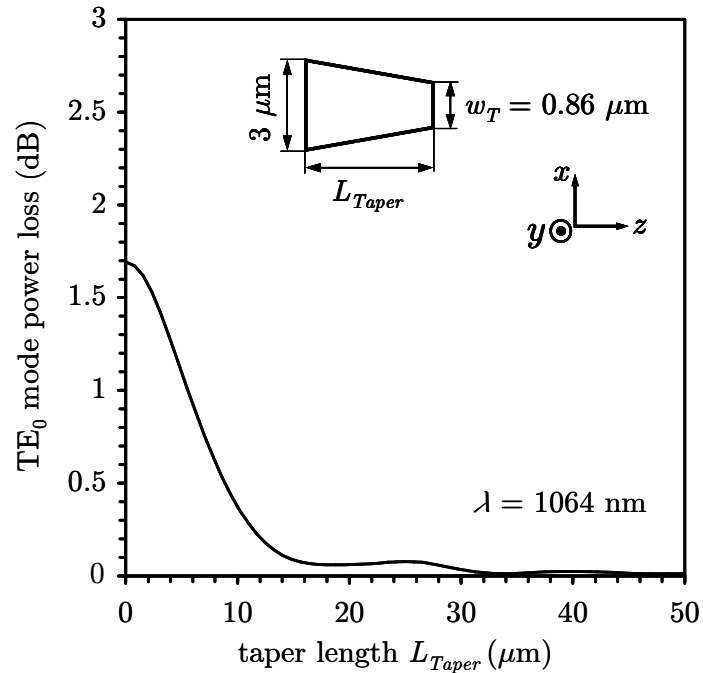


Figure 8-5: Normalised transmitted power of the fundamental TE mode (TE_0) versus the taper length L_{taper} ($\lambda = 1064 \text{ nm}$).

TE_0 mode power at the input (Figure 8-5). The insert in Figure 8-5 illustrates the top view of the modelled taper configuration. The linear taper shows an almost adiabatic behaviour for $L_{Taper} \geq 30 \mu\text{m}$, as the loss is $\leq 0.05 \text{ dB}$. Hence, in order to assure a loss-less coupling of the launched input signal from the input waveguide section through the taper section into the intermediate waveguide section, a taper length of $L_{Taper} = 30 \mu\text{m}$ was chosen.

8.3.5 Optimisation of the transversal offset τ

The aforementioned fabrication simplification by bypassing of mask misalignment at the periphery of the converter section at subsequent etch-process steps does not come without a price. An additional optical power loss occurs at each intersection, as compared with an optimised device design. Figure 8-6 shows the contour plots of the mode profile (magnitude of the E_x component) at both the end of the intermediate waveguide section ($L = 0^-$ (grey line)) and the beginning of the converter waveguide section ($L = 0^+$ (dashed line)). The not optimised overlap of both mode profiles due to different waveguide cross section geometries causes a coupling loss at the intersection. In order to optimise the mode profile overlap, a transversal converter section offset τ was introduced (Figure 8-7 (Insert)). A zero-offset corresponds to the lateral alignment of the vertical converter section sidewall with the vertical intermediate- (or output-) waveguide section. The cross-sectional view of the intersection at $\tau = 0 \mu\text{m}$ is shown in Figure 8-6. w_T was chosen as the optimum value of $w_T = 0.86 \mu\text{m}$. A positive value of τ corresponds to a shift of the converter section towards the positive x -direction, whereas the intermediate- (or output-)

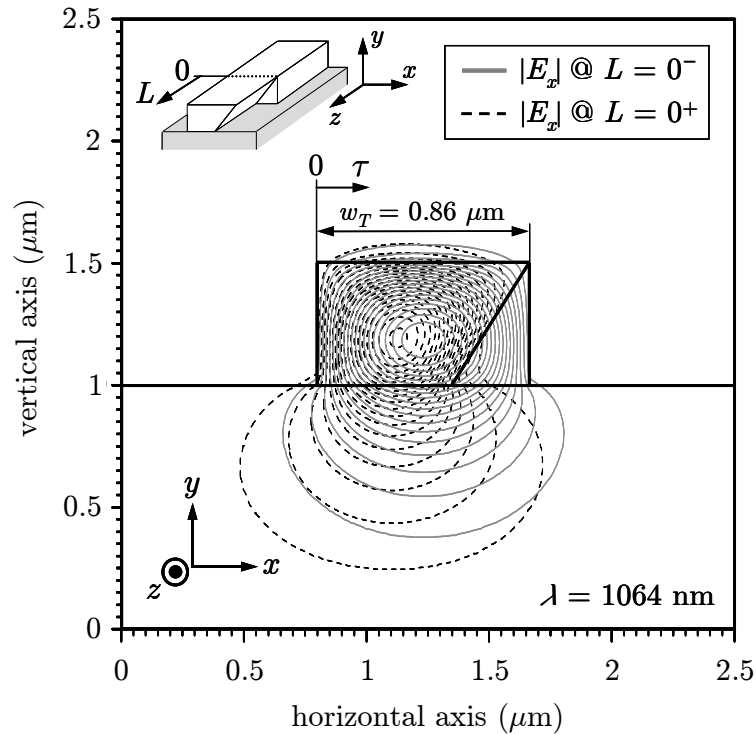


Figure 8-6: Illustration of the overlap of the mode profile contour plots (here: magnitude of the E_x component for the case of a TE polarised input signal) directly before ($L = 0^-$ (grey line)) and directly after ($L = 0^+$ (dashed line)) the intersection between converter- and intermediate- (or output-) waveguide section.

waveguide section remains in place. The optimisation was conducted in the same manner as the taper length L_{Taper} optimisation by utilising the wave propagation calculation module that comes with the commercially available mode solver. The modelled waveguide section configuration is illustrated in Figure 8-6(Insert). As the TE polarised input power (P_{INPUT}) was kept constant, the transmitted power (P_{OUTPUT}) - depending on the transversal offset τ - was monitored and normalised to the input power. The intersection loss was defined as $-10 \times \log_{10}(P_{OUTPUT}/P_{INPUT})$ (in dB). Figure 8-7 illustrates the dependence of the intersection loss on the transversal offset of the converter section. At the initial transversal position of the converter section ($\tau = 0 \mu\text{m}$) occurs an intersection loss of 0.69 dB. The intersection loss could be minimised to 0.24 dB by introducing a transversal offset of $\tau = 0.1 \mu\text{m}$ - leading to an optimised mode profile overlap.

An introduced transversal offset in the device design, however, would negate the fabrication simplification. The cutback of the fabrication simplification is therefore an additional optical power loss of 0.45 dB per intersection compared to an optimised device design.

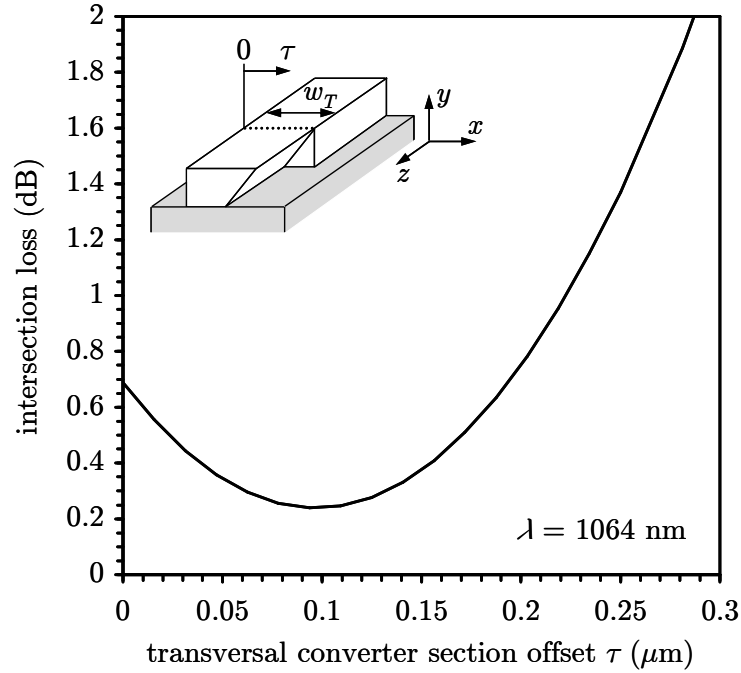


Figure 8-7: Dependence of the intersection loss on the transverse converter section offset τ at the intersection between intermediate waveguide section and converter waveguide section. (Insert) Definition of the transversal converter section offset τ .

8.4 Analysis of the optimised device structure

The optimised device dimensions at the given wafer material structure for a maximum achievable TM polarisation purity P_C of 98.4% at the output are $w_T = 0.86 \mu\text{m}$, $L_{Beat/2} = 62 \mu\text{m}$ and $\alpha = 58^\circ$ for an operating wavelength $\lambda = 1064 \text{ nm}$. Figure 8-8 to Figure 8-11 illustrate the electric and magnetic, respectively, vector field plots and their corresponding mode profile and contour plot of the transverse (x, y) components of both

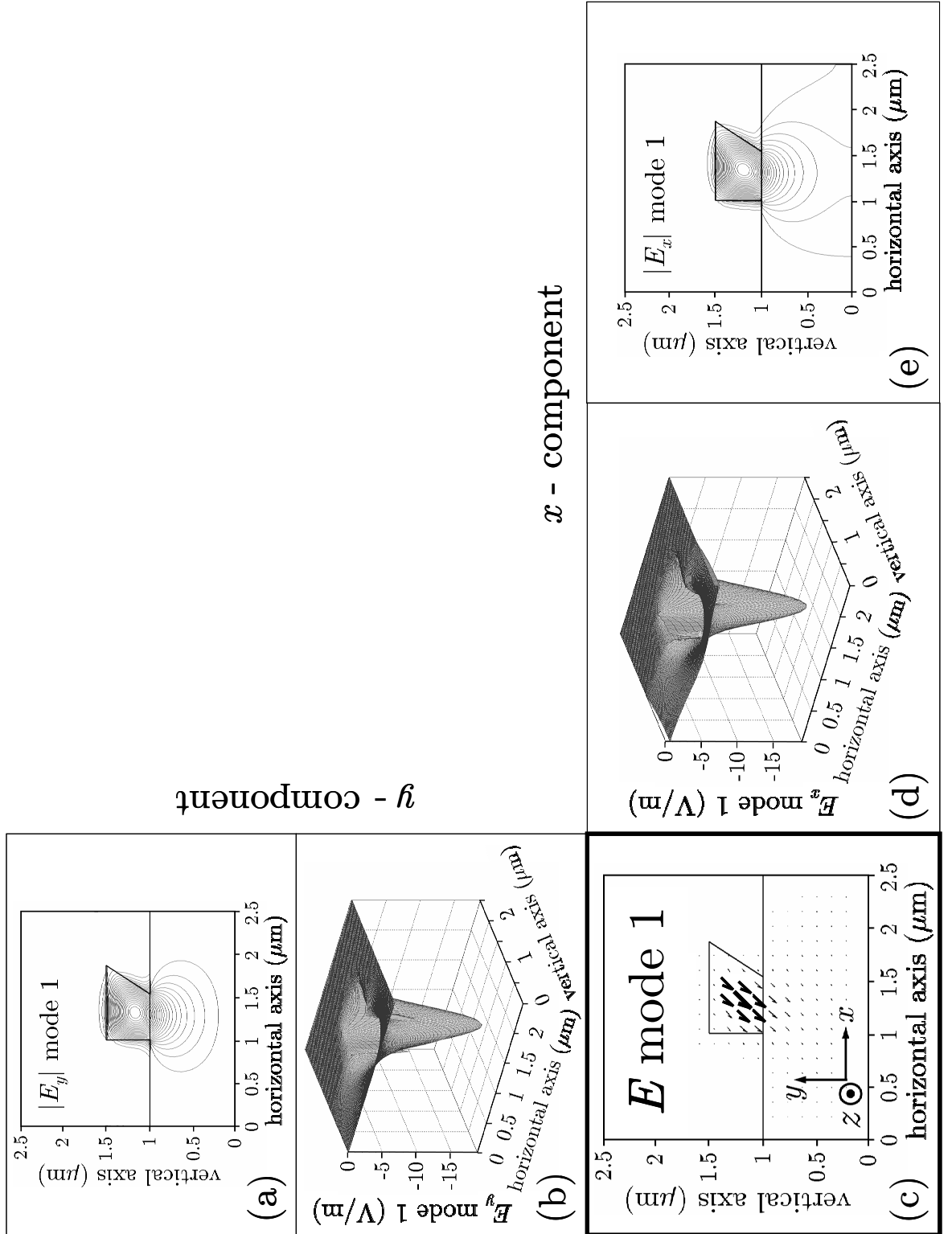


Figure 8-8: (a)-(e) Electric vector field plot and corresponding mode profile and contour plot of the transverse (x , y) components of fundamental mode 1 in a stripe waveguide comprising an undercut of an angle of $\alpha = 58^\circ$ with respect to the horizontal axis and a waveguide top width w_T of 860 nm in the core profile for an operating wavelength $\lambda = 1064$ nm.

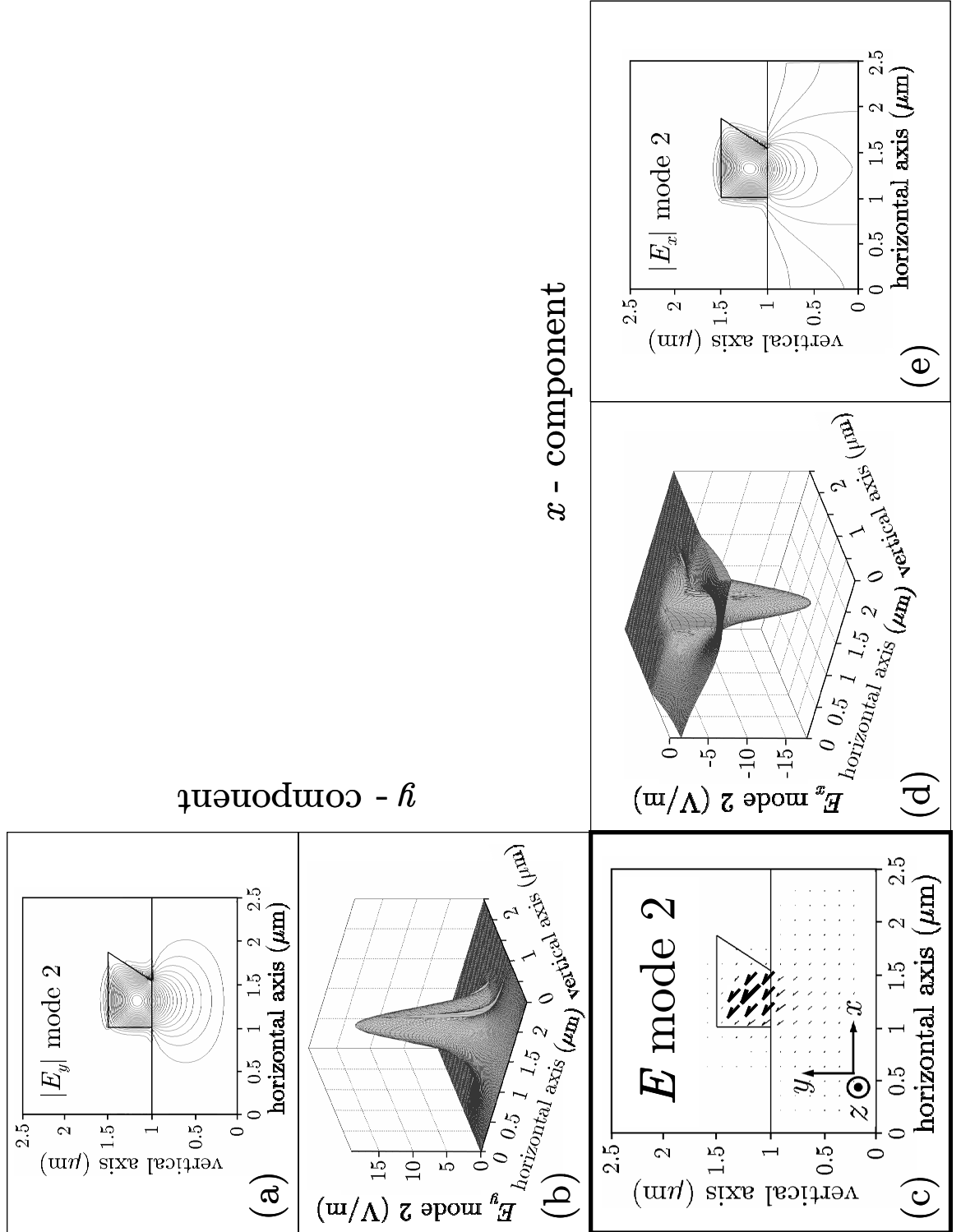


Figure 8-9: (a)-(e) Electric vector field plot and corresponding mode profile and contour plot of the transverse (x , y) components of fundamental mode 2 in a stripe waveguide comprising an undercut of an angle of $\alpha = 58^\circ$ with respect to the horizontal axis and a waveguide top width w_T of 860 nm in the core profile for an operating wavelength $\lambda = 1064$ nm.

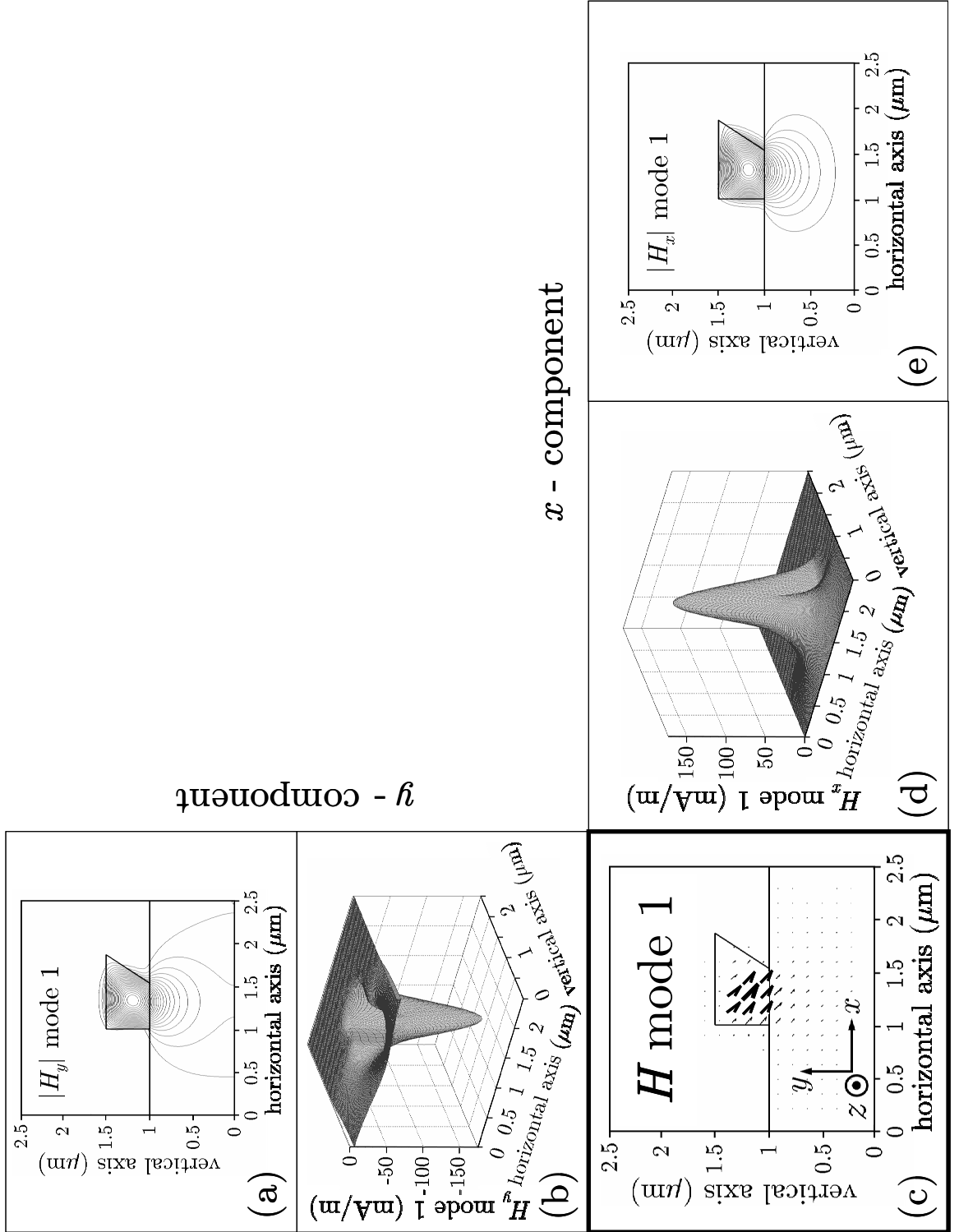


Figure 8-10: (a)-(e) Magnetic vector field plot and corresponding mode profile and contour plot of the transverse (x , y) components of fundamental mode 1 in a stripe waveguide comprising an undercut of an angle of $\alpha = 58^\circ$ with respect to the horizontal axis and a waveguide top width w_T of 860 nm in the core profile for an operating wavelength $\lambda = 1064$ nm.

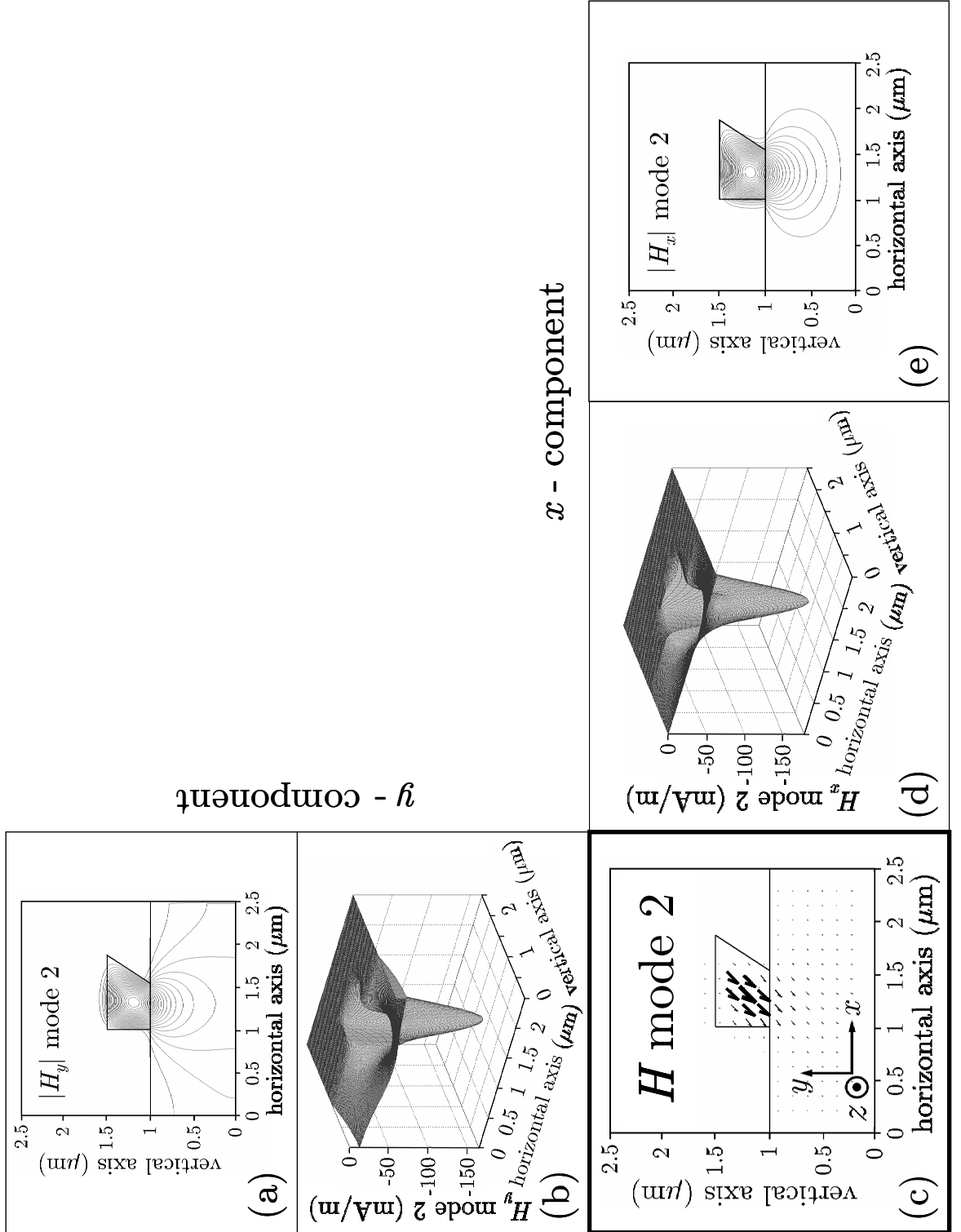


Figure 8-11: (a)-(e) Magnetic vector field plot and corresponding mode profile and contour plot of the transverse (x , y) components of fundamental mode 2 in a stripe waveguide comprising an undercut of an angle of $\alpha = 58^\circ$ with respect to the horizontal axis and a waveguide top width w_T of 860 nm in the core profile for an operating wavelength $\lambda = 1064$ nm.

fundamental modes (mode 1, mode 2) for the optimised waveguide cross section profile. As the relations of the magnetic field are analogous to the electric field, only the electric field was considered for analysis. The electric field vectors of both orthogonal modes in the waveguide core area, which are parallel to the optical axes, are, as desired, at an angle of 45° with respect to the vertical axis (Figure 8-8(c), Figure 8-9(c)). Each mode has a similar profile of their horizontal (E_x (TE)) (Figure 8-8(d), Figure 8-9(d)) and vertical (E_y (TM)) (Figure 8-8(b), Figure 8-9(b)) components as well as an approximately equal field distribution between them.

It can be noted from the contour plots that the evanescent tails of the E_x (Figure 8-8(e), Figure 8-9(e)) (and H_y (Figure 8-10(a), Figure 8-11(a))) components of both modes penetrate relatively deep into the lower cladding. This indicates that the waveguide profile is close to the cut-off dimensions for both modes. Figure 8-8 to Figure 8-11 show that most of the optical power launched into the converter waveguide section is confined within both lowest order modes in the core area and only an insignificant amount penetrates into the lower cladding or radiates.

An illustration of the functionality of the optimised device is represented in Figure 8-12. It displays the contour plots of the magnitude of both the E_x (TE)- and E_y (TM) components in the converter section as a TE (in this case TE_0 , given by the dimension of w_T) polarised input signal propagates down the device. The interference between the two excited modes (mode 1 and mode 2) results in a harmonic beating pattern of the transversal components with the periodicity of $L_{Beat/2}$. The inserts show the magnitude profiles of both components at the characteristic converter section distances $L = 0 \mu\text{m}$, $L = L_{Beat/4} = 31 \mu\text{m}$ and $L = L_{Beat/2} = 62 \mu\text{m}$.

- At $L = 0 \mu\text{m}$, the electric field distribution equals the one of the launched TE polarised signal. Almost all the electrical field is contained within the E_x component, whereas the E_y component only contains an insignificant amount.
- At $L = L_{Beat/4} = 31 \mu\text{m}$, the electric field is equally distributed in both components.
- At $L = L_{Beat/2} = 62 \mu\text{m}$, almost all the electrical field is contained within the E_y component, whereas the E_x component only contains an insignificant amount. This corresponds to a TM polarised signal, which is, with the converter length being equal to $L_{Beat/2}$, the desired output characteristic of the device.

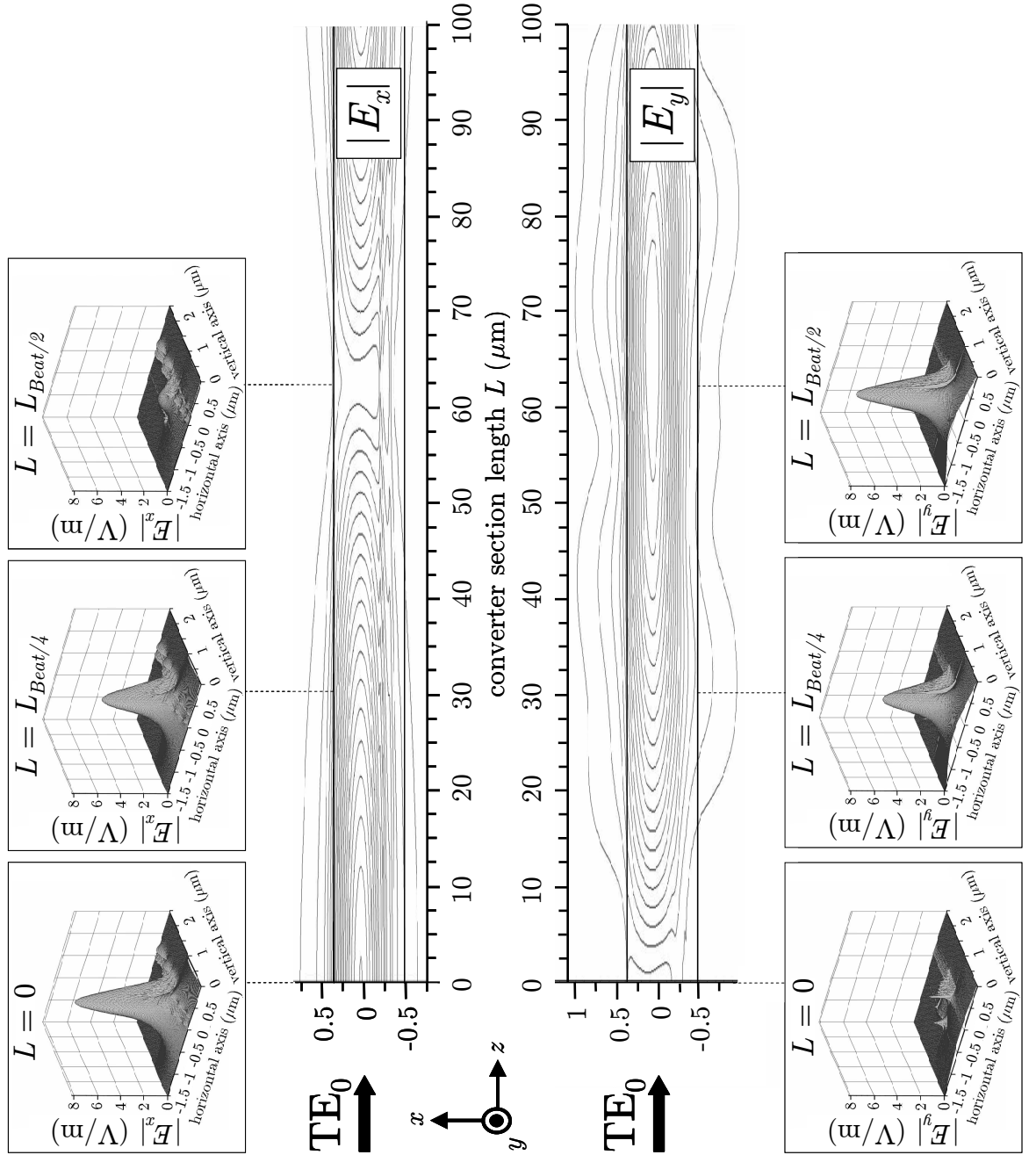


Figure 8-12: Top view of the simulated contour plot of both the E_x (TE) and E_y (TM) component of a TE_0 mode launched from the intermediate waveguide section into the optimised converter section. (Inserts) Magnitude of both E_x and E_y components at $L = 0 \mu\text{m}$, $L = L_{\text{Beat}}/4 = 31 \mu\text{m}$ and $L = L_{\text{Beat}}/2 = 62 \mu\text{m}$.

8.5 Device fabrication

8.5.1 Fabrication process steps

A schematic process flow diagram of the realised device is illustrated in Figure 8-13. The initial realisation of the e-beam alignment markers is not included in the schematic as the emphasis is given on the actual fabrication of the device.

Step 1: Creation of e-beam position calibration markers

The e-beam position calibration markers were fabricated according to the description in Section 5.4.1.

Step 2: Realisation of waveguide outline SiO_2 mask pattern

1. Deposition of 200 nm PECVD SiO_2 .
2. Spin-coat positive e-beam resist (PMMA 4% ELV 2041) at 5000 rpm for 60 seconds.
3. Clean backside of sample with in acetone soaked cotton bud before a 15 minutes bake in oven @ 180°C .
4. Spin-coat second positive e-beam resist layer (PMMA 4% ELV 2041) at 5000 rpm for 60 seconds (Figure 8-13(a)).
5. Clean backside of sample with in acetone soaked cotton bud before a 90 minutes bake in oven @ 180°C .
6. Exposure of waveguide outline pattern. EBP5 e-beam-writer control file parameters: resolution: 25 nm (high) / 250 nm (low), proximity correction file: gaas200-50b.pec, prox min: 0.1, prox grid: 0.025, dose: $136\ \mu\text{C}/\text{cm}^2$ (high resolution) / $250\ \mu\text{C}/\text{cm}^2$ (low resolution), spot size: 56 nm (high resolution) / 400 nm (low resolution), job type: simple.
7. Development of waveguide pattern using 2:1 IPA:MIBK developer solution for 75 seconds @ 23.1°C . Dip in IPA for 10 seconds; Blow dry with nitrogen (Figure 8-13(b)).
8. SiO_2 dry-etch of waveguide pattern using CHF_3 as a reactive gas in the BP80 machine (Figure 8-13 (c)). BP80 parameter settings: process gas: CHF_3 , corrected gas flow: 20 sccm, process pressure: 17 mTorr, forward RF power: 100 W, temperature: 25°C , BIAS: -280 V, process time: 13 minutes.
9. Removal of e-beam resist mask via an O_2 ash process using the BP80 machine (Figure 8-13(d)). BP80 parameter settings: process gas: O_2 , corrected gas flow: 20 sccm, process pressure: 20 mTorr, forward RF power: 100 W, temperature: 25°C , BIAS: -320 V, process time: 25 minutes.

Step 3: Realisation of the rib waveguide structure

21. Vertical GaAs dry-etch of the rib waveguide pattern using SiCl_4 as a reactive gas in the S100 machine (Figure 8-13(e)).
Vertical waveguide etch S100 process parameters: process gas: SiCl_4 , corrected gas flow: 18 sccm, process pressure: 9 mTorr, forward RF power: 250 W, temperature: 25 °C, process time: 5:30 minutes, quartz carrier wafer used.

Step 4: Realisation of the converter section

22. Spin-coating of positive e-beam resist (PMMA 15% ELV 2010) at 5000 rpm for 60 seconds (Figure 8-13(f)).
23. Clean backside of sample with in acetone soaked cotton bud before a 90 minutes bake in oven @ 180 °C.
24. Exposure of converter section area. EBPG 5 e-beam-writer control file parameters: resolution: 25 nm (high) / 250 nm (low), proximity correction file: gaas200-50b.pec, prox min: 0.1, prox grid: 0.025, dose: 270 $\mu\text{C}/\text{cm}^2$ (high resolution) / 490 $\mu\text{C}/\text{cm}^2$ (low resolution), spot size: 56 nm (high resolution) / 400 nm (low resolution).
25. Development of converter waveguide section using 2.5:1 IPA:MIBK developer solution for 30 seconds @ 23.1 °C and subsequent dip in IPA for 10 seconds; Blow dry with nitrogen (Figure 8-13 (g)).
26. Angled GaAs dry-etch of converter waveguide section using SiCl_4 as a reactive gas in the S100 T-Gate machine (Figure 8-13 (h)).
Angled waveguide-etch S100 T-Gate process parameters: process gas: SiCl_4 , corrected gas flow: 9 sccm, process pressure: 9 mTorr, forward RF power: 100 W, temperature: 25 °C, BIAS: -346 V, process time: 4:20 minutes, customised anodised aluminium sample holder used (slope angle of sample holder is 60 ° with respect to horizontal plane).
27. Removal of e-beam resist dry-etch mask via an O_2 ash process using the BP80 machine (Figure 8-13(i)). BP80 process parameter settings: process gas: O_2 , corrected gas flow: 20 sccm, process pressure: 20 mTorr, forward RF power: 100 W, BIAS: -320 V, temperature of 45 °C, process time: 25 minutes.
28. Removal of SiO_2 layer via wet chemical etching using a buffered (hydrofluoric acid) HF:RO (reverse osmosis) water solution (ratio 5:1) for 45 seconds at a temperature of 45 °C; Rinse thoroughly in RO water for 10 minutes; Blow dry using nitrogen (Figure 8-13(i)).

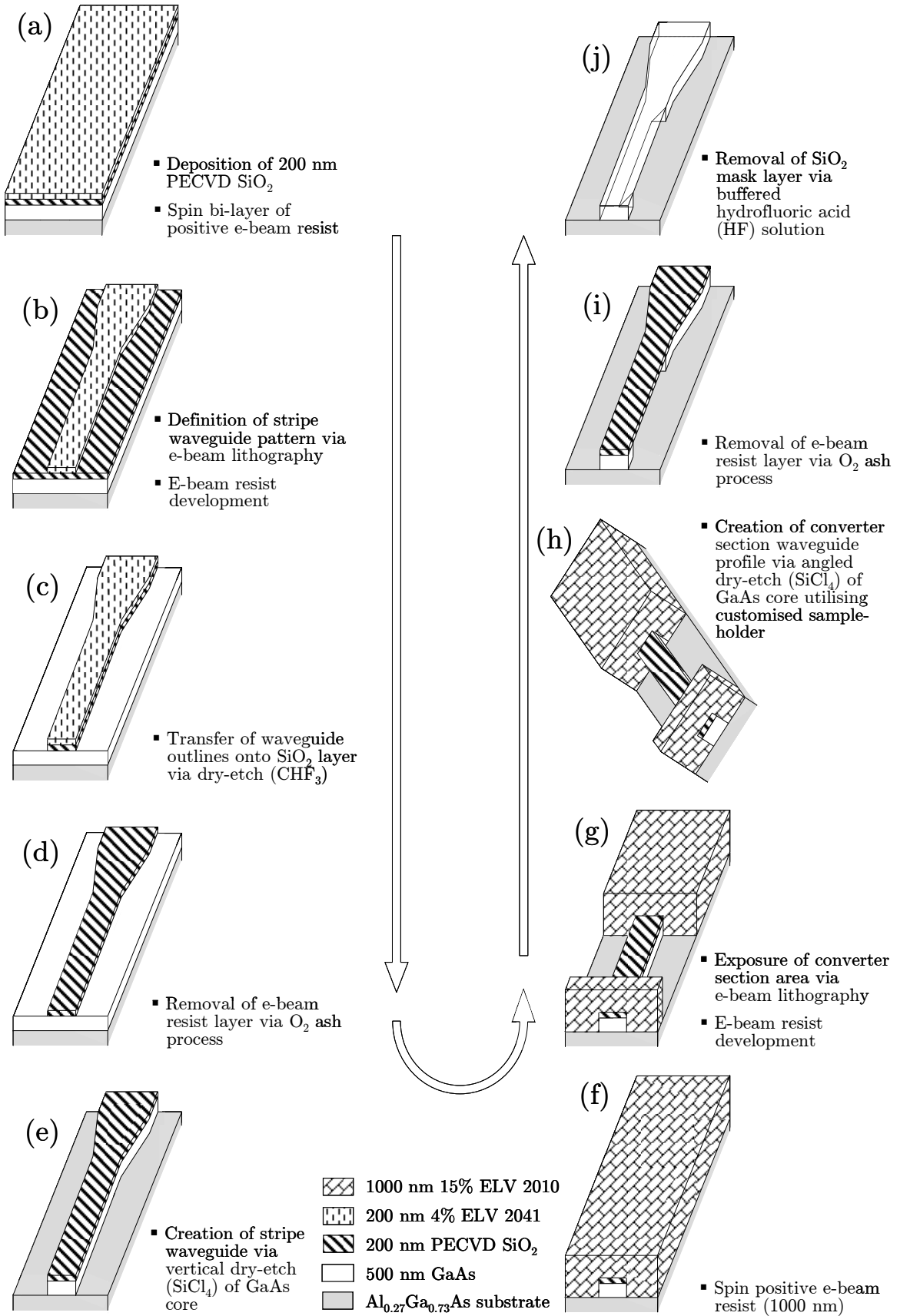


Figure 8-13: (a)-(j) Schematic process flow diagram of the realised polarisation converter device.

8.5.2 Realised device

The fabricated device is displayed in Figure 8-14 and Figure 8-15. The SEM overview in Figure 8-14(a) shows the different sections of the device, as schematically illustrated in Figure 8-2. An insert of the intersection between the converter section and intermediate/output waveguide section can be depicted in Figure 8-14(b). The sidewall

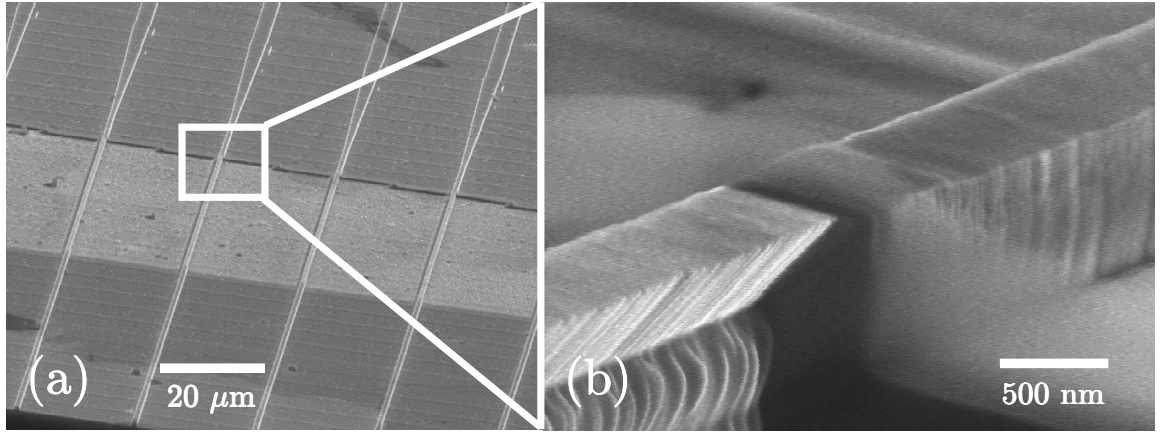


Figure 8-14: (a) SEM overview of the fabricated device. (b) SEM of the intersection between the converter section and the input/output waveguide section.

roughness at the converter section is clearly noticeable. This was caused by the commenced erosion of the SiO_2 mask edges during the tilted dry-etch process (Figure 8-13 (h)). Considering the top view of the intersection in Figure 8-15(a), the intermediate waveguide section converts into the converter section directly without misalignments - demonstrating the fabrication simplification in this polarisation converter design. Figure 8-15(b) shows the fabricated waveguide cross section profile of the converter section. The profile consists of an undercut angle of $\alpha = 52^\circ$ and a waveguide top width w_T of 980 nm. The PMMA mask appearing at the left waveguide sidewall in Figure 8-15(b) was not completely removed from a previous fabrication step. The mask has no impact on the device functionality. The deviations of the fabricated profile dimensions from the

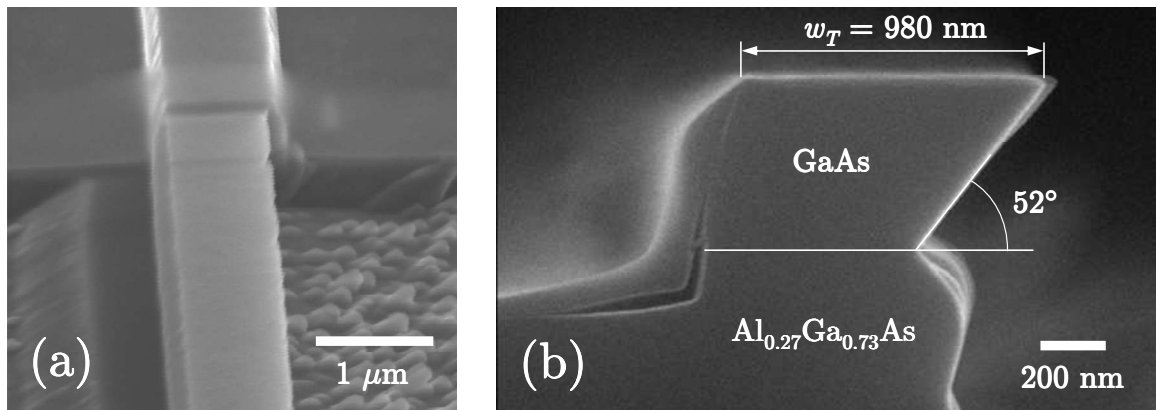


Figure 8-15: (a) SEM top view of the intersection between the converter section and the input/output waveguide section. (b) SEM of the waveguide cross section profile of the fabricated converter section waveguide.

theoretically optimised ones ($\alpha_{OPTIMISED} = 58^\circ$ and $w_{T, OPTIMISED} = 860$ nm) are $\Delta\alpha = 6^\circ$ and $\Delta w_T = 120$ nm.

8.6 Device characterisation

8.6.1 Converted TM polarisation purity

Devices consisting of different converter section lengths were fabricated and characterised via the measurement method described in chapter 4. Figure 8-16 displays the dependence of the TM polarisation purity P_C on the converter section length L . The diamond - shaped markers correspond to the measured P_C of the fabricated device. With the fabricated waveguide profile dimensions of $\alpha = 52^\circ$ and $w_T = 980$ nm, a maximum of 90% for a converter section length of $56 \mu\text{m}$ (encircled data point) can be achieved. These values are in good agreement with the calculated maximum P_C of 89%, which was achieved at a converter section length of $55 \mu\text{m}$ for these waveguide core profile dimensions (dashed line). It is believed that the good agreement is based on the fact that the undercut in the waveguide core profile pinches-off the mode from the lower cladding and keeps it concentrated in the core area. The actual difference in the shape of the lower cladding layer in the simulated waveguide profile (Figure 8-2(Insert)) to the one of the fabricated device (Figure 8-15(b)) has therefore no impact. In general, deviations of data points from theoretically predicted values can occur due to inaccuracies of the refractive index models

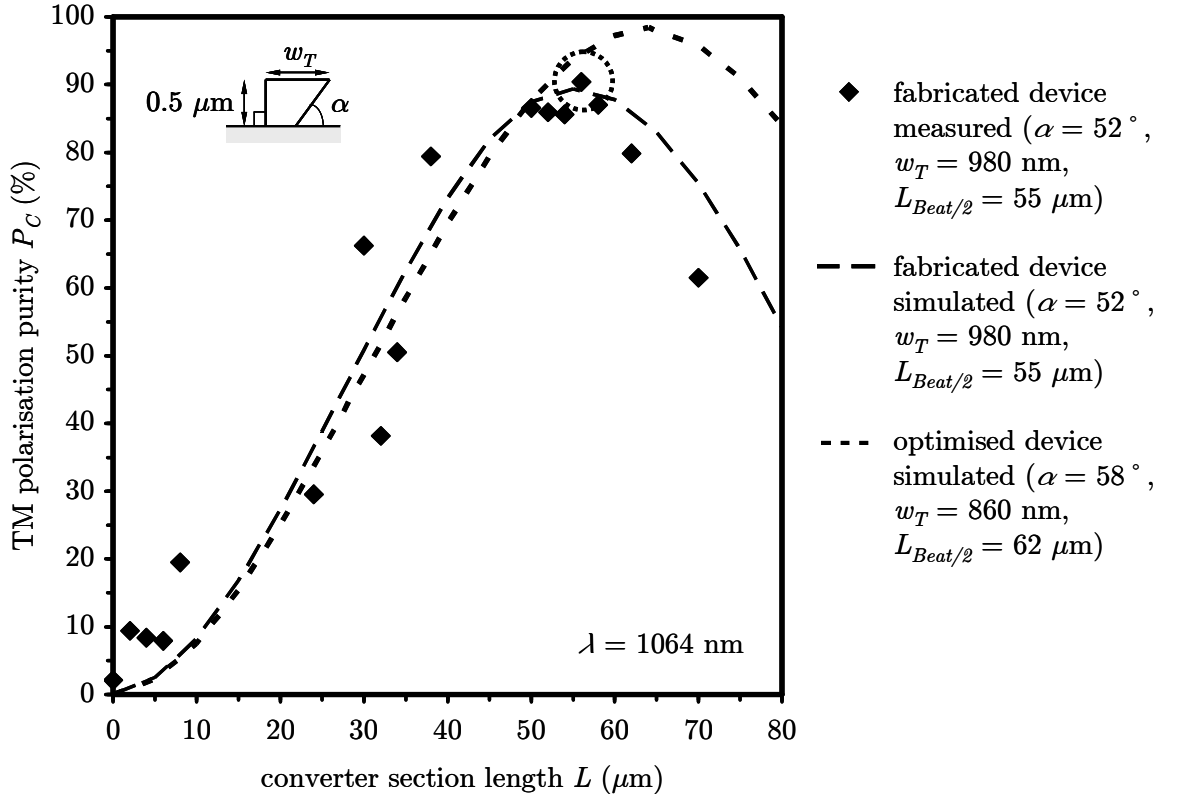


Figure 8-16: Measured and calculated TM polarisation purity at the output of the device versus the converter section length for a TE polarised input signal at $\lambda = 1064$ nm.

for semiconductor materials used in the simulation as well as due to possible slightly thickness deviations of the deposited semiconductor layers from the modelled wafer structure. Badly cleaved input- and/or output waveguide facets also contribute to deviations from theoretically predicted values as coupling errors occur due to the use of the end-fire coupling technique. In comparison, the theoretically optimised device achieves a P_C of 98% at $L_{Beat/2} = 62 \mu\text{m}$ (dotted line) for $\alpha = 58^\circ$ and $w_T = 860 \text{ nm}$. This confirms the earlier theoretically investigated fabrication tolerances, which predicted a P_C - drop by 10% for a deviation of the actual waveguide core dimensions from the optimised ones of about 10%.

8.6.2 Losses

The insertion loss and propagation loss of the realised device were evaluated via the cut-back method as described in chapter 4. The trend line of the linear extrapolated normalised measured total power, expressed by the linear function $y = -0.0017x + 0.72$, yielded an insertion loss of 1.4 dB and a propagation loss of 1.2 dB / 100 μm - caused by the converter section. The encircled data point corresponds to a fabricated device with a converter section length of 56 μm ($\alpha = 52^\circ$, $w_T = 980 \text{ nm}$) - imposing a total device loss (including propagation- and insertion/exit losses) of 0.47 dB. The scattering of the data points from the trend line is a result of coupling errors that occur due to the application of the end-fire coupling technique.

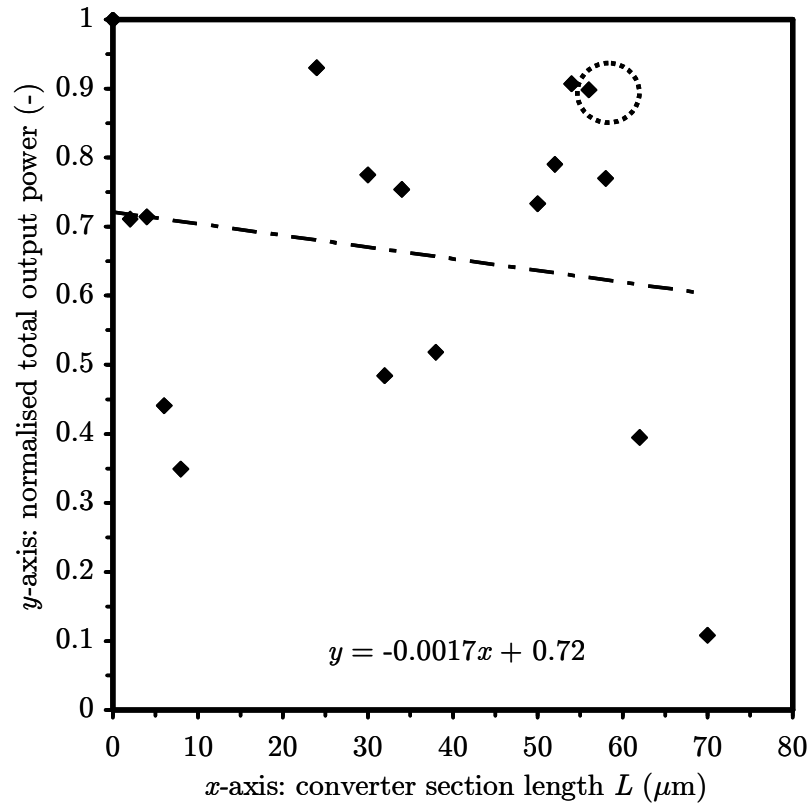


Figure 8-17: Normalised measured total power at the output of the device versus the converter section length. The linear extrapolation of the measured data is indicated by the chain dotted line and expressed by the mathematical formula $y = -0.0017x + 0.72$.

8.6.3 Wavelength dependence

The device was optimised for a designated wavelength ($\lambda = 1064$ nm). Figure 8-18 illustrates the calculated wavelength dependence of the TM polarisation purity P_C for both the theoretically optimised device ($\alpha = 58^\circ$, $w_T = 860$ nm and $L = L_{Beat/2} = 62$ μm) and the fabricated device ($\alpha = 52^\circ$, $w_T = 980$ nm and $L = 56$ μm). As the dimensions of the converter waveguide cross section profile are close to the mode cut-off at the designated wavelength, modes at wavelengths higher than the designated are therefore not excited in the waveguide. The designated wavelength represents the upper limit of the operational wavelength range of the device. This is indicated by the horizontal line at $\lambda = 1064$ nm. In the wavelength range from 950 nm to 1064 nm, a P_C - decrease of approximately 12%/100 nm, with respect to the designated wavelength $\lambda = 1064$ nm, occurs for the theoretically optimised device. A P_C - decrease of approximately 18%/100 nm, with respect to the designated wavelength $\lambda = 1064$ nm, occurs for the fabricated device within the investigated wavelength range from 850 nm to 1064 nm. This is indicated by the chain-dotted triangles in Figure 8-18. The lower limit of the operational wavelength range of the device is determined by the bandgap energy of GaAs (1.43 eV), which corresponds to a wavelength of 867 nm at room temperature.

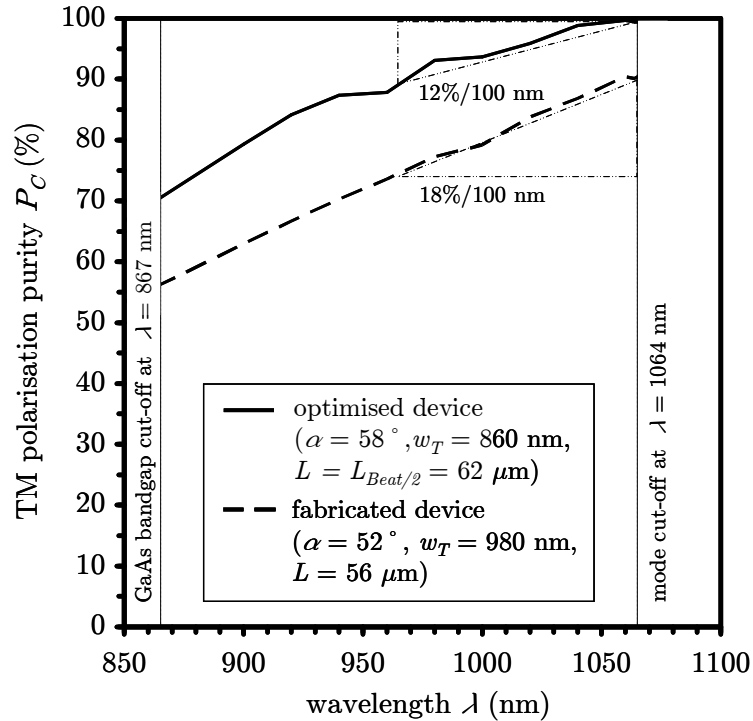


Figure 8-18: Simulated wavelength dependence of the TM polarisation purity P_C for the theoretically optimised device and the fabricated device.

8.7 Summary

This novel, on the principle of mode beating based, passive polarisation converter design bypasses mask realignment errors at subsequent etch steps which can occur in other converter designs. Here, a tilted undercut in the cross profile of an existing stripe waveguide structure was introduced on a GaAs/Al_{0.27}Ga_{0.73}As wafer structure. A converted TM polarisation purity P_C of 90% for a converter section length of 55 μm and waveguide width w_T of 980 nm was achieved for an operating wavelength of $\lambda = 1064$ nm. The optical loss imposed by this device was evaluated to be 0.47 dB via the cut-back method.

Chapter 9

Conclusions and perspectives towards future developments

Two novel integrated passive polarisation converter designs were introduced, rigorously theoretically optimised, fabricated and characterised. These on mode beating based designs were realised in a single reactive ion dry-etch process step, utilising an in-situ custom built sample holder incorporating a recessed slanted groove. As the height of the sample holder of 5 mm is limited by the headroom of the slit valve between the load lock and the etch chamber of the RIE machine, the geometrical width of the sample is limited to 5 - 7 mm, depending on the angle of the sample holder slope.

The first passive polarisation converter design, which consists of two sloped waveguide sidewalls, was initially realised on a passive GaAs/AlGaAs material structure. Initially appearing etch-mask misalignment problems - which cause etch-overlaps into adjacent waveguide sections at the converter section periphery - were solved by introducing transversal rib waveguide stripes at the intersections. This fabrication method also allows the implementation of adiabatic tapers comprising sloped waveguide sidewalls in order to avoid any mask (re-)alignment problems and mode size matching at the converter section periphery.

The implementation of this design on an unstrained GaAs/AlGaAs DQW heterostructure was used to realise a Fabry-Perot laser diode comprising a monolithically integrated single-section passive polarisation converter in the cavity.

This realised device demonstrated only the principle of incorporating a passive polarisation converter in the cavity and is by no means an optimal structure. For other than narrow line width applications, it may be desirable to further reduce the optical loss at the intersection between at the pumped shallow etched section and the deeply etched converter section. This could be achieved e.g. by apodisation, in order to reduce unwanted coupled cavity effects.

An optimisation of the converter section geometry fabrication should allow the device polarisation purity to approach 100%, as predicted by theoretical calculations.

The non-pumped, angle-etched section (converter plus tapers) experiences significant band-tail absorption and it is only because this entire section is relatively short that lasing can be observed albeit at raised threshold current levels. The influence of the optical losses in the non-pumped section were ascertained by further cleaving of the device to isolate the current-pumped section, where the threshold current was observed to decrease by 12%.

This parasitic band-tail absorption in the passive sections could be eliminated using selective area *quantum well intermixing* (QWI) prior to waveguide fabrication [1, 2].

The second passive polarisation converter design is based on the modification of an already existing stripe waveguide structure. This method bypasses mask realignment errors, which can occur in other passive polarisation converter designs at subsequent etch steps. As this converter design does not require crucial mask alignments and the minimum feature size in this device is 980 nm (for the given material structure and wavelength), it offers the option for the utilisation of photolithography in the fabrication of the entire device.

In general, the accurate adjustment of the fabrication process regarding the optimum sidewall slope angle(s) and the waveguide width imposes an important and crucial necessity for both device designs.

As the optimum operating point in these device designs is close to the mode-cutoff dimension of the waveguide, the evanescent tails of the mode field distribution in the waveguide are close to the waveguide sidewalls. The propagation loss due to rough waveguide sidewalls could therefore be reduced by smoother waveguide sidewalls. This could be achieved by applying a spin coated *hydrogen silsequioxane* (HSQ) [3] mask - which offers a higher dry-etch durability than the used PMMA/SiO₂ mask - for the stripe waveguide outline transfer.

It is believed that these novel reciprocal polarisation converter device designs will enable effective control of the state of polarisation in many potential integrated optoelectronic devices and applications.

The monolithic integration of a polarisation converter within a semiconductor laser diode introduces a useful functionality, which can be applied to on *polarisation division multiplexing* (PDM) [4] based optical transport systems. Moreover, by establishing a polarisation conversion of 50% by modifying the converter section length, this device demonstrates the integration of two essential components, which, when combined with a nonreciprocal mode converter [5], would allow a monolithically integrated optical source and isolator to be realised [6].

9.1 References

- [1] Marsh J. H., "Quantum well intermixing", *Semiconductor Science and Technology*, vol. **8**, pp. 1136 - 1155, (1993).
- [2] Kowalski O. P., Hamilton C. J., McDougall S. D., Marsh J. H., Bryce A. C., Button C. C. and Roberts J. S., "A universal damage induced technique for quantum well intermixing", *Applied Physics Letters*, vol. **72**, no. 5, pp. 581 - 583, (1998).
- [3] Word M. J., Adesida I. and Berger P. R., "Nanometer-period gratings in hydrogen silsesquioxane fabricated by electron beam lithography", *Journal of Vacuum Science & Technology B*, vol. **21**, no. 6, pp. L12-L15, (2003).
- [4] Chraplyvy A. R., Gnauck A. H., Tkach R. W., Zyskind J. L., Sulhoff J. W., Lucero A. J., Sun Y., Jopson R. M., Forghieri F., Derosier R. M., Wolf C. and McCormick A. R., "1-Tb/s transmission experiment", *IEEE Photonics Technology Letters*, vol. **8**, no. 9, pp. 1264 - 1266, (1996).
- [5] Holmes B. M. and Hutchings D. C., "Demonstration of quasi-phase-matched nonreciprocal polarization rotation in III-V semiconductor waveguides incorporating magneto-optic upper claddings", *Applied Physics Letters*, vol. **88**, no. 6, pp. 061116.1 - 0061116.3, (2006).
- [6] Hutchings D. C., "Prospects for the implementation of magneto-optic elements in optoelectronic integrated circuits: A personal perspective", *Journal of Physics D: Applied Physics*, vol. **36**, no. 18, pp. 2222 - 2229, (2003).